SYNTHESIS, FABRICATION AND CHARACTERIZATION OF SOLID TITANIUM DIOXIDE - BASED SOLAR CELL DOPED WITH DIFFERENT ORGANIC AND INORGANIC LUMINESCENT MATERIALS

NJOROGE DAVID KIMEMIA
I84/38848/2017

A THESIS SUBMITTED IN FULFILLMENT OF THE REQUIREMENTS FOR THE AWARD OF THE DEGREE OF DOCTOR OF PHILOSOPHY (ELECTRONICS AND INSTRUMENTATION) IN THE SCHOOL OF PURE AND APPLIED SCIENCES OF KENYATTA UNIVERSITY

JANUARY, 2024

DECLARATION

This thesis is my original work and has not been presented for a degree in any other University

Signature…… Date……..

SUPERVISORS

This thesis has been submitted for review with our approval as university Supervisors

Dr. WALTER K. NJOROGE
DEPARTMENT OF PHYSICS
KENYATTA UNIVERSITY

Signature……. Date……..

Dr. ISAAC W. MWANGI
DEPARTMENT OF CHEMISTRY
KENYATTA UNIVERSITY

Signature……. Date……

DEDICATION

I dedicate this work to my spouse Dr. Millcent Kimemia and my children Faith Wanjiku Kimemia and Simon Njoroge Kimemia.

ACKNOWLEDGEMENT

I want to express my heartfelt gratitude and appreciation to my supervisors: Dr. Walter K. Njoroge and Dr. Isaac W. Mwangi for their dediction , encouragement, intellectual direction, and constructive criticism throughout this study. I extend much appreciation to all Lecturers in the Physics department of Kenyatta University for the support they accorded me.

I acknowledge Kenyatta University and Muranga University of Technology for providing me with research equipment and space to pursue my experiment. Extended appricatıons goes the highlab enterprises who provided me with reagents which enabled me obtain the results reported in the study.

To my family members; my husband Mr. Kimemia, Simon Kimemia and Faith Kimemia, thank you for being a tremendous source of encouragement, and even more so for allocating sufficient time and family resources for this research. God bless everyone.

TABLE OF CONTENTS

LIST OF FIGURES

LIST OF TABLES

LIST OF ABBREVIATIONS, SYMBOLS AND ACRONYMS

Ag^{+}	Silver ion
Δ E	Change in Energy
A	Ammeter
Ag	Silver
AL	Alluminium
c	Velocity of light
C	Carbon
Ca (OH_2)	Calcium hydroxide
Ca	Calcium
CB	Conduction band
Cm	Centimeters
CO	Carbon monoxide
CQD	Carbon Quantum Dots
Cx	graphite
D:A	Donar: Acceptor
DCNC	Glucopyranosyl cellulose nonoxrystal
DIO	Diiodooctane
DNI	Direct Normal Irradiation
DSSC	Dyesentize solar cell
E_g	Energy Gap
EL	Electroluminescent
Er	erbium
Eu	europium
eV	Electron Volt

FF	Fill factor
FSC	Fluorescent Solar Cells
FTIR	Fourier Transform Infrared
FTO	Fluorine-dope tin oxide
H	Hydrogen
h	planks constant
I	Iodine
IR	Infrared
J_{MP}	Maximum Power Point Current Density
J_{SC}	Short Circuit Current Density
KI	Potassium Iodine
LEDS	Light Emitting Diodes
LSCs	Luminescent Solar Cells
mA	miliampere
Mm	millimeters
Mn	Manganese
Mn	Manganese
MoO	Molybdenum oxide
N	Nitrogen
Na	sodium
NIR	Near Infrared
nm	nanometer
Nm	Nonometers
NO	Nitrodide
NPs	Nanoparticles
NR	Nanorod
O	Oxygen

OH	Hydroxide
OPV	Organic Photo Voltaic
OPV	Organic Photovoltaic
OSCs	Organic Solar Cells
Pb	lead
PCDTBT	Poly [[9-(1-octylnonyl)- 9H-carbazole-2,7-diyl]-2,5-thiophenediyl-2,1,3 Benzothiadiazole-4,7-diyl-2,5-thiophenediyl]
PCE	Power Conversion Efficiency
PF	Photo Fluorescence
pH	Measure of acidity or basicity in an aqueous solution
PL	Photolumnescence
PLQY	Photoluminesense Quantaum Yield
P_{max}	Power maximum
PO	Phosphate ion
PSCs	Photosensitive Solar Cells
P-T	Potential difference with Time
PV	Photovoltaic
Rrec	Recombination Resistance
Rt	Transport resistance
Sb	Antimony
Sc/M	Semi-conductor metal hybrid
TiO_2	Titanium Dioxide
Tm	thulium
UCNP	Upconvernated nanoparticles
UV	Ultra-Violet radiation
V	Voltmeter

V_{mp}	maximum Power Point Voltage
V_o	Oxygen vacancy
V_{OC}	Open circuit Voltage
V-T	Voltage with Time
Yb	Ytterbium
Yf	Yttrium
ZnS	Zinc Sulphide
Ω	ohm
$\boldsymbol{\eta}$	eta
$\boldsymbol{\lambda}$	ramda
$\boldsymbol{\mu}$**A**	Micro ampere
$\boldsymbol{\nu}$	Frequency of light

ABSTRACT

Energy is globally recognized as an important resource for social and economic development. Majority of the world population relies on fossil fuels, hydro and solar radiation as a source of energy. Fossil fuels immensely contribute to air pollution and global warming. Solar cells have been exploited and controlled to generate electrical energy from solar radiation. The available solar radiation is not constant at all times of the day and differs depending on the season of the year. Consequently, the solar cell output varies with the incident radiation. The study investigated use of photo luminescent materials as dopants in the photoactive layer of TiO_2 –based solar cells with an aim to prolong the cell output in diminished radiation. Inorganic (Sb/Ca/Mn/Ag:) and organic (rhiodamine, allicin, gingerol, quinolone and neohesperidosyl: extracted from their fresh organic complexes) photo luminescent materials were used as dopants in TiO_2 photoactive layer of the solar cell while a mixture of graphite, iodine and potassium iodate was used as the receptive layer. The effect of varying mass ratios and the thicknesses of both photo active and the receptive layers was investigated based on the solar cell output parameters. The synthesized inorganic (Sb/Ca/Mn/Ag) and the extracted organic luminescent materials were chemically characterized using the FTIR. Different masses of the photoactive TiO_2 material, inorganic and organic luminescent materials were weighed separately and compressed to form the photoactive layer. Known masses of graphite powder mixed with a matrix of potassium iodate (KI_3) were introduced into the molding dice over the photoactive layer and compressed to bind them sufficiently. Potential and short circuit generated by the cells were monitored and the data obtained used to determine their fill factor, and efficiency. The study concluded that the inorganic (Sb/Ca/Mn/Ag) and organic rhiodamine, flourene, allicin, gingerol, quinoline and neohesperidosyl particles absorbed radiation at different wavelengths. The absorption bands were evident at {(360 – 3750), (434.96-3950), (697.28-3750), (290.29-3850), (463.89-3850), (260.39-3750) and (273.90-3700)} cm^{-1} respectively. All the investigated photo luminescent materials showed promising properties for improving solar cell output in diminished solar radiation. The results obtained also showed different potential delay by the varied thicknesses with improved responsivity and efficiency. The fabricated solar cell employing rhiodamine doped -TiO_2 photoactive layer (0.136) mm and 0.164 mm receptive thickness layer had the highest open circuit voltage (V_{OC} =1.023V), and a residual potential of 0.586 V in diminished radiation after one hour. The corresponding fill factor and efficiency were determined as 0.416 and 2.32%, respectively. The study also concluded that optimized FSCs layers generated enhanced open circuit and residual potentials (V_{OC}) observed after 60 minutes. The study recommends that dopant synthesis should be expanded to enhance further d-orbitals splitting for improved charged species d→d transitions and transpose IR spectrum into fluorescence, dopants molecular size with less energy instability should be extended to achieve uniform potential difference with less attenuation, wider dopants complexes ratios should be done to minimize recombination at the convergence within the solute and enhance quantum yield for higher charge carriers' densities excitation, modified ratios relative dimensions should be investigated together with ambient conditions moderating pigments to balance FSCs interacting systems for uniform output parameters.

CHAPTER ONE: INTRODUCTION

1.1 Introduction

This chapter includes background information, statement of the problem, objectives of the study and justification.

1.2 Background Information

Evolution of organic−inorganic photo luminescent solar cells (PSCs) has accomplished notable progress in photovoltaics (PV). The high performance and low-cost solution-based processes used for their fabrication technology attest to their potential future utilization. Interestingly, with their enormous potential properties, perovskites have found numerous applications beyond PV, expanding into light emitting diodes, photo detectors, X-ray detectors, memory devices among others. Such multiple functions have advanced considerable interdisciplinary research.

The vast majority of the world's population relies on fossil fuels as a source of energy that immensely contributes to air pollution and global warming (Komolafe *et al.*, 2014). Others depend on energy from hydro sources which is challenged by temperature changes that result to rapid evaporation giving rise to reduced water reservoirs. The rest exploit solar radiation by the use of solar cell that is cost effective and environmental friendly. However, this resource is affected by weather and light conditions leading to inadequate and inefficient output. This affects sustainability of the required services negatively.

As solar cells have been exploited and controlled to generate electrical energy, there are limitations as solar radiation is not constant at all times of the day and also differs depending on the season of the year. The net result is reduction in the potential energy (PV) caused by such changes. Spectral losses contribute to low response and the

achievable efficiency of solar cells. Direct dependence of normal solar irradiation (DNI) using the existing solar cell devices is thus affected. To increase efficiency of such devices, there is need to enhance spectral radiation by use of photo luminescent (inorganic and organic) materials which trap incident solar radiation, at a certain wavelength and release emissions at a different wavelength later. Such a delay was utilized to extend supply of energy for a predetermined period after the source of solar radiation diminished (McArthur *et al.,* 2010). Antimony and manganese doped calcium phosphors discovered in 1942 has the ability to transform ultraviolet radiations to delayed emission for a prolonged length of time (Shiyou, 2013).

A study by Basnet *et al.* (2019) reported the application of TiO_2 microcrystalline powders as a heterogeneous catalyst with ability to generate electrons and holes in the presence of light. Addition of activation dopant in TiO_2 increases radiation absorption in the whole visible region and was used to enhance electroluminescence time from milliseconds to several hours (Qu *et al.,* 2015). Calcium compounds form double-activated crystal structures which accommodate Sb^{3+} ions and Mn^{2+} ions into their apatite lattice sites. The radiation absorbed by Sb^{3+} ions in the crystal lattice was partly transferred to Mn^{2+} ions leading to high electroluminescence (EL) with a narrow band gap (E_g) (Pandey *et al.,* 2006). When doped TiO_2 was illuminated with UV radiation, the impurities introduced energy levels which downshifted solar radiation in the energy gap between valence and conduction bands (CB) (Li *et al.,* 2016). The downshifted radiation stimulated electrons towards the conduction band and they were trapped into the d-donor levels for a while until they relaxed to the valence band thus emitting lower energy photons (Park, (2018).

Schwede *et al.* (2010) and Tummeltshammer *et al.* (2016) reported that the absorbed energy is transferred to the neighboring luminescent impurities and emitted after a specific time of delay as illustrated by the following equations.

$$Ca^{2+} + hv \longrightarrow (Ca^{2+})^*$$
$$(Ca^{2+})^* + (Sb^{3+}) \longrightarrow Ca^{2+} + (Sb^{3+})^*$$
$$(Sb^{3+})^* + (Mn^{2+}) \longrightarrow (Sb^{3+}) + (Mn^{2+})^*$$
$$(Mn^{2+})^* + (Ag^{1+}) \longrightarrow (Mn^{2+}) + (Ag^{1+})^*$$
$$(Ag^{1+})^* \longrightarrow (Ag^{1+}) + hv$$

A study by Qu *et al.* (2015) reported that when doped TiO_2 was exposed to solar radiation, electrons were excited and migrated towards the conduction band (CB). They were captured for a short period by the empty defect levels below the conduction band. According to Alkiswani (2015), materials such as calcium, antimony, manganese and silver have been found to have a persistent afterglow after withdrawal of incident radiation and thus find a large scientific application in the exploitation of that afterglow. Calcium and antimony compounds are widely applied to manufacture battery anodes because they exhibit superior cycling stability with high charge retention capacity of 87.7% (Liu *et al.*, 2016). Li (2016) noted that a mixture of the phosphor material at varying ratios yielded different afterglow durations. This study exploited this observation to establish the ratio that can result in the desired radiation required to satisfy the optimal performance of a TiO_2 solar cell co-doped with the different mixtures.

The doping which homogeneously distributes the phosphor material with the photo effective material enhances distribution and subsequent maintenance of the emitted light resulting to better charge compensation as electrons migrate (Chen *et al.*, 2013). This migration of electrons was made possible by use of potassium iodate and

graphite which are inert and have unique conducting electronic properties (Chen and Wu, 2016; Umemoto *et al.*, 2019).

After considering the high absorption of co-doped TiO_2 and its subsequent generation of high amount of charge carriers, this study considered fabrication of photo cell with improved potential to operate after solar radiation diminishes. It was investigated by using powdered TiO_2-doped with different photo luminescent materials of both organic and inorganic origin separately. The study exploited their persistent time of afterglow emission due to the doped luminescent materials producing radiations of different wavelengths. The impurities consisted of (Sb/Ca/Mn/Ag) inorganic compound, and organic materials derived from highlighter dye, flouren, ginger, garlic, tonic water and bitter lemon which introduced defect traps and alter the band gaps of TiO_2 (Gao *et al.*, 2019). The fabricated solar cells were found to have improved light harvesting properties and prolonged dispersion of the emitted light.

The effect of varying impurity mass ratios on the delayed radiation combined with the net incident energy was explored to optimize on the time resolution before interacting with the photo active material.

1.3 Statement of the Problem

Photoresponsivity is notably important for social and economic operations. Extensive work has focused on development of photoresponsivity to harness solar energy for practical application. Al-Alwani *et al., (*2016) and Fakharuddin *et al.,* (2019) noted that there are significant disparities in the level of potential generated by photocells which are fabricated using pure photo active materials to the fluorescent enhanced doped host photosensitive materials. The available solar radiation is not constant at all times of the day and differs depending on the season of the year. Consequently,

the solar cell output varies with the incident radiation. The data on potential delay in diminishing natural radiation with time is very scanty. There is need to counter challenges on energy sustainance to sensitive health services, ladder, industrial and security systems. The study by Al-Alwani *et al.*,(2016) noted that the developed photovoltaic devices have limited spectral responses. Their defficiency create room exploration of devices with improved output parameters and efficiency. Doping the desired photosensitive materials with suitable trases increases photoactivity for a wide absorption range. Prescence of luminescent dopants leads to stimulation of charge carriers by internally activated radiation to the host material when the incident radiation is disturbed. The available photo cells waste much of the near-infrared (NIR) - (UV) (750- 400) nm wavelength (λ) of solar spectrum. TiO_2 has a wide band gap of is not sensitive to radiation in the visible region. TiO_2 photovoltaic cells have a limited spectral response that limit their expected efficiency at different times and seasons of the year (Hamdoush, 2019). The current study applied radiation enhancement by use of dopants activated between (UV – IR) of {(750 - 400) nm and 1 mm} (λ) of solar spectrum which enabled achievement of longer time constant to supply activation energy to solar dependent devices. Titanium dioxide (TiO_2) with a wide (3.2 eV) band gap is known to generate electron in the presence of incident energy in the UV region. Doping TiO_2 with sensitizers would lower the band gap to extend their absorption range.Applied hybridized inorganic and organic dopants formed a sheath that reduced ingress of moisture and minimized susceptibility of solar radiation dependent devices to corrosion with low level of toxicity. The ability of TiO_2 to constantly generate multiple electron in the prescence of radiation established charge carriers traped in the dopant introduced defects for fluorescence

enhancement. The prefered dopants increased TiO_2 effective range and enhanced spectral energy in the prescence of natural radiation and when the source diminishes.

1.4 Objectives of the Study

1.4.1 General Objective

The objective of the study was to fabricate and characterize a TiO_2 based solar cell doped with different luminescent materials of both organic and inorganic origin for photovoltaic application

1.4.2 Specific Objectives

i. To investigate the properties of synthesized inorganic and the extracted organic dopants by chemically characterizing the luminescent materials.

ii. To explore the performance of fabricated TiO_2 - based solar cell doped with different organic and inorganic photo luminescent materials separately by
characterizing.

iii. To determine the effect of varying mass ratios of TiO_2: inorganic and organic photo luminescent impurities separately on the cell output parameters.

iv. To investigate the effect of different thicknesses of doped TiO_2 layer on the cell output parameters holding the receptive layer constant.

v. To investigate the effect of different thicknesses of receptive layer on the cell output parameters holding the photoactive layer constant.

vi. To fabricate and characterize a TiO_2- based solar cell doped with optimized mass ratios and thicknesses.

1.5 Justification

Development of solar cells takes advantage of the limitless solar radiation to generate potential energy (PV) from the sun radiations. However, these radiations are not constant at night and during varied weather conditions. At such times, the present solar radiation does not sufficiently activate photovoltaic cells to generate adequate and constant potential. By use of organic and inorganic photo luminescent materials, the absorbed radiation can be enhanced and released after a delayed duration. Such dopants are exploited to enhance photovoltaic activity and efficiency of photovoltaic cells. The Sb^{3+} and Mn^{2+} co-doped calcium halophosphate inorganic materials, highlighter dye, flourene, garlic, ginger, tonic water and bitter lemon biological organic chemical materials were preferred because of their stoke shift property for a prolonged duration within the UV region. The study introduced Sb^{3+}, Mn^{2+} and Ag^{1+} ions in the lattice sites by doping TiO_2 photo active material with inorganic synthesized double-activated Sb/Ca/Mn/Ag, organic tonic water and bitter lemon beverage impurities. The substances were applied to introduce empty d-defects which trapped photon excited electrons to increase photoluminescence (PL) within the photo active material when disturbance of external optical fields occurred causing persistent emission for an extended length of time. This is expected to improve the photovoltaic activity and efficiency of the fabricated solar cells.

CHAPTER TWO: LITERATURE REVIEW

2.1 Introduction

This chapter gives an account of what has been reported by other findings in relation to this study. It contains, synthesis and chemical characterization of both organic and inorganic luminescent materials, fabrication and characterization of TiO_2 - based solar cell doped with different organic and inorganic photo luminescent materials separately, effect of varying mass ratios of TiO_2: inorganic and organic photoluminescent materials impurities separately on the cell output parameters, effect of different thicknesses of doped TiO_2 layer by varying their mass ratios on the cell output parameters holding the receptive layer constant, effect of different thicknesses of receptive layer by varying their mass ratios on the cell output parameters holding the doped TiO_2 layer constant, fabrication and characterization of a TiO_2- based solar cell doped with optimized mass ratios and thicknesses as well as summary of the identified gap.

2.2 Chemical Characterization of Organic and Synthesized Inorganic Photo Luminescent Materials

Reports by Chen *et al*. (2016), noted that most of the solar cells focus on 48% visible light solar spectrum. The near-infrared (NIR) and ultraviolet (UV) light of the incident sunlight is wasted in form of thermalization and non-absorption of photons. A study by Liang *et al.* (2018) reported that improving the power conversion efficiency (PCE) of photovoltaic devices is achieved by tuning the properties of interfaces when crystallization of photo sensitive host material layers complex is controlled, engineered the chemical composition of host complex and introduction of additives. According to Chen *et al.* (2016), host complex with a bandgap of about 1.5

eV absorbs only a small fraction of incident photons in the visible range (up to 800 nm), though the standard spectrum of AM 1.5 G sunlight ranges from 280 nm to 2500 nm.

Li *et al*. (2016) reported that only a few developed phosphors excite charge carriers under natural light. Antimony (Sb) is a multivalent element that bonds with ligands to form complexes which coagulate when oxidizing agents are added and changes its ionic valence (Barbooti, 2015). Reports by Wei *et al.* (2018) indicated that external excitation spectra shifted emitted energy of synthesized Mn^{2+}-doped ZnS DCNCs nano materials when change in band gap improved external quantum efficiency of up to 18%. Double-activated phosphors are applied in industries because of their ability to transform UV radiation into visible light emissions within a wide distribution of the solar spectrum (Joanna *et al.,* 2014). Presence of antimony compounds in sodium based battery anodes exhibits superior cycling stability with high charge retention capacity of 87.7% achieved after 200 cycles (Liu *et al.,* 2016).

Hydrothermally prepared inorganic structure of Ca and Ag origin formed a coating which allowed deposition of semiconductor-metal (sc/m) hybrid interface nanostructure sheath with electronic structured atoms (Rezazgui, 2016). These reduced to form defects with charge carrier traps dominated by varied Ag nanoparticles (NPs) with random physical interactions interfaces.

According to Ma *et al*. (2020), reorganization of excitation sites by partial substitution of cations increases phase stability of host material complex. The growing single crystal and resolution of its molecular and atomic configurations microstructure of provides a stable black-phase. Reports by Fang *et al.* (2016) indicated that Sb forms multiple isolable functional groups that are coordinated into one to three resulting to

two-, four-, six- or eight- electron donors with transition metal fragments of η1 (terminal), η2 (side- on) face- bridging modes. The resulted system generates polycyclic species with ionic and molecular functional groups which binds to a central metal atom Mondal *et al.,* 2019). When photons strike the ionized complex, absorption of energy (hν) occur due to the resulted energy difference (ΔE) splitting the d-orbitals into several groups that differ in energy. These complexes emit photons as they return to their ground state with natural flourescence of shiny silvery golden colours, whose frequencies are at lower bandwidth than those of the absorbed radiation (Fang *et al*., 2016 and Ken *et al.,* 2020). A study by (Alkiswani, 2015) reported that luminescent phosphor has a long relaxation time glow in the dark .However, addition of activation dopants increase photo luminescence from milliseconds to several hours but varied due to oxidation of the photo luminescent materials (Alkiswani, 2015). These compounds are applied to manufacture low-pressure vapour discharge lamps, due to their high efficiency of converting radiation into visible light (Shiyou, 2013).

A study by Luo *et al*. (2019) noted that introduction of calcium impurities in the host material yields a sharp luminescence due to strong charge carrier distribution. Pandey *et al.* (2006) reported that double-activated crystals of Sb/Ca/Mn/Ag impurities accommodate Sb^{3+} ions and Mn^{2+} ions in their apatite lattice sites which partly transfer Sb^{2+} ions into Mn^{2+} centers leading to high photoluminescent (PL) with a narrow band gap (E_g). When illuminated with solar radiation, the excited electrons migrate away from the valency band (VB) towards the conduction band (CB), and they are trapped by the empty defect which then release light emission due to the

disturbance of external optical fields giving control of persistent duration (Qu *et al.,* 2015 and Li, 2016).

Researches by Ameta *et al.* (2018) indicated that antimony and manganese crystals are applied to enhance more light absorption within UV region which then improves luminescence of the solar cell and enhances its spectral response. This improved the duration of solar cell utilization even under minimum solar radiation (Horoz & Sahin, 2017). Transfer of charge carriers into electronic levels of Ag^{2+} lead to emission of UV radiations of short wavelength (Horoz & Sahin, 2017). Inorganic phosphors demonstrated high brightness with photoluminescence quantum yields (PLQYs) of over 90%, due to their relatively insulating nature and long radiative lifetimes result in high turn-on voltages and this limits their application in light emitting diodes (LEDs) (Smith *et al.*, 2019).

Tsai & Hamblin (2017) reported that the best powders which emit photoluminescence colours are frequency dependent and mainly applied with background lighting for their applications. Prescence of Nd^{3+} dopants within the structure of $CaAl_2O_4:Eu^{2+}$ yielded a strong emission peak at wavelength 440 nm corresponding to blue light. The resulted calcium complex was thought to contain divalent Ca^{2+} with electron transited from $4f^{6}$ 5d to $4f^{7}$ in Eu^{2+} (Fakharuddin *et al.,* 2019; Souza *et al.,* 2017). When organic flourene is exposed to different monochromatic radiations, it flourescence giving a myriad of colours ranging from blue to green to red depending on the frequency of the illuminating radiation as reported by Esmaelpourfarkhani *et al.*, (2023).

2.3 Fabrication and Characterization of TiO2 - Based Solar Cell Doped with Different Organic and Inorganic Photo Luminescent Materials

Photoluminescence have been exploited to promote emission of optical energy in lighting, display, solar cells, sensing and biomedical applications materials at diverse wavelength (Soni & Singh, 2019). Qu *et al.* (2015) noted that co-doped TiO_2 have a high photon absorption in the whole visible region. Life time of the excited electrons is usually longer than that of the excited state of partical which returns to the ground state instantly (Qu *et al.*, 2015). Emission of shorter wavelength occurred because the photon excited electrons acquired energy in excess to that derived from the exciting radiation (Park, 2018).

A study by Xia and Meijerink (2017) reported that the desired down shifting of the absorbed radiation was a consequence of mixing host material with varying ratios of phosphor. This altered the photo active material band gap and the fabricated photo sensitive electrode widened the light harvesting range (Hildebrandt, 2011; Lee, 2013). Semiconducting conjugated polymers organic materials are applied in OPV cells, since they possess the base property required to activate the fundamental mechanisms to transform the radiative energy of light into electric current (Zhang, 2013).

Kwanghee *et al.* (2010) reported that flourene have potential application in two-photon absorption dyes, fluorescent probes, and light-emitting materials because of its delay in fluorescence decay. According to Haubitz *et al.*, (2020), dioxolo [4, 5-f] [1, 3] benzodioxole) dyes have tunable photophysical properties of fluorescence delay due to stokes shift of the absorbed radiation. Some organic and inorganic materials acquired non-linear anti-stokes optical down-conversion properties with low photon energy input resulting to high energy output (Kwanghee *et al.*, 2010). This

fluorescence from carbon quantum dots (CQDs) is induced by the presence of radiative functional groups attached to the edge of the CQDs in garlic and ginger organic materials. Such materials can be manipulated to enhance delay in photovoltaic devices for sustenance of energy in the absence of natural sources (Chellamuthu *et al.,* 2019). A study by Spence (2019) noted that prolonged fluorescence in tonic water and bitter lemon beverages yield constant glow temporary in the dark environments and in photochemistry.

A study by Liao *et al*. (2016) reported downshifting of solar radiation and light emission from Cap Corse, sweet Malaga, Barolo Chinato, tonic water and better lemon beverages by observing constant fluorescence in dark environments. According to Liao *et al.* (2016), quinine which is an ingredient of tonic water contributed to outstanding glow of these organic materials when exposed to short UV radiation. A study by National Science (2016) noted that quinine processed from edible roots gives tonic water and bitter lemon a characteristic of brilliantly bright blue when exposed to ultraviolet radiation. The absorbed light energy, makes them excited, and release light emission as they return to their normal unexcited state. This experiment was conducted to tonic water glow in a dark room when a little bleach was added (Spence, 2019). Studies by Belitz and Wieser (2013) reported that cyclic dipeptides are persistent bitter than their corresponding open- chain peptides and their intensity of taste increases with higher density of closed chains in their molecules. Cyclo (Leu-Trp) was proposed as a bitter principle for soft drinks because of its open-chain. Reports by Yamamoto et al., (2016) indicated that heat-treated cyclic dipeptides isolate the; l-acetoxy-2,4-dihydroxyheptadeca-16-ene (77: R = CH_3CO) and l,2,4,-trihydroxyheptadeca-16-ene (77: R = H) complexes resulting to more open

chains. These complexes fluorescents when transferred to dark environment (Yamamoto *et al.,* 2016).

The photo activity of the cyclic dipeptides was observed to extend electron-hole generation for a longer duration at minimum solar radiation (Gong *et al.,* 2017). This reduced potential instability for practical applications (Gong *et al.,* 2017). Bi *et al.* (2016) fabricated a TiO_2 gell-metal halide solar cell with intense electroluminescence and excellent solar-to-electric power conversion efficiency of 15.3% with desirable time-resolution photoluminescence decay. When TiO_2 microcrystalline are modified, the downshifting of absorbed radiation occasioned to extended absorption range within infrared and visible regions at a high efficiency (Nikolai & Lev, 2010; Snaith, 2013).

Tricoli *et al.* (2019) reported that solar cells with downshifting impurities generate higher outputs. When doped with suitable phosphor materials, TiO_2 host material extends the absorption range to the visible region and beyond resulting to high efficiency (Pu *et al.,* 2013). Beng *et al*. (2020) reported that flouren organic material and its derivatives have a unique class of electron acceptors whose molecules form charge-transfer complex with electron donors. According to (Pupkaite, 2020 & Mehta *et al.,* 2019) flourene have been extensively employed as a photosensitizer and active constituent of photosensitive composites. Research by Mehta *et al.* (2019) reported that the band gap edge passivation induce the electrons conduction and increase the surface energy which prevent fluorescence decay. However, the cell lost 55% of its performance in 3 days due to oxidation and the aqueous solution contributed to air pollution (Quan *et al.,* 2016). N'Sondé and Lindo (2018) noted that glow-in-the-dark powders downshift radiations when illuminated with natural light. These powders

were preferred for the manufacture of glowing paints applied for advertisement and out-standing sign post visibility (N'Sondé & Lindo, 2018). Distribution and subsequent maintenance characteristics of the emitted light within the host materials is enhanced by the impurities for a wide range of light spectrum resulting to better charge compensation (Shiyou, 2013). Hildebrandt (2011) and Lee, (2013) reported that the presence of Ca/Sb/Mn/Ag dopant enhances absorbance of solar radiation with subsequent improved external circuit parameters. The duration at which a solar cell generates potential is extended by coloured afterglow impurities (Hildebrandt, 2011; Lee, 2013).

2.4 Effect of Varying Mass Ratios of TiO_2: Inorganic and Organic Photoluminescent Materials Impurities separately on the Cell Output Parameters

A study by Liang *et al.* (2018) noted that down-conversion occurred due ($NaYF_4$:Yb^{3+}·Tm^{3+}) dopants nanoparticles after absorption of optical radiation near 980nm bandwidth within the photo sensitive electrode. The light response properties of TiO_2 perovskite solar cells improved when the photo anode was doped with ($NaYF_4$:Yb^{3+}.Tm^{3+}) at (5:1, 2:1, 1:1 and 1:2) g mass ratios. The research reported that (22.01mA/cm^2, 67.42%, 16.07%, and 1.08V) of J_{SC}, FF,PCE and V_{OC} improved the parameters of the perovskite solar with dopants compared to (20.03 mA/cm^2 ,63.65%, 13.53% and 1.06V) control sample (Liang *et al.*, 2018). Chatterjee *et al.* (2020) and others investigated the effect of nanorod-nanoparticle (NR-NP) on nanocomposite photoanodes for dye-sensitized solar cell prepared by mixing nanorod and nanoparticle in different weight ratios. The mass ratio 1:1 had a well decorated surface with nanoparticles spread onto individual nanorods. The study achieved a

power conversion efficiency of 8.61% from TiO_2 nanorods which was synthesized from hydrogen titanate nanorod precursor: nanoparticles at 1:1 mass ratios which was 14% higher than control sample nanorods. These ratios provided pathways to the photogenerated charge carriers (Chatterjee *et al.*, 2020). A research by Liang *et al.* (2018) indicated that there was frequency deviation due to NaYF4:Yb^{3+}, Tm^{3+} on TiO_2 as-synthesized nanoparticles (UCNPs) core-shell mesoporous layers of (5:1, 2:1, 1:1 and 1:2) mass ratios. Both the light absorbance and the light scattering of the composite films increased, with the addition of UCNPs core-shell (Liang, *et al.*, 2018). These results suggested that the core-shell UCNPs enhanced as scattering centers and increased light paths within the mesoporous photoanode.

By optimizing the amount of the core-shell UCNPs in the TiO_2 mesoporous layer, the best efficiency of the devices was 16.07%, which was 18.7% higher than that of the devices without core-shell UCNPs. The obtained results indicated that significant enhancement in the performance of the photosensitive solar cells (PSCs) with the core-shell UCNPs contributed to light scattering, NIR light upconversion and electron injection from the UCNPs to the CB of TiO_2 (Liang *et al.*, 2018).

2.5 Effect of Different Thicknesses of Doped TiO_2 Layer on the Cell Output Parameters

A study by Shah *et al.* (2017) reported that optimization of the active-layer film-thicknesses resulted to sufficient light absorption, excitons dissociation and maximum charge carriers transportation. The porous rutile TiO_2 nanorod arrays (NRAs) with a large internal surface area was fabricated on the FTO (fluorine-doped tin oxide) substrate photoanodes in DSSCs, with 7.91% efficiency (Lv et *al.*, 2020). Photovoltaic devices with 60 wt. % ($1.8\mu m$ thickness), x-H_2P_c / indium luminescent

organic semitransparent photo active electrode generated V_{OC} of 0.39V, J_{SC} ($\mu A/cm$) of 180, FF of 0.33 and η of 2.12% (Zhang *et al.,* 2016). Kalpani *et al.* (2016) and others noted that enlarging TiO_2 dye sensitized solar cells film thickness from 5.57 to 12.73 µm resulted to an upward trend of short circuit photo current density (J_{SC}) from 10.29 to 12.98 mA cm^{-2} with enhancement of efficiency (4.85 to 6.07)%. Beyond 12.73 µm, there was increase in the number of trapping surface states, through which the back electron transfer were increased, resulting to lowering of Voc (Kalpani, *et al.,* 2016). The higher current density observed was due to improved conduction band edges of TiO_2 which shifted positively (Kalpani *et al.,* 2016). According to Erin *et al.* (2016), hole-collecting anode configurations affected solar cell efficiency and stability.

2.6 Effect of Varying Thicknesses of Receptive Layer on the Cell Output Parameters

Reports by He *et al.* (2020) noted that the anode of solar cells is crucial because when determining the capability of light harvesting, high electron transfer, low recombination and optimal as these affects the device efficiency. Zhou *et al.* (2014) noted that, carbon electrode in a solar cell system acts as a conductive electrode to transport holes to the external circuit. Graphite was preferred due to its suitable band edge positions and high electrical conductivity as a hole acceptor (Zhou *et al.,* 2014). He *et al.* (2020) noted that electrons and hole are injected efficiently into an n-type semiconductor and carbon electrode, respectively, because of bipolar perovskite and energy-level alignment. A study by He *et al.* (2020) used graphite to prepare a receptor electrode for conducting electrons sent by the photoanode because of its excellent conductivity and it does not support corrosion and achieved 9.08% PCE.

Ray (2015) indicated that graphite offers good connectivity (adhesion) and mechanical properties for holes collection at low resistance in solar cells. The ease of graphite manipulation in varied shapes at low temperature offered promising advantage for production of flexible solar cells (Ray, 2015). Zhou *et al.* (2014) employed these properties of graphite to fabricate the M-TiO_2/$CH_3NH_3PbI_3$/C HJ solar cell. Gao *et al.* (2019) applied graphite powder, potassium iodide and iodine to enhance charge carriers conductivity and indium-doped tin oxide to fabricate a receptor and photosensitive layers. The thickness of carbon film influences the electrical conductivity. Their study noted that thicknesses of {(2.1 $\pm$ 0.2) and (40.5 $\pm$ 1.5)} mm generated a potential of {(0.67, 0.76)} V, {(10.1, 16.27)} mA/cm^2 short circuit current densities and {(0.33), 0.53) %} FF with {(2.25, 6.6)%} photon conversion efficiencies (PCEs), respectively.

Reports by Tran *et al.* (2019) noted that thinner layers devices were more stable while the conventional electrodes which employed MoO_3/Al had higher resistance to degradation when compared to those of Au or Ag electrodes. Cells with MoO_3 in the receptive layer of 8 nm, 15 nm, 50 nm, 100 nm and 200 nm yielded efficiencies between 9.2%–9.8% (Erin *et al.*, 2021). Erin *et al*. (2016) also noted that thicknesses which exceeded 10 nm decreased the device PCE with hole-collecting electrode. However, lower parameters were observed for an 8 nm MoOx receptive layer thickness. Beyold a thickness of 200 nm, the series resistance of MoOx interlayers increased during their continuous operation due to increase in delumination and optical strain (Erin *et al.*, 2016).

2.7 Fabrication and Characterization of Doped TiO_2- Based Solar Cell with Optimized Electrodes Thickness

Wang *et al.* (2017) reported that optimization of solar cell electrodes was a requirement for the purpose of compensating polymer content with reduced charged species which improved their PCEs relative to their reference cell. A study by Zhou *et al.* (2014) reported that solidly combining carbon electrodes with $CH_3NH_3PbI_3$ layer without destroying their complex structures offered numerous possibilities to choose optimal ratios for the device. A study by Yin et al., (2017) explored alternative donor – acceptor (D:A) weight ratios to varying the concentration of 1,8-diiodooctane (DIO) in the acceptor layer to modify electron mobilities when investigating its effect on power conversion efficiencies (PCEs) of BHJ solar cells.

According to Kim *et al.* (2016) increase in Polycarbazole-decanyl-benzothiazole (PCDTBT) polymer content with constant DIO concentration reduced electron mobilities. To examine the effect of $CaAl_2O_4:Eu^{2+}$, Nd^{3+} phosphor on DSSC photovoltaic performance, (Luo *et al.*, 2019) fabricated photoelectrodes using varied fractions of TiO_2 pastes for dye-sensitized solar cells (DSSCs) application. The DSSCs' J_{SC} and PCE were found to improve with ($CaAl_2O_4:Eu^{2+}$, Nd^{3+}) phosphor particle content increase as TiO_2 matrix was increased to 5%. However, the DSSC photovoltaic performance was found to decline when the phosphor ratios increased beyond 5 %. Luo *et al.* (2019) reported that presence of varied interfaces resulted to rapid recombination of photogenerated electrons with holes which simultaneously hindered charge carrier transport. This caused reduction in the photocurrent due to increased recombination resistance (R_{rec}) and transport resistance (R_t). Kim *et al.* (2016) attributed this performance to rapid recombination of photogenerated

electrons with holes and perturbation of the charge carrier transport due to increases in the grains and interfaces. This suggests that addition of critical amount of the phosphor enhanced the DSSC light harvesting efficiency, by creating a greater number of light sources for the dye molecules in the photoelectrodes.

A study by Luo *et al.* (2019) was confirmed by (Zhou *et al.*, 2020) that mixing ratios were responsible for emission spectra for $TiO_2/CaAl_2O_4:Eu^{2+}$, Nd^{3+} composite. The ($CaAl_2O_4:Eu^{2+}$, Nd^{3+}) phosphor particles effectively converted UV irradiation into visible light absorbed by N719 dyes in DSSC photoelectrodes, enhancing a higher efficiency when the complex was mixed with TiO_2. Reports by Souza *et al.* (2017) and Zhou *et al.* (2020) indicated that luminescent decay due to phosphors irradiated radiations occurred in several tens of microseconds. According to Souza *et al*. (2017), the values of V_{OC} and FF did not change appreciably in response to the different phosphor mixing ratios, suggesting that the relatively small phosphor content did not perturb the functionality of the TiO_2 NP-based matrix. This behavior suggests that more photogenerated electrons were rapidly combined with the dyes and electrolytes, and also, that these electrons were directly captured by the excessive phosphors (Zhou *et al.*, 2021). The optimized IPCE was obtained at 5 % $CaAl_2O_4:Eu^{2+}$, Nd^{3+} phosphor content to the TiO_2 matrix confirming that that the presence of the phosphors critical amount played a key role of increasing the light harvesting efficiency in DSSCs (Yin *et al.*, 2017). A study by Kwon *et al.* (2017), indicated that compensation of electron mobilities in PCDTBT, 1,8-diiodooctane (DIO) was increased to sustain dispersion of the fullerene domains, for electron extraction.

According to Wang *et al.* (2017), the PCE of PTB7:PC71BM solar cells were enhanced by a factor of 10%, from that of a control device with a PCE of 7.0% and

7.7%. This contributed to enhancement of J_{SC} which increased from 15.1 mA/cm^2 of the control device to 16.8 mA/cm^2 of the polymerrich device. Wang *et al.* (2017) fabricated the polymer: fullerene OPV solar cell with reduced fullerene content. The J_{SC} of device was improved by the reduction of PC71BM content with a higher DIO concentration at an optimized thickness of PTB7:PC71BM bulk-heterojunction active layer of 90 nm, for the best PCE performing for t PTB7:PC71BM organic solar cells (Yin *et al.,* 2017).

When $CaAl_2O4:Eu^{2+}$ particles (without Nd^{3+} doping) were fabricated and exposed to the UV light irradiation, a strong major emission peak clearly appeared at ∼440 nm. This wavelength corresponds to blue light (Souza *et al.,* 2017). The results suggests that the obtained particles possessed monoclinic calcium aluminate phase doped with divalent Eu^{2+} (for blue emission) rather than trivalent Eu^{3+} (for red emission). Souza *et al.* (2017) and Zhou *et al.* (2020) noted that the emission was generated by electron transition from $4f^6$ 5d to $4f^7$ in Eu^{2+}. This confirmed that the originally white phosphor powder of $CaAl_2O_4:Eu^{2+}$, Nd^{3+} emitted blue light upon exposure to UV light irradiation in a dark room. However presence of light would blend the diverse wavelengths and the resolution present equally intense within the visible region.The emission intensity of the $CaAl_2O_4:Eu^{2+}$, Nd^{3+} increased when the role of $CaAl_2O_4:Eu^{2+}$, Nd^{3+} was examined in the TiO_2 matrix. A higher emission intensity in the wavelength range of (370–600) nm was clearly observed for the $CaAl_2O_4:Eu^{2+}$, Nd^{3+} -added TiO_2 composites than that obtained for the pure TiO_2 (Souza *et al.,* 2017 and Zhou *et al.,* 2020).

Report by Zhou *et al.* (2015) noted that different strategies are used to realize OPV cells with enhanced polymer contents. A study by Wang *et al.* (2017) indicated that

when DSSCs are exposed to sunlight for several seconds their current density of DSSC was extremely low. They employed well-known BHJ system PTB_7:$PC_{71}BM$ to fabricate polymer-rich OPV devices with better performances. Wang *et al.* (2017) reported that increased polymer content, reduced fullerene concentration in the BHJ with a consequence to suppression of electron mobilities. Intermittent reduction of fullerene concentration resulted to higher DIO concentration which further dispersed the fullerene domains, and enhanced retention of electron mobility during the process of electron extraction (Wadsworth *et al.,* 2020). Yin *et al.* (2017) reported the same strategy of re-optimization BHJs resulting to improved PCEs relative to their reference cell. The polymer-rich BHJ film exhibits improved optical absorption and hole mobility. The fullerene concentration polymer-rich improved the performance of other BHJ systems based on PCDTBT: $PC_{71}BM$ and PDTSTPD:$PC_{71}BM$ due to enhanced hole mobility by UV and visible absorption by the higher polymer contents (Yin *et al.,* 2017). Their finding provided an insight on the existing limitation of D: A ratio on the photovoltaic performance.

2.8 Summarry of the Identified Gap

The revieved studies reports that the host complex applied to develop photovoltaic devices have band gaps of 1.5 eV and below. This enabled only a small fraction of incident photons in the visible range (up to 800 nm) to be absorbed, though the standard spectrum of AM 1.5 G sunlight ranges from 280 nm to 2500 nm. Few of the developed phosphors are applied to excite charge carriers under natural light. Application of $LiYF^4$: Yb^{3+}, Er^{3+} as host materials for solar cells active materials harvested only near-infrared (NIR) of sunlight and transformed it into visible. The current study used TiO_2 with (3.2 eV) wide band gap which was moderated by

inorganic and organic dopants to extend absorption of solar spectrum between (UV – IR) (λ) of {(750 - 400) nm and 1 mm}.

The reviewed cells experienced reduced performance because of oxidation, and their liquid solution released pollutants into the air. The doped TiO_2 based cells in this study were void of poisonous emissions because the ingredients used were in powder form

Application of $LiYF^4$: Yb^{3+}, Er^{3+} solar cell active materials harvested only near-infrared (NIR) of sunlight and transformed it into visible light resulting to unstable source of energy production. The reorganization of excitation sites had partial substitution of cations which increased phase stability of host material complex. Co-doping TiO_2 resulted to high photo absorbility in the whole visible region.

Few of the developed phosphors are applied to excite charge carriers under natural light. The developed $AISnI_2SnF_2C$ based solar cells were susceptible to corrosion degradation with majority of their charge traps neutralized. These could only sustain potential for periods less than one hour. The hybridized inorganic and organic in this study formed a sheath that reduced ingress of moisture. When they were added to TiO_2, the result was a complex of crystals that were stable with a black-phase which subsequently distributed and maintained downshifted wavelength radiations for a wide range of optical spectrum that last for one hour and beyond.

The reviewed literature on receptive layers fabricated from MoO_3 / Al contributed to higher resistance and were prone to degradation due to corrosion. The receptive layer developed from graphite/ iodide/potassium iodate (C_X /I_2/ KI) complex powder in the current study did not support corrosion and had higher power conversion efficiency.

The complex offered good connectivity and mechanical properties for holes collection at low resistance in solar cells. The ease of graphite manipulation in varied shapes at low temperature offered promising advantage for production of flexible solar cells when applied in powder form.

CHAPTER THREE: MATERIALS AND METHODS

3.1 Introduction

This chapter includes research design, assumptions made, chemicals and reagents, analysis of functional groups, fabrication of the (Inorganic/Organic materials) doped -TiO_2 luminescent solar cells, I-V characterization, optimization of parameters, evaluation of the luminescent solar cell derived parameters and appraisal of the derived fluorescent solar cell parameters

3.2 Research Design

The experimental design which was carried out in this study was in three fold. These were systematically executed by synthesizing the inorganic dopants and extracting the organic luminescent materials, doping of TiO_2 photo catalyst to lower its band gap, fabrication and characterizations of the luminescent TiO_2 based solar cells. All the materials and experimental work of the entire study have been listed and explained in details giving details of the procedures and instruments used in the study.

The fabricated cells were characterized to establish their optimal output electrical parameters. The experimental research design was achieved by preparing solar cells with different mass ratios of TiO_2/ (Ca/Sb/Mn/Ag): I_2KI/Cx and TiO_2/ (highlighter dye, flouren garlic, ginger, tonic water and bitter lemon) composites after finely blending with a set of motor and pestle. The time-voltage and short circuit current density output parametric quantities were determined and the optimum variables applied to fabricate a solar cell with optimized mass ratios.

3.3 Assumptions made

i) It was assumed that the dark room would not have negligible irradiance.

ii) The solar density on the solar cell was assumed that it would not be uniform.

iii) The voltage drop in the digital meter leads was assumed that it would not be inconsequential to the output parameters.

3.4 Chemicals and reagents

Apparatus were cleaned using double deionized distilled water throughout the experiment.

Chemical reagents were sourced from Sigma Aldrich in their analytical grade form. The inorganic dopant complex (Antimony (Sb), Calcium Hydroxide [$Ca(OH_2)$], Manganese Oxide (MnO), Silver Nitrate [$Ag(NO)_3$]), the photo active titanium dioxide (TiO_2), and receptive layer materials {iodine (I_2), potassium iodide (KI) and graphite [C_X]} in their powder form were used. Analytical grade organic flourene powder was sourced from the supplier while bitter lemon, tonic water, Pink highlighter dye from pink highlighter pen, allicin and gingerol from fresh garlic and ginger were extracted after mixing them with accetone and double deionised distilled water. A rotary water evaporator was used for the extraction process. Analytical grade phosphoric acid together with dilute ammonium solution were applied in the preparation of inorganic luminescent material. The cells were made into circular discs of various mass ratios and composition, and their photo generation activities monitored.

3.4.1 Synthesis of Sb/Ca/Mn/ Ag phosphor materials

To prepare the inorganic fluorescent material, Sb/Mn/Ag doped calcium hydroxyapatite, 0.22g Sb, 12g [$Ca(OH)_2$], 0.2g (MnO_4) and 0.04g of $AgNO_3$ were weighed into a (250ml) beaker and 20 ml of dilute phosphoric acid (H_3PO_4) was added drop wise. The solution was thoroughly stirred using a stirring rod as 10 ml of

aqueous ammonium solution was added drop wise adjusting the pH of the system to 8. The stirring continued until a homogeneous phase was formed. The mixture was then placed into an oven at a temperature of 140 ^{0}C for 48 hours. The resultant was allowed to cool to room temperature then washed with acetone to remove ionic impurities then ready for use.

3.4.2 Preparation of Organic luminescent materials

Rhiodamine from pink highlighter dye was obtained by soaking wet foam of the highlighter dye content into (3ml) acetone while quinine was extracted by evaporating 300 ml of bitter lemon and tonic water soft drinks using a rotary evaporator. Allicin and gingerol were derived by mixing (2 kg) of minced fresh garlic and ginger with 100ml of accetone and double deionised water. Extraction was then carried out using rotary evaporator at 70^{0}C.

3.5 Analysis of functional groups

A Shimadzu FTIR 2014 model spectrometer with ATR mode was used to confirm the presence of functional groups responsible for luminescence. The beam detector and splitter within the equipment analysed the variation of the IR spectra due to the inorganic and organic materials particals three dimension motion. Figure 3.1 shows the schematic presentation of the FTIR.

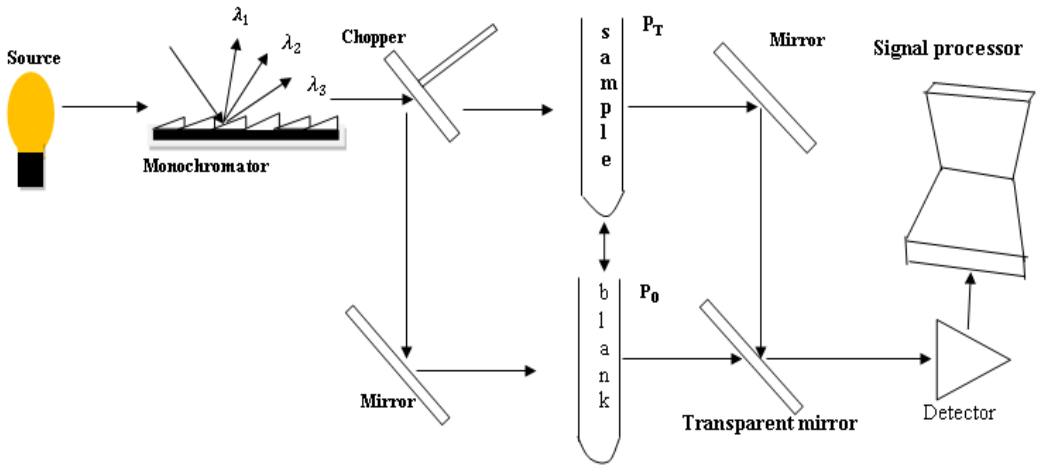

Figure 3.1: A schematic presentation of the spectrometer (for IR absorbance measurement) as applied by Hunt & Speakman (2015)

3.6 Fabrication of the (Inorganic/Organic materials) doped -TiO2 Luminescent Solar cells

This was achieved by taking varying masses within the range (0.1-0.8) g of the finely ground photo active material in a molding pellet press and the material compressed at a constant pressure of 10000 psi. The anode layer was prepared by varying mass ratios from (0.12:0.1) g to (0.2:0.5)g of I_2KI/Cx mixture and disposed on the previously molded photo active disc. The resulting respective discs were then carefully removed and placed on a conductor to monitor the cell properties.

3.7 I-V Characterization

The I-V characterization of the cells was carried out using the circuit shown in Figure 3.2.

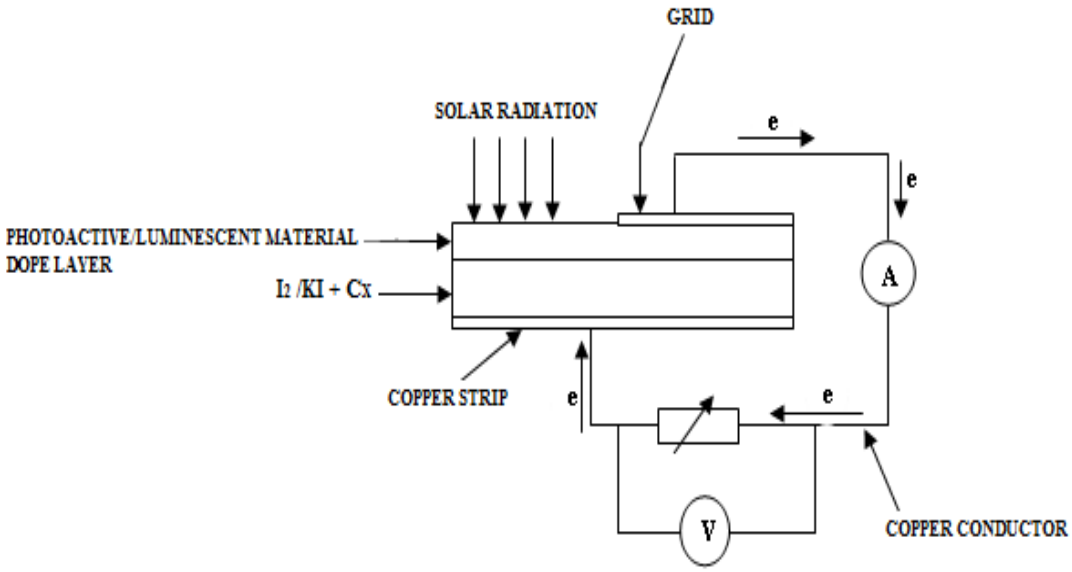

Figure 3.2: I-V Characterization Circuit as applied by (Jiang et al., 2010)

The like polarities of a (0 – 10 A) ammeter and those of the dynamic cells terminals were connected together, with a set of a highly sensitive (0- 40) Ω potentiometer shunted to a (0- 50) V galvanometer inserted between them. The assembly was employed to monitor the current density (J_{SC}) and open circuit potential (V_{OC}) output parameters of the regenerative fluorescent solar cells (FSCs) which were adopted to construct I-V characteristic curves similar to the one illustrated by Figure 3.3.

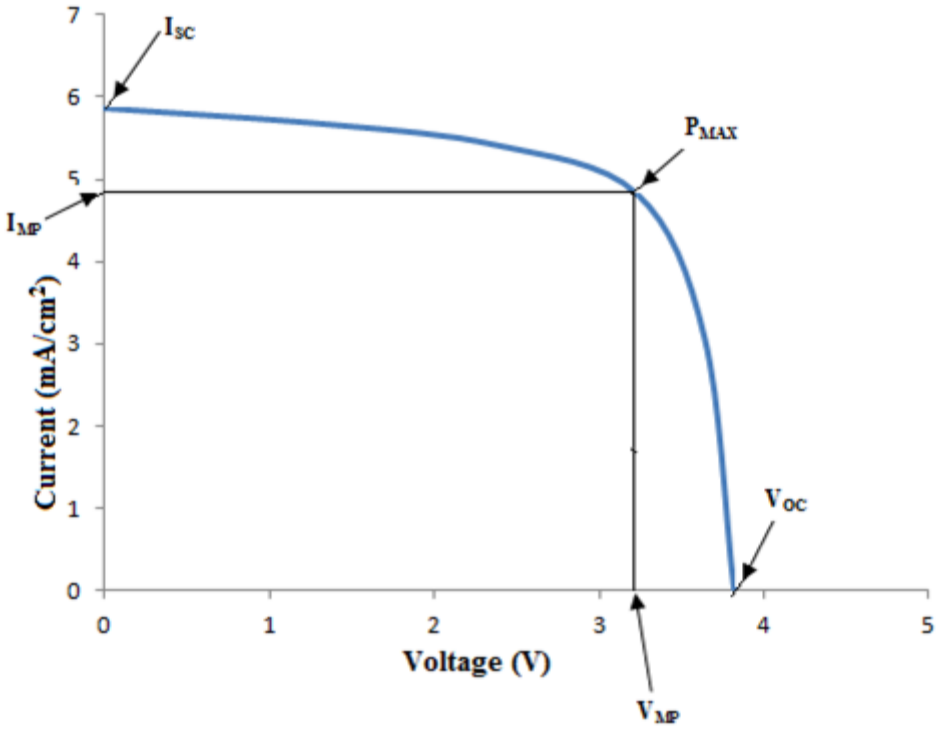

Figure 3.3: I-V Characteristic Curve for the TiO_2 doped Fluorescent Solar Cell (FSC) (Sharma et al., 2021)

The variable resistor served the purpose of an external energy dissipating element as the observed potential (V_{MP}) ratios to the established charge carriers opposition validated the current density (J_{MP}). The magnitude of the current density (J_{SC}) generated was ascertained at negligible potential in clear daylight. In addition, a set of I-V characteristic assembly together with a stop watch were applied to assess the open circuit voltage (V_{OC}) V and (V-T) with time (minutes) for one hour upon transfer of the cell to a darkroom as applied by Sun *et al.* (2018).

The ratio of terminal short circuit current to the area (I_{SC}/A) and the open circuit potential (V_{OC}) generated by the fabricated fluorescent solar cells were evaluated and the data obtained applied to determine the maximum power (P_{MAX}) output, fill factor, efficiency and the current density. The results were analysed to determine the

optimum thicknesses and the mass ratios properties of the samples applied to enhance charge generation of the materials used to fabricate fluorescent solar cells.

3.8 Optimization of parameters

To determine the mass ratios that would present exceptional edge of the cells output parameters, the fluorescent dopants and TiO_2 host matrix mass ratios, optimization experiments ensued to investigate the suitable values that would retain the highest potential (V_{OC}) with time of potential decay, and the optimal parameters were applied to fabricate the optimized cell.

Beer-Lambert Law equations were used to analyse the cells parameters as applied by (Manyasree *et al.,* 2018). According to Manyasree *et al.* (2018), the amount of homogenous particals in a sample and its thickness is proportional to the absorbed UV-visible spectrum. Beer-Lambert set of equations were applied to minimize the overlapping absorption bands after the samples absorbed photon energy where change in energy within the sample occurred. The relationship between energy (joules), frequency and wave number were determined by equations (3.1) as applied by Sohrab (2021) when analyzing statistical kinetic theory of practices.

$E = h\nu = \Delta E =$

$\frac{hc}{\lambda}$(Joules)…….... (3.1)

where h is Planck's constant, which has a value of 6.626×10^{-34} J s.

The observed parameters from the I-V characteristic set were as outlined in Table 3.1.

Table 3.1: Parameters observed from the luminescent solar cell terminals

Measured Parameters
Open circuit Voltage (V_{OC}/A)
Short Circuit current density (J_{SC})
Residual potential (V/A)

3.9 Evaluation of the Luminescent solar cell Derived parameters

The fluorescent solar cells {Ø 1.4 cm (A = 1.539 cm^2)} dimentions in this study were applied to computed the parameters outlined in Table 3.2 as applied by Jao et *al.* (2016) while calculating 1.5cm^2 rectangular blocks cells parameters.

Table 3.2: Expressions for calculating the derived parameters of the fluorescent solar cells

Parameters to be Calculated
Maximum Power (P_{MAX}) = (J_{MP}) × (V_{MP})
Total radiant PIN = 1000W/m^2 = 100 mW/cm^2
Fill Factor(FF)= $\frac{J_{MP} \times V_{MP}}{J_{SC} \times V_{OC}}$
Efficiency (η) = $\frac{V_{OC} \times I_{SC} \times FF}{P_{IN}}$

3.10 Appraisal of the Derived Fluorescent solar cell parameters

Open Circuit Voltage per unit area (VOC)/cm2 = $\frac{V_{OC}}{A}$ (V/cm2). Jain (2013) reported that the voltage of a unit area (V_{OC}/cm^2) delivered by a solar cell when the electrodes are isolated represents the maximum potential energy stored to initiate the

flow of electrons which are yet to be dissipated. This parameter was measured at the cells terminals.

Maximum Power Point Voltage (V_{MP}/cm^2). Jao *et al.* (2016) noted that the maximum voltage per unit area (V_{MP}) for a solar cell characteristic curve is the voltage that gives the maximum power point on the I-V curve.

Short-circuit current density (J_{SC}). This is the density of charge carriers per unit area of a solar cell when the voltage is zero: is the same condition as when the two electrodes of the cell are short-circuited together and, (J_{SC}/cm^2) is the photocurrent density (Potscavage, 2011).

Maximum Power Point current density (J_{MP}) was the amount of charge carriers per unit area at maximum power point (Chen *et al.,* 2020) whose values were derived from the I-V curves of the solar cells.

Fill Factor (FF). Yella *et al*. (2011) reported that fill factor (FF) is a measure of how the I-V characteristic of an actual PV cell differs from that of an ideal cell when calculated from the maximum power equation as outlined in Table 3.2. Graphically, FF is the measure of the squareness of the solar cell I-V curve (Adegbenro, 2016)

Maximum Power Point (P_{MAX}). Nizamettin (2018) reported that (P_{MAX}) is the product of (J_{MP}) and (V_{MP}) of the rectangle formed by the largest rectangle, of the two axes representing the point of maximum power output of an I-V curve. Power of incident light (PT) is the total incident energy on the surface of the cell ($P_{IN} = 1000 W/m^2 = 100 mW/cm^2$) (Scott, 2009).

Wavelength (λ meters). Campos-Fernández et *al.* (2011) noted that wavelength (λ) is the distance between successive maxima of a waveform and the frequency (`v') of electromagnetic radiation differs from one medium to another.

CHAPTER FOUR: RESULTS AND DISCUSSION

4.1 Introduction

This chapter reports on the results obtained from the experimental work in this study. These results are discussed according to their order in the experimental methods. The results are presented in spectral data as well as in Tables and are each discussed in their respective sections each providing evidence for the improvement of the performance of the photo active material.

4.2 UV and FTIR spectra analysis of the fluorescent materials

The Sb/Ca/Mn/Ag inorganic semiconductor-metal (sc/m) hybrid powder was observed to vary from brown, light blue, blue to red before fading gradually under UV radiation sourced from a UV lamp. The sample powder was then relocated to an FTIR spectrometer for absorption analysis and the observed spectrum was presented in Figure 4.1.

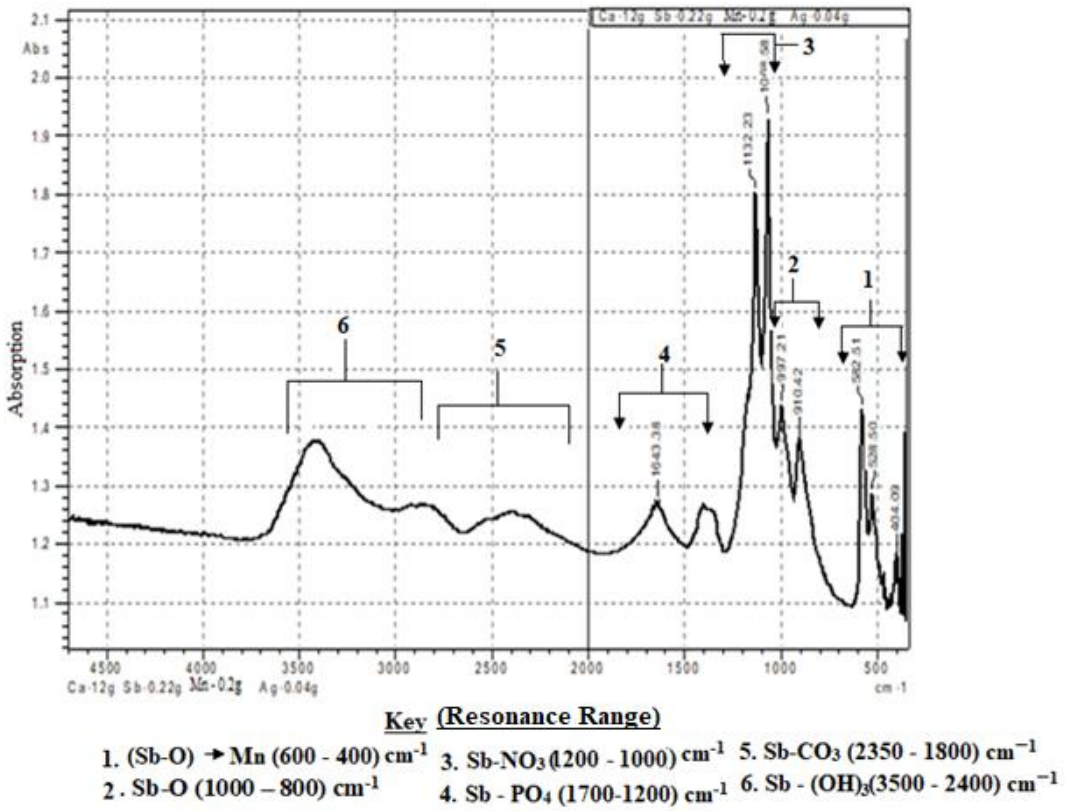

Figure 4.1: FTIR Absorption Spectrum analysis of photo luminescence (Sb/Ca/Mn/Ag) inorganic material complex

Figure 4.1 shows an FTIR spectrum of (Sb/Ca/Mn/Ag) inorganic material complex with different frequency bands which resulted due to the dissimilar functional groups in the material. The bands were observed in the regions between 1200 and 1000 cm^{-1}, 1700-1200 cm^{-1} and 800-1000 cm^{-1}. These frequencies were assigned to transfer of energy by Sb-NO_3, Sb-PO_4, Sb-CO_3 and Sb-O centres in the same order. Peaks of weaker free nitrate ion were observed to resonated at 1356 - 828 cm^{-1} while that due to carbonate ion resonated at 1690 cm^{-1} due to stretching vibrations of the bond. The absorption peak shifted red to 1593 cm^{-1} and that at 1353 cm^{-1} shifted blue in the range (1402 - 1385) cm^{-1} for an antimony complex with the same anions. Studies by Olajire *et al.* (2018) reported that absorption peaks of the ligands of C–N and C–C

bonds were observed at 1082 and 1039 cm^{-1} respectively. The band at 460 - 448 cm^{-1} and 434 - 426 cm^{-1} were attributed to Sb-O transferring energy to Mn centres (Kumaravel *et al.,* 2020).

According to Kaviyarasu *et al.* (2013) and Nahyoon *et al.* (2018), the bands between 1650-2100 and 800-1000cm^{-1} were due to (Sb–O) ionic bond while that between 1250 -1650 cm^{-1} was contributed by the phosphate ion. Duward *et al.* (2019) reported that splitting of d-orbitals groups differed in energy resulting to d→d transitions which are relatively weak hence IR active, that is, responded to IR radiation. The varied colours observed were as a result of delayed relaxation of excited electrons (Duward *et al.,* 2019).

These results indicated that antimony ionic bonding with different anions transposed the absorbed radiations to varied wavelength spectrum as evidenced with their respective resonant frequencies. The difference in the change of wavelength of the asymmetric and symmetric stretching vibration confirmed that the oxygen atoms were coordinated to metallic ions by the monodentate and bidentate bridge mode within the crystal structure of the complex. These results concur with Poulsen (2010) who reported that when materials of different elements are mixed and synthesized, radiations of different frequencies are emitted. Reports by Rezazgui *at al.* (2016) noted that the presence of species such as NO_3, PO_4 and $(OH)_3$ ions in antimony, enhanced fluorescence activity of the material. Studies by Parola *et al.* (2016) indicated that the infrared radiations absorbed by luminescent materials result to electronic transitions, thermal motion, vibration, oscillation and rotation of their atoms and molecules. Reports by Rezaie *et al.* (2021) noted that absorption of energy (**h***v*) occurred when photons strock the inorganic/organic materials crystals which

excited ions and molecular orbitals resulting to energy difference (ΔE) between the ground state and the excited states of the charge carriers. This was further enhanced by splitting of $\boldsymbol{d}$-orbitals into a multiple of more groups with differed energy as the ionized inorganic/organic crystals returned to their ground states (Lakshmanan and Daniel, 2018). A study by Hussein (2010) indicated that the overall photon emitted energy was lower (and longer in wavelength) than the photon that was initially absorbed. The delayed relaxation was exploited in this study with a view to increase spectral trapped by $SbNO_3$, Sb-PO_4, Sb-CO_3 and Sb-O material, and released later to prolong radiation to the titanium dioxide (TiO_2) photo active material for solar cell applications.

4.3 Fabricated Solar Cell

The assembled active luminescent solar cell was placed on a (2cm × 2cm) copper plate with an external terminating conductor in contact with the anode as a tinned (0.4cm ∅) copper grid was sandwiched on the photo sensitive layer with an external terminal drawn for external circuit connection. Some transparent araldite raisin was applied over the entire batch for compatibility (solidly binding the entire cell with external conductors). The photograph provided in Figure 4.2 shows one of the fabricated cells in this study.

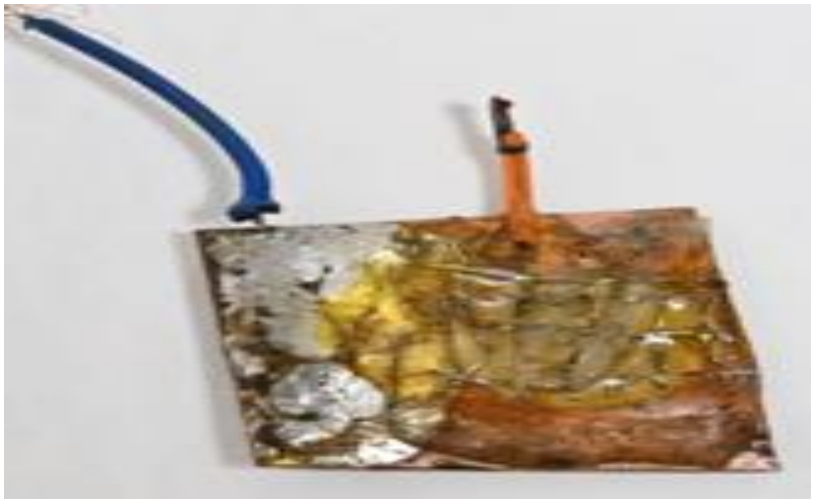

Figure 4.2: Photograph of the Assembled Solid TiO_2- Based solar cell Doped with Different Inorganic and Organic Luminescent Material

The researcher investigated the delay in photo activity after withdrawal of incident radiation to interrogate the potential in exploitation of TiO_2 material as discussed below.

4.3.1 Quantitative Analysis of Ionic Bonds Properties in (Sb/Ca/Mn/Ag) Mixed Metal Material

Different varying masses of the inorganic fluorescent mixed metal material were thoroughly mixed with TiO_2 photoactive material as presented in Table 4.1

Table 4.1: Materials Composition of Sb/Ca/Mn/Ag -TiO_2 Photo Active Layer

Cell	Mass/g (±0.001)	
	Allicin Luminescent Material	TiO_2
Z_1,b	0	1
Z_2,b	0.01	1
Z_3,b	0.02	1
Z_4,b	0.03	1
Z_4,b	0.04	1
Z_5,b	0.05	1
Z_6,b	0.06	1

From the mass ratios of table 4.1 seven photo active cells were fabricated by taking 0.4 g TiO_2 for each (Sb/Ca/Mn/Ag)-TiO_2 mixture. The receptive layers were made using (0.48 g) of graphite-iodine (Cx /I/KI) composition of 30, 17 and 1 mass ratios respectively. The resulting (Z_1, Z_2, Z_3, Z_4, Z_5, Z_6 and Z_7) cells were analyzed using a constant radiation in clear daylight and their derived parameters were calculated from the observed (potentials and current densities) quantities and recorded as shown in Table 4.2.

Table 4.2: Derived parameters from inorganic (Sb/Ca/Mn/Ag)/TiO_2 solar cells at varied (0 -0.06)g holding (0.4 g) TiO_2 in the photo active layer

Cell (Dopant mass/g)	V_{OC}(V)	I_{SC}(mA) ($\pm$0.001)	FF	Efficiency (η%)
Z_1 (0 g)	0.51	0.37	0.299	0.056
Z_2 (0.01g)	0.381	2.35	0.258	0.231
Z_3 (0.02g)	0.521	3.25	0.193	0.327
Z_4 (0.03g)	0.59	2.27	0.303	0.405
Z_5 (0.04g)	0.721	3.49	0.308	0.775
Z_6 (0.05g)	0.735	4.18	0.353	1.085
Z_7 (0.06g)	0.699	2.716	0.306	0.581

The results of Table 4.2, graphical presentation of efficiency (η %) against the varied inorganic dopant material masses were plotted as shown in Figure 4.3

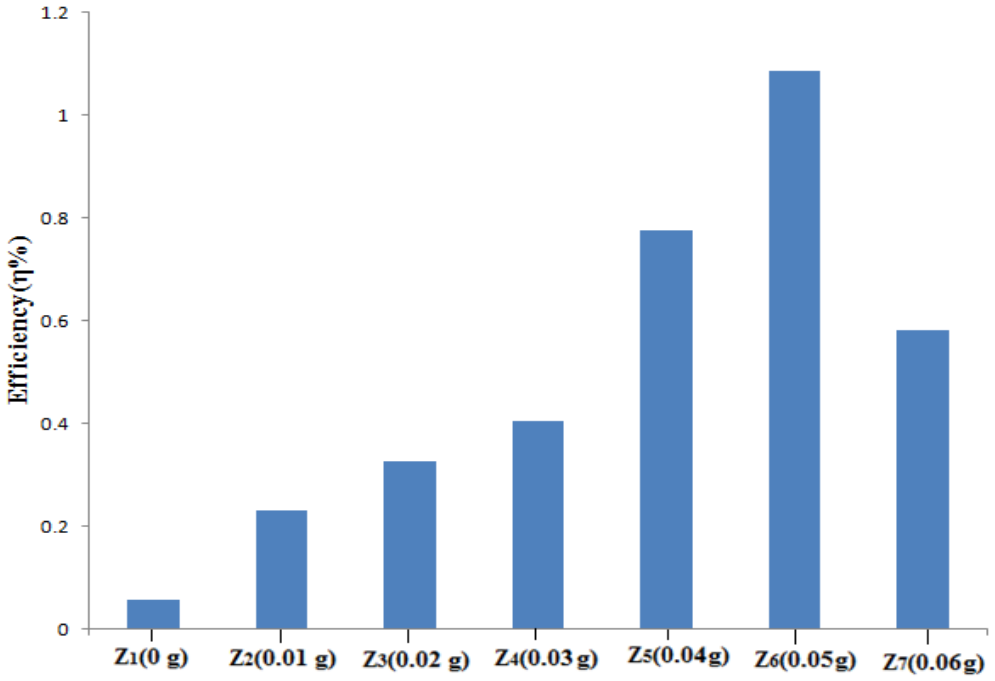

Figure 4.3: Efficiency (η): inorganic dopant mass (g) characteristics of the (Sb/Ca/Mn/Ag) -TiO_2 fluorescent solar cells

From the characteristic evidence in Figure 4.3, cell [Z_1 (0 g)] void of (Sb/Ca/Mn/Ag) dopant complex had a lower (0.0.056%) efficiency compared to the rest of the cells. However, the power conversion efficiency (PCEs) was observed to increase uniformly up to (5: 40) mass ratios of {(Sb/Ca/Mn/Ag) -TiO_2} fluorescent photo active layer after which a significant reduction ensued. The values of Table 4.2 shows that (0.735V and 4.18mA) potential (V_{OC}) and short circuit current (I_{SC}) were generated by Z6 (0.05 g) yielding improved (FF and efficiency) of (0.353 and 1.085%). Above (0.05 g) mass of (Sb/Ca/Mn/Ag) inorganic dopant, the population of holes increased resulting to a massive holes density recombination with the electrons released by the host material having a negative consequence of the observed potential difference and current density from the cell terminals. The higher PCE for the [Z_6 (0.05 g)] sample was attributed to improved band gap edges which enhanced smooth

transition of the excited charge carriers with less recombination centres. The undesirable parameters observed from Z_1 (0g) cell were attributed to minimal interaction in the composite complex. Reports by Kapil *et al.* (2019); Emami *et al.* (2021) noted that interaction of photo conversion dopants under favourable conditions characterized sequential repositioning of ligand with broad PF emission culminating to efficient charge transfer. A study by Ren *et al*. (2021) indicated that inferior generated parameters was a consequence of higher charge recombination at the host/dopant convergence within the reduced solute levels. Another examination was conducted after transferring the cells to a dark room where variation of potential differences were observed with time for an interval of one hour. The results obtained were as recorded in Table 4.3.

Table 4.3: Potential (V_{OC}) against time characterization of (Sb/Ca/Mn/Ag) / TiO_2 solar cells for (0-0.06)g varied inorganic (Sb/Ca/Mn/Ag) hybrid employing 0.4g of the mixture for the photo active layer

Time / min	**Potential (V_{OC}) ($\pm$0.005)V**						
	Z_1 (0g)	Z_2 (0.01g)	Z_3 (0.02g)	Z_4 (0.03g)	Z_5 (0.04g)	Z_6 (0.05g)	Z_7 (0.06g)
0	0.51	0.345	0.462	0.58	0.68	0.7	0.691
1	0.518	0.357	0.475	0.59	0.7	0.711	0.699
3	0.444	0.36	0.521	0.57	0.721	0.735	0.697
7	0.262	0.381	0.502	0.53	0.69	0.71	0.66
11	0.194	0.378	0.494	0.56	0.71	0.72	0.67
17	0.094	0.342	0.432	0.47	0.65	0.67	0.52
30	0.04	0.33	0.419	0.51	0.51	0.54	0.48
33		0.309	0.391	0.35	0.52	0.53	0.49
45		0.327	0.365	0.38	0.49	0.5	0.385
51		0.281	0.318	0.328	0.38	0.49	0.394
57		0.269	0.301	0.32	0.35	0.46	0.382
60		0.218	0.25	0.307	0.34	0.45	0.376

From the statistical information of Table 4.3, a graphical presentation of potential against time was prepared as shown in Figure 4.4

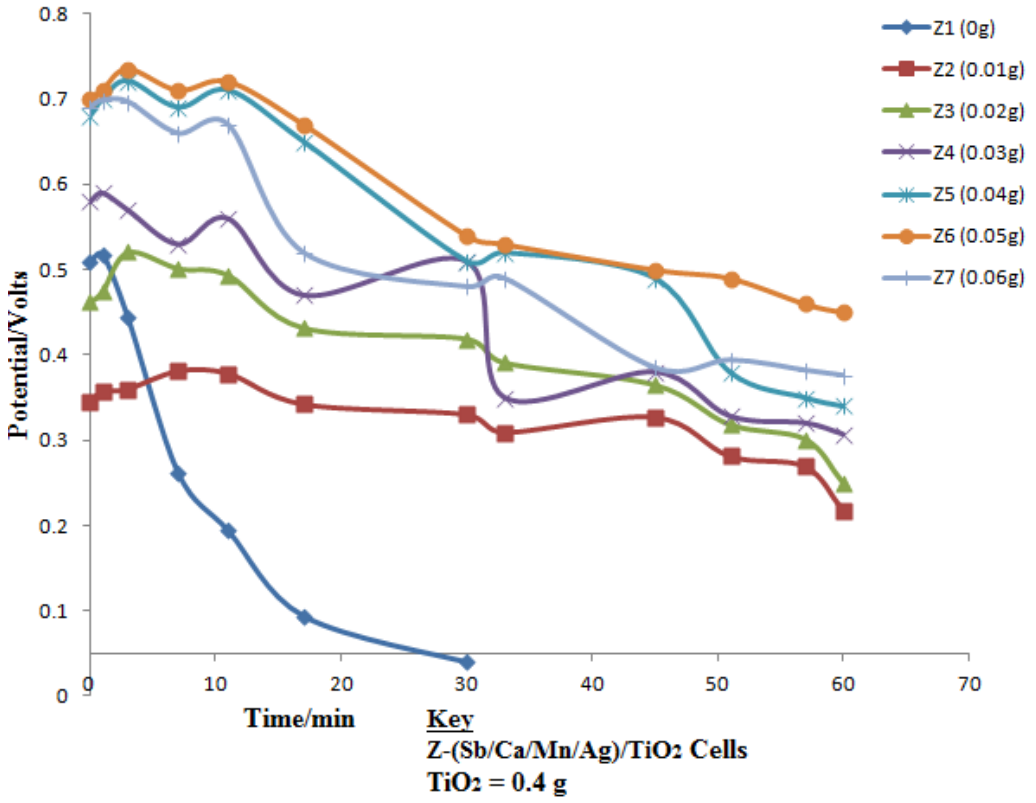

Figure 4.4: Potential-Time profiles for (Sb/Ca/Mn/Ag) -TiO2 luminescent solar cells

The information in Figure 4.4 shows that there was sustenance of radiation by the **(**Sb/Ca/Mn/Ag) inorganic material after withdrawal of incident radiation. The profile due to cell Z_1 was different from the rest because it was void of **(**Sb/Ca/Mn/Ag) photo fluorescence material. Higher level of excitation energy was thought to be derived from the angular and horizontal relaxation of defect trapped charge carriers thus characterizing the response presented by {Z_2(0.01 g)}and {(Z_3 (0.02 g)}. However, the control {Z_1(0 g)}cell presented higher potential at 0 minutes than the Z_2 and Z_3 due to momentarily higher radiation decay rate in the white TiO_2 solid crystals. That triggered excited substantial density of charge carriers, temporarily raising the generated potential which diminished at a higher rate to a negligible value. Absence of dopants in the control {Z_1(0 g)}cell contributed to deficiency of the internally

activation energy to support charged species excitation subsequenting to negligible time constant of potential sustainance.

A significant increase in potential was observed immediately after withdrawal of solar radiation for the six cells enhanced with the inorganic dopant. However, cell Z_6 (0.035 V) was the highest in (3 minutes) which diminished gradually and maintained at (0.45 V) in the next 57 minutes compared to Z_7 with 0.376V. The potential due to Z_4 (0.03 g) revamped between (20-30) minutes. This was attributed to increase in charge carriers trapped species that relaxed to their ground states at varied wavelengths, resulting to proportional externally transiting charged species. This observation indicated that the delay in radiation was proportional to the mass of dopant. However, the highest mass of dopant did not produce the best potential difference. The research by Zhou *et al.* (2020) noted that electron withdrawing dopant ions hgh concentration interfered with the population of charge carriers responsible for fluorescence. High concentration of dopant material in the host photoactive material immensely repressed uniform potential difference promotion (Shi et al., 2019). Reports by Parola *et al*. (2016) indicated that interaction of inorganic dopants with other systems enhanced flexibility of rigid hybrid system. Prafullya *et al*. (2020) reported that the force constant (k) and reduced mass (μ) within the crystalized particles differed resulting to emission of a spectrum with varied long wave number which enhanced the duration at which the photo active (TiO_2) generated charge carriers.

Reports by Yu *et al*. (2018) indicated that absorption of a photon is accompanied by the excitation of electrons from a lower-energy atomic orbital to an atomic orbital of higher energy resulting to smaller discrete absorption peaks due to transitions between the ground state orbitals such as (the 3s atomic orbital). The absorption from

these excited states, (3p → 4s) and the 3p → 3d) are too weak. This state returns an excited atom lower energy state in 10^{-7} to 10^{-8} seconds. Attenuation (reflection, scattering absorption of radiation and refractive index) by other components in the sample's matrix affected the lifetime of particles' and their excited state (Cheng *et al.*, 2017). A study by Ghanipour & Dorranian (2013) noted that for highly concentrated mediums, the particle of such homogenous matrices are not independent at the instance of external energy ingress but result to pigments interaction with consequence alteration to the materials absorptivity.

A research conducted by Tress (2017), reported that the refractive index for any material is dependent on the complex matrix. For low traces of dopants, the refractive index remains constant resulting to linear responses as guided by Beer's law (Tress, 2017). The mass of TiO_2 photo sensitive host material was varied to 0.5 g and fluorescent solar cells were made by mixing (Sb/Ca/Mn/Ag)/TiO_2 for each (0 - 0.06) g mass, as the receptive layer was held constant employing (0.48 g) of iodine- graphite (I_2/KI/Cx) and a similar procedure was followed to characterize the resulting cells. The results of their I-V characteristics for the seven cells were employed to determine the computed parameters recorded in Table 4.4.

Table 4.4: Parameters evaluated from (Sb/Ca/Mn/Ag)/TiO_2 solar cells at varied (0 - 0.06) g Sb/Ca/Mn/Ag mass employing (0.5) g TiO_2 in the photo active layer

Cell (dopant/g)	V_{OC} (V)	I_{SC}(mA) ($\pm$0.001)	FF	Efficiency (η %)
$Z_{1,a}$ (0 g)	0.302	0.07	0.002	4.228E-5
$Z_{2,a}$ (0.01g)	0.261	0.007	0.021	3.837E-5
$Z_{3,a}$ (0.02g)	0.323	0.099	0.003	9.593E-5
$Z_{4,a}$ (0.03g)	0.431	0.1	0.023	9.913E-4
$Z_{5,a}$ (0.04g)	0.493	0.105	0.126	6.52E-3
$Z_{6,a}$ (0.05g)	0.511	0.126	0.129	8.305E-3
$Z_{7,a}$ (0.06g)	0.437	0.102	0.128	5.705E-3

The impact of escalating (TiO_2) host material to (0.5 g) mass confirmed that smaller values of open circuit potential (V_{OC}) and short circuit current (I_{SC}) were generated. The effect of the (0) g and (0.01) g {Sb/Ca/Mn/Ag} inorganic dopant masses indicated that the cell void of dopant fluorescent material generated substantial (0.302 V and 0.07 mA) potential difference V_{OC} (V) and short circuit current (I_{SC}) respectively exceeding (0.261 V and 0.007 mA) of Z_2, a (0.1 g) cell. However, a {(0.323 – 0.437) V and (0.099 – 0.102) mA} upward surges were observed from the (0.02–0.06) g masses with the (0.511V and 0.126 mA) highest recorded from Z_6 (0.05) g, with corresponding fill factor (FF) and efficiency (η) of {(0.001- 0.126) and (2×10^{-6}- 5×10^{-3}) %} respectively. The comparable results from {(0 g) and (0.01-0.06)} Sb/Ca/Mn/Ag doped photo active layers implied that fluorescent nanoparticles exhibited distribution of radiations. Part of the excited charged carriers populations

were thought to be trapped in the d-defects resulting to substantial potential deviating trend as observed from cell Z_2, a (0.01g) parameters. A study by Ulatowski *et al.* (2020) observed that proportions of complimentary implications were obstructive on nanoelectronics features. That presence of charge carrier generation supportive enhancement had a consequence of intensified current density and potential outputs. Reports by Ahmed *et al.*, (2016) noted that increase in charge generation was necessitated by the enhanced photo active layer. Assessment of the TiO_2 (0.5 g) mass host material increment on the fluorescent solar cells was done in a radiation diminished radiation environment and the results were presented in Table 4.5.

Table 4.5: Potential difference (V_{OC}) against time characterization of (Sb/Ca/Mn/Ag) -TiO_2 solar cells at varied (0 - 0.06) g Sb/Ca/Mn/Ag mass ratios employing (0.5 g) TiO_2 constant in the photo active layer

Time/(min)	Potential (V_{OC}) ($\pm$0.005)V						
	Z_1,a (0 g)	Z_2,a (0.01 g)	Z_3,a (0.02 g)	Z_4,a (0.03g)	Z_5,a (0.04g)	Z_6,a (0.05 g)	Z_7,a (0.06g)
0	0.300	0.224	0.347	0.431	0.493	0.501	0.437
1	0.302	0.239	0.381	0.427	0.489	0.502	0.433
3	0.213	0.257	0.393	0.372	0.475	0.505	0.378
7	0.187	0.261	0.384	0.383	0.448	0.511	0.348
11	0.101	0.258	0.311	0.369	0.424	0.486	0.322
17	0.093	0.253	0.276	0.321	0.356	0.451	0.296
30	0.044	0.257	0.279	0.284	0.314	0.443	0.311
33	0.020	0.229	0.257	0.263	0.288	0.382	0.291
45	0.010	0.217	0.221	0.246	0.271	0.359	0.285
51		0.219	0.213	0.222	0.242	0.337	0.269
57		0.203	0.209	0.218	0.228	0.326	0.232
60		0.198	0.203	0.207	0.224	0.317	0.229

The data of potential (V_{OC}) against time in table 4.5 was presented graphically shown in Figure 4.5.

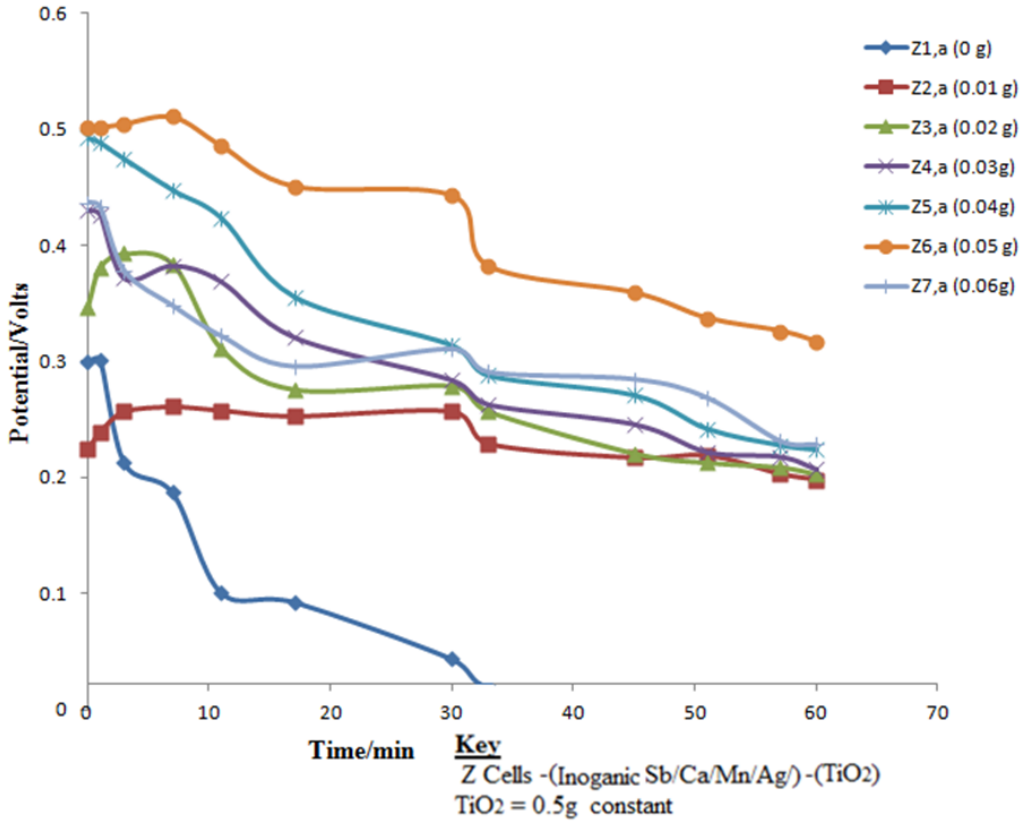

Figure 4.5: Open Circuit Potential difference against Time characterization for (Sb/Ca/Mn/Ag)- (TiO_2) solar cells with different dopant mass ratios employing (0.5 g) (TiO2) constant

The effect of (0.5 g) TiO_2 host material mass to radiation decay was occasioned by reduction in the potential observed with time as evidenced from the results of Figure 4.5. The cell void of the (Sb/Ca/Mn/Ag) inorganic fluorescent dopant maintained a diminishing tread up to a time constant of 10 minutes after which 0.09 V negligible potential difference was observed. Sample Z_6,a (0.05) was characterized displayed a sinusoidal signal response between (0- 11) minutes preceded by a uniform plateau (20-30)minutes terminating to a negligibly underdamped signal for the last (30-60) decay time. High population density defect trapped charged species relaxed to ground state downshifting a relatively varied intensities of the absorbed incident energy. The higher density species released shorter wavelength energy as returned back to the

valency band. That implied (0.01) V potential increased due to particles excited by the internally sourced long wavelength radiations. The even signal sustained for 10 minutes was attributed to constant density of the negatively charged particles releasing long wavelength radiations. Negligible change in population density allowed for (0.337 – 0.317) V underdamped signal. An increase of (0 – 0.05) g (Sb/Ca/Mn/Ag) mass presented improved lapsing at (0.198 – 0.317) V potential (V_{OC}) by the end of the experiment. However, the mass of (0.06) g ensued a declining trend recording 0.229 V after 60 minutes of observation. The (0.5 g) mass of TiO_2 was thought to inhibit efficient radiation absorption due to intensified packings along the transition paths. The diminishing scattered radiation trend due to Z_4, a (0.03 g) Sb/Ca/Mn/Ag –TiO_2 doped cell excited deviating population of charge carriers which promoted constrained (-0.011 V) potential hyperbolic featured observed between (0 - 7) minutes. Varied frequency bands with deviating internal optical oscillatory amplitudes, triggered sample Z5,a(0.04 g) to present declining ramp potential signal at the initial (0 - 10) minutes interval, trailed by a shallow hyperbolic drift for the next 20 minutes. Sinusoidal (0.01 V) amplitude signal was observed from the inorganic (0.05 g) doped (Sb/Ca/Mn/Ag) – TiO_2 samples were characterized between (0-11 minutes). That was preceded by a uniform plateau at the (20-30) minutes interval. Varied density defect trapped charged species relaxed to their ground states implying (0.01) V increase, ensued by (0.327 – 0.317) V uniformly clipped signal for the next 9 minutes. Wu *et al*. (2019) noted that the radiated stoke shift with rectangular featured signal occasioned corresponding observed parameters. The sample inhomogeneity impeded dopant activation within the sample sections (Wu *et al*. 2019). A study by Lee *et al.* (2019) noted negligibly varied wavelengths downshifted signal occasioned proportionate observed parameters.

The shortened lifetime contributed to the excited charge carriers with consistent minimization of their quantum yield. Similar findings reported by Wu *et al.* (2019) noted that the effect of spin-orbital coupling (SOC) induced within the larger crystals resulted to more dispersed conduction band with reduced electron effective mass which in effect reduced their absorption coefficient. Their deep valency band minimum (VBM) and hole transporting characteristics resulted to sparsely occupied highest molecular orbital with low energy levels which leads to a low open circuit potential differences (Wu *et al.,* 2019). A study by Lee *et al.* (2019) noted that recombination losses in dominated massive homojunctions structures, occurred when electron-hole pairs repositioned at the donor/acceptor junction due to counter energy disorders from the triplet state (3CT) to the lowest singlet (S1) of supplementing nanoparticle.

The mass of TiO_2 was changed to (0.25g) as that of the (Sb/Ca/Mg/Ag) varied to (0, 0.01, 0.02 0.03, 0.04, 0.05 and 0.06) g holding that of I_2KI/C_X at (0.48) g and the resulting cells change in potential differences (V_{OC}) V against short current (I_{SC}) (mA) in solar radiation was presented in Table 4.6.

Table 4.6: Potential (V_{OC}) against current density (J_{SC}/cm^2) characterization of (Sb/Ca/Mn/Ag) -TiO_2 solar cells at varied (0 -0.06)g Sb/Ca/Mn/Ag mass ratios employing (0.25 g) TiO_2 constant in the photo active layer

Cell (Dopant mass/g)	V_{OC} (V)	I_{SC} (mA) ($\pm$0.001)	FF	Efficiency (η %)
$Z_{1,b}$ (0g)	0.136	0.243	2.158E-4	7.13E-6
$Z_{2,b}$ (0.01g)	0.129	0.239	4.301E-4	1.326E-5
$Z_{3,b}$ (0.02g)	0.146	0.279	2.849E-4	1.161E-5
$Z_{4,b}$ (0.03g)	0.193	0.286	4.421E-4	2.441E-5
$Z_{5,b}$ (0.04g)	0.263	0.334	1.586E-2	1.393E-3
$Z6_{,b}$ (0.05g)	0.381	0.565	2.978E-2	6.411E-3
$Z7_{,b}$ (0.06g)	0.251	0.452	1.152E-2	1.307E-3

The I-V characteristics results of Table 4.6 shows that (0.25 g) TiO_2 sample void of (Sb/Ca/Mn/Ag) impurity generated considerable {(0.136) V and 0.243mA/cm2 } potential difference (V_{OC}) and short circuit current (I_{SC}) respectively. However, improved (0.146– 0.381) V and (0.279 – 0.381) mA open circuit potentials and short circuit currents were recorded as the (Sb/Ca/Mn/Ag) impurity masses were progressively incremented above 0.01 g through to 0.05g. The ensuant result of the fill factors (FF) and power conversion efficiencies (PCEs) followed the same progression. Beyond 0.051 g, a declining 0.251V potential lean with (1.52×10^{-2} and 1.307×10^{-3}) of (FF and PCE) respectively were observed. A correlative observation between the parameters generated from constant (0.25) g TiO_2 host material to that of (0.4 and 0.5)g respectively showed that the decreased quantity resulted to a minifying performance. This was thought to be contributed by the scanty

population of electron- hole pairs proportional density of the excited charge carriers. This agreed with the results reported by Ruiz-Jorge *et al.* (2020) who noted that reduction in charge carriers density give rise to instantaneous downturns of potential profiles. Similar results reported by Quan *et al.* (2019) indicated that dielectric constant of solvent material was proportional to the excited electron holes pairs density which determined the ensued ionic dissociation.. Imbalance between dopant and perovskite species affected the parameters of interest due to reduction of the intensity of excitation energy (Singh *et al.*, 2020). The change in potential against the time in negligible solar radiation was monitored and the results were recorded as shown in Table 4.7.

Table 4.7: Potential (V_{OC}) against time characterization of (Sb/Ca/Mn/Ag) - TiO_2 solar cells at varied (0 -0.06)g Sb/Ca/Mn/Ag mass ratios employing (0.25 g) TiO_2 constant in the photo active layer

Time/ min	Potential (V_{OC}) ($\pm$0.005)V						
	$Z_{1,b}$ (0g)	$Z_{2,b}$ (0.01g)	$Z_{3,b}$ (0.02g)	$Z_{4,b}$ (0.03g)	$Z_{5,b}$ (0.04g)	$Z_{6,b}$ (0.05g)	$Z_{7,b}$ (0.06g)
0	0.300	0.127	0.153	0.202	0.254	0.332	0.246
1	0.302	0.129	0.139	0.186	0.263	0.381	0.251
3	0.213	0.119	0.146	0.193	0.239	0.349	0.277
7	0.187	0.114	0.141	0.172	0.221	0.307	0.239
11	0.091	0.107	0.139	0.143	0.219	0.266	0.228
17	0.073	0.089	0.127	0.125	0.189	0.243	0.218
30	0.044	0.086	0.105	0.128	0.163	0.193	0.178
33	0.02	0.072	0.106	0.106	0.132	0.135	0.146
45	0.010	0.076	0.082	0.098	0.135	0.125	0.101
51		0.041	0.067	0.072	0.098	0.111	0.094
57		0.049	0.054	0.068	0.074	0.099	0.091
60		0.033	0.038	0.052	0.065	0.086	0.076

The results of potential against time recorded in Table 4.7 was presented graphically as shown in Figure 4.6.

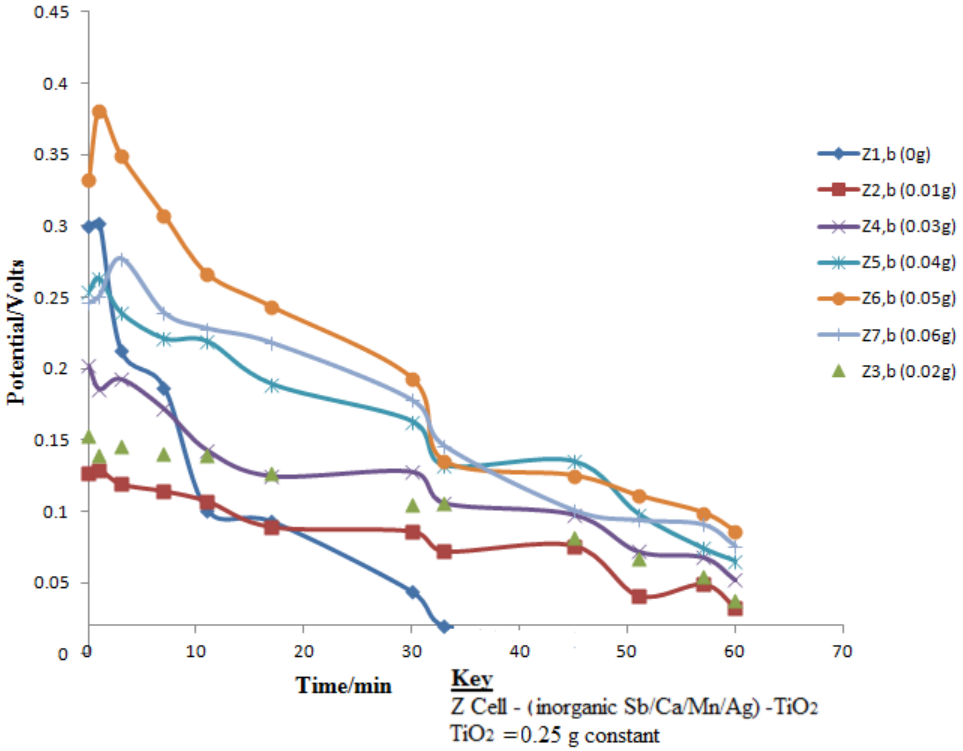

Figure 4.6: Potential (V_{OC}) against Time characterization for (Sb/Ca/Mn/Ag)-TiO_2 luminescent solar cells employing different inorganic dopant masses with TiO_2 (0.25) g constant

The characteristic potential (V_{OC}) delay observed in Figure 4.6 had a positive ramp inclination between 0 and 3 minutes intervals followed by a diminishing trend in the next 57 minutes. The cells properties were characterized by irregular gradually declining profiles with cell Z_1(0g) retaining negligible (0.091 V) after the 11 minutes. However, the mass ratio of 0.05 g (Sb/Ca/Mn/Ag) inorganic dopant sustained (0.111 V) residual potential after 50 minutes time constant. The singlet ionic dominated defects combined with the internal losses within the {(0.25 g) TiO_2 photo active layer and the (0-0.06) g (Sb/Ca/Mn/Ag)} matrix had a consequence of short lifetime defect supported charge carriers particles and the bottlenecked potentials observed. Report

by Du *et al.* (2020) noted that radiation delay excitons stimulation devices should suppress energy losses which considerably quenched fluorescence in solar cells. Similar findings reported by Jahani Bahnamiri (2016) indicated that the main loss of energy in hetero-structures is the presence of charge transfer (CT) states and recombination of electron-hole pairs state at the electron contributing / recipient interphases. A study by Younis *et al*. (2020) noted that lower mass ratios nanocomposites contained energy levels of singlet (S1) states whose band gap were unfavourable for FSCs. Such extremely minimum energy transfer advanced excitons to excited states by recessive intersystem crossing (RISC) of very short S1 state lifetime (Younis *et al*., 2020). A comparative study of the residual potential against TiO_2 host material varied masses at (0.05)g Sb/Ca/Mn/Ag inorganic dopant mass constant was done and the results were as presented in Table 4.8

Table 4.8: Potential delay due to (0.25, 0.4 and 0.5) g TiO_2 at (0.05) g (Sb/Ca/Mn/Ag) matrix constant for inorganic (Sb/Ca/Mn/Ag)/TiO2 photo active layer solar cells

Cell (TiO_2)/g	Residual Potential (V) ($\pm$0.005)
0.25	0.086
0.4	0.451
0.5	0.317

The analysis in Table 4.8 were presented graphically as shown in Figure 4.7

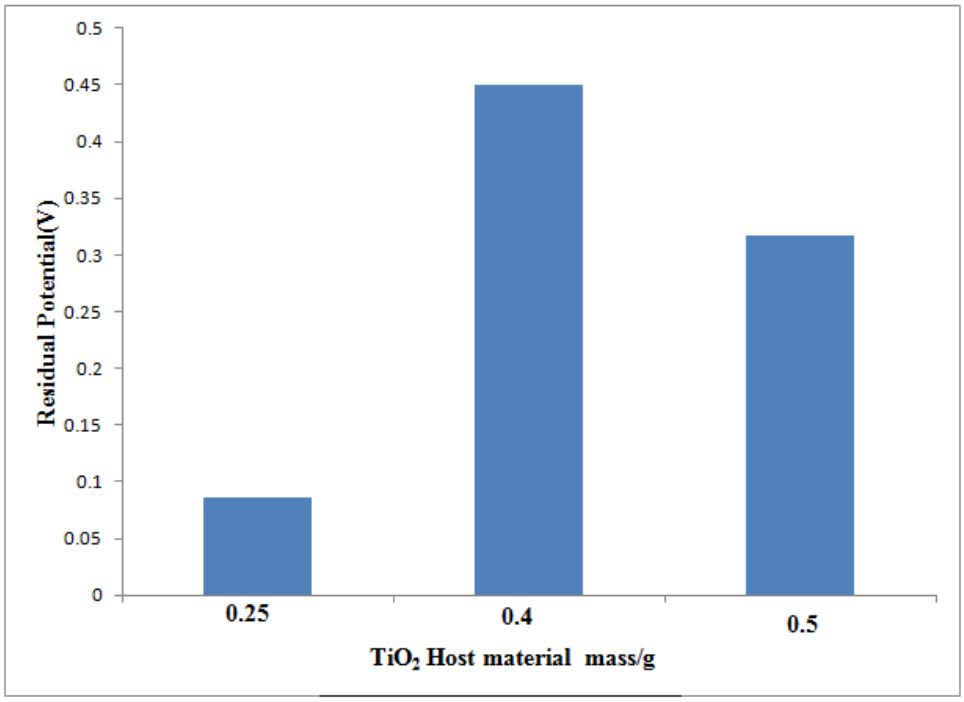

Figure 4.7: Residual Potential (V) against Mass/g of TiO_2 Host material mass/g at (0.05)g (Sb/Ca/Mn/Ag) constant

From the distinctive exhibit of Figure 4.7, the quantity of TiO_2 host material relative to Sb/Ca/Mn/Ag inorganic dopant had significant influence on the potential (V) magnitude sustained by the (Sb/Ca/Mn/Ag)/TiO_2 matrix. The quantity of TiO_2 (0.25) g mass host material supported 0.086 V. However an increase to 0.45 V was observed after the fundamental photo active material quantity was incremented to 0.4 g. A characteristic downward trend to (0.317 V) was observed with further mass increase. The {(Sb/Ca/Mn/Ag)/TiO_2} matrix 40:5 mass ratio was thought to support a conducive environment for duplet interactive arrangement which supported energy transfer for extensive S1 state electron-hole pairs oscillation. This provided adequate lapse for excitons donors /acceptors interphase diffusion thereby inhibiting reverse energy transfer process states, with a consequence of higher electron-hole pair density separation. Similar finding by Ma, *et al*. (2021) indicated that elaborate selected delayed fluorescent (DF) materials for ternary FSCs design entailed matching of host

system to substantiate improved output parameters. That concurred with the findings reported by Wang *et al*. (2019) which indicated that photo fluorescence (PF) of duplet nanocomposite exhibited a large delayed fluorescence (DF) absorption spectra in the system matrix.

4.4 Analysis of rhiodamine dye luminescent material

Rhiodamine dye material whose structure is presented in Figure 4.8 imparts pink colour used as an additive to highlighter ink.

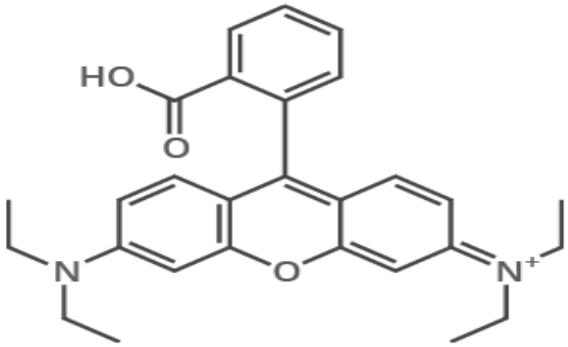

Figure 4.8: Rhiodamine chemical structure in pink highlighter Dye organic photo luminescence material (Van Marrewijk et al., 2016)

A sample of the dye was observed under UV radiation which produced greenish-yellow coloured radiation. This could be due to the property of rhiodamine being highly sensitive to long wavelength radiations due to their conjugated σ and weak π bonds (Huang *et al.*, 2017).

A sample of the material was analyzed using FTIR spectrophotometer and the results obtained are as provided in Figure 4.9.

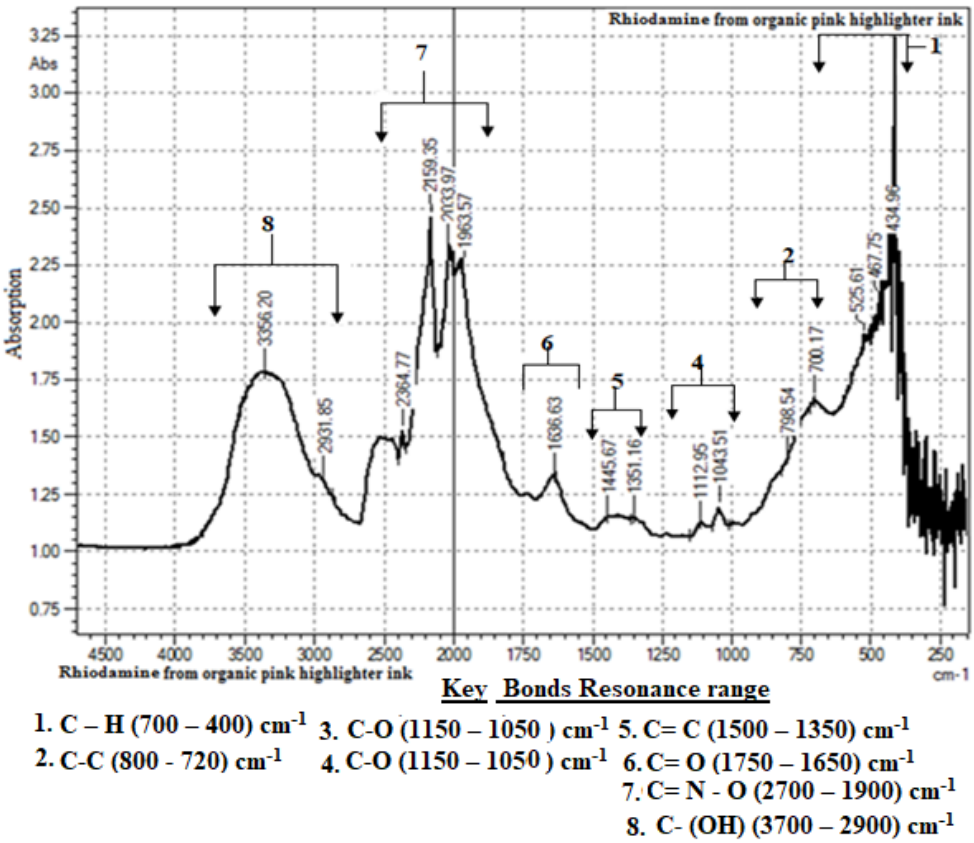

Figure 4.9: FTIR Absorption Spectrum analysis of a pink highlighter Dye Organic photoluminescence material

The different functional groups in rhiodamine resonated at varying frequency bands. This is as evidenced in the spectrum of Figure 4.9 with resonating bands in the mid-region of (1636.63, 1445.67, 1351.16, 1112.95 and 1043.15, 1963.57, 434.96) cm^{-1} and fundamental region of (3356.20, 2931.85, 2364.77, 2159.35 and 2033.97) cm^{-1}. This was attributed to the bending vibration characteristic of C= O and $C = N$, C – C, C – H, C-N, C-O, and C-OH bonds, whose peaks had bold and sharp characteristics due to infrared energy. This agrees with Dayal *et al*., (2017) who reported that the presence of the functional groups contributes to its florescence. Strong bond stretching was thought to contribute to large change in the mode of dipole

moment resulting to vibration due to absorption of infrared radiation (Dayal *et al.,* 2017).

The peaks at (2159.35, 2033.97, and 1963.57) cm^{-1} were attributed to C−OH bands with strong and intense moments due infrared absorbance, impinging on the rhodamine molecules of the particles resulting to vibrational energy level difference within the particles. This agreed with the findings of Xue *et al.,* (2018) which indicated that the OH functional groups were responsible for luminescence in carbon compounds while investigating sensing of Fe^{3+} ions. These resulted to chemical bond's force constant (k) reduced mass (μ) of the rhiodamine in the pink highlighter dye particles contributed to gradual emission of the spectrum which enhanced on the duration at which the photo active (TiO_2) generated charge carriers.

That fluorescent property and the high sensitivity of pink highlighter dye to long wavelength radiations was exploited in this study with a view to increase spectral trapped by rhiodamine and released later to prolong radiation to the photo active titanium dioxide (TiO_2) material.

4.4.1 Rhiodamine fluorescence properties assessment for solar cell application

Varying ratios of pink highlighter dye solution were thoroughly mixed with different samples of constant mass (5.00 g) photoactive material (TiO_2) in the proportions outlined in Table 4.9.

Table 4.9: Volumes (ml) of Accetone mixed with Dopant Highlighter Dye and percentages employing constant (5) g TiO_2

TiO_2	**Pink highlighter dye**	
(Mass/g) (±0.001)	Volume (ml) (±0.001)	%
5	10	100
5	7.5	75
5	5	50
5	4	40
5	3	30
5	2	20
5	1	10

From each of the mixtures presented in Table 4.9, 0.4 g samples were weighed and used to make the photo active layers of the fabricated cells. The resulting cells were analyzed using a constant solar radiation and their parameters presented in Table 4.10.

Table 4.10: Potential (V_{OC}) against short circuit current characterization of (Rhiodamine) -TiO_2 solar cells at varied (0 -0.100) % Rhiodamine volume ratios employing (0.4 g) TiO_2 constant in the photo active layer

Cell (% dopant Volume)()	V_{OC}(V)	I_{SC} ($\pm$0.001)	FF	Efficiency (η %)
A_1 (0%)	0.418	1. 871	0.198	0.155
A_2 (10%)	0.409	2.041	0.193	0.161
A_3 (20%)	0.501	2.432	0.207	0.252
A_4 (30%)	0.516	3.171	0.223	0.364
A_5 (40%)	0.531	3.680	0.244	0.477
A_6 (50%)	0.559	3.972	0.336	0.746
A_7 (75%)	0.519	2.861	0.243	0.361
A_8 (100%)	0.508	2.471	0.204	0.256

The observation recorded in Table 4.10 shows that the observed potentials difference (V_{OC}) and the generated short circuit current (I_{SC}) appreciated as the rhiodamine percentage volumes were incremented sequentially. Beyond 50% volume ratio, a descending trend (0.519V and 0.508V) was observed. The 50% of rhiodamine volume ratio was thought to enhance band gap tuneability which improved excitons mechanical resilience with (0.336 and 0.746%) fill factor and power conversion efficiency, respectively. The low percentage volumes in {A_2, (10%) and A_3 (20%)} cells populated few electron hole particles resulting to proportionate (0.409 and

0.501) V inductive capacity due to strained excitons with strongly coulomb coherent energy. A study by Yu *et al.* (2020) noted that void of organic supplementary material in the photo active layer presented retrospective specific capacitance originating from insufficient energy density. Vecellio (2020) reported that balanced hybridized FSCs materials were observed to actualize operationalization. The solar cells were then transferred to a dark room and the variation of potential (V_{OC}) was observed with time and recorded as shown in Table 4.11.

Table 4.11: Potential (V_{OC}) against time characterization of (organic rhiodamine doped)-TiO_2 luminescent solar cells at varied (0-100) % volume ratios employing 0.4 g TiO_2 constant in the photo active layer

Time/ Min	Potential(V_{OC}) ($\pm$0.005)V							
	A_0 (0%)	A_1 (10%)	A_2 (20%)	A_3 (30%)	A_4 (40%)	A_5 (50%)	A_6 (75%)	A_7 (100%)
0	0.511	0.321	0.451	0.471	0.482	0.502	0.485	0.512
1	0.501	0.311	0.461	0.481	0.501	0.542	0.505	0.509
3	0.487	0.315	0.501	0.521	0.531	0.559	0.515	0.512
7	0.119	0.331	0.491	0.501	0.511	0.531	0.519	0.495
11	0.104	0.301	0.421	0.511	0.495	0.52	0.499	0.421
17	0.091	0.291	0.441	0.451	0.461	0.486	0.453	0.388
30	0.035	0.272	0.311	0.421	0.452	0.432	0.411	0.324
33		0.242	0.282	0.412	0.421	0.401	0.392	0.333
45		0.191	0.262	0.381	0.402	0.399	0.352	0.312
51		0.152	0.191	0.312	0.382	0.375	0.298	0.292
57		0.142	0.161	0.273	0.312	0.365	0.276	0.271
60		0.131	0.152	0.251	0.313	0.362	0.253	0.263

From the tabulated potential- time results, graphical presentations were prepared as shown in Figure 4.10

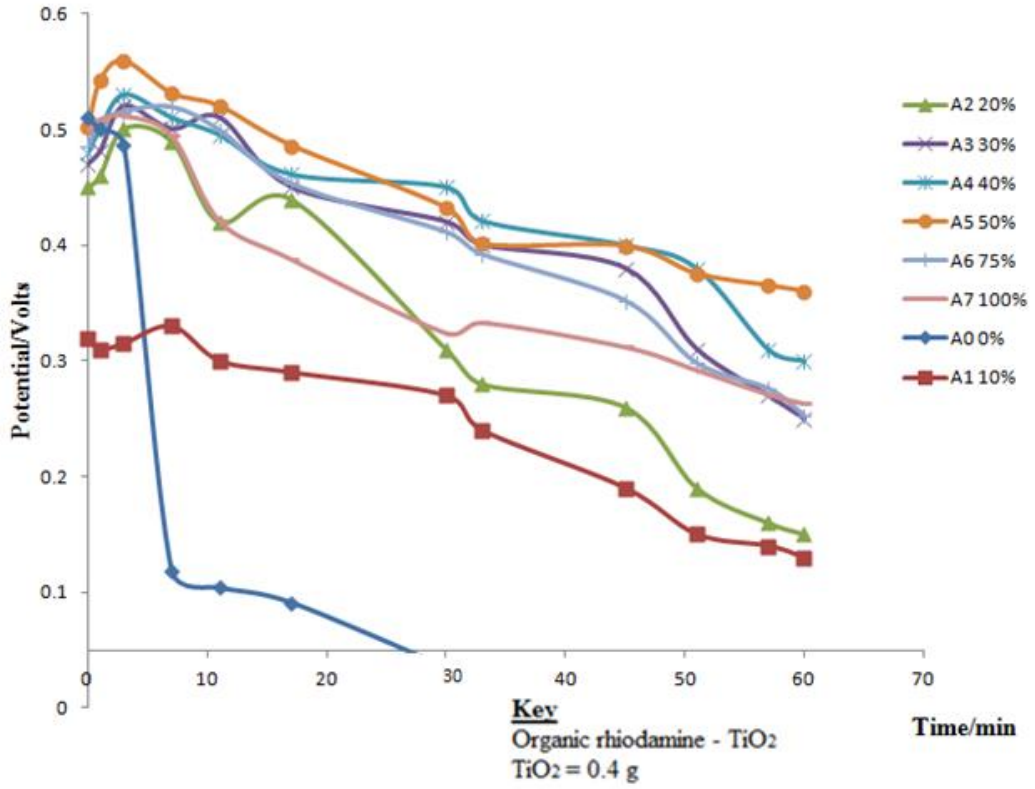

Figure 4.10: Potential (V_{OC}) against Time characterization for rhiodamine - TiO_2 luminescent solar cells employing 0.4 g TiO_2 constant

Figure 4.10 shows potential signal delay due to the varied organic rhiodamine dopant at 0.4 g TiO_2. The signal initiated within A_4(40%) and A_5(50%) after withdrawal of incident solar radiation displayed relatively similar unique (0.049 and 0.057) V amplitude sinusoidal signal responses between (0 – 10) minutes. Sample A_3(30%) presented identical (0.05 and 0.01) V amplitude sinusoidal resonating features for two {(0 - 7) and (9 -15)} minutes consecutive intervals. The (40, 50 and 30) % of rhiodamine dopant concentration introduced sub-orbitals which resonated at varying frequency and stokeshifted the absorbed optical energy to activate charge carriers transition resulting to the observed potential energy. Different intensities of defect trapped charged species released energy as they returned to ground state. The resulted diverse rectangular (0.031, 0.05, 0.009, 0.019 and 0.03) V due to {A_5 (50%), A_4 (40),

A_3 (30%) A_6 (75%) and A_1 (10 %)} FSCs fast decaying surges were observed between (30 - 33) minutes. However, the of effect diminishing radiation in A_1(10 %) FSC stimulated rhiodamine dopant defect trapped charge carrier density concentration to release exciting energy between (0 - 3) minutes. The angular relaxation excited reduced density of transiting charged particles subsequenting -0.011 V observed potential. The ensued enhanced density vertical relaxation presented improved 0.016 V potential energy. Varying radiated downshifted energy wavelength activated A_2 (20%), A_3 (30%), A_5 (50%) and A_7 (100%), diverse potential decay between (15 - 34) minutes. Rhiodamine dopant sub-orbital trapped species relaxed to their ground states releasing equivalent longer wavelengths energy, triggering non-varying potential energy drifts stimulation as observed from A_1(10%), A_2(20%), A_4(40%) and A_5(50%) samples at varied intervals. The dopant concentration disparity influenced the magnitude of the terminal potential delay of the cells under investigation within the 60 minutes of the experiment.

Absence of rhiodamine luminescent dopnats resulted to A_0 (0 g) sample fast extinction with its potential decreasing uniformly in 17 minutes and to negligible potential thereafter. Cell A_5 (0.559 V) potential difference delay was the highest in (3 minutes) which then was ensued by a gradual decay and maintained at (0.365 V) after the next 57 minutes. This was thought to be activated by excitation of more than one normal mode during bond vibration and charge carriers transition which contributed to varied retention of the emitted radiation as the particles returned to their ground state. The presence of (C-O, C-OH, C-N, C=N and C=O) conjugated $\sigma\ vs\ \sigma\pi$ bonds structure in rhiodamine dye -TiO_2 absorbed radiation at different wavenumbers which enhanced delayed fluorescence with diverse wavelengths exhibiting different colours.

Varied intermittent time constants of electron-hole pairs dispersal spans of deviating nanometer ranges detered the charge carriers clustering ability was attributed to deep and shallow rippled potential difference profiles. Similar results by Parola *et al.* (2016) indicated that dye-matrix interaction improved tuneability of other systems and greatly increased the switching speed in a rigid hybrid system. Higher percentage of the dopant material was thought to incorporate electron withdrawing compounds such as COOH, -N= *N*- at varied intervals. This interfered with uniformly distributed migrating population of the excited charge carriers from that which relaxed to the ground state hence contributing to iregular gradients of the generated potential difference profile at varied intervals. A study reported by Nakano and Tajima (2016), noted that non uniformity in structural homogeneity was comparable to the charge transition section proportional to the excited charge carriers dispersion radius.

Identical group of eight luminescent (organic rhiodamine-TiO_2) cells were fabricated with different volume percentages of rhiodamine organic dopant at 0.6 g (TiO_2) constant and characterized in a clear daylight. The results observed from their I-V characteristics were recorded in Table 4.12.

Table 4.12: I-V characterization of (rhiodamine) -TiO_2 solar cells at varied (0 - 100) % rhiodamine volume ratios employing (0.6 g) TiO_2 constant in the photo active layer

The data presented in Table 4.12 shows decreased marginal potentials when the mass of TiO_2 was increased to 0.6 g with varying (0 - 100) % rhiodamine volume

Cell (% dopant Volume)	V_{OC}(V)	I_{SC}(mA) (±0.001)	FF	Efficiency (η %)
A_1,a (0%)	0.254	0.529	0.049	6.58E-3
A_2,a (10%)	0. 223	0.526	0.057	6.69E-3
A_3,a (20%)	0.259	0.538	0.061	8.49E-3
A_4, a (30%)	0.264	0.637	0.074	1.24E-2
A_5, a (40%)	0.275	0.821	0.075	1.69E-2
A_6,a (50%)	0.322	1.280	0.081	3.34E-2
A_7, a (75%)	0.247	0.814	0.058	1.17E-2
A_8,a (100%)	0.239	0.762	0.047	8.56E-3

percentages. However, cell A_6,a (50%) maintained a leading performance with (0.322 V and 1.28 mA) potential (V_{OC}) and short circuit current (I_{SC}) respectively. Comparable (FF and PCE) of (0.081 and 0.0334%) parameters were derived. The adjacent A_7, a (75%) and A_5, a (40%) cells had (0.247 and 0.275) V potentials(V_{OC}) with (0.821 and 0.814) mA short circuit current (I_{SC}) minimum deviations respectively. That was thought to be contributed by the marginal gaps polymer generated cations and anions densities which were relatively proportional to delocalized charge carriers. A study by Muench *et al.* (2016) reported that carbon enhanced composites found wide application due to negligible charge carrier concentration gradient deviation in their FSCs photo active layers. The variation of

potential against time at minimum solar radiation was then monitored and recorded as shown in Table 4.13.

Table 4.13: Potential (V_{OC}) against time characterization of (organic rhiodamine doped)- (TiO_2) solar cells at varied (0 -100) % organic rhiodamine percentage ratios employing (0.6 g) TiO_2 constant in the photo active layer

Time/ Min	Potential(V_{OC}) ($\pm$0.005) V							
	$A_{1,a}$ (0%)	**$A_{2,a}$ (10%)**	**$A_{3,a}$ (20%)**	**$A_{4,a}$ (30%)**	**$A_{5,a}$ (40%)**	**$A_{6,a}$ (50%)**	**$A_{7,a}$ (75%)**	**$A_{8,a}$ (100%)**
0	0.269	0.16	0.25	0.273	0.284	0.295	0.239	0.247
1	0.251	0.171	0.305	0.311	0.271	0.322	0.254	0.234
3	0.227	0.169	0.267	0.255	0.275	0.313	0.249	0.241
7	0.208	0.162	0.232	0.237	0.261	0.277	0.246	0.243
11	0.168	0.158	0.228	0.231	0.245	0.261	0.233	0.224
17	0.093	0.134	0.216	0.224	0.239	0.247	0.227	0.221
30	0.046	0.114	0.201	0.212	0.231	0.242	0.216	0.219
33	0.03	0.111	0.176	0.204	0.224	0.236	0.203	0.189
45	0.01	0.101	0.131	0.183	0.211	0.227	0.187	0.185
51		0.063	0.119	0.151	0.178	0.213	0.164	0.161
57		0.051	0.091	0.137	0.166	0.2	0.148	0.131
60		0.047	0.083	0.131	0.161	0.195	0.133	0.121

The results of Table 4.13 were presented graphically as shown in Figure 4.11.

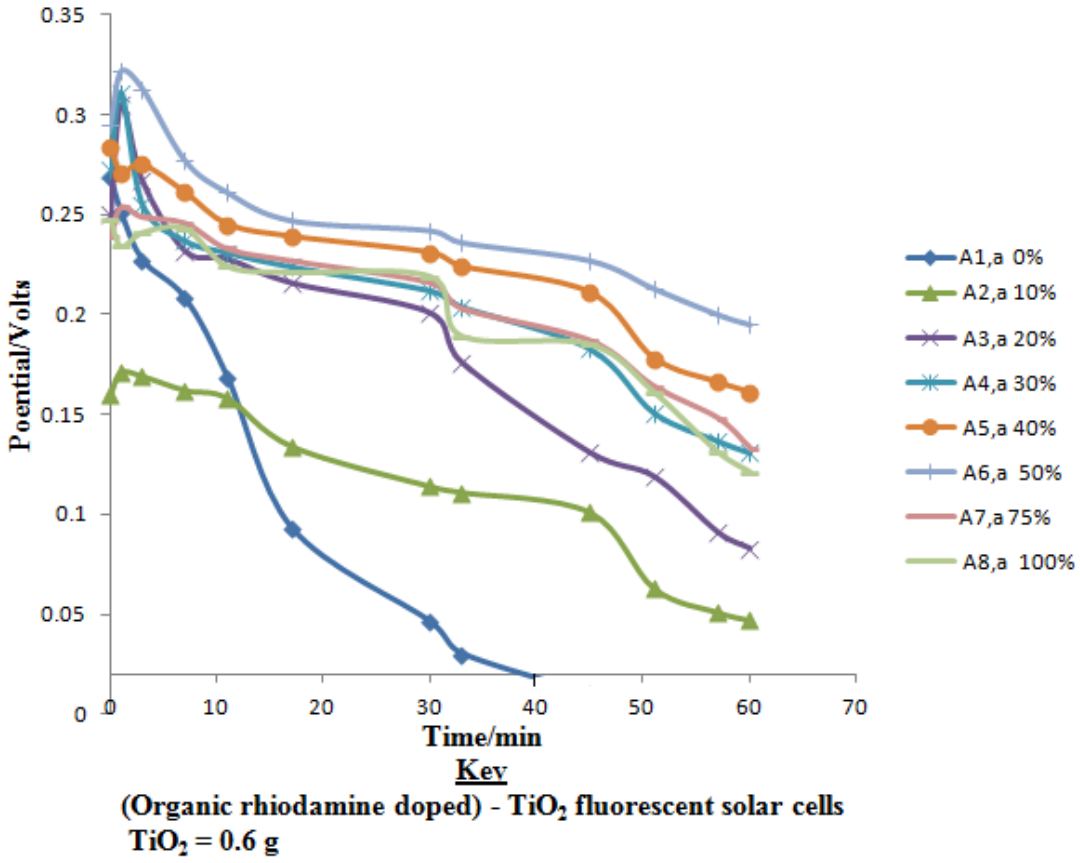

Figure 4.11: Variation of potential (V_{OC}) against time for (organic rhiodamine doped)-(TiO_2) luminescent solar cells employing 0.6g TiO_2 constant mass ratio

Figure 4.11 shows results of diminishing potential difference profiles with (0.195) V most significant potential (V_{OC}) delay observed from cell A_6, a (50%), as the rest retained less than 0.17 V in minimal solar radiation. This was attributed to inconsistent lasing action of the rhiodamine species due to the long distance the optical energy had to travel to stimulate the charged particals. Similar results by Niu *et al*. (2021) indicated that point defects were a consequence of deep-level defects with variance in energies within the band gap. The photo sensitive perovskite with higher ratios was characterized by fast recombination of the disassociated charge carriers due to the longer path encountered before migrating to the external circuit (Li

et al., 2019). The exciton with slightly lower energy than their band gap had distortions resulted from potential barrier within the two-dimensional self-trapping systems (Belisle *et al.,* 2016). Another group of eight luminescent (organic rhiodamine-TiO_2) cells were fabricated with different percentages of rhiodamine organic dopant at 0.3 g (TiO_2) constant. The parameters derived from their I-V characteristics variables were recorded in Table 4.14.

Table 4.14: Parameters evaluated from (Organic Rhiodamine)/TiO_2 solar cells at varied (0 - 100) % Rhiodamine percentage volumes employing (0.3) g TiO_2 in the photo active layer

Cell (%dopant Volume)	$V_{(OC)}$ (V)	$I_{(SC)}$ (mA) ($\pm$0.001)	FF	(η %)
A_1,a (0%)	0.211	0.526	5.75E-3	6.382E-4
B_1,a (10%)	0.154	0.518	7.26E-3	5.791E-4
C_1,a (20%)	0.166	0.529	1.73E-2	1.519E-3
D_1,a (30%)	0.178	0.659	1.84E-2	2.158E-3
E_1,a (40%)	0.211	0.796	1.86E-2	3.124E-3
F_1,a (50%)	0.235	0.825	2.05E-2	3.974E-3
G_1,a (75%)	0.215	0.726	1.63E-2	2.544E-3
H_1,a (100%)	0.185	0.713	1.08E-2	1.425E-3

From the I-V analytical values recorded in Table 4.14, the {(0.3 g) TiO_2} sample void of optical energy supporting material generated (0.211 V) potential difference (V_{OC}) which was higher than the cells with up to 30% rhiodamine fluorescence material. Rehabilitating TiO_2 photo active material with higher rhiodamine volume ratios, (0.235V and 0.825mA) open circuit voltage (V_{OC}) and short circuit current (I_{SC}) were

observed from F_1, a (50%) specimen, with (0.0205 and 0.004%) fill factor and efficiencies derived parameters respectively. Beyond that volume margin, disorder in potential alignment was observed with (0.185 V, 0.0108 and 0.00143%) potential (V_{OC}), FF and PCE recession of up to H_1, a (100%) volume percentage ratio sample. Enhanced results were attributed to presence of adequate trap filling balanced with generated charged particles. Dynamic disarrayed quantum trappings were attributed to lower dopants volume ratios with unsatisfactory (V_{OC}, FF and PSC) performance. A study by Zhao *et al.* (2016) reported that dilutely-doped photo active layers depreciated charge carrier aggregation and elevated recombination of electron hole pairs. The variation of potential against time at minimum solar radiation was monitored and recorded as shown in Table 4.15.

Table 4.15: Potential (V_{OC}) against time characterization of (organic rhiodamine-TiO_2) luminescent solar cells at varied (0-100)% (organic rhiodamine) percentage ratios employing 0.3g (TiO_2) constant in the photo active layer

Time/ Min	Potential(V_{OC}) ($\pm$0.005) V							
	$A_{1,b}$ (0 %)	$B_{1,b}$ (10 %)	$C_{1,b}$ (20 %)	$D_{1,b}$ (30 %)	$E_{1,b}$ (40 %)	$F_{1,b}$ (50 %)	$G_{1,b}$ (75 %)	$H_{1,b}$ (100 %)
0	0.208	0.124	0.136	0.178	0.211	0.231	0.213	0.185
1	0.211	0.13	0.142	0.153	0.208	0.235	0.215	0.173
3	0.168	0.107	0.115	0.149	0.189	0.232	0.182	0.154
7	0.115	0.078	0.125	0.134	0.137	0.229	0.166	0.163
11	0.074	0.056	0.121	0.141	0.139	0.179	0.131	0.142
17	0.052	0.048	0.105	0.121	0.126	0.163	0.126	0.136
30	0.015	0.043	0.097	0.114	0.112	0.134	0.119	0.122
33		0.04	0.067	0.098	0.105	0.132	0.112	0.108
45			0.06	0.087	0.081	0.119	0.092	0.086
51			0.054	0.071	0.076	0.107	0.08	0.076
57				0.059	0.07	0.101	0.07	0.06
60						0.098	0.065	0.053

From the information recorded in Table 4.15, a graphical representation of the generated potential against time was made as shown in Figure 4.12.

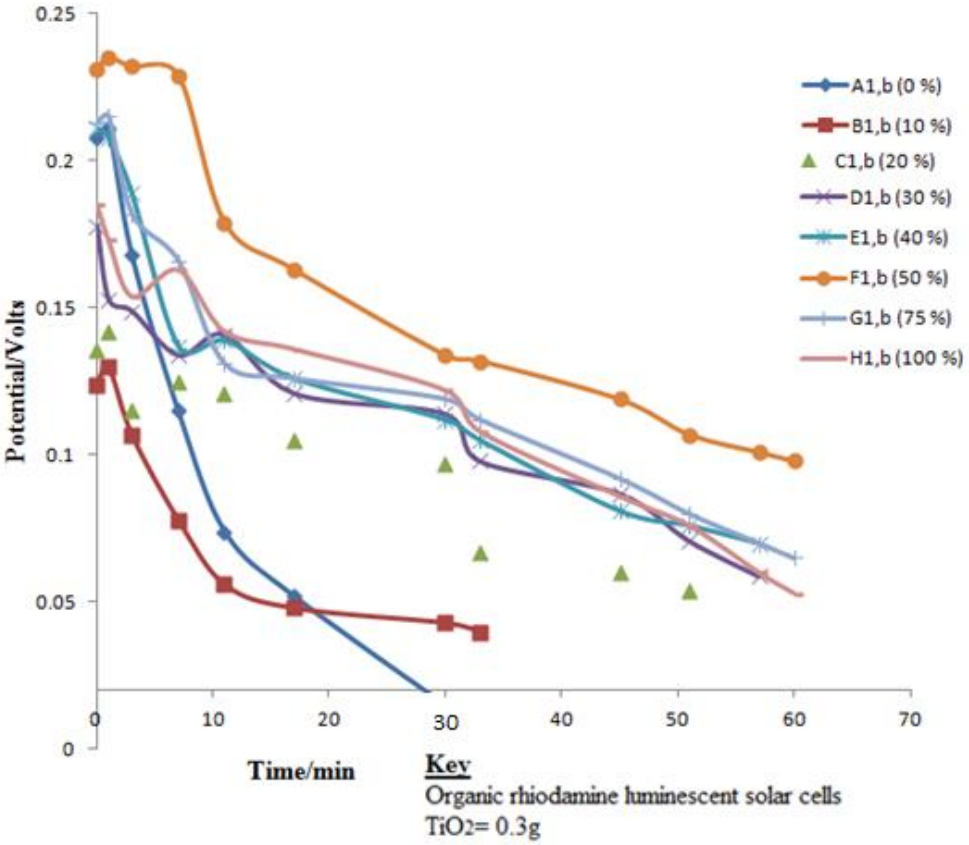

Figure 4.12: Potential (V_{OC}) against Time characterization for the organic rhiodamine Doped luminescent solar cells employing 0.3 g TiO_2 constant

The results of Figure 4.12 shows that there was (0.083 V) residual potential diffences disparity (V_{OC}) between the {A_1,(0%)} weakest and the utmost performing cells within the time of the investigation. The improved (0.098) V residual potential from cell {F_1,b (50%)} was attributed to the moderated electronic traps near the band edges due to the (50% : 0.3g) (rhiodamine/TiO_2) cell matrix. The low ratios of the TiO_2 fundamental material were thought to contribute to few vacancy defects within crystallites shallow level electronic traps near band edges. A Similar study by Ryu *et al.* (2019) noted that change in electron - hole diffusion relative to perovskites: dopant variation mixtures, proportionally contributed to the magnitude of output parameters

due to variation of their concentrations. Such variations had different band gap effects on the host materials.

4.5 Analysis of Flourene Organic Fluorescent Material for Solar Cell Application

Flourene is an organic compound with the formula $(C_6H_4)_2CH_2$ which appears as white powdery crystal that exhibit a characteristic, violet – bluish fluorescence when exposed to solar radiation as reported by Kim *et al.* (2020). When applied as a dopant, it shifts optical energy to a range of fluorescent bands relative to the frequency of incident radiation based on its source (Kim *et al.*, 2020). Report by Esmaelpourfarkhani *et al.* (2023) noted that when flourene is exposed to different monochromatic radiations, it can fluorescence giving a myriad of colours ranging from blue to green to red depending on the frequency of the illuminating radiation. The structure of flourene is as provided Figure 4.13

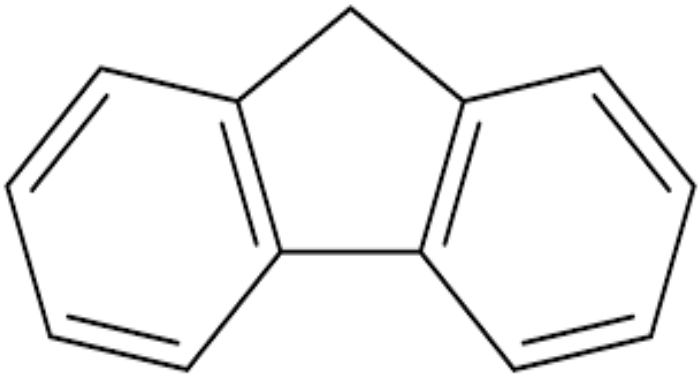

Figure 4.13: Benzene Chemical structure in flourene

Its molecular structure with weak $\sigma\pi$ bending and stretching paired bonds emit radiations ranging from blue to red shift λ when co polymerized with other material (Do *et al.*, 2016). One of the copolymers is as provided in Figure 4.14.

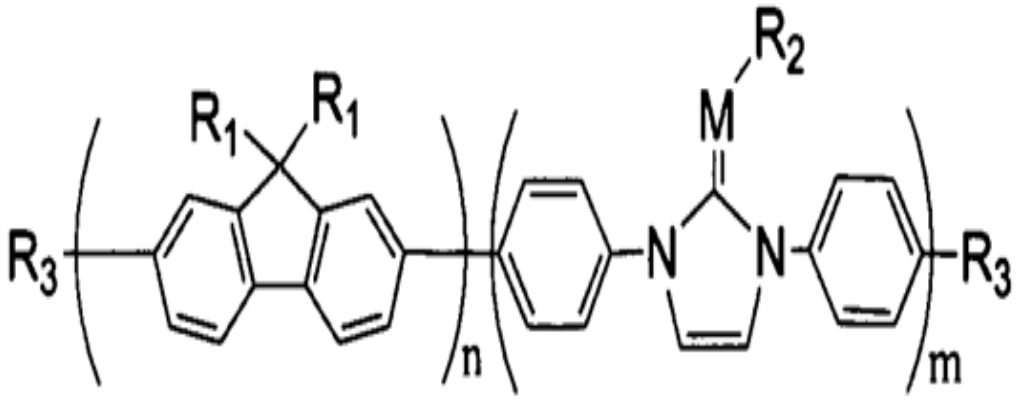

Figure 4.14: Chemical Structure of copolymer Flourene

This study applied FTIR analysis on flourene in its pure powdery form**.**

4.5.1 FTIR analysis of flourene fluorescent material for solar cell application

The solid monomer flourene samples with pairs of aromatic rings joined by nitrogen containing a sigma bond linkage were characterized separately using FTIR spectrophotometer as presented in Figure 4.15.

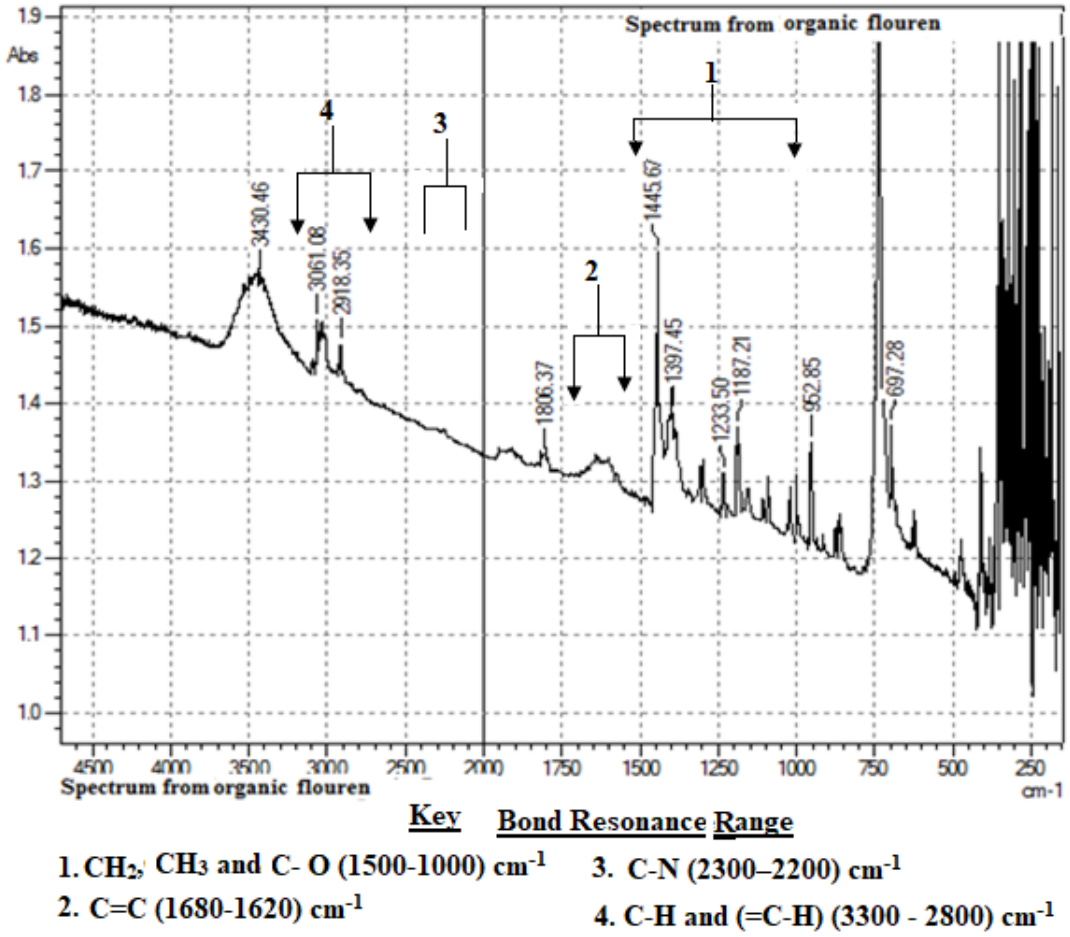

Figure 4.15: FTIR Absorption Spectrum analysis of Flourene Photo Luminescence Organic Material

The presence of aromatic rings was evidenced in Figure 4.15 as the copolymer flourene absorbed IR radiation. The spectrum shows different frequency bands appearing between (1300 to 1650) cm^{-1} due to (CH_2, CH_3, C-O and C=C) bending and stretching moments in the flourene copolymer. The stretching and bending moments of (C-H) and (=C-H) bonds functional groups resonated and absorb optical energy at frequency bands between (3650 to 2800) cm^{-1} and (1250 to 600) cm^{-1} at varied intensities. The nitro group of (C-N) was observed to resonate between

(1300 to 2000) cm^{-1}. The strong intense peaks observed at (650, 697.28, 700) cm^{-1} and (3043.46, 3050, 3000) cm^{-1} were contributed by (=C-H) bonds bending and stretching moments.

The peaks in the region (500 to750) cm^{-1} were contributed by the bending moments of C-H bonds during the monosubstitution of the functional groups. The flourescence of the organic materials contributed to varied spinning moments and relocation of nitro functional group within the molecular structure. That agreed with a study by Morris *et al.* (2016) which noted that substitution in different meta , beta and alfa {(1,3),(1,4) and (1,4) positions of aromatic ring carbon centres resulted to the varied absorption frequency bands. That substitution in long distances varied electronic defects densities in the aromatic ring localized sites with varied quantized resonance in different localized regions deviated net charge densities. Reports by Manzoor *et al.* (2019) indicated that the more strainous the bonds structure resulted to higher frequency of absorption with narrow bands. Studies by Dayal *et al.* (2017) noted that the presence of benzene rings connected by a direct carbon-carbon bond and an adjacent methylene bridge in aromatic ring was responsible for high fluorescence quantum yield and photostability. According to Chen et *al*. (2015), Xie *et al*. (2020), the peaks of the flourene sample due to fluorescence of functional groups in benzene rings.

That property of flourene was exploited in this study with a view to increase spectral trapped by benzene rings and released later to prolong radiation to the photo active titanium dioxide (TiO_2) material.

4.5.2 Influence of doping TiO2 with flourene on solar cell output

Varying masses (0.01 to 0.06) g of powdered flourene fluorescent material were thoroughly mixed with different samples of constant mass (1.00 g) of the photoactive material (TiO_2). The proportions are as shown in Table 4.16.

Table 4.16: Composition materials of cells (L_0, L_1, L_2, L_3, L_4, L_5 and L_6)

Cell	Mass/g (±0.001)	
	Flourene Luminescent Material	TiO_2
L0	0	1
L1	0.01	1
L2	0.02	1
L3	0.03	1
L4	0.04	1
L5	0.05	1
L6	0.06	1

The mixtures were used to fabricate different photo cells which were used to study delay in photo activity after withdrawal of radiation.

For each cell, 0.4 g of the mixture were used to fabricate the photo active electrode while 0.48 g of graphite- iodine (Cx /I/KI) composition formed the receptive layer whose composition was 0.3 g, 0.17 g and 0.01 g, respectively. The resulting cells were analyzed using constant radiation and their I-V potentials were record in the Table 4.17.

Table 4.17: Parameters derived from (Organic Flourene)/TiO_2 solar cells at varied (0 – 0.06) g Flourene masses employing (0.4) g TiO_2 in the photo active layer

Cell (%dopant)	$V_{(OC)}$ (V)	$I_{(SC)}$ (mA) ($\pm$0.001)	FF	(η %)
L_1 (0g)	0.52	1.69	0.018	0.016
L_2, (0.01g	0.34	4.13	0.119	0.167
L_3 (0.02g)	0.36	4.14	0.185	0.276
L_4 (0.03g)	0.44	4.35	0.187	0.358
L_5 (0.04g)	0.69	4.75	0.219	0.718
L_6 (0.05g)	0.73	5.58	0.341	1.389
L_7 (0.06g)	0.64	3.55	0.265	0.602

From the comparative I-V characteristics results shown in Table 4.17, the open circuit voltage (V_{OC}) and short circuit current (I_{SC}) observed varied proportionally from {(0.34 V and 4.13 mA facilitated by (0.01 g)} to {(0.73 V and 5.58 mA) promoted by (0.05 g)} flourene dopant mass mixed with constant (0.4 g) TiO_2 photo active material. A recession characteristic preceded with (0.64 V, 3.55mA, 0.265 and 0.602%) [Potential (V_{OC}), short circuit current (I_{SC}), FF and PCE] output and derived parameters respectively. The consolidated optical energy divergencies to the charge carriers in the varied (0.01 – 0.04)g and (0.05)g masses was attributed to the differences FSCs performances. A study by Kashif and Khan (2020) noted that optical energy instability significantly degraded conformities in structures actualization. The performance of the cells was investigated in a dark room and the variation in potentials decay with time was recorded in Table 4.18.

Table 4.18: Potential (V_{OC}) against Time characterization of organic Flourene -TiO_2 luminescent solar cells at varied (0 -0.06)g flourene employing 0.4 g TiO_2 constant photo active layer

Time/ min	Potential(V_{OC}) ($\pm$0.005) V						
	L_1 (0g)	L_2 (0.01g)	L_3 (0.02g)	L_4 (0.03g)	L_5 (0.04g)	L_6 (0.05g)	L_7 (0.06g)
0	0.5	0.3	0.34	0.4	0.64	0.71	0.6
1	0.52	0.32	0.35	0.43	0.65	0.72	0.63
3	0.49	0.34	0.36	0.44	0.66	0.73	0.64
7	0.29	0.31	0.34	0.42	0.68	0.72	0.61
11	0.103	0.29	0.32	0.4	0.69	0.7	0.58
17	0.078	0.3	0.33	0.41	0.67	0.69	0.56
30	0.025	0.28	0.33	0.35	0.61	0.67	0.53
33		0.25	0.31	0.33	0.59	0.65	0.5
45		0.2	0.29	0.3	0.56	0.58	0.48
51		0.17	0.23	0.27	0.49	0.49	0.41
57		0.14	0.2	0.22	0.43	0.45	0.38
60		0.119	0.18	0.2	0.408	0.43	0.36

From the tabulated potential time graphical were presented are as shown in Figure 4.16.

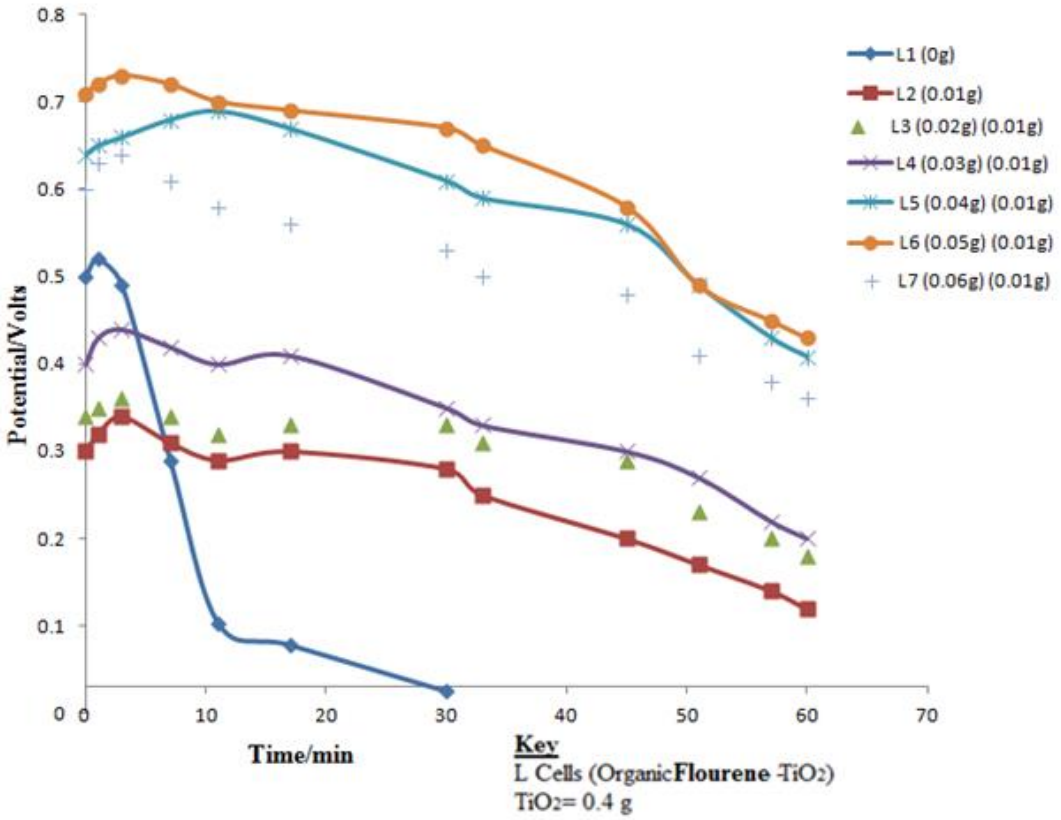

Figure 4.16: Variation of potential (V_{OC}) with time for organic Flourene doped luminescent Cells employing 0.4 g TiO_2 constant

The ability to generate differing (0.119 -0.43) V potential delayed capacities with time was observed to vary as the (0.01-0.05) g mass of flourene was proportionally incremented as depicted in Figure 4.16. That potential sustenance (0.025 V) margin for cell L_1 (0 g) after 30 minutes in minimum radiation confirmed that flourene had significant contribution to excitation energy. The trend of potential increase was observed with cell L_6 (0.05g) Flourene/TiO_2 mixture generating the highest (0.73 V) in (3 minutes) and gradual decay for the subsequent 57 minutes to 0.43 V. The disparity in d-defect population for the lower (0.01 – 0.04) g and (0.05) g masses were thought to influence the difference in the flourene doped FSCs performance. A study by Hamdoush *et al*. (2019) noted that variation of exciton binding energy was proportional to the electron-hole recombination rates with a corresponding charge

carriers population exiting the external surface. Figure 4.17 presents commensurate effect on the delayed potential due to flourene dopant masses 40 minutes after the natural radiation was withdrawn.

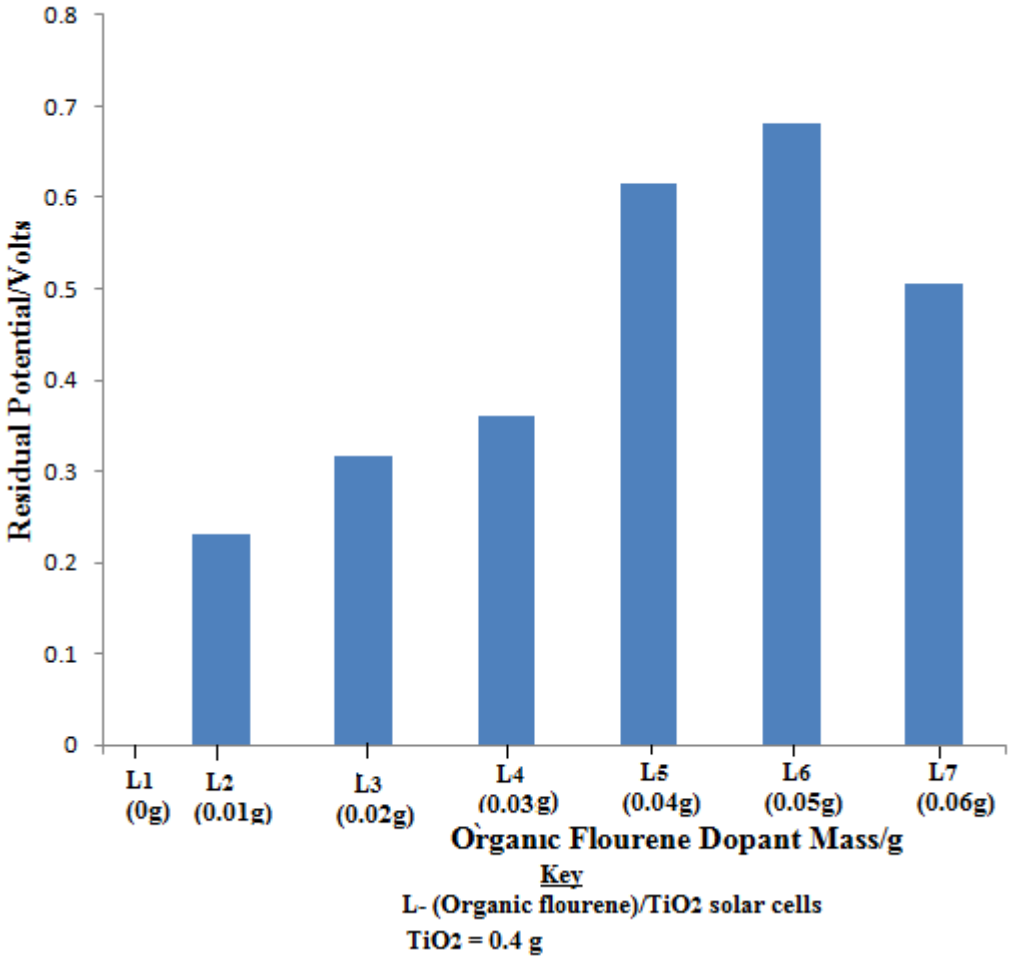

Figure 4.17: Potential (V_{OC}) against time properties of organic Flourene doped luminescent Solar cells employing (0.4 g) TiO_2 constant 40 minutes in minimum solar radiation

The results show improved retention of potential difference increase with mass ratios after 40 minutes of withdrawal solar radiation. The ratio with the highest residual potential was that of L_6 (0.05g Flourene) – **(**TiO_2) luminescent solar cell. Flourene (0.05 g) mass ratio adequately enhanced enhanced band gap edges in (0.4 g) TiO_2 host material. The long distance due to higher (dopant: TiO_2) mass ratio quenched the

d-orbital charged particles activation energy. (Do *et al.*, (2016) noted that favourable mass ratios contributed achieved superior charged species stimulating energy characteristics. Deviation from the profiles gradient uniformity was attributed to gap disparity as the charge carriers returned to their ground states (Harrison, 2012). Another experiment was set up to investigate the effect of increasing the main (0.7) g TiO_2 photo sensitive material with (0 – 0.06) g varying mass of flourene in the photo active layer.

Table 4.19: Parameters derived from (Organic Flourene)/TiO_2 solar cells at varied (0 – 0.06) g Flourene masses employing (0.7) g TiO_2 in the photo active layer

Cell (dopant mass/g)	**$V_{(OC)}$ (V)**	**$I_{(SC)}$ (mA) ($\pm$0.001)**	**FF**	**(η %)**
L_1,a (0 g)	0.224	0.099	0.0102	2.262E-4
L_2,a (0.01g	0.198	0.095	0.0141	2.652E-4
L_3, (0.02g)	0.209	0.102	0.0175	3.552E-4
L_4, a (0.03g)	0.214	0.155	0.0154	4.845E-4
L_5, a (0.04g)	0.269	0.164	0.0183	8.073E-4
L_6,a (0.05g)	0.301	0.186	0.0231	1.293E-3
L_7,a (0.06g)	0.242	0.137	0.0112	3.713E-4

The effect of increasing TiO_2 host material to 0.7 g relative to (0- 0.06) g of organic flourene dopant analysed in Table 4.19 shows that PCE and FF of {(8.073E-4 to 1.293e-3)% and (0.0102 to 0.0231)} were computed from the [(0.198 to 0.301) V and

(0.095 to 0.186)] mA open circuit potentials (V_{OC}) and short circuit current (I_{SC}) observed parameters. This was attributed decreased interaction between internally produced optical energy and the electron-hole pairs. Reports by Gong *et al.* (2018) noted that the lower mass dopant crystals yielded narrow deep-white light emissions at low band width with a consequence of diminishing end result performance.

Table 4.20: Potential (V_{OC}) against time characterization of organic Flourene -TiO_2 luminescent solar cells at varied (0 -0.06)g flourene employing 0.7 g TiO_2 constant photo active layer

Time/ min	Potential(V_{OC}) ($\pm$0.005) V						
	$L_{1,a}$ (0g)	$L_{2,a}$ (0.01g)	$L_{3,a}$ (0.02g)	$L_{4,a}$ (0.03g)	$L_{5,a}$ (0.04g)	$L_{6,a}$ (0.05g)	$L_{7,a}$ (0.06g)
0	0.224	0.174	0.181	0.186	0.258	0.265	0.238
1	0.221	0.188	0.199	0.214	0.269	0.271	0.242
3	0.216	0.198	0.191	0.203	0.236	0.301	0.238
7	0.211	0.179	0.187	0.194	0.224	0.288	0.231
11	0.19	0.151	0.179	0.184	0.229	0.237	0.223
17	0.105	0.129	0.145	0.176	0.213	0.228	0.218
30	0.031	0.115	0.138	0.147	0.211	0.231	0.208
33	0.02	0.111	0.133	0.151	0.205	0.219	0.199
45		0.108	0.119	0.142	0.156	0.215	0.167
51		0.101	0.111	0.137	0.144	0.206	0.131
57		0.093	0.098	0.121	0.126	0.189	0.113
60		0.088	0.093	0.114	0.12	0.186	0.109

From the information shown in Table 4.20, a graphical presentation of potentials against time was made as shown in Figure 4.18.

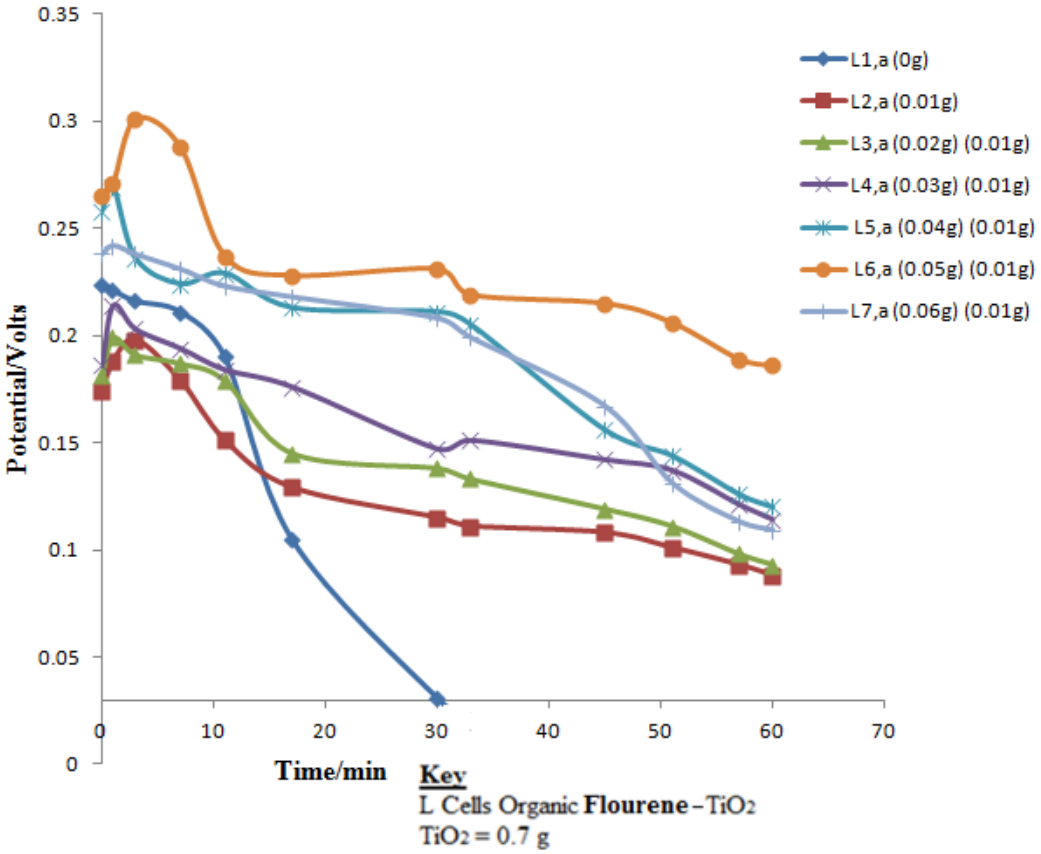

Figure 4.18: Potential (V_{OC})- Time characteristics for organic Flourene doped fluorescent solars cells employing (0.7 g) TiO_2 constant mass ratio

The result of Figure 4.18 shows {(organic Flourene) - (TiO_2)} FSCs V-T characteristics at (0.7 g) TiO_2 constant mass. The curtailed {0.114, 0.12, 0.186 and 0.109} V residual potentials difference were observed from {L_4,a (0.03g) L_5,a(0.04 g), L_6,a(0.05 g) and L_7,a (0.06g)} FSCs, respectively. Below (0.3 g) mass of dopant flourene, 0.100 V and beneath residual potentials were recorded. The higher host mass was thought to recede charge carrier lifetime with a diminishing trend of their fluorescence. Research by Meng (2017) indicated that non-radiative decay was significantly supplemented by the higher perovskite mass ratios. A study by Meng (2017) noted that s-p anti-bonding coupling provided favorable band gap conditions

with strong defect tolerance and shallow point defects which consequently reduced surface recombination of charge carriers.

Another investigation was done by mixing (0.35 g) TiO_2 photo active material with the different (0.01 to 0.06) g flourene fluorescent material and the fabrication process followed as explained in section 3.5. The resulting cells were observed in clear daylight and their performance were presented in Table 4.21.

Table 4.21: Parameters derived from (Organic Flourene)/TiO_2 solar cells at varied (0 – 0.06) g Flourene masses employing (0.35) g TiO_2 in the photo active layer

Cell (%dopant)	**$V_{(OC)}$ (V)**	**$I_{(SC)}$ (mA) ($\pm$0.001)**	**FF**	**(η %)**
L_1,b (0 g)	0.425	0.93	8.116E-4	3.208E-4
L_2,b (0.01g	0.207	0.76	2.447E-3	3.849E-4
L_3,b (0.02g)	0.246	0.82	3.761E-3	7.585E-4
L_4, b (0.03g)	0.258	1.156	3.884E-3	1.158E-3
L_5, b (0.04g)	0.357	1.615	3.94E-3	2.272E-3
L_6,b (0.05g)	0.497	1.88	5.47E-3	5.111E-3
L_7,b (0.06g)	0.223	0.943	3.61E-3	7.596E-4

The I-V characteristics in Table 4.21 shows potentials (V_{OC}) generated by (0-0.6)g flourene doped FSCs at 0.35 g constant. The V_{OC} and I_{SC} {(0.207, 0.246, 0.246, 0.258, 0.357, 0.497) V and (o.76, 0.82, 1.156, 1.615 and 1.88) mA} parameters were

observed to improve proportionally with the fluorescent material mass increase. Cell L_1, b (0 g) without flourene dopant generated 0.425 V higher potential compared to (0.01 – 0.04) g with (2.45E-3 to 3.94E-3) declining fill factors. The sample void of energy enhancing material was thought to provide regular guided waveguide paths with higher charge carrier density at the specimen external surface. Prescience of flourene dopant created varied scattered energy sources (defect derived) centres which interfered with the normal charge carrier guided paths to the outer surface. A study by Wang *et al*., (2018) noted that high binding energies in the dominant closed – azo samples radiated short bandwidth energy in varied dimensions. Performance of the samples was investigated in a dark environment for one hour and the results obtained presented in Table 4.22.

Table 4.22: Potential (V_{OC}) against time characterization of organic Flourene -TiO_2 solar cells at varied (0 -0.06)g flourene employing 0.35 g TiO_2 constant photo active layer

Time/ min	Potential (V_{OC}) ($\pm$0.005) V						
	$L_{1,b}$ (0g)	$L_{2,b}$ (0.01g)	$L_{3,b}$ (0.02g)	$L_{4,b}$ (0.03g)	$L_{5,b}$ (0.04g)	$L_{6,b}$ (0.05g)	$L_{7,b}$ (0.06g)
0	0.425	0.193	0.246	0.256	0.345	0.486	0.219
1	0.321	0.207	0.243	0.258	0.357	0.497	0.223
3	0.218	0.188	0.203	0.234	0.342	0.431	0.184
7	0.114	0.156	0.189	0.209	0.336	0.374	0.165
11	0.1	0.133	0.164	0.199	0.309	0.328	0.154
17	0.083	0.121	0.133	0.187	0.281	0.291	0.145
30	0.01	0.108	0.124	0.156	0.269	0.246	0.141
33		0.099	0.118	0.132	0.155	0.209	0.137
45		0.04	0.1	0.117	0.113	0.193	0.13
51			0.07	0.072	0.1	0.157	0.101
57				0.052	0.099	0.129	0.044
60				0.043	0.09	0.118	0.036

From the information recorded in Table 4.22, a graphical representation of the potential against the time was made as shown in Figure 4.19.

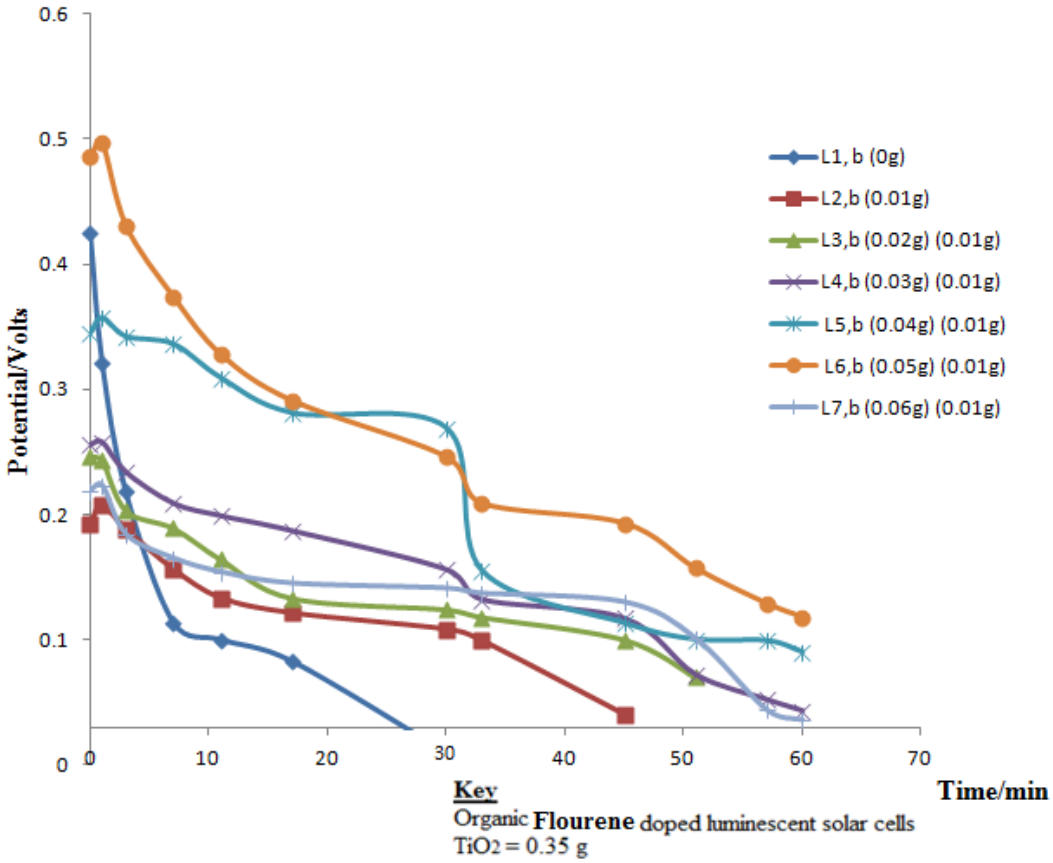

Figure 4.19: Potential - Time characteristics for organic Flourene doped luminescent solar cells employing (0.35 g) TiO_2 constant mass ratio

Observations from Figure 4.19 indicate that { $L_{7,b}$(0.06 g), $L_{6,b}$ (0.05 g), $L_{5,b}$(0.04g) and $L_{4,b}$ (0.03g) organic (flourene-TiO_2) FSCs resulted to (0.036, 0.118,0.09 and 0.043) V residual potentials in 60 minutes due to 0.35 g mass. Cells $L_{3,b}$(0.02 g) and $L_{2,b}$(0.01 g) recorded below 0.001V delayed potentials. These potentials were attributed to the corresponding electronic charges due to the varying flourene dopant masses. However, the (Organic Flourene – TiO_2) mixture hormogeneinity at (TiO_2 = 0.4 g) resulted to uniform optical scattering energy of the defect trapped charged species as they relaxed to their ground states. That longer wavelength radiated activation potential had lesser deviations because of its smooth transition to excite

externally transiting species with more gradual slopes than for (0.7 and 0.35) g TiO_2) masses. A study by Strunk (2021) indicated that charge carriers recombination suppressed the expected results with fast diminishing fluorescence in the scanty trapping and clamped sites for both shallow and deep diffused centres.

4.6 Analysis of Garlic Organic luminescent material

Allicin (diallyl-thiosulfinate) active compound in garlic is rich of carbon sulfur compounds. The structure of the allicin is provided in Figure 4.20.

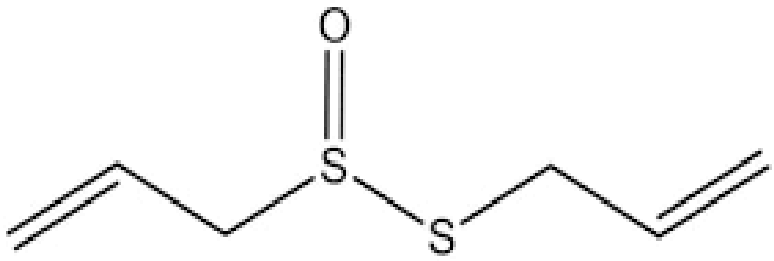

Figure 4.20: Structure of Allicin (diallyl-thiosulfinate) active compound in garlic

The garlic sample was observed to vary progressively from blue, red and brown under UV radiation. This was attributed to the presence of disulfides, which fluoresce in UV/Vis radiation. This was enabled by the presence of σ π double bonds which absorb radiation due to their constant vibration and rotation of molecules as reported by (Spence, 2019).

4.6.1 FTIR analysis of Allicin in Garlic sample for luminescent solar cell application

Solid samples of garlic were characterized separately using FTIR spectrophotometer. The spectrum obtained is as shown in Figure 4.21.

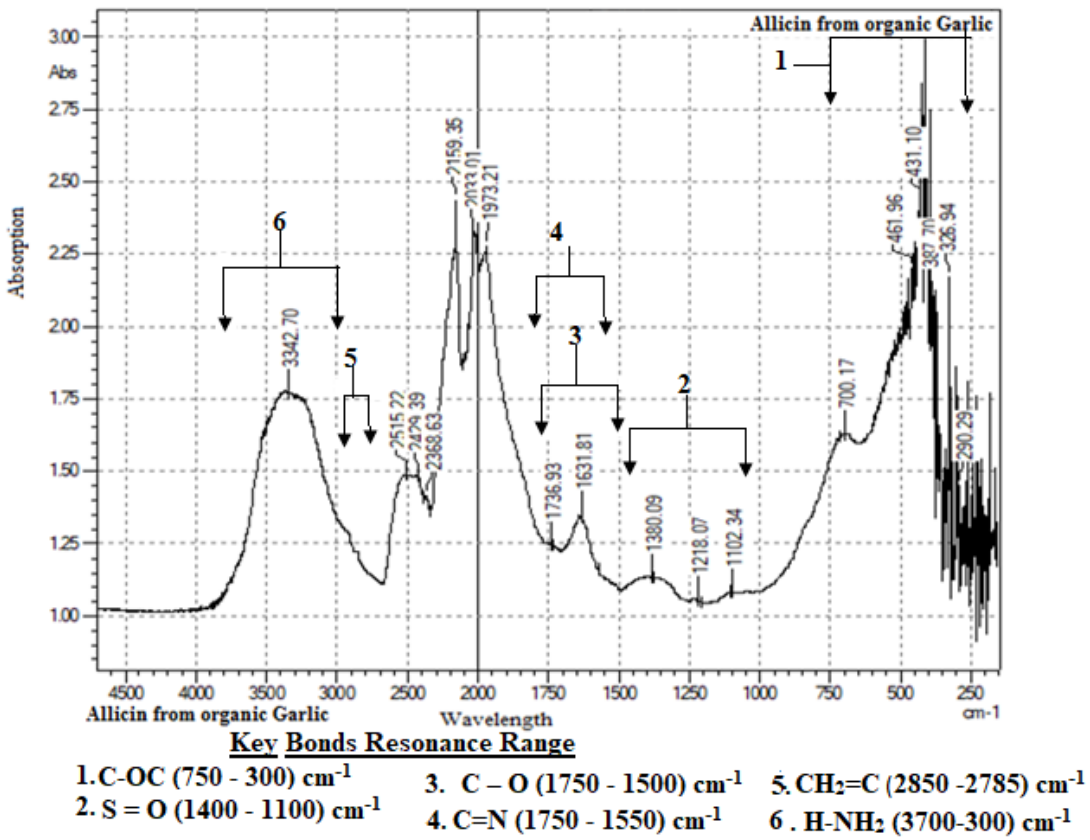

Figure 4.21: FTIR Absorption Spectrum analysis of Allicin from Garlic organic photo luminescence material

Garlic has sulphur atoms within its structure whose prescence was confirmed by the results shown in Figure 4.21. The properties of allicin (diallyl-thiosulfinate) different functional groups were evidenced by their respective resonant frequencies. The {CH_2=C ,C=N, S=O, C-O, H-NH} open chain bonds were observed to resonate in the frequency bands between {([2850 -2785) and 1500- 1250] stretching and scissor, [(2700-2200) and (2200-1800)], [(1250-1000 and 600-350)] stretching moments and bending moments), (824), [(3100-3070), (1420-1410) and (900-880)] and [(3800-2600)]} cm^{-1}. The peak at (2159.35, 2033.01 and 1973.21) cm^{-1} were contributed by C=N functional in Allicin (diallyl-thiosulfinate) with varied stretching moments due to their varied sites. The (1380.09, 1218.07 and 1102.34) cm^{-1} observed peaks

resulted due to S=O stretching moments. Peaks at (2515.22, 2429.39 and 2368.63) cm^{-1} stretching resonated due to CH_2=C, while that at 3342.70 cm^{-1} resulted from H-NH_2 bonds in the allicin structure. The C-O bonds were observed to resonate between (1102 - 700) cm^{-1} frequency bands. These conjugated bonds structures in combination with alphatic/alicyclics contributed to the exhibited flourescence.That agreed with Pupkaite (2020) who noted that structures propensity to aggregate of allicin in garlic had considerable influence on the absorption spectrum. The observed peaks were as a result of functional groups responsible for fluorescence of in garlic (Guo *et al.*, 2017). A study by Zhang *et al.* (2016) noted that the structure bonds band gaps of organic luminescent materials were activated to transform light energy to long wavelength radiations. That property of allicin in garlic was exploited in this study with a view to increase spectral trapped by allicin and released later to prolong radiation to the photo active titanium dioxide (TiO_2) photo active material. Varying masses of allicin were thoroughly mixed with different samples of (TiO_2) photoactive material of constant mass (1.00 g) as outlined in Table 4.22.

4.6.2 Fluorescence property of allicin in garlic.

The different ratios of the mixture were used to fabricate photo cells and applied to study their delay in photo activity after withdrawal of radiation. Different cells were fabricated by taking 0.4 g of each Allicin -TiO_2 mixture to make the photo active layer. The receptive layer was made using (0.48 g) of graphite-iodine (C_x/I_2/KI) mass composition whose ratios were 0.3 g, 0.17 g and 0.01 g respectively for each receptive electrode. The resulting cells were analyzed using a constant radiation in a clear daylight and the observation made were recorded in Table 4.22.

Table 4.22: Parameters derived from (Organic Allicin)/TiO_2 solar cells at varied (0 – 0.06) g Allicin masses employing (0.4) g TiO_2 in the photo active layer

Cell (allicin mass/g)	$V_{(OC)}$ (V)	$I_{(SC)}$ (mA) ($\pm$0.001)	FF	(η %)
Q_1 (0 g)	0.521	0.382	0.295	0.0587
Q_2 (0.01g	0.632	0.291	0.134	0.0246
Q_3 (0.02g)	0.675	0.533	0.176	0.0633
Q_4 (0.03g)	0.662	1.63	0.229	0.247
Q_5 (0.04g)	0.711	2.191	0.249	0.388
Q_6 (0.05g)	0.842	1.953	0.385	0.633
Q_7 (0.06g)	0.741	1.851	0.279	0.383

The results of Table 4.22 shows enhanced potential differences proportional to allicin dopant mass increase observed from allicin doped FSCs samples. The terminal voltage gap between [Q_1 (0g) through Q_5 (0.04 g)] samples progressively widened as {(0.521 - 0.711) V proportional to (0.382 - 1.63) mA short circuit current respectively. The (0.05g) allicin dopant mass had outstanding (0.84V and 1.953mA) output parameters successfully with significant (0.385 and 0.33%) fill factor and power conversion efficiency correspondingly. The least (0.521) V potential energy observed from sample Q_1, (0g) was attributed to the marginal photo activity due to defect triggered unidirectional optical energy. Deviations effected to allicin/TiO_2 mixture masses affected the symmetrical balance with a comparable terminal parameters.

Harmonised mass ratio to molecular bonds excited states contributed to stimulation of diverging multiple charged species (McArthur *et al.,* 2018). The cells were then relocated to a diminished radiation environment for an interval of one hour where variation of potential energy was monitored with time and the results were recorded in Table 4.23.

Table 4.23: Potential (V_{OC}) against Time characterization of (Allicin / TiO_2) luminescent solar cells at varied (0 -0.06)g allicin employing 0.4 g TiO_2 constant photo active layer

Time/ min	**Potential (V_{OC}) ($\pm$0.005) V**						
	Q_1 (0g)	Q_2 (0.01g)	Q_3 (0.02g)	Q_4 (0.03g)	Q_5 (0.04g)	Q_6 (0.05g)	Q_7 (0.06g)
0	0.51	0.63	0.672	0.65	0.675	0.71	0.72
1	0.52	0.632	0.673	0.66	0.677	0.72	0.74
3	0.47	0.634	0.675	0.66	0.68	0.74	0.73
7	0.101	0.629	0.674	0.65	0.69	0.79	0.75
11	0.059	0.618	0.671	0.66	0.7	0.84	0.72
17	0.03	0.62	0.644	0.62	0.69	0.82	0.71
30		0.51	0.591	0.61	0.65	0.79	0.68
33		0.4	0.478	0.63	0.62	0.76	0.65
45		0.39	0.38	0.58	0.49	0.69	0.55
51		0.24	0.3	0.54	0.4	0.6	0.5
57		0.21	0.27	0.42	0.39	0.5	0.45
60		0.2	0.26	0.36	0.38	0.48	0.43

From the tabulated potential- time results, graphical presentations were prepared as shown in Figure 4.22.

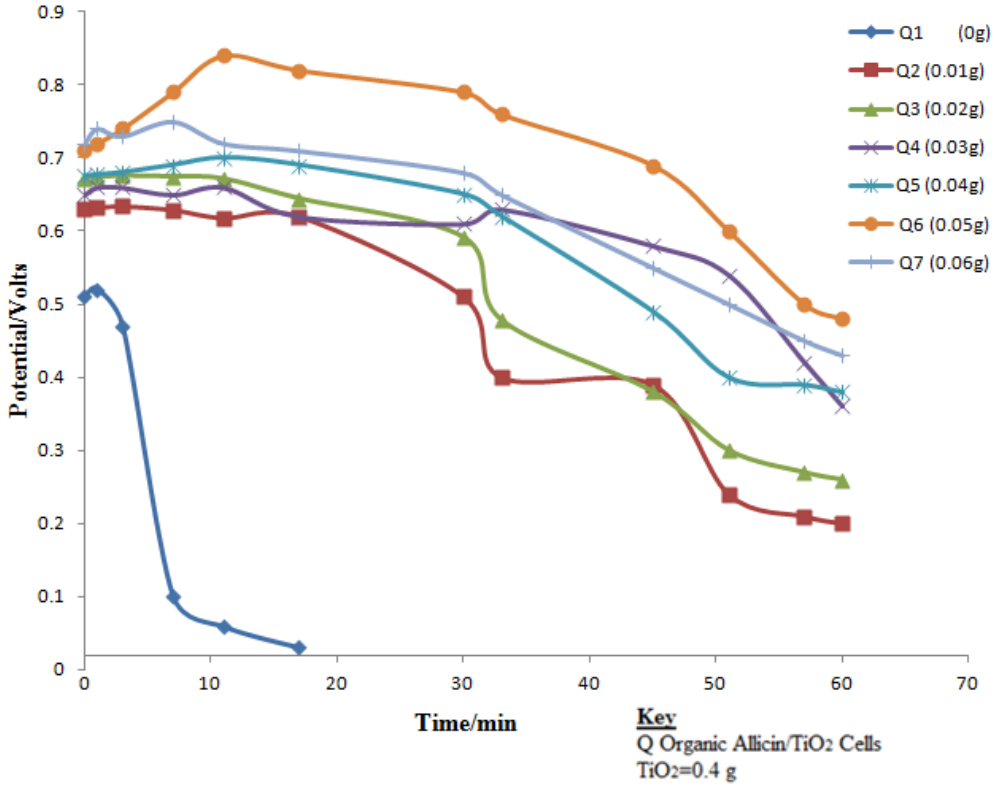

Figure 4.22: Potential (V_{OC}) - Time characterization for Allicin /TiO_2) luminescent solar cells employing 0.4 g TiO_2 constant

Resembling features of Figure 4.22 presents fluctuating potential decay corresponding to the changing masses of allicin in allicin/TiO_2 complex samples after withdrawal of solar radiated incident energy. Magnificent (0.09-0.043) V potential difference ripples due to cells Q_2,(0.01 g) and Q_3, (0.02)g were observed between (30 - 33) minutes time constant. That Q_4,(0.03 g) sample residual potential was uniformly enhanced until a limit of 50 minutes when a declining response ensued. Cell Q_6,(0.05) g exhibited (0.48) V most improved potential delay after the lapse time of observation. However, cell Q_1, (0g) extinguished before lapse quarter of the entire time constant.

The introduced multiple defects sustained sequence of surplus energy in allicin-TiO_2 matrix at varied bandwidth. Proportionate allicin masses supplimented for optical

energy enhancement at varied wavenumbers. A study by Yu *et al.* (2017) reported that presence of $\sigma\pi$-systems supported generation of both donor and acceptor charge carriers by releasing delayed radiations. The interferance with band gap energy affected rigidity of three-dimensional lattice which provided large carrier mobility leading to broad conduction (Yu *et al.*, 2017).

Further investigation was done on cells $Q_{1,a}$, $Q_{2,a}$, $Q_{3,a}$, $Q_{4,a}$, $Q_{5,a}$, $Q_{6,a}$ and $Q_{7,a}$ fabricated with different masses of allicin at constant TiO_2 (0.76 g) and the results were characterized in a clear daylight and their photo activity response was presented in Table 4.24.

Table 4.24: Parameters derived from (Organic Allicin)/TiO_2 solar cells at varied (0 – 0.06) g Allicin masses employing (0.76) g TiO_2 in the photo active layer

Cell (Allicin mass/g)	**$V_{(OC)}$ (V)**	**$I_{(SC)}$ (mA) ($\pm$0.001)**	**FF**	**η%**
Q_1, a (0 g)	0.267	0.063	0.203	3.415E-3
Q_2, a (0.01g	0.152	0.051	0.029	2.248E-4
Q_3, a (0.02g)	0.189	0.058	0.032	3.508E-4
Q_4,a (0.03g)	0.199	0.07	0.033	4.597E-4
Q_5,a (0.04g)	0.247	0.073	0.034	6.551E-4
Q_6,a (0.05g)	0.259	0.078	0.035	7.071E-4
Q_7, a (0.06g)	0.235	0.069	0.026	4.216E-4

The impact of incremented (0.76 g) TiO_2 with respect to (0 – 0.05) g varying allicin presented in Table 4.24, had uncomplimentary {(0.152- 0.259) V and (0.051 – 0.078) mA} potential (V_{OC}) and short circuit current (I_{SC}) respectively of [Q_2,a (0.01g) - [Q_6,a (0.05g)] FSCs. However, the negligible difference did not match (0.267 V) of the [Q_1,a (0g)] undoped terminal potential (V_{OC}) sample with (0.203 and 3.415E-3 %) fill factor and power conversion efficiency. The high TiO_2 mass was thought to encapsulate the σ π disulfide structural defects moments. A study by Baloch *et al*. (2018) noted that high levels of photosensitive material resulted to quenching of the time resolved photoluminescence signal within the perovskite layer with a faster decay. A study of the cells performance in a diminished radiation condition was carried out for an interval of one hour and the results presented in Table 4.25.

Table 4.25: Potential (V_{OC}) – Time characterization of Allicin / TiO_2 luminescent solar cells at varied (0 -0.06)g allicin employing 0.76 g TiO_2 constant photo active layer

Time/ Min	Potential (V_{OC}) ($\pm$0.005) V						
	$Q_{1,a}$ (0g)	$Q_{2,a}$ (0.01g)	$Q_{3,a}$ (0.02g)	$Q_{4,a}$ (0.03g)	$Q_{5,a}$ (0.04g)	$Q_{6,a}$ (0.05g)	$Q_{7,a}$ (0.06g)
0	0.267	0.135	0.169	0.173	0.242	0.259	0.231
1	0.212	0.143	0.183	0.199	0.247	0.241	0.235
3	0.206	0.152	0.189	0.188	0.229	0.239	0.226
7	0.179	0.132	0.164	0.167	0.231	0.235	0.221
11	0.138	0.127	0.141	0.171	0.227	0.23	0.211
17	0.101	0.119	0.135	0.165	0.221	0.226	0.211
30	0.083	0.11	0.131	0.153	0.216	0.207	0.109
33	0.052	0.105	0.129	0.147	0.192	0.184	0.104
45	0.034	0.101	0.119	0.138	0.151	0.171	0.101
51	0.011	0.081	0.111	0.132	0.138	0.153	0.09
57		0.060	0.101	0.119	0.121	0.131	0.074
60		0.051	0.093	0.109	0.115	0.123	0.066

From the information recorded in Table 4.25, a graphical presentation of potentials against the time was made as shown in Figure 4.23.

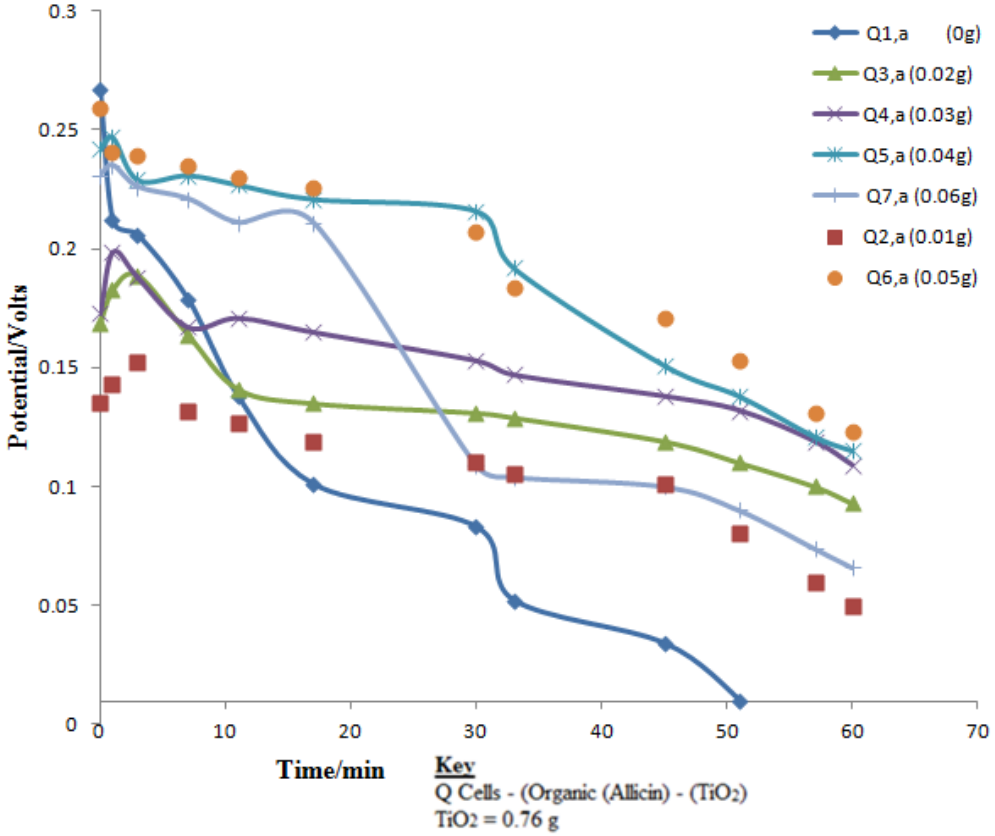

Figure 4.23: Potential-Time characterization for (Allicin -TiO_2) luminescent solar cells employing (0.76 g) TiO_2 constant mass ratio

The notable constrained features of the (0.76V) TiO_2 constant at varying (0-0.06) g allicin solar cells shown in Figure 4.23 depicting varying potential - time characteristics. The monitored {(Q_1,(0g), Q_5,(0.04g), Q_6,(0.05g), and Q_7,(0.06g) potential had remarkable unsteady crest-troughs characteristics. Abrupt changes in potentials due to these samples cells occurred between (12- and 48) minutes. That parameter was observed to vary between { (0.05 V) for Q_1,a(0g), (0.11V) for Q_7,a(0.06 g), (0.073V) for Q_5,a(0.04g), and negligible (0.035 V) for Q_6,a(0.05 g). Regular with sine wave features were observed were observed between (0 - 8) minutes for cells Q_2,a(0.01 g) and Q_4,a(0.03g), This was indicative to presence of abrupt changes in band gap energies due to varying optical energy bandwidths. A study by Baloch *et al*. (2018) noted that high levels of photosensitive material result

to quenching of the time resolved photoluminescence signal within the perovskite layer with a faster decay. Higher recombination rate occurs by bimolecular process of the band to band transition leading to low conditions of the photo carrier density giving rise to imbalance to density of the majority carriers resulting to lower potential Baloch *et al.,* 2018). Another investigation was done with TiO_2 varied to 0.2g mass and the I-V monitored data was recorded in Table 4.26.

Table 4.26: Parameters derived from (Organic Allicin)/TiO_2 solar cells at varied (0 – 0.06) g Allicin masses employing (0.2) g TiO_2 in the photo active layer

Cell (allicin mass/g)	**V(OC) (V)**	**ISC) (mA) (±0.001)**	**FF**	**η %**
Q_1,b (0 g)	0.273	1.336	6.048E-4	2.206E-4
Q_2,b (0.01g	0.245	1.225	5.137E-4	1.542E-3
Q_3,b (0.02g)	0.262	1.965	4.699E-4	2.419E-4
Q_4,b (0.03g)	0.318	3.975	3.233E-4	4.087E-4
Q_5, b (0.04g)	0.408	4.896	2.581E-4	8.947E-4
Q_6,b (0.05g)	0.419	6.385	2.414E-4	6.458E-4
Q_7,b (0.06g)	0.392	7.841	1.134E-4	3.486E-4

The I-V of (0 – 0.06) g varying $\sigma\ \pi$ dially-thiosulfinate properties in (0.2 g) TiO_2 constant analysed in Table 4.26, was characterized with recuperative potentials (V_{OC}) and short circuit current (I_{SC}) parameters. The {Q_2, b(0.01)g – Q_6, b(0.05) g potential yield developed [(0.245 -0.419) V and (1.23 – 6.38)mA] progressively with (1.54 – 8.95)% series repetitive PCE and (5.14E-4 - 1.11E-4) uniformly improving fill factor. This was attributed to a condusive interactive medium for the defect generated charge carrier optical energy. Reports by Previtali (2021) noted that fluorescence spectra of allicin (σ-π) alicyclics rings in dilute solvent enhanced generation or multiple charge carriers. The response of $\sigma\ \pi$ dially-thiosulfinate properties in (0.2 g) TiO_2 constant under minimum radiation circumstances was recorded in Table 4.27.

Table 4.27: Potential (V_{OC}) - Time characteristics of Allicin / TiO_2 luminescent solar cells at varied (0 -0.06)g employing 0.2 g TiO_2 constant photo active layer

Time/ min	Potential(V_{OC}) ($\pm$0.005) V						
	Q_1,b (0g)	Q_2,b (0.01g)	Q_3,b (0.02g)	Q_4,b (0.03g)	Q_5,b (0.04g)	Q_6,b (0.05g)	Q_7,b (0.06g)
0	0.273	0.245	0.262	0.293	0.385	0.413	0.392
1	0.238	0.227	0.251	0.318	0.408	0.411	0.382
3	0.207	0.204	0.248	0.298	0.399	0.419	0.337
7	0.179	0.189	0.234	0.262	0.382	0.405	0.285
11	0.137	0.138	0.219	0.256	0.369	0.372	0.242
17	0.102	0.116	0.206	0.247	0.284	0.328	0.227
30	0.084	0.105	0.191	0.198	0.267	0.251	0.219
33	0.032	0.094	0.177	0.173	0.211	0.254	0.203
45		0.048	0.118	0.128	0.165	0.218	0.173
51		0.037	0.103	0.102	0.127	0.173	0.133
57			0.071	0.091	0.108	0.149	0.115
60			0.061	0.076	0.102	0.136	0.109

From the results in Table 4.27 a graphical presentation of potential (Voc) against time was made as shown in Figure 4.24.

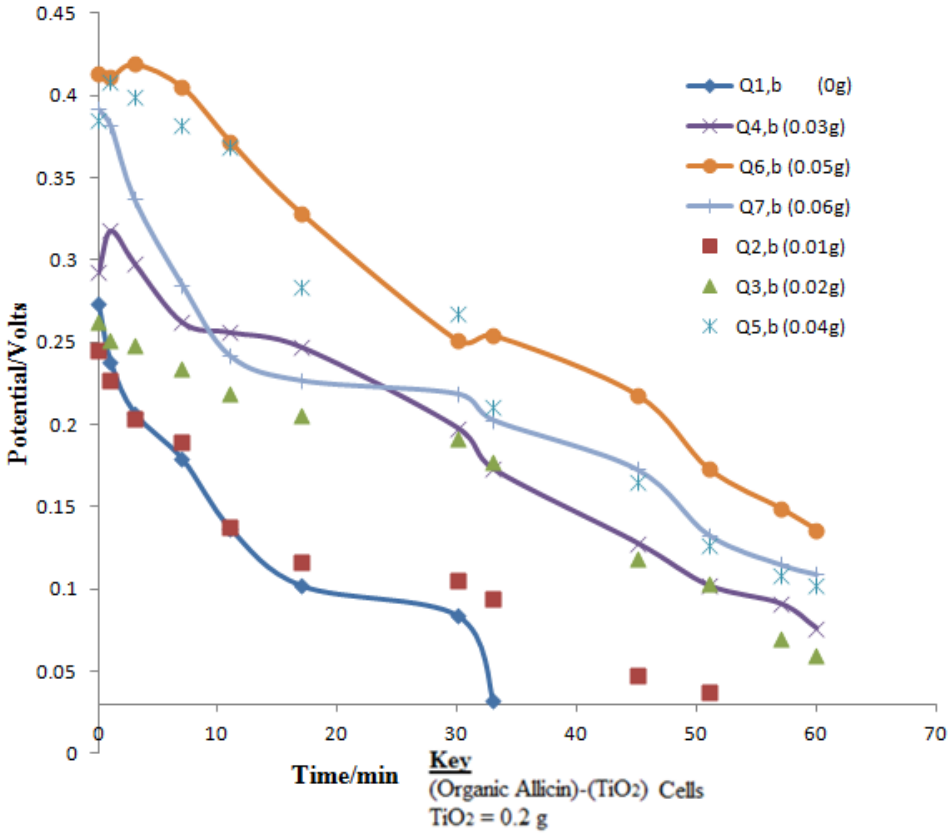

Figure 4.24: Potential-Time characterization for (Allicin -TiO_2) luminescent solar cells employing (0.2 g) TiO_2 constant mass ratio

Rapid diminishing{Q_6,b (0.05)g, Q_7,b (0.06)g , Q_5, b(0.04)g and Q_1,b (0)g (0.17, 0.15 ,0.08 and 0.2) V potential between [(9-30), (0 - 15), (0-15) and (0-30) minutes time constants were observed from Figure 4.24. Potentials rise of (0.025, and 0.08)V magnitude step and saw –tooth signals were observed from [Q_4,b(0.03)g and Q_6,b(0.05)g] profiles in {(0- 2) and (0-3)} minutes time constant correspondingly. The instant appreciated potentials were attributed to excitation of dipoles by short bandwidth energy at the interfaces between the dially-thiosulfinate complex and TiO_2 host material. A study by Steckl *et al.* (2012) noted that suitable interacting complex masses generated multicolored radiation exciting varying proportion of charge carriers responsible for the terminal potentials. According to Liaw *et al*. (2012) some

interacting molecules did not display aggregation-induced emission (AIE) because their bridging oxygens hindered nonradiative activation through intermolecular rotation with a consequence of inadequate quenching by the aggregation.

In conclusion, the allicin dopant: host material mass of {(0.05:0.2), (0.05:0.4) and (0.05:0.76)} g gradually generated improved {0.136, 0.48 and 0.123}V potentials delay within the 60 minutes time constant compared to rest of the mass.

4.7 Analysis of gingerol as photo luminescent material

The gingerol was obtained from biomaterial (ginger) and was extracted as explained in the methodology for use in this study (Santos-Sánchez *et al.,* 2017). The structure of the gingerol photo luminescent material is shown in Figure 4.25.

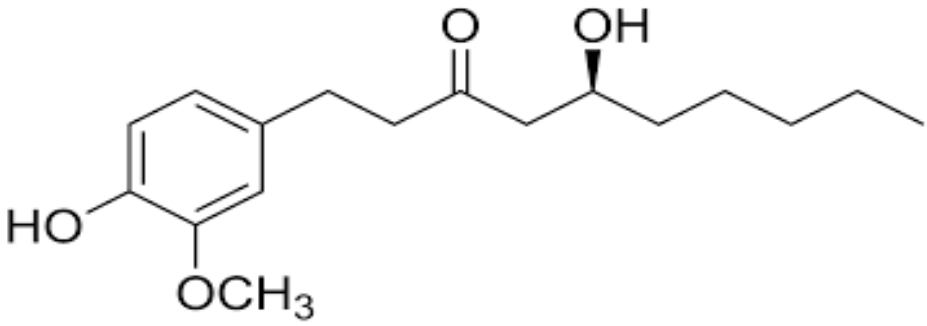

Figure 4.25: Active gingerol structure in ginger photo fluorescent material

Illumination of gingerol with UV radiation yielded a yellow coloured radiation. The fluorescence property is enabled by the presence an aromatic ring structure within the structure of ginger as well as carbonyl functional groups that contribute to its fluorescence property when subjected to radiation with frequencies above the visible region (Meng *et al.*, 2019).

Gingerol has a low aqueous solubility with high sensitivity to light due to its chemical structure and hence suitable for this study (Tavares *et al.*, 2022). The information regarding the composition and functional groups in gingerol was provided by FTIR analysis.

4.7.1 FTIR analysis of Gingerol material for luminescent solar cell application

Solid samples of ginger were characterized separately using FTIR spectrophotometer. A typical FTIR absorption spectrum is as shown in Figure 4.26.

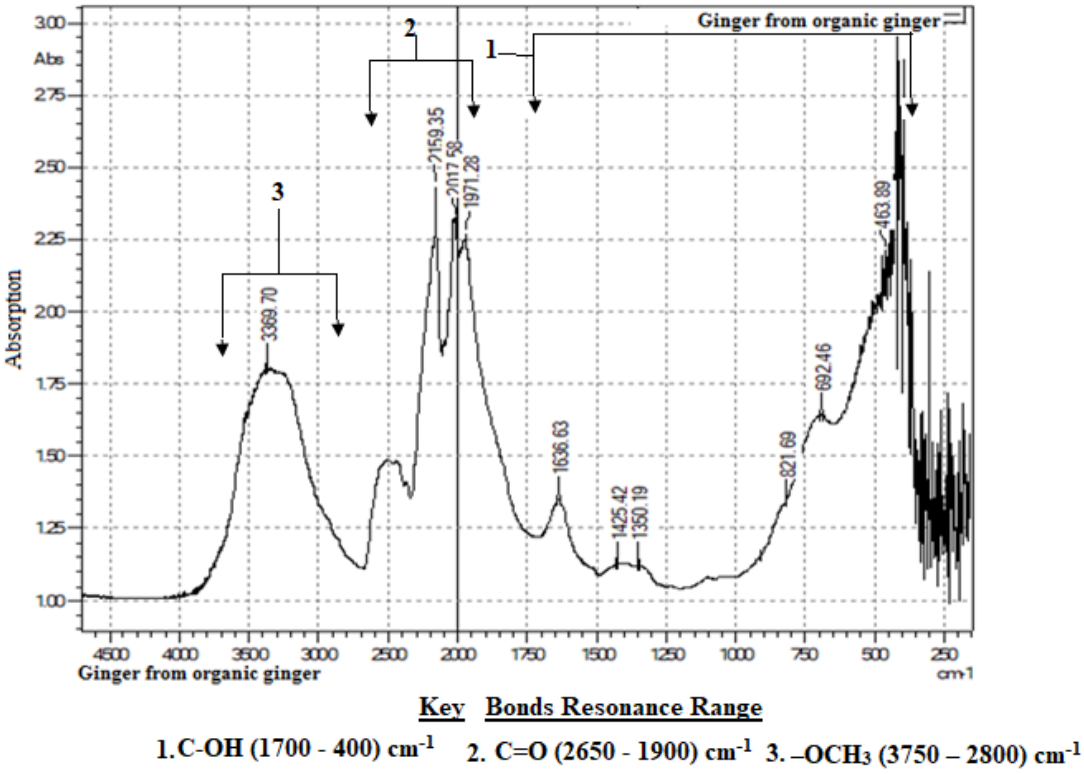

Figure 4.26: FTIR Absorption Spectrum analysis of Gingerol Extract Photo Luminescence Organic Material

The response of resonating gingerol functional groups to infrared radiation was presented as shown in Figure 4.26. Oscillating frequency bands were observed between {(2350-1700), (1500-1200) and (3800-2750)} cm^{-1} fundamental and mid-

regions, respectively. The strong and broad peak at 3369.70 cm^{-1} were resulted due to stretching of $–OCH_3$ while the strong and intense peaks at (2159.35, 2017.58 and 1971.28) cm^{-1} occurred due to three dimensional moments of C=O bonds. The sharp and intense 1636.63cm^{-1} and the (1425.42 and 130.19) cm^{-1} weak and bold peaks were contributed by the C-OH bonds of open azo gingerol molecular structure. Studies by Zhang *et al*., (2020) noted that presence of functional groups contributes to florescence in gingerol. That agreed with the findings of Abderrazak *et al*. (2021), Alexey *et al*. (2016) who reported that agitation of conjugated $\sigma\ vs\ \sigma\pi$ bonds in NH_2, OH and OCH_3 functional groups shifted the absorbed radiation to different wavelengths. Studies by Zawada & Mazel (2014) reported that peaks in the spectrum result from functional groups and are responsible for fluorescence in organic materials.

That fluorescent property of gingerol in ginger was exploited in this study with a view to increase spectral traps by gingerol and released later to prolong radiation to the photo active titanium dioxide (TiO_2) material.

Varying masses of gingerol which is an organic luminescent material were thoroughly mixed with different samples of constant mass (1.00 g) of the photoactive material (TiO_2) in the proportions outlined in Table 4.28.

4.7.2 Radiation Delay by Gingerol Fluorescent Material

Different cells were fabricated by taking 0.4 g of each Ginger-TiO_2 mixture to make the photo active layer. The receptive layer was made using (0.48 g) of graphite-iodine (Cx /I/KI) mass composition whose ratios were 0.3 g, 0.17 g and 0.01 g respectively

for each receptive electrode. The resulting cells were analyzed in constant solar radiation and their corresponding I-V characteristics were presented in Table 4.28

Table 4.28: Parameters derived from (Organic Gingerol)/TiO_2 solar cells at varied (0 – 0.06) g Gingerol masses employing (0.4) g TiO_2 in the photo active layer

Cell (gingerol mass/g)	**$V_{(OC)}$ (V)**	**$I_{(SC)}$ (mA) ($\pm$0.001)**	**FF**	**(η %)**
R_1 (0 g)	0.518	0.382	0.016	3.166E-3
R_2 (0.01g	0.341	1.15	0.065	0.025
R_3 (0.02g)	0.629	1.44	0.166	0.151
R_4 (0.03g)	0.683	1.82	0.194	0.241
R_5 (0.04g)	0.712	1.85	0.247	0.325
R_6 (0.05g)	0.719	1.94	0.372	0.519
R_7 (0.06g)	0.709	1.74	0.232	0.286

Table 4.28 shows I-V varied responses due to (0 – 0.06) g gingerol incrementing mass at constant (0.4g) TiO_2 fluorescence solar cells. Modest 0.581 V was observed from R_1 (0 g) void of gingerol dopant material. The doping enhancement indicated that potential improved through (0.341-0.719) V as gingerol (0.01 to 0.05) g mass was incremented correspondingly resulting to {(0.065 – 0.372) and (0.025 -0.519) %} fill factor and PCE increase. Comparable (1.15 – 1.94) mA appreciating short circuit current parameters were observed. Exceeding (0.05) g gingerol mass potential difference trimming trend ensued. The blending of distributed bandwidths with incident radiation enhancement material was thought to support excitation of more

charge carriers. A study by Kužel and Němec (2020) noted that enhancement of optical energy absorbility was achieved by supplementing varied band gap substances with subsidiary ingredients. The terminal potentials were again monitored in a dark room and the results presented in Table 4.29.

Table 4.29: Potential (V_{OC}) - Time characterization of Gingerol-TiO_2 luminescent solar cells at varied (0 -0.06)g gingerol employing 0.4 g TiO_2 constant photo active layer

Time/ min	Potential (V_{OC}) ($\pm$0.005) V						
	R_1 (0 g)	R_2 (0.01g)	R_3 (0.02g)	R_4 (0.03g)	R_5 (0.04g)	R_6 (0.05g)	R_7 (0.06g)
0	0.51	0.338	0.594	0.677	0.683	0.687	0.701
1	0.518	0.34	0.606	0.679	0.698	0.692	0.703
3	0.47	0.341	0.619	0.682	0.708	0.699	0.709
7	0.39	0.36	0.62	0.683	0.712	0.703	0.704
11	0.102	0.39	0.629	0.678	0.707	0.719	0.7
17	0.052	0.34	0.621	0.672	0.692	0.708	0.699
30	0.02	0.33	0.597	0.659	0.677	0.704	0.659
33		0.3	0.571	0.599	0.643	0.685	0.641
45		0.25	0.501	0.546	0.612	0.651	0.639
51		0.21	0.493	0.521	0.592	0.625	0.594
57		0.19	0.413	0.505	0.585	0.617	0.552
60		0.17	0.395	0.493	0.576	0.601	0.543

From the tabulated potential- time results, graphical presentations were plotted as shown in Figure 4.27.

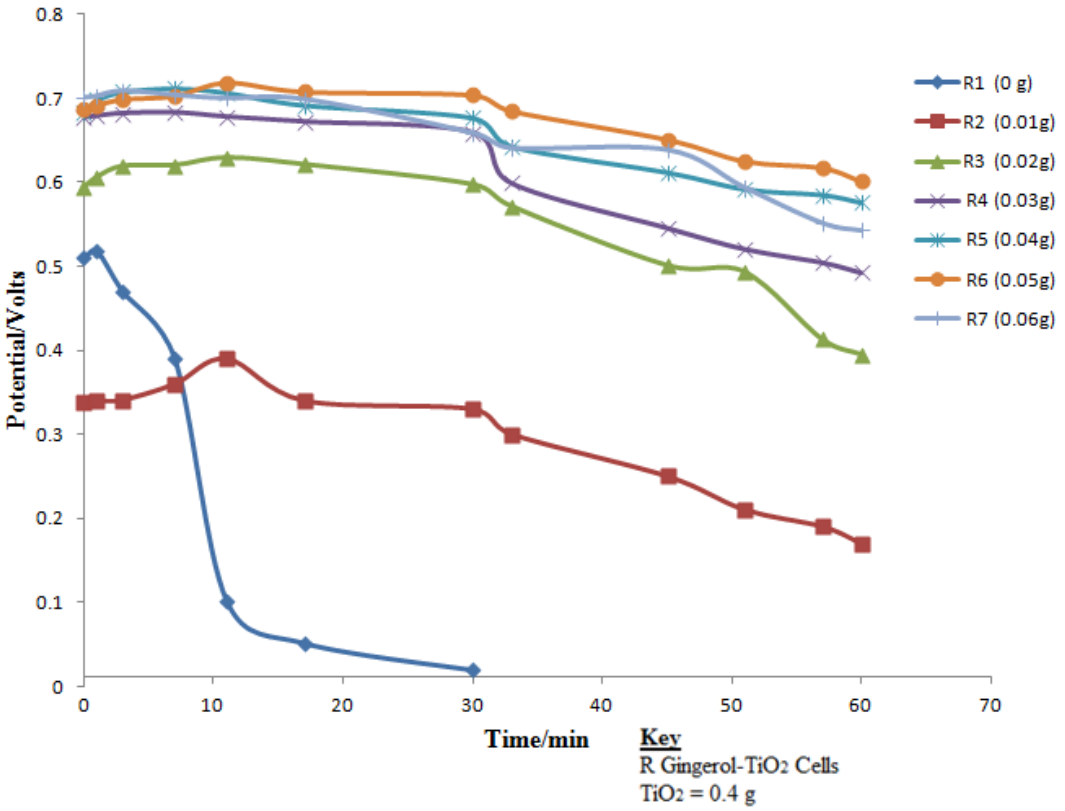

Figure 4.27: Potential (V_{OC}) - Time characterization for (Gingerol/TiO_2) luminescent solar cells employing 0.4 g TiO_2 constant

Evidence of {(0.619 V to 0.629), (0.679 to 0.683) V potential difference increase was observed from Figure 4.27 due to gingerol (0.02g) and (0.03g)] dopant masses in (8 and 6) minutes time of delay. Exemplary (0.576) V potential difference was evoked by (0.04g) gingerol mass with higher compared to (0.493V) observed from cell R_3 (0.03 g). Significant 0.032 V improvement was observed as the mass of gingerol was increased to (0.05) g with ability to sustain 0.601 V in the 60 minutes time constant. After attainment of (0.05 g) gingerol dopant mass ratio, a declining pattern ensued with a (0.543) V potential delay as verified in Figure 4.27. The prescence of the conjugated ($\sigma - \sigma\pi$) spectral traps in gingerol molecular structures was thought to split the absorbed radiation into varied bandwidths with a consequence of enhancing substantial fluorescence time constant in the gingerol/TiO_2 matrix. Approaching

ginger-TiO_2 mass optimization evoked favourable defects for higher charge carrier density habitation as reported by (Ahmadi *et al.*, 2017).

A different approach was taken with TiO_2 mass held at (0.8 g) on cells $R_{1,}$a, $R_{2,}$a, $R_{3,}$a, $R_{4,}$a, $R_{5,}$a, $R_{6,}$a and $R_{7,}$a at varying (0-0.06) g gingerol dopant and the fabricated cells I-V response were presented in Table 4.30.

Table 4.30: Parameters derived from (Organic Gingerol)/TiO_2 solar cells at varied (0 – 0.06) g Gingerol masses employing (0.8) g TiO_2 in the photo active layer

Cell (gingerol mass/g)	**$V_{(OC)}$ (V)**	**$I_{(SC)}$ (mA) ($\pm$0.001)**	**FF**	**(η%)**
R_1, a (0 g)	0.301	0.072	8.342E-3	1.808E-4
R_2,a (0.01g	0.132	0.069	0.0131	1.193E-4
R_3,a (0.02g)	0.165	0.158	0.015	3.911E-4
R_4,a (0.03g)	0.196	0.184	0.0169	6.095E-4
R_5,a (0.04g)	0.233	0.204	0.023	1.093E-3
R_6,a (0.05g)	0.241	0.218	0.031	1.629E-3
R_7,a (0.06g)	0.217	0.173	0.021	7.884E-4

The receding fluctuating terminal (0.241 – 0.132) V potentials differences were observed at varying (0-0.06) g gingerol dopant with (0.8) g TiO_2 constant in Table 4.30. Enhanced and deviated {0.301 and 0.217} V results from (R_1 (0g) and R_7 (0.06g)

is a demonstration of TiO_2 higher mass contribution in contrast to the already established gingerol /TiO_2 matrix mass ratio limit. The comparative [(8.342E-3 – 0.031) and (6.095E-4 – 1.09E-3) %] FF and PCE results are clear exhibits that the charge carriers habitating traps existed were sparsely induced in rich (0.8) g TiO_2 constant photo active material as manifest in Table 4.30 I-V characteristics. A study by Stolterfoht *et al.,* (2018) reported that recombination losses were inflated in bulk embodying structures. Additionally, more losses were derived due to inhomogeneities of active composites and the matrices interfaces (Stolterfoht *et al.,* 2018). Performance of the same samples in a dark environment was carried and the results were presented in Table 4.31.

Table 4.31: Characterization of potential (V_{OC})- time of gingerol-TiO_2 luminescent solar cells at varied (0 -0.06)g gingerol employing 0.8 g TiO_2 constant photo active layer

Time/ min	Potential(V_{OC}) ($\pm$0.005) V						
	R_1,a (0 g)	R_2,a (0.01g)	R_3,a (0.02g)	R_4,a (0.03g)	R_5,a (0.04g)	R_6,a (0.05g)	R_7,a (0.06g)
0	0.301	0.129	0.159	0.162	0.233	0.238	0.217
1	0.282	0.132	0.161	0.192	0.229	0.24	0.189
3	0.218	0.129	0.165	0.196	0.222	0.227	0.193
7	0.168	0.123	0.152	0.177	0.224	0.226	0.195
11	0.105	0.134	0.131	0.163	0.206	0.225	0.187
17	0.051	0.122	0.123	0.161	0.179	0.218	0.179
30	0.02	0.116	0.125	0.135	0.157	0.193	0.167
33		0.103	0.121	0.131	0.146	0.2	0.152
45		0.095	0.113	0.127	0.141	0.16	0.125
51		0.08	0.107	0.118	0.134	0.138	0.108
57		0.07	0.08	0.101	0.113	0.123	0.08
60		0.065	0.066	0.094	0.109	0.117	0.068

A graphical presentation of potentials difference against time for the $R_{1,a}$, $R_{2,a}$, $R_{3,a}$, $R_{4,a}$, $R_{5,a}$, $R_{6,a}$ and $R_{7,a}$ luminescent solar cells was made as shown in Figure 4.28.

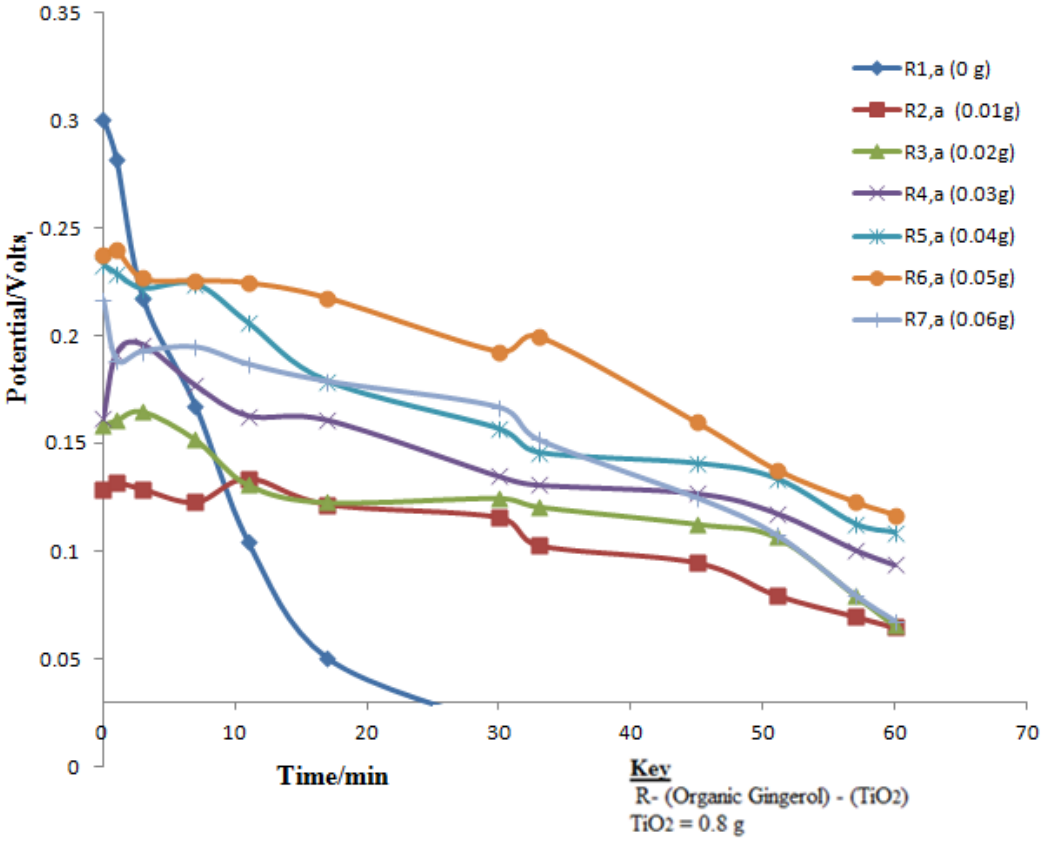

Figure 4.28: Potential (V_{OC}) -Time characteristics for gingerol/TiO_2 luminescent solar cells employing 0.8 g TiO_2 constant

Irregular {0.002, 0.03 and 0.013) V rectangular step signals were observed between [(0-1) and (30-33)] minutes for {(R_6, a (0.05 g) and (R_2, a (0.01 g) respectively from Figure 4.28. Sample (R_5, a (0.04 g) embraced (0.004 V) short-lived negative surge followed by fluctuating magnitude sine wave characteristicss between{(3-17) and (33-57)} with a rectangular signal conformity between (30-333) minutes, terminating at (0.109 V). The (R_4, a (0.03 g) signal specimen assumed a normal (0.014) V magnitude half potential difference wave sine turbulence, for the first (0 - 3) minutes with a distinguishing damping characteristic stabilizing at (0.094 V). However, the response of (R_6, a (0.05 g) had minimal oscillatory at (0.117) V after the 60 minutes time constant. Cell (R_1, a (0 g) potential signal was observed to be negligible after 25

minutes in a minimum natural radiation environment. When the white highly bright and high refractive index with divalent TiO_2 crystallinity was exposed to UV radiation, high density of the 0.8 g mass charge carriers on the surface were activated and flew to the external circuit. The relative homogeneity harnessed uniform scattering of the decaying absorbed radiation.That excited sufficient charge carrier density compared to the gingerol doped- TiO_2 samples and promoted development of slighly higher potential difference due to the electron-deficient vacancies (holes) left behind. The high crystallinity mass released the absorbed energy, allowing the surface radiation to decay faster, while that from within delayed and excited electrons on the surface promoting development of delayed potential difference. Researches by Jiang *et al*.(2021) indicated that when the establishment of charge carrier deficiency ceased, promotion of potential energy faded away. Peiris *et al*. (2021) noted that TiO_2 yield charge carriers when exposed to light.

A study by Stolterfoht *et al.* (2018) indicated bulk composites had higher recombination losses amplified at the trapping sites. Escalated losses were further derived from inhomogeneities of the interacting complexes surfaces. These nonradiative recombination losses manifested increased dark currents which limits both the cells open-circuit voltage (V_{OC}) and the fill factor (Stolterfoht *et al.*, 2018). The mass of TiO_2 was varied to 0.1 g and the I- V characteristics results of the fabricated cells presented as shown in Table 4.32.

Table 4.32: Parameters derived from (Organic Gingerol)/TiO_2 solar cells at varied (0 – 0.06) g Gingerol masses employing (0.1) g TiO_2 in the photo active layer

Cell (gingerol mass/g)	$V_{(OC)}$ (V)	$I_{(SC)}$ (mA) ($\pm$0.001)	FF	(η%)
R_1, b (0 g)	0.167	0.169	0.011	2.822E-4
R_2,b (0.01g	0.115	0.149	0.022	3.769E-4
R_3,b (0.02g)	0.128	0.151	0.121	2.339E-3
R_4,b (0.03g)	0.142	0.158	0.124	2.782E-3
R_5,b (0.04g)	0.148	0.159	0.128	3.012E-3
R_6,b (0.05g)	0.158	0.183	0.154	4.452E-3
R_7, b (0.06 g)	0.139	0.173	0.034	8.175E-4

The (0.115 – 0.158) V revamping potential differences transients responses varied sluggishly from (0.006 – 0.014) V due varying (0 – 0.06) g gingerol dopant mass mixed with (0.1) TiO_2 constant compound, when activated by solar radiation as observed from Table 4.32. The sluggish sequential {(0.006 – 0.014) V potential increase of different magnitudes was bounded at {R_2 b (0.01g) and R_6, b (0.05g)} cells margins assumed a recession progression due to R_7,b(0.06 g) sample. That was accompanied by {(0.022 -0.154) with intermittent receding {(4.452E-4 – 2.339E-4) %} FF and PCE parameters. The R_1, b (0g) depicted (0.116) V improved potential. This was contributed to the close location of the ‘‘energy donor species ’’ relative to the ‘‘energy acceptor species’’ due to the limited radius of energy transfer. The

contrasting centre radius of the optical energy sources largely contributed to the parameters disparity. A study by Ahn *et al.* (2017) noted that dopant excitation energy sources enhanced rupture of donar - acceptor particals as the contrary presented unstable characteristics. Investigation of the cells response in a dark environment was done in a dark environment and the potential against time results were recorded in Table 4.33.

Table 4.33: Potential (V_{OC}) - time characterization luminescent gingerol-TiO_2 solar cells at varied (0 – 0.06)g gingerol employing 0.1 g TiO_2 constant photo active layer

Time/ Min	**Potential(V_{OC}) ($\pm$0.005) V**						
	$R_{1,b}$ (0g)	**$R_{2,b}$ (0.01g)**	**$R_{3,b}$ (0.02g)**	**$R_{4,b}$ (0.03g)**	**$R_{5,b}$ (0.04g)**	**$R_{6,b}$ (0.05g)**	**$R_{7,b}$ (0.06g)**
0	0.167	0.115	0.127	0.142	0.145	0.156	0.139
1	0.132	0.112	0.128	0.143	0.148	0.158	0.134
3	0.128	0.107	0.126	0.135	0.144	0.147	0.126
7	0.109	0.092	0.119	0.123	0.137	0.141	0.121
11	0.038	0.061	0.114	0.117	0.123	0.139	0.119
17	0.025	0.059	0.102	0.116	0.118	0.136	0.114
30	0.011	0.048	0.099	0.11	0.115	0.129	0.103
33	0.01	0.039	0.094	0.101	0.111	0.124	0.1
45		0.015	0.019	0.093	0.108	0.119	0.091
51				0.032	0.095	0.117	0.089
57				0.025	0.092	0.102	0.073
60					0.086	0.097	0.058

The results of potential against time obtained were as presented in Figure 4.29.

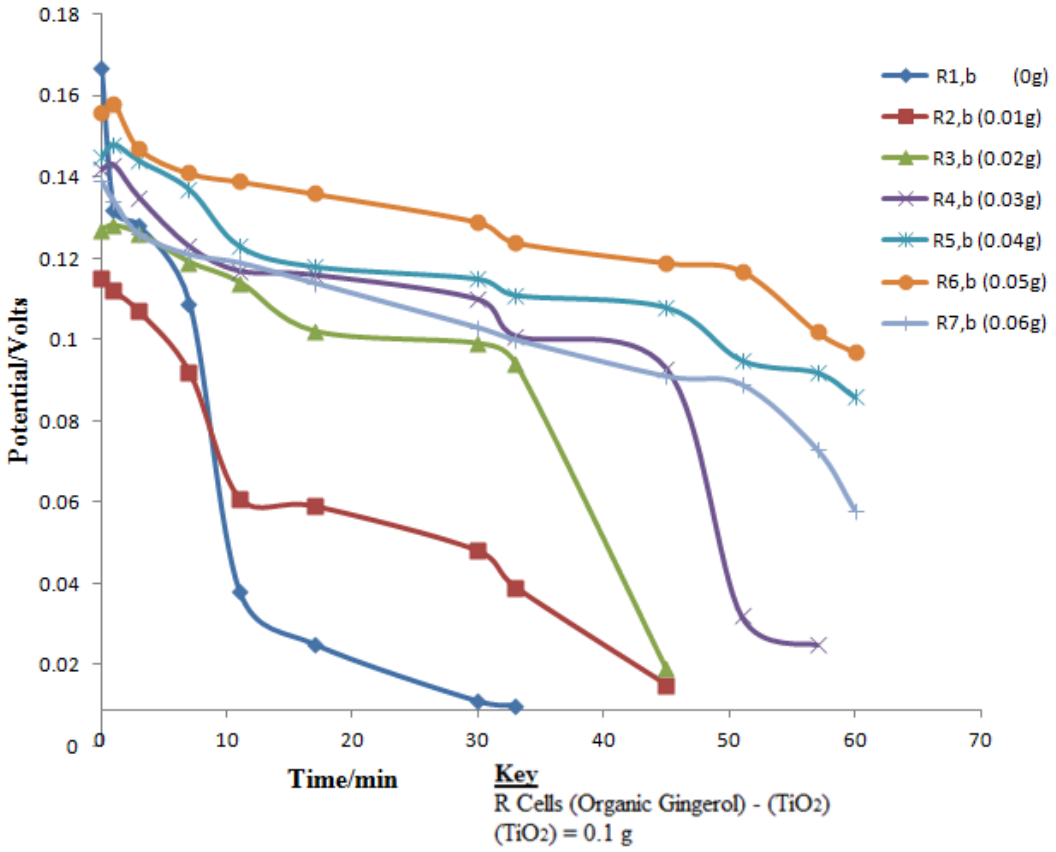

Figure 4.29: Potential (V_{OC}) - Time characterization for gingerol/TiO_2 luminescent solar cells at (0.1 g) TiO_2 constant

The corresponding {R_6, b (0.05) g, R_5, b (0.04) g and R_3, b (0.03) g} cells of (0.002, 0.003 and 0.001) V amplitude step and ramp overshoots signals occurred within a peak time of 1 minute as observed from Figure 4.29. Declining (0.011, 0.02, 0.039, 0.029 and 0.099) V step and ramp signals were enfolded by {R_6,b (0.05)g, R_5,b (0.04)g, R_7,b (0.06)g, R_3,b (0.02)g and R_2,b (0.01)g}FSCs in (4, 9, 10, 49, 17 and 10) minutes delay time. Step declining (0.035 and 0.09) V signals ensued in (2 and 4) minutes delay time as evidenced from R_2, b (0.01) g FSC. A similar (0.001) V of R_6,b (0.05) g response was observed between (30 - 33) minutes followed by almost a clipped steady state response for next 17 minutes. A steady state (0.02) V error occurred on the same sample in the next 6 minutes with a clipped response of 0.097

V magnitude for the rest 3 minutes settling time. The other cells displayed decaying characteristics of negligible amplitude at negligible delay time. That was attributed to inpenetratable acceptor and donor particals bunched together with spectral traps which highly enhanced electron – hole pairs separation. A study by Liu *et al.* (2018) noted that intramolecular donor–acceptor structures of different ratios had varied proportions of atomic non conformity hindrance with a versatile enhancement process to charge transfer.

4.8 Analysis of quinine sourced from Tonic Water

Tonic water is known to contain quinine which is a natural cinchona alkaloid that has been used for the prevention and therapy of malaria. Quinine in this study was obtained by crystaliztion as explained in the methodology. Quinine is used as flavoring component of soft drink such as tonic water and bitter lemon drink (Marjanska and Szpakowska, 2017). Quinolines fall in the class of organic compounds with aromatic heterocyclic series characterized by a double-ring structure composed of benzene and pyridine rings fused at two adjacent carbon atoms (de Carvalho *et al.*, 2018). The double-ring structure of benzene and pyridine rings makes quinoline a flourescent material when subjected to radiation with frequencies above the visible region (Prushan, 2018; Harvey, 2020).

4.8.1 FTIR analysis of Quinoline

Samples of tonic water were characterized using FTIR spectrophotometer. The results obtained were as provided in Figure 4.30.

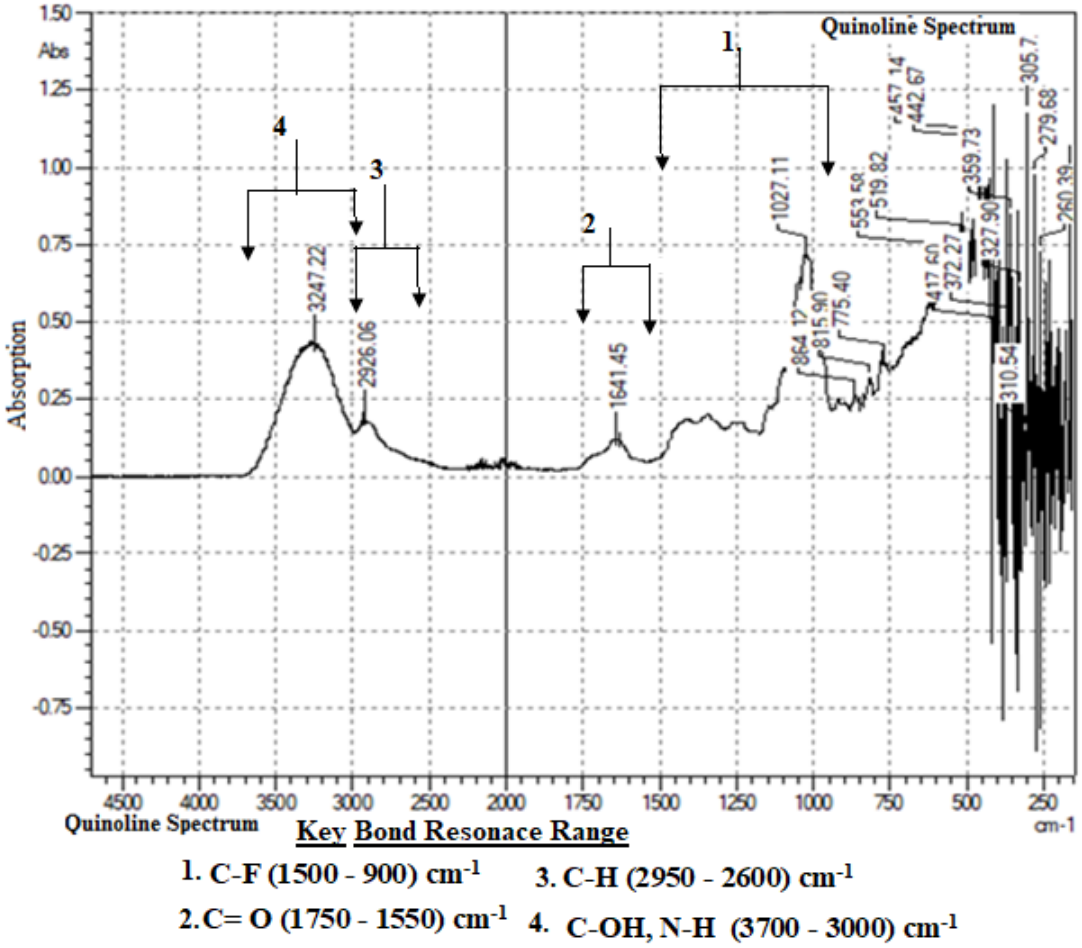

Figure 4.30: FTIR Absorption Spectrum analysis of Quinoline Photo Luminescence Organic Material from Tonic Water

The results of Figure 4.30 show the presence of different functional groups as evidenced with their respective resonant frequencies. The structure bonds with three dimensional moments occurred in the bands of {(3700 - 3000), (2900-2600), (1750-1600) and (1500-1000),} cm^{-1}. Those peaks at (3247.22, 2926.06, 1641.45, 1350cm^{-1}, and 1027.11) cm^{-1} resulted when the pulsating {(N-H), (C-OH), (C=O), (C-F) and (C-H)} functional groups were activated to transform light energy into long wavelength radiations. This agrees with Dong *et al*. (2020) and Harvey, (2020) who noted that aromatic ring allows molecules to bond easily and absorbs radiation due to constant vibration resulting to the observed functional groups peaks responsible for

fluorescence in tonic water. The active molecular chemical structure of quinoline in tonic water is as provided in Figure 4.31 below.

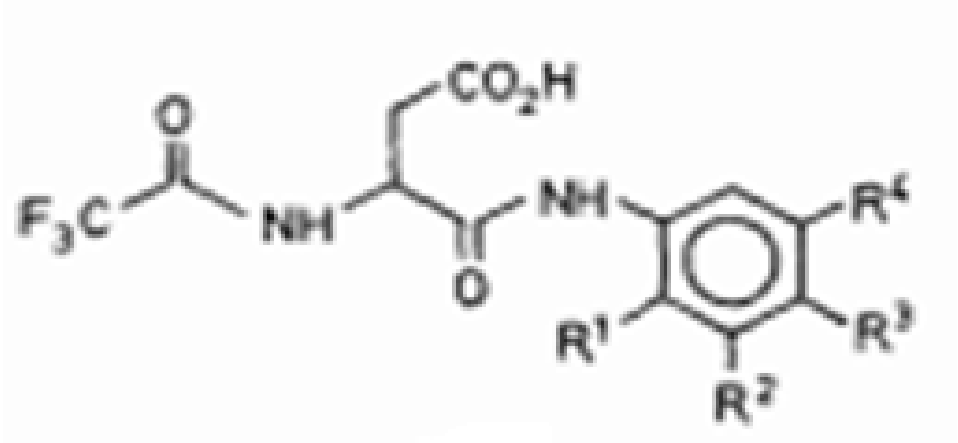

Figure 4.31: Active Quinoline structure in tonic water photoluminescent material

That fluorescent property of quinoline in tonic water was exploited in this study with a view to increase spectral traps by benzene and released later to prolong radiation to the photo luminescent titanium dioxide (TiO_2) material.

4.8.2 Fluorescence property of Quinoline

Varying masses of tonic water which is an organic luminescent material were thoroughly mixed with different samples of constant mass (1.00 g) of the photoactive material (TiO_2). The different ratios of the mixture were used to fabricate photo cells to study their delay in photo activity after withdrawal of radiation. Different cells were fabricated by taking 0.4 g of each Tonic Water-TiO_2 mixture to make the photo active layer. The receptive layer was made using (0.48 g) of graphite-iodine (C_X /I/KI) mass composition whose ratios were 0.3 g, 0.17 g and 0.01 g respectively for each receptive electrode. The resulting cells were analyzed using constant solar radiation

by illuminating them in a clear daylight and their I-V characteristics were presented in Table 4.34.

Table 4.34: Parameters derived from (Organic Quinoline)/TiO_2 solar cells at varied (0, 0.04, 0.05 and 0.06) g Quinoline masses employing (0.4) g TiO_2 in the photo active layer

Cell (quinoline mass/g)	$V_{(OC)}$ (V)	$I_{(SC)}$ (mA) ($\pm$0.001)	FF	PCE
T_1 (0 g)	0.518	0.431	0.028	6.251E-3
T_5 (0.04g	0.128	1.855	8.48E-3	2.013E-3
T_6 (0.05g)	0.265	2.043	0.036	1.019E-2
T_7 (0.06g)	0.125	1.76	0.012	2.642E-3

The (0.128 – 0.265) V passively building potentials (V_{OC}) and short circuit currents (I_{SC}) (I-V) characteristic responses at varying and constant {(0 – 0.06) g increasing quinolone and (0.4) g TiO_2} mass were observed from Table 4.34. The first (0.518) V transient overshoot was observed from T_1, (0) g cell followed by the shrinking (0.128) V ensued by the improved (0.265) V ramp signal, and terminated to a diminishing (0.125) V. The (0.431 2.043) mA short circuit current (I_{SC}) increased uniformly with (0 – 0.05) g quinolone mass with non-uniformly varying {(8.48E-3 to 0.036) and (6.251E-3 to 1.019E-2)} FF and PCE respectively. Varied quinolone aromatic heterocyclic series population contributed to sequential improving output parameters. The (0.518) V at T_1 (0 g) was attributed to presence of favourable band gap edges for enhanced photons absorption as reported by (Jaiswal *et al.,* 2015). A study by Prushan (2018) and Harvey, (2020) noted that .aromatic heterocyclic series

in quinoline fluorescent when subjected to radiation of varied frequencies above the visible region. The performance of the cells in a dark room was investigated and the variation of potential with time was recorded in Table 4.35.

Table 4.35: Potential (V_{OC}) –Time characterization of the fabricated Quinoline -TiO_2 luminescent solar cells at varied (0 -0.06)g quinoline employing 0.4 g TiO_2 constant photo active layer

Time/ Min	**Potential (V_{OC}) ($\pm$0.005)V**			
	T_1 (0 g)	T_5 (0.04g)	T_6 (0.05g)	T_7 (0.06g)
0	0.51	0.125	0.123	0.123
1	0.518	0.127	0.125	0.125
3	0.47	0.128	0.265	0.119
7	0.19	0.12	0.251	0.105
11	0.101	0.119	0.244	0.097
17	0.064	0.122	0.234	0.094
30	0.02	0.116	0.219	0.093
33		0.113	0.208	0.098
45		0.105	0.194	0.097
51		0.09	0.168	0.091
57		0.079	0.125	0.084
60		0.076	0.121	0.088

The potential – time tabulated results of Table 4.35 were presented graphically as shown in Figure 4.32.

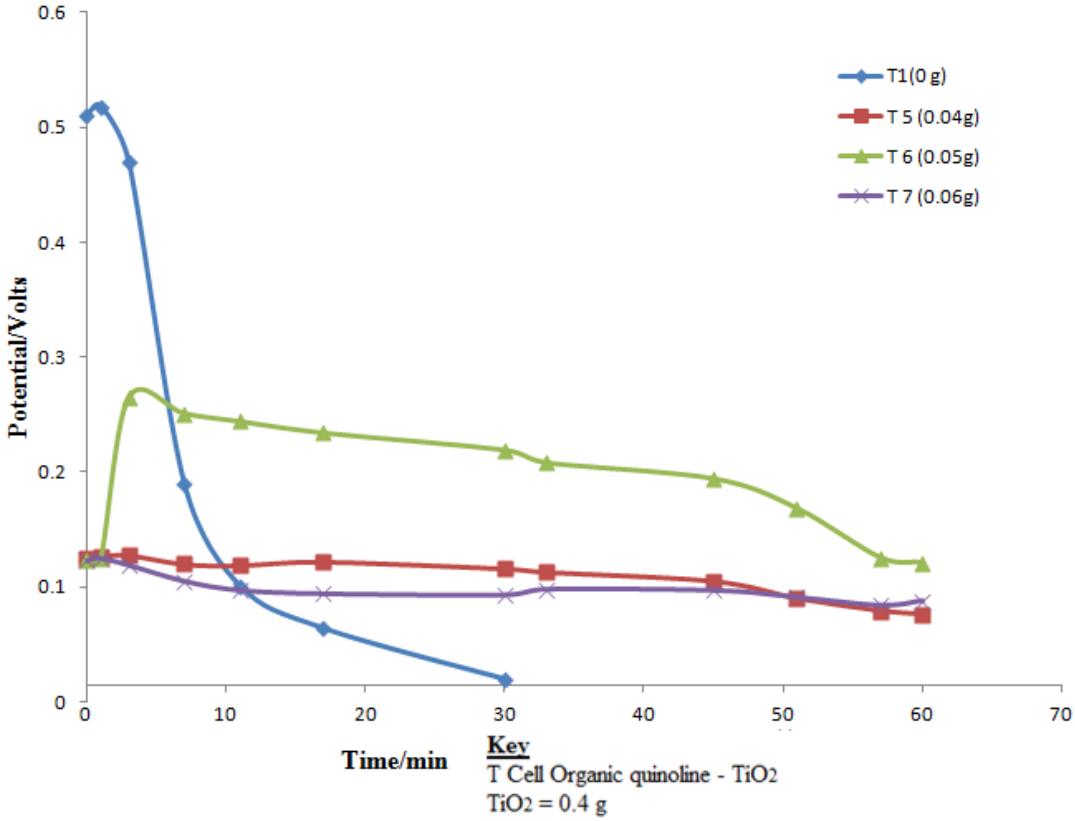

Figure 4.32: Potential-Time profiles for (Quinoline /TiO_2) luminescent solar cells employing 0.4g TiO_2 constant

The {T_1 (0) g and T_1(0) g} (0.003 and 0.14) V in (1 and 3) minutes respectively were observed from Figure 4.32. The critically T_5 (0.04) g damped signal with a clipped tail at (0.1) V sustaining the rest of the tail potential at (0.076) V 34 minutes. The varying (0.144) V T_6 (0.05) g steady state signal was marginally higher than the rest of the cells. However, its (0.121) V residual potential difference was the most improved in the 60 minutes of the experiment T_1 (0) g extinguishing 30 minutes earlier. The limited functional groups in the multiple cyclopeptides closed chains were attributed to the low (0.025) V open circuit potentials of T_2 and T_3. A study by Harvey, (2020) noted that limited quinoline active molecular electronic states, inhibited the desired parameters

Reports by Babu, *et al.,* (2018) indicated that interfacing quinoline nanoparticles with photo active composites improved organic solar cells (OSCs) performance. Enesca *et al.,* (2016) indicated that limitation fluorescence in TiO_2 preceded inadequate spectral traps. The I-V response on varied quinoline (0 – 0.06) g and (0.65) g TiO_2 constant mass were presented in Table 4.36.

Table 4.36: Parameters derived from (Organic Quinoline)/TiO_2 solar cells at varied (0 – 0.06) g quinoline masses employing (0.65) g TiO_2 in the photo active layer

Cell (quinoline mass/g)	$V_{(OC)}$ (V)	$I_{(SC)}$ (mA) ($\pm$0.001)	FF	PCE
T_1, a (0 g)	0.36	0.264	1.175E-3	1.117E-4
T_4,a (0.03)g	0.1	0.752	0.0228	1.713E-3
T_5,a (0.04g)	0.11	0.691	0.032	2.432E-3
T_6,a (0.05g)	0.113	0.842	0.038	3.616E-2
T_7,a (0.06g)	0.068	0.168	8.594E-5	9.818E-7

Agitated (0.752 – 0.842) mA charge transition due to varying (0.1 – 0.113) V were observed from the sequential (0.03 -0.05) g increasing quinoline and (0.65) g TiO_2 constant mass doped FSCs. Corresponding improving {(0.0228 – 0.038) and (2.432E-3 – 3.616E-2) %} parameters were derived as shown in Table 4.36. Outside these mass limits, different {(0.36V and 8.794 E-50.264mA) and (1.175E-3 and 8.594E-5 FF) and (9.818E- 7 and 7.1117 E-4 PCE)} resulted. A study by Jin *et al*. (2020) indicated that higher solvent composites mass inhibited cyclic dipeptides molecular

open chains activation. The aromatic heterocyclic double-ring structures absorbed lower bandwidth optical energy at the moment of excitation (Zhang *et al.,* 2019; de Carvalho *et al.,* 2018). A study of the quinoline doped cells response with time in dark environment is presented in Table 4.37.

Table 4.37: Potential (V_{OC}) -Time characterization of the fabricated Quinoline -TiO_2 luminescent solar cells at varied (0 -0.06)g quinoline employing 0.65 g TiO_2 constant photo active layer

Time/ Min	**Potential (V_{OC}) ($\pm$0.005) V**				
	T_1,a (0 g)	**T_4,a (0.03g)**	**T_5,a (0.04g)**	**T_6,a (0.05g)**	**T_7,a (0.06g)**
0	0.36	0.08	0.11	0.113	0.052
1	0.201	0.1	0.102	0.116	0.068
3	0.109	0.09	0.0931	0.119	0.051
7	0.09	0.083	0.064	0.121	0.032
11	0.084	0.072	0.061	0.117	0.025
17	0.068	0.061	0.055	0.111	0.031
30	0.013	0.055	0.059	0.108	0.021
33		0.046	0.045	0.096	0.022
45		0.019	0.047	0.085	0.019
51			0.028	0.083	0.018
57			0.016	0.081	0.017
60			0.014	0.08	0.016

The information of potential against time in Table 4.37 were presented graphically as shown in Figure 4.33.

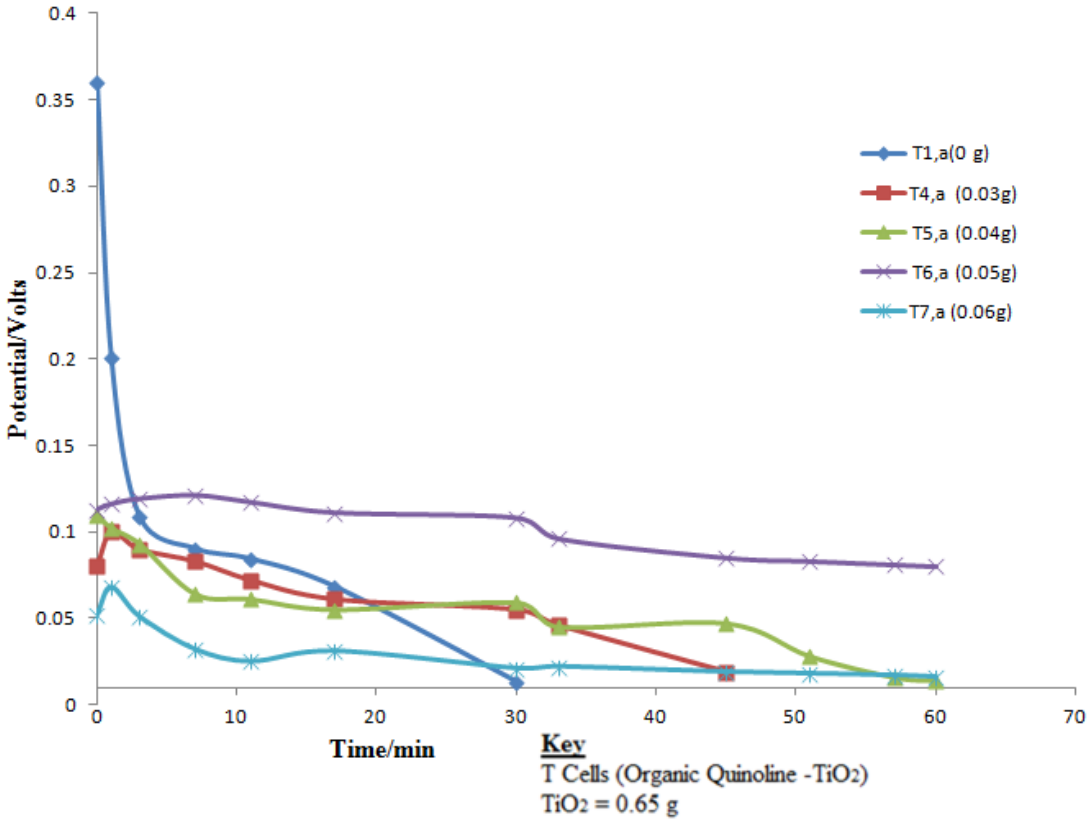

Figure 4.33: Potential (VOC) -Time characterization for (Quinoline /TiO_2) luminescent solar cells at 0.65 g TiO_2 constant

Figure 4.33 shows fast {[T_4,a(0.03 g) and T_7,a(0.06 g)] and T_6,a(0.05 g) } relatively stable transient responses embraced (0.02, 0.016 and 0.008) V surges between{(0-1) and (0-7)} minutes time rise. Sequential T_7,a(0.06 g) (0.043)V and the T_4,a(0.03 g) (0.01)V rapidly decreasing signals were observed from Figure 4.32. Cell T_5,a(0.04 g) signals was characterized by (0.055) V unsteady decaying transient response between (0-17) minutes decay time. This was clipped between (0.055 – 0.047) V for the next 28 minutes after which negligible (0.028) V potential was observed. The stable T_6,a(0.05 g) signal was held at (0.1) V clipped potential for the last 27 minutes settling. The sparsely populated aromatic heterocyclic double-ring structure in the (0.65 g) TiO_2 host material were thought to support excitation of negligible charge density. A study by Dhall *et al.* (2021) that weak signals were characterized from the

insufficient heterocyclic double-ring structures of contrasting sizes functional groups. Another investigation was done by varying TiO_2 mass to (0.38) g and the cells I-V characteristics responses are presented in Table 4.38.

Table 4.38: Parameters derived from (Organic Quinoline)/TiO_2 solar cells at varied (0 – 0.06) g quinoline masses employing (0.38) g TiO_2 in the photo active layer

Cell (quinoline mass/g)	$V_{(OC)}$ (V)	$I_{(SC)}$ (mA)	FF	PCE
T_1, a (0 g)	0.501	0.193	5.698E-5	5.509E-6
T_4,a (0.03)g	0.113	0.974	4.429E-3	4.875E-4
T_5,a (0.04g)	0.126	1.062	5.493E-3	7.351E-4
T_7,a (0.06g)	0.095	0.368	9.574E-4	3.347E-5

The progressively increasing (0 – 0.06) g quinoline at constant TiO_2 mass varied (0.501 – 0.095)V I- V step impulse responses were observed from Table 4.38. Similar (0.193 – 0.368) mA progression short circuit current (I_{SC}) resulted after the optical energy interacted with {T_1,a(0g), T_4,a(0.03g), T_5,a(0.04g), T_6,a(0.05g) and T_7,a(0.06g)} samples. Corresponding varying {(5.698E-4 - 4.429E-3) and (5.509E-6 – 4.875E-4)} FF and PCE parameters were derived. The majority C-H functional groups bonded to aromatic ring molecules absorbed radiation between (1500 - 1000) cm^{-1} resulting to a fast extincting signal. The reduced N-H mass constant moment was attributed to the orbiting population negligible effect in the T_6, a(0.05g) sample, with a similar precedence of the succeeding cells. The elevated quinoline mass contributed to scattered excited charge carriers due to the unpolarised spectral trap based optical energy. A study by Dong *et al*. (2020) and Harvey (2020) noted that elevated dopant

proportions unpolarised optical spectral trap with consequence of scattered excited charge carriers. The experiment was carried further in a radiation diminished confinement and results were presented in Table 4.39.

Table 4.39: Potential (V_{OC})-Time characterization of fabricated Quinoline - TiO_2 luminescent solar cells at varied (0 -0.06)g quinoline employing 0.38 g TiO_2 constant photo active layer

Time/ Min	**Potential (V_{OC}) ($\pm$0.005) V**			
	T_1,b (0 g)	**T_5,b (0.04g)**	**T_6,b (0.05g)**	**T_7,b (0.06g)**
0	0.501	0.11	0.118	0.095
1	0.467	0.113	0.126	0.093
3	0.405	0.108	0.123	0.087
7	0.144	0.091	0.115	0.077
11	0.079	0.093	0.108	0.065
17	0.05	0.084	0.103	0.059
30	0. 02	0.089	0.079	0.061
33		0.079	0.077	0.058
45		0.082	0.071	0.052
51		0.072	0.068	0.049
57		0.065	0.064	0.045
60		0.044	0.061	0.038

From the results of Table 4.39, a graphical presentation was made as shown in Figure 4.34.

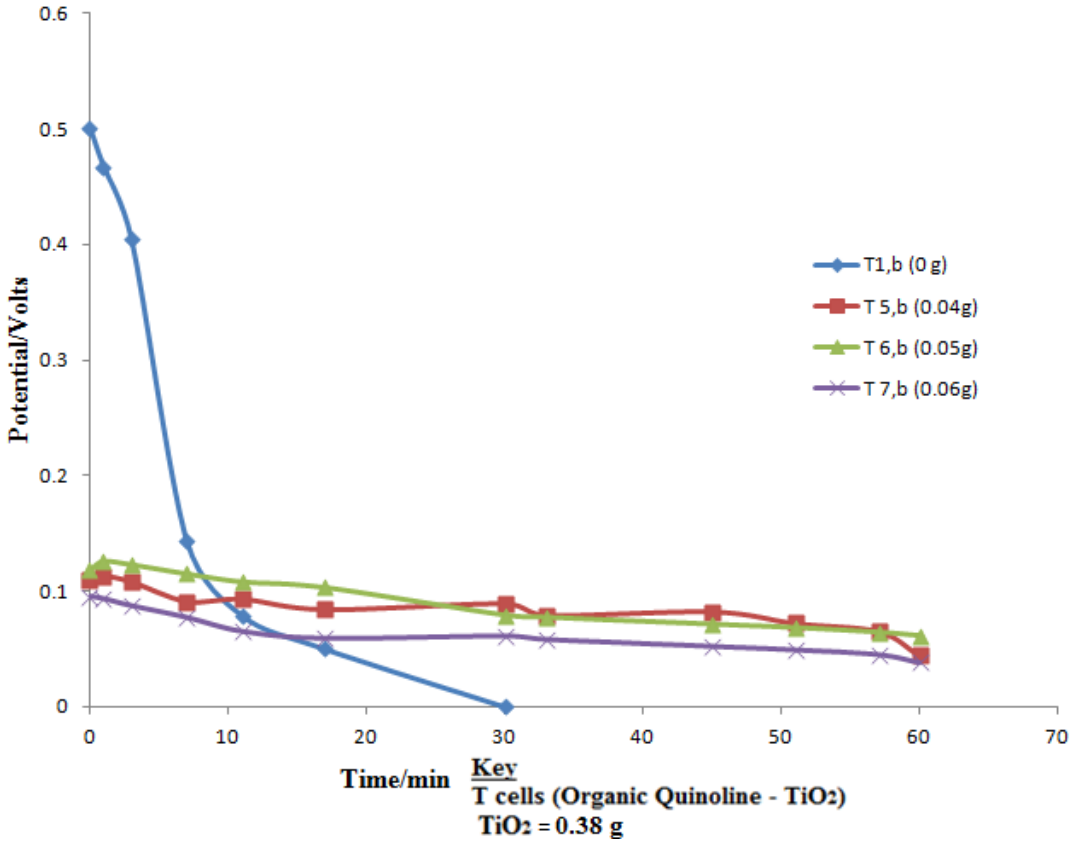

Figure 4.34: Potential (V_{OC})-Time characterization for (Quinoline /TiO_2) luminescent solar cells employing 0.38 g TiO_2 constant

The {(0.118 - 0.126) V and (0.110 – 0.113)V} impulse responses were observed in (1 minute) time rise of [T_6,b(0.05)g and T_5,b(0.04)g] cells respectively from Figure 4.34. Subsequent varied irregular step signals were induced by [(0.06)g, (0.04)g and (0.06)g] quinoline dopant mass at (0.38) g TiO_2 photo active layers for the initial 30 minutes followed by steady state signals of the remaining time of the experiment. The significant (0.061) V characteristic was occasioned by T_6,b(0.05) g sample compared to (0.044 V and 0.0.038 V) from (T_5,b(0.04)g and T_7,b(0.06)g) cells, respectively. The motor and pestle mixture grinding was thought to interfere with fluorescent particals packings subsequenting few excited nanoparticals at shortened settling time. A study by Martínez-Abadía *et al*. (2018) indicated that many inefficient π-conjugated luminophores suffer from weakening of their luminescence, due to their

low concentration quenching. The crystalline powder molecules could only show highly blue emissive radiation due to lateral displacement stimuli with distorted tight π-stacking (De *et al.,* 2018).

4.9 Analysis of neohesperidosyl in bitter lemon soft drink

Bitter lemon is a natural cinchona alkaloid, a popular soft drink containing quinine which is neohesperidosyl that has been used for the prevention and therapy of malaria. The structure of the photo fluorescent material is shown in Figure 4.35.

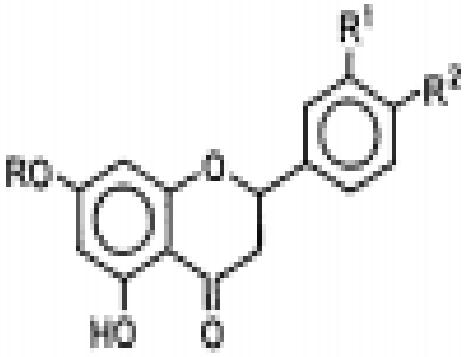

Figure 4.35: Active neohesperidosyl structure in bitter lemon photoluminescent material

The extraction of neohesperidosyl was done by crystallization as explained in the methodology. When excited by UV radiation, neohesperidosyl complex was observed to adjust its colour from blue, green, yellow, orange and finally to red in UV radiation. This could be contributed by the presence of benzene functional groups making it to shine by the process of fluorescence as reported by Egle *et al.* (2020). The extracted material was analyzed using FTIR analysis equipment.

4.9.1 FTIR analysis of neohesperidosyl from bitter lemon

A sample was characterized using FTIR spectrophotometer and the results obtained were as provided in Figure 4.36.

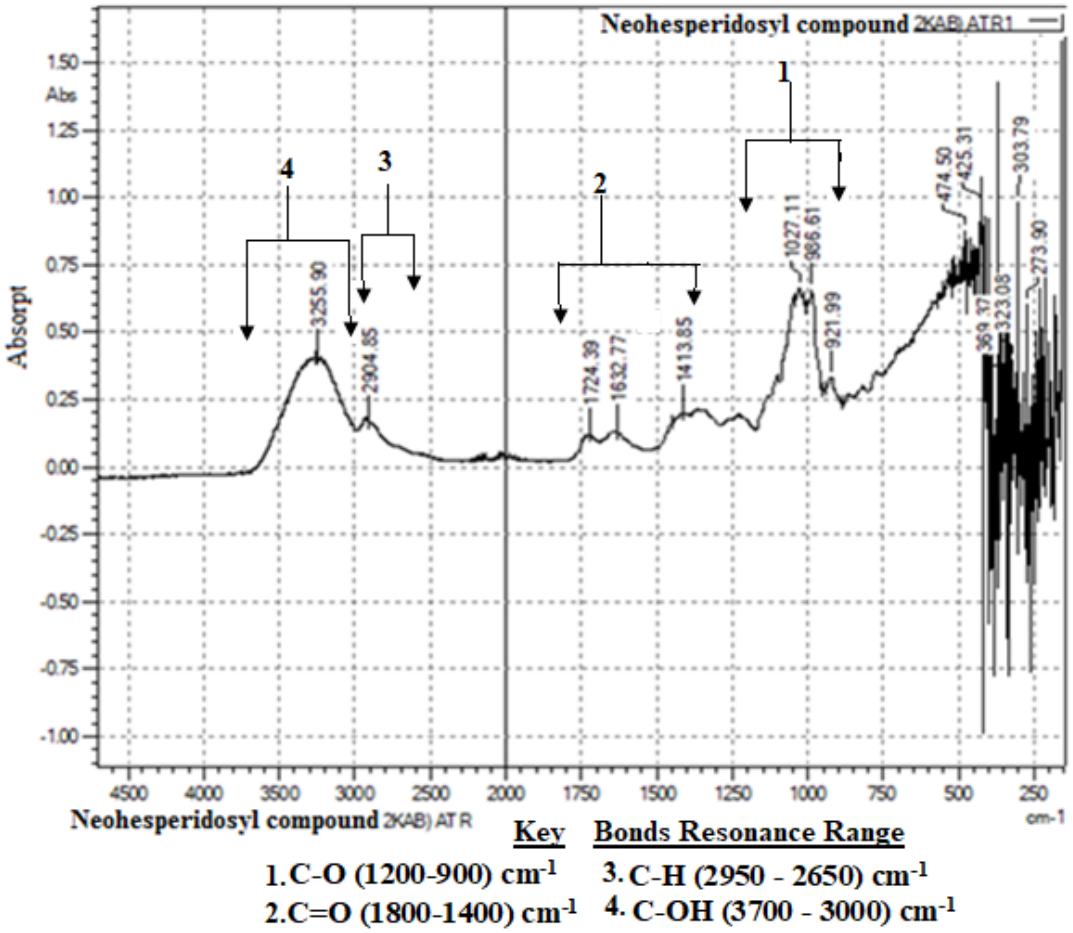

Figure 4.36: FTIR Absorption Spectrum analysis of Neohesperidosyl compound in Bitter lemon soft drink photo luminescence organic material

The results of Figure 4.36 shows presence of different functional groups resonating between {(3700 -3000), (2900-2700), (1800-1550) and (1200-900)cm^{-1}} frequency bands. The vibratory movement of {(C-OH), (C-H), (C=O) and (C-O)} bonds were observed to occur at {(3255.90), (2904.5), (1724.39 and 1632.77) and (1027.11 and

986.61)] cm^{-1} strong, bold and intense peak with similar findings reported by reported by (Dayal *et al.,* 2017). That fluorescent property of neohesperidosyl compound was exploited in this study with a view to increase spectral trapped by quinine and released later to prolong radiation to the photo active titanium dioxide (TiO_2) material.

4.9.2 Fluorescence property of Neohesperidosyl compound from Bitter lemon

Varying masses of neohesperidosyl compound in bitter lemon quinine organic luminescent material were thoroughly mixed with different samples of constant mass (1.00 g) of the photoactive material (TiO_2).

The different ratios of the mixture were used to fabricate photo cells to study their delay in photo activity after withdrawal of radiation. Different cells were fabricated by taking 0.4 g of each bitter lemon-TiO_2 mixture to make the photo active layer. The receptive layer was made using (0.48 g) of graphite-iodine (C_X /I/KI) mass composition whose ratios were 0.3 g, 0.17 g and 0.01 g respectively for each receptive electrode. The resulting cells were analyzed using a constant radiation by placing them in the open during the day and their response were recorded in Table 4.40.

Table 4.40: Parameters derived from (Organic Neohesperidosyl)/TiO_2 solar cells at varied (0 – 0.06) g neohesperidosyl masses employing (0.4) g TiO_2 in the photo active layer

Cell (neohesperidosyl mass/g)	**$V_{(OC)}$ (V)**	**$I_{(SC)}$ (mA) (±0.001)**	**FF**	**PCE**
K_1 (0 g)	0.518	0.638	0.028	9.254E-3
K_4 (0.03)g	0.125	2.461	0.099	0.031
K_5 (0.04g)	0.14	2.332	0.143	0.047
K_6 (0.05g)	0.296	2.531	0.146	0.109
K_7 (0.06g)	0.131	2.143	0.093	0.026

The characteristic (0.125, 0.14 and 0.296)V overdamped response from the {(0.4)g TiO_2 constant at varying (0 – 0.06)g neohesperidosyl dopant} mass of [(K_4,(0.03)g, K_5,(0.04)g and K_6,(0.05)g] cells was observed from Table 4.40. Corresponding (2.461, 2.332 and 2.531) mA charge migration rate was monitored. Derived {(0.099 - 0.146) and (0.031 -0.109) %} FF and PCE parameters preceded the cells I-V properties. Outside these neohesperidosyl mass limits, significant (0.518) V and (0.131) V reduced output potential differences were monitored. A study by Dayal *et al.* (2017) noted that different neohesperidosy prorportions presented varied spectral trap edges sequencing corresponding charge carriers' densities. Such proportions had an effect of scattered optical energy conforming to similar repercussion on charge carriers (Dayal *et al.* 2017). The performance of the cells in a dark room was investigated and the data obtained was recorded in Table 4.41.

Table 4.41: Potential Difference (V_{OC}) –Time characterization of fabricated Neohesperidosyl-TiO_2 luminescent solar cells at varied (0 -0.06)g neohesperidosyl employing 0.4 g TiO_2 constant photo active layer

Time/ Min	Potential (V_{OC}) ($\pm$0.005) V				
	K_1 (0 g)	K_4 (0.03g)	K_5 (0.04g)	K_6 (0.05g)	K_7 (0.06g)
0	0.51	0.099	0.129	0.206	0.135
1	0.518	0.107	0.13	0.208	0.138
3	0.47	0.12	0.131	0.21	0.139
7	0.39	0.121	0.15	0.236	0.141
11	0.107	0.125	0.14	0.245	0.129
17	0.064	0.103	0.15	0.296	0.131
30	0.023	0.044	0.11	0.265	0.125
33		0.04	0.105	0.23	0.112
45			0.1	0.229	0.091
51			0.08	0.2	0.083
57				0.175	
60				0.168	

From the tabulated voltage - time results, graphical presentations were prepared as shown in Figure 4.37.

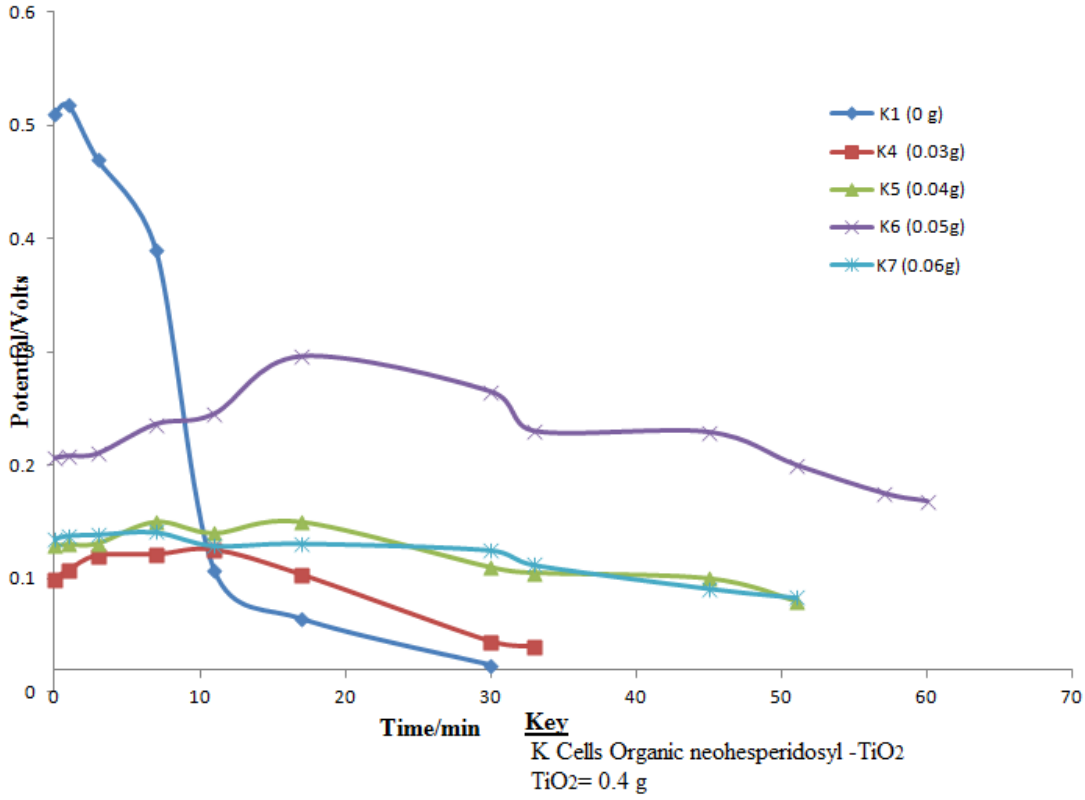

Figure 4.37: Potential (V_{OC}) - Time profiles (Neohesperidosyl -TiO_2) from Bitter lemon luminescent solar cells at 0.4 g TiO_2 constant mass ratio

Continuous {(0.099 – 0.125) V and (0.206 – 0.296) V} irregular unit step signals of [K_4 (0.03) g and K_6 (0.05) g] FSCs were evidenced between [(0 - 11) and (0- 17)] minutes time rise from Figure 4.37. Stable signals were observed from [K_5 (0.04) g and K_7 (0.04) g] cells between (0 - 1) minutes. Exemplary (0.236 - 0.296 - 0.23) V potentials (V_{OC}) decay were observed between (11 - 33) minutes by K_6 (0.05) g ensued by a polarized trend and clipped at 0.168 V for the last 10 minutes of the experiment. The rest of the cells retained below 0.1 V margin.

Neohesperidosyl different resonant frequencies enhanced varied delayed relaxation with a consequence of diverse charge carriers edges (Dayal *et al.*, 2017). A study by Dayal *et al.* (2017) noted that varied neohesperidosyl flourescence intensities resulted

from conjugated (δ -$\delta\pi$) species disparity. Further investigation was done with 0.68 g mass of TiO_2 mixed with varied masses of neohesperidosyl and the I-V observed results were recorded in Table 4.42.

Table 4.42: Parameters derived from (Organic Neohesperidosyl)/TiO_2 solar cells at varied (0 – 0.06) g neohesperidosyl masses employing (0.68) g TiO_2 in the photo active layer

Cell (neohesperidosyl mass/g)	**$V_{(OC)}$ (V)**	**$I_{(SC)}$ (mA) ($\pm$0.001)**	**FF**	**PCE**
$K_{1,a}$ (0 g)	0.472	1.446	1.921E-3	1.311E-3
K_5,a (0.04)g	0.106	0.109	7.722E-3	8.676E-5
K_6,a (0.05g)	0.184	0.179	0.0109	3.590E-4
K_7,a (0.06g)	0.097	0.0864	8.095E-4	6.784E-6

The {(0.106, 0.184 and 0.097) V potentials difference (V_{OC}) together with (0.109, 0.179 and 0.086) mA short circuit current (I_{SC})} presented impulse response signals. The corresponding fluctuating {(8.095E- 4 to 0.0109) and (6.784E-6 to 1.311E- 3) FF and PCE parameters were derived from the I-V output parameters as recorded in Table 4.42. That was thought to be contributed by the higher spectral losses incurred within the (0.68) g /(0-0.06)g mass TiO_2 /neohesperidosyl matrix with proportionate effect on the excited charge carriers density. A research by Das *et al*. (2019) indicated that most of the δ –$\delta\pi$ spectral traps population was minimized by high composite compatibility. The distinguished fluorescence in higher solvents masses was a consequence of short-lived spectral traps excited states (Vardy *et al*. 2015). The

potential difference against time performance results of the same samples in a dark environment were presented graphically as shown in Table 4.43.

Table 4.43: Potential(V_{OC})-Time characterization of fabricated Neohesperidosyl-TiO_2 luminescent solar cells at varied (0-0.06)g neohesperidosyl employing 0.68 g (TiO_2) constant photo active layer

Time/ Min	Potential (V_{OC}) ($\pm$0.005) V			
	K_1,a (0 g)	K_5,a (0.04g)	K_6,a (0.05g)	K_7,a (0.06g)
0	0.472	0.106	0.172	0.097
1	0.316	0.098	0.184	0.089
3	0.113	0.1	0.163	0.091
7	0.108	0.084	0.169	0.084
11	0.07	0.086	0.158	0.076
17	0.03	0.081	0.145	0.078
30		0.075	0.141	0.069
33		0.069	0.133	0.071
45		0.063	0.116	0.059
51		0.058	0.109	0.051
57		0.024	0.102	0.033
60			0.096	

The potential-Time characteristics results of Table 4.43 were presented graphically as shown in Figure 4.38.

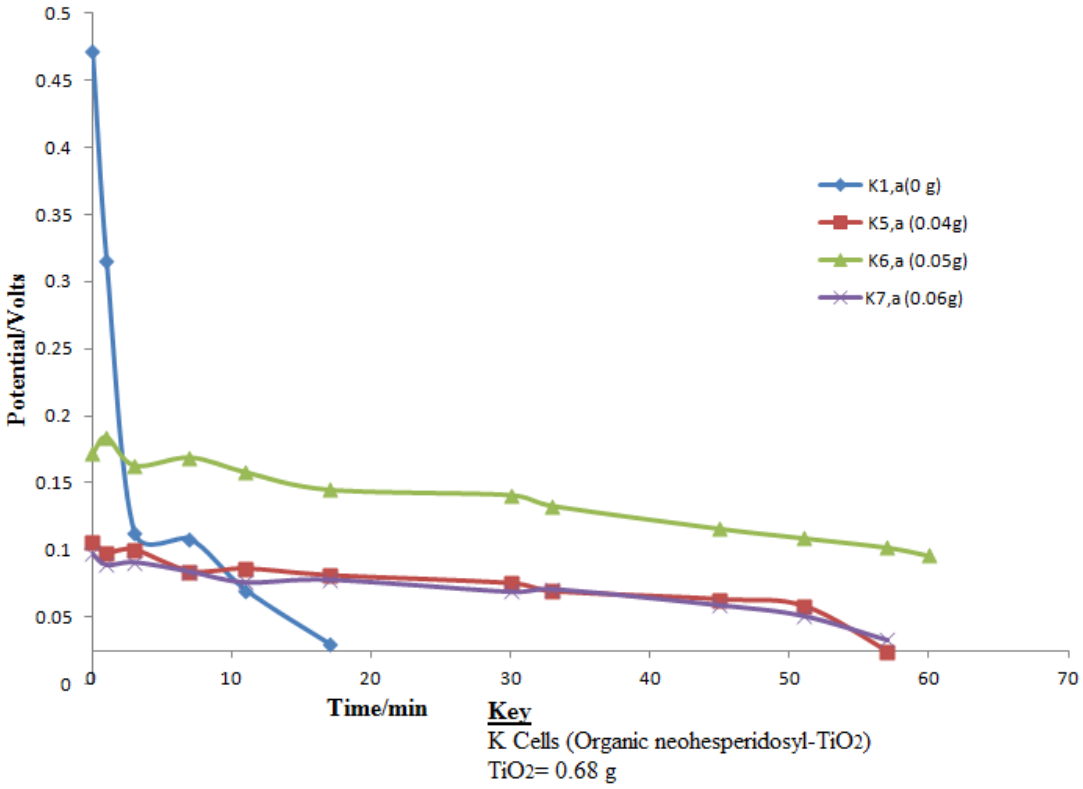

Figure 4.38: Potential (V_{OC})-Time characteristics of (Neohesperidosyl -TiO_2) luminescent solar cells employing 0.68 g TiO_2 constant mass ratio

The K_6, (0.05) g (0.172 to 0.184) V regular decay unit step response was observed between (0 to 1) minutes with (0.088) V minimum variation for next 59 minutes in diminished radiation from Figure 4.38. Similar properties were displayed by cell K_5, b (0.04) g retaining negligible (0.024) V potential between (51 to 57) minutes with an extinguishing tail potential. The neohesperidosyl (0.06) g mass gradually generated irregular (0.058) V critically damped potential difference, retaining (0.033) V in the next 57 minutes. A report by Guo *et al.* (2016) indicated that higher concentration composites had narrower bandwidths radiations with negligible variation for their terminal parameters output. Lack of equilibria between the interacting optical centres sterically prohibited the spectral traps excitation (Jun *et al.*, 2018).

Another investigation on I-V characteristics with TiO_2 reduced to 0.28 g and neohesperidosyl varied at (0.01, 0.04, 0.05 and 0.06) g mass in clear daylight and the results presented in Table 4.44.

Table 4.44: Parameters derived from (Organic Neohesperidosyl)/TiO_2 solar cells at varied (0, 0.04, 0.05 and 0.06) g neohesperidosyl masses employing (0.28) g TiO_2 in the photo active layer

Cell (neohesperidosyl mass/g)	**$V_{(OC)}$ (V)**	**$I_{(SC)}$ (mA) (±0.001)**	**FF**	**PCE**
K_1,b (0 g)	0.27	4.018	4.252E-4	4.613E-4
K_5,b (0.04g)	0.097	3.242	3.526E-3	1.109E-3
K_6,b (0.05g)	0.141	4.996	0.011	7.749E-3
K_7,b (0.06g)	0.077	3.335	4.006E-3	1.029E-3

The constant (0.28) g TiO_2 host material doped with varied (0 – 0.06)g organic neohesperidosyl samples were characterized at constant solar radiation and their separate I-V characteristic step signals responses were recorded in Table 4.44, presented. The most improved fill factor and PCE of (0.011 and 7.749E-3)% for the K_6, b(0.05)g sample were derived. Those organic neohesperidosyl doped cells marginal results compared to the other flourescent dopants samples were atributed to the inadequacy of the mixture to bind effectively. A research by Zhang *et al*. (2017) noted that marginalized shift mechanism of host solvent could not efficiently influence spectral kinetics due to concentration disparity. The potential against time responses for the samples investigation in a dark room for 1 hour were presented in Table 4.45.

Table 4.45: Potential (V_{OC}) - Time characterization of Neohesperidosyl -TiO_2 luminescent solar cells employing at varied (0, 0.04, 0.05 and 0.06) g neohesperidosyl 0.28 g (TiO_2) constant photo active layer

Time/ Min	Potential(V_{OC}) ($\pm$0.005) V			
	$K_{1,b}$ (0 g)	$K_{5,b}$ (0.04g)	$K_{6,b}$ (0.05g)	$K_{7,b}$ (0.06g)
0	0.27	0.092	0.172	0.089
1	0.26	0.074	0.148	0.075
3	0.202	0.071	0.137	0.077
7	0.191	0.069	0.141	0.068
11	0.121	0.065	0.133	0.062
17	0.034	0.064	0.124	0.059
30	0.02	0.054	0.126	0.051
33		0.052	0.121	0.043
45		0.049	0.118	0.03
51		0.043	0.115	0.026
57		0.035	0.089	
60			0.084	

Graphical presentation was made from the results of Table 4.48 as shown in Figure 4.39

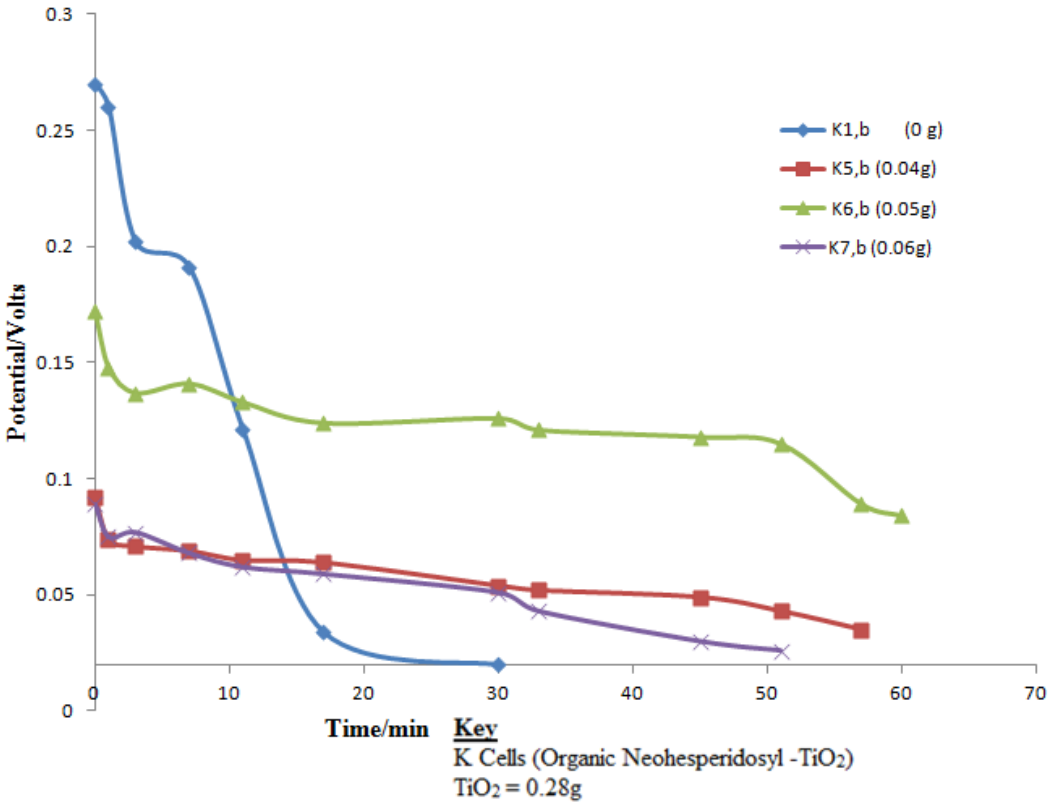

Figure 4.39: **Potential (V_{OC})-Time characteristics of (Neohesperidosyl - TiO_2) luminescent solar cells employing 0.28 g TiO_2 constant mass ratio**

The declining {(0.092 to 0.074) V, (0.172 to 0.148) V and (0.089 to 0.075) V }potential differences of the varied K_5,b(0.04)g, K_6,b(0.05)g and K_7,b(0.06)g step signals occurred between (0-1) minute as observed from Figure 4.39. Varied signal characteristics were observed between (3 to 30) minute period after which (0.02, 0.005 and 0.008) V declining ramp response occurred. Critically damped signal tails ensued with K_6,b(0.05)g displaying the highest (0.003) V unstable response terminated at 0.084 V. The reduced mass effect correspondingly contributed to declined photo fluorescence activation shift. Research by Zhang *et al.* (2017) reported that minimization of defects density interfered with fluorescence stability.

4.9.3 Responsivity of inorganic and the different organic dopant on residual potential (VOC)

The residual potential was investigated within 60 minutes duration in diminished solar radiation and the results were as presented in Table 4.46.

Table 4.46: Residual potentials(V_{OC}) of cells Z_6(0.05 g), A_6(0.05 g), L_6(0.05 g), Q_6(0.05 g), R_6(0.05 g),T_6(0.05 g) and K_6(0.05 g) in 60 minutes

Cell	Potential (V_{OC})V($\pm$0.005)
Z_6(0.05g)	0.45
A_6(0.05g)	0.195
L_6(0.05g)	0.44
Q_6(0.05g)	0.48
R_6(0.05g)	0.601
T_6(0.05g)	0.121
K_6(0.05g)	0.168

The results of delayed potential difference against the respective cells in minimum solar radiation graphical presentation were as depicted in Figure 4.40.

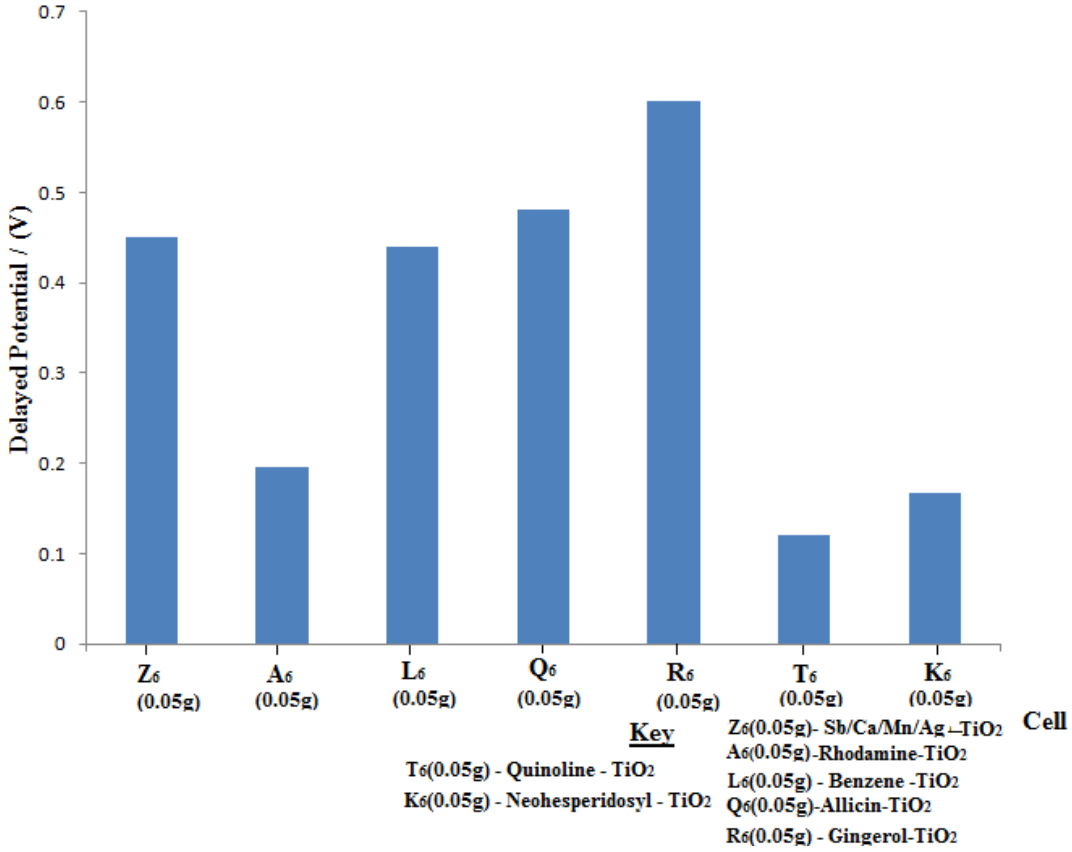

Figure 4.40: Potential responsivity of inorganic (Z6) and the organic (A6, L6, Q6, R6, T6 and K6) photofluorescent solar cells

Figure 4.40 shows decline in residual potential from (0.45 to 0.195) V for the inorganic Sb/Ca/Mn/Ag to the organic rhodamine doped solar cells. Flourene doped TiO_2 contributed to enhancement of (0.44) V potential difference. The (0.48) V potential energy was sustained due to organic allicin fluorescent material after which (0.601) V surge was evidenced from the gingerol doped TiO_2 FSCs. The favourable response of the inorganic dopant was attributed to radiation stimulated trapped electrons in the d-donor regenerating photo responsivity of the TiO_2 host material. A study by Ochsmann (2016) indicated that the longer wavelength radiation stimulated electrons trapped in the d-donor towards the valence band. That lower energy photons regenerated higher charge density enhancing the electron-hole pairs settling time

(Ochsmann, 2016). Reduction in the activating populations diminished radiative process with a proportional decline in the excited charged species life time (Liu *et al.*, 2020)

4.10 Effect of electrodes thickness on the flourescence cells performance

The effect of thickness of photoactive and receptive layers were investigated to obtain optimal thickness for the best performance. This was done to acquire a balance between the energy (light) required for the charged species excitation and the resistance offered to their migration.

The thicknesses of the luminescent solar cells were selected at {(0.071, 0.136, 0.227 and 0.318) and (0.109, 0.164, 0.273 and 0.382)} mm for the photo active layers and receptive layers receptively. A micrometer screw gauge was used to establish the measurements of thicknesses of interest.

4.10.1 Effect of heterogeneous inorganic (Sb/Ca/Mn/Ag)-TiO_2 photoactive l ayer electrodes thickness variation on I-V characteristics and potential delay

The potential response of Sb/Ca/Mn/Ag-TiO_2 heterogeneous electrodes varied thickness FSCs were investigated in clear daylight and diminished solar radiation environments. The Z_6 fluorescence solar cell whose observed highest (0.721 and 0.34) V open circuit and residual potentials respectively was preferred. Random (20, 40, 70 and 90) % selection was done for the organic/inorganic doped TiO_2 FSCs (0.4 g) mass ratio that presented the most improved output and derived parameters for the thicknesses variation. The I-V characteristics results were presented in Table 4.47.

Table 4.47: I-V characterization of (Inorganic Sb/Ca/Mn/Ag)-(TiO_2) layer varied thickness employing constant (0.545 mm) receptive layer

Cell (Sb/Ca/Mn/Ag)(TiO_2) Thickness	**$V_{(OC)}$ (V)**	**$I_{(SC)}$ (mA) ($\pm$0.001)**	**FF**	**PCE%**
$Z_{6,c1}$ (0.071 mm)	0.45	4.34	0.169	0.331
$Z_{6,c2}$ (0.136 mm)	0.712	6.38	0.294	1.336
$Z_{6,c3}$ (0.227mm)	0.537	5.14	0.173	0.478
$Z_{6,c4}$ (0.318 mm)	0.358	3.84	0.104	0.143

The effect of varying the (Sb/Ca/Mn/Ag-TiO_2) doped (0.071, 0.136, 0.227 and 0.318) mm photo active layer thicknesses shown in Table 4.47 generated fluctuating potential differences continous signals. Improved (0.712 V and 6.38 mA) terminal potential and short circuit current were observed from (0.136 mm) electrode thickness, with corresponding (0.294 and 1.336 %) fill factor and power conversion efficiency. Varied marginal (0.45 and 0.358) V were observed from (0.071 and 0.318) mm respectively. The externally transtiting high density of charge carriers due to cell $Z_{6,\ c2}$ (0.136 mm) was attributed to the photo active layer thickness ability to detect high intensity of optical excitation energy. Zhong et al., (2019) reported that balance between transparence and thickness resulted to higher potential due to high charge carrier excitation and vice versa. The cells were then characterized in a dark room and the results presented in Table 4.48

Table 4.48: Potential (V_{OC}) - Time characterization of (Inorganic Sb/Ca/Mn/Ag)-(TiO_2) layer varied thickness employing constant (0.545 mm) receptive layer on radiation delay

Time/ Min	Potential(V_{OC}) ($\pm$0.005)V			
	$Z_{6,c1}$ (0.071 mm)	$Z_{6,c2}$ (0.136 mm)	$Z_{6,c3}$ (0.227mm)	$Z_{6,c4}$ (0.318 mm)
0	0.45	0.712	0.537	0.358
1	0.405	0.678	0.517	0.338
3	0.355	0.636	0.485	0.311
7	0.325	0.583	0.395	0.307
11	0.319	0.546	0.369	0.291
17	0.308	0.494	0.338	0.249
30	0.273	0.443	0.272	0.224
33	0.264	0.432	0.261	0.205
45	0.228	0.361	0.238	0.189
51	0.225	0.328	0.224	0.153
57	0.197	0.311	0.211	0.143
60	0.185	0.306	0.209	0.139

A graphical presentations prepared from the tabulated potential- time results was presented in Figure 4.41.

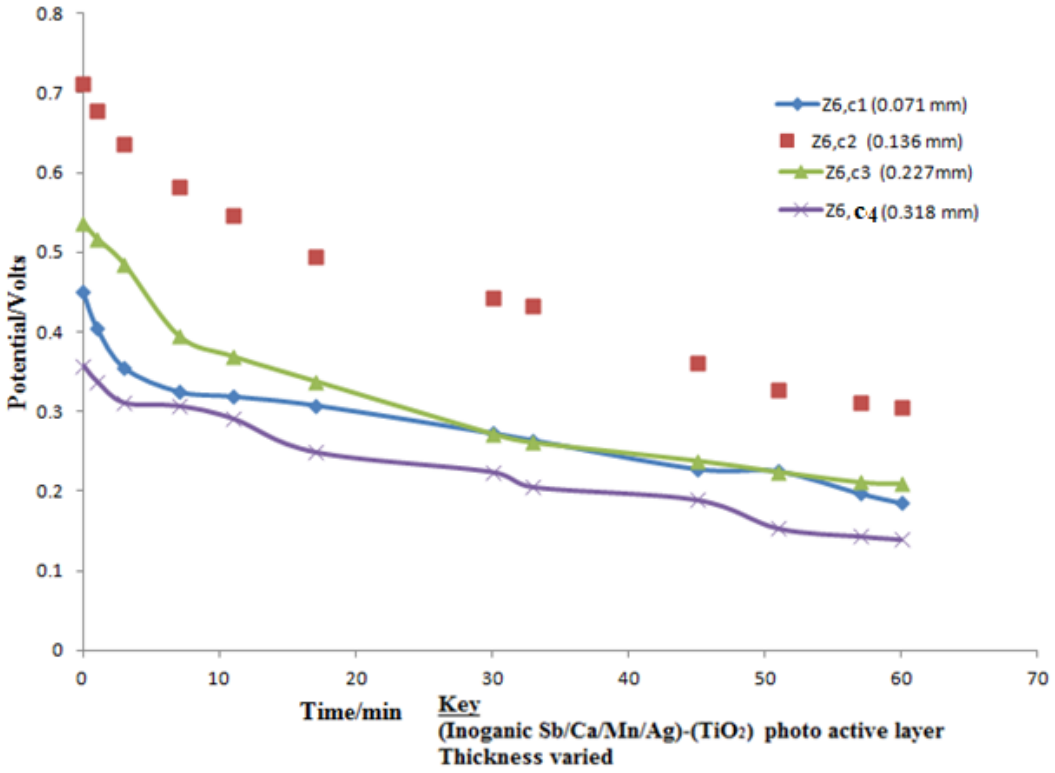

Figure 4.41: Potential (V_{OC})-Time characteristics of (Sb/Ca/Mn/Ag-TiO_2) photo active layers varied thicknesses on radiation delay

Varying (0.095, 0.129, 0.142 and 0.046) V were observed from Figure 4.41 between {(0-3) and (0-7)} minutes due to {(0.071 and 0.318) and (0.136 and 0.227)} mm varied (Sb/Ca/Mn/Ag)-TiO_2) photo active layers thickness. Nonlinear potential difference signal occurred due to (0.136 mm) thickness which terminated at 0.306 V minimum unstable damped voltage varying with time after the next 57 minutes of the experiment. The rest electrode thickness sustained between (0.209 to 139) V delayed potential diffence between (7 to 60) minutes interval. Wang *et al.*, (2021) noted that activation capacity for equitable charge transition evolved from the photosensitivity alignment derived from the interdependence between donor - acceptor enhancement radiation absorption.

4.10.2 Effect of Organic Rhodamine -TiO_2 photoactive layer varied thickness on radiation delay

Characterization of four Rhodamine-TiO_2 OFSCs with different photo active layers thicknesses at 0.545 mm (C_X/I_2/KI) receptive layer constant was done. The rhiodamine doped TiO_2 {A_6 (50%)} FSC with the highest (0.559 and 0.362) V open circuit and residual potentials differences, respectively was selected for the investigation. The exhibited open circuit potential (V_{OC}) with short circuit current were outlined in Table 4.49.

Table 4.49: I-V characterization of (rhiodamine-TiO_2) layer varied thickness employing constant (0.545 mm) receptive layer

Cell (rhiodamine TiO_2 layer Thickness	**$V_{(OC)}$ (V)**	**$I_{(SC)}$ (mA) ($\pm$0.001)**	**FF**	**PCE%**
$A_{6,c1}$ (0.071 mm)	0.633	3.824	0.212	0.513
$A_{6,c2}$ (0.136mm)	0.756	6.841	0.223	1.153
$A_{6,c3}$ (0.227mm)	0.641	5.314	0.172	0.586
$A_{6,c4}$ (0.318 mm)	0.429	4.532	0.114	0.222

The variation of rhiodamine FSCs thickness results displayed in Table 4.49 depicts a non-linear signal with varying (0.633, 0.756, 0.641 and 0.429) V potential amplitudes. The highest (0.756 V) V_{OC} terminal potential difference was attributed to 0.136mm thickness capacity to allow efficient interaction between the absorbed optical energy and the doped TiO_2 particles. The disparity (1.527 and 3.017) mA in charge migration rates between (0.227 and 0.136) mm compared to (0.071 and 0.136)

mm thicknesses was indicative of the excited charge density with higher material content. That had contradictory (0.051 and 0.011) fill factor gaps with output parameters and proportionate (0.513, 1.153 and 0.586) % PCEs. The highest (0.318) mm thickness generated (0.429V and 4.532mA) limited output parameters with unsatisfactory (0.114 and 0.222%) FF and PCE.

The varied thicknesses were thought to progressively provide diverse sensitivity levels with wider margins to orient molecular coupling conjugation with different adaptability. Reports by Zhang *et al.,* (2021) indicated that better π-molecular particals alignment and their complementing arrangements with elaborate structured π–π linkages, improved exciton disintegration enhancing better charge transition and electron – hole interaction. The exhibited open circuit voltage (V_{OC}) with time after withdrawal of solar radiation were recorded in Table 4.50.

Table 4.50: Potential Difference (V_{OC})-Time characterization of rhiodamine-TiO_2 layer varied thickness employing constant (0.545mm) receptive layer on radiation delay

Time/ Min	Potential(V_{OC}) ($\pm$0.005)V			
	$A_{6,c1}$ (0.071 mm)	$A_{6,c2}$ (0.136 mm)	$A_{6,c3}$ (0.227 mm)	$A_{6,c4}$ (0.318 mm)
0	0.633	0.756	0.641	0.429
1	0.578	0.642	0.609	0.377
3	0.531	0.615	0.584	0.343
7	0.469	0.573	0.559	0.326
11	0.427	0.528	0.497	0.301
17	0.359	0.467	0.461	0.269
30	0.317	0.419	0.367	0.221
33	0.311	0.386	0.348	0.21
45	0.265	0.342	0.299	0.194
51	0.209	0.325	0.255	0.174
57	0.199	0.318	0.226	0.146
60	0.187	0.316	0.217	0.138

The results obtained from {A6,c_4(0.28g), A6,$_{C3}$(0.2g), A6,c_2 (0.12g) and $A_{6,}c_1$(0.08g)} rhodamine dye doped solar cells varied thicknesses were presented graphically as shown in Figure 4.42.

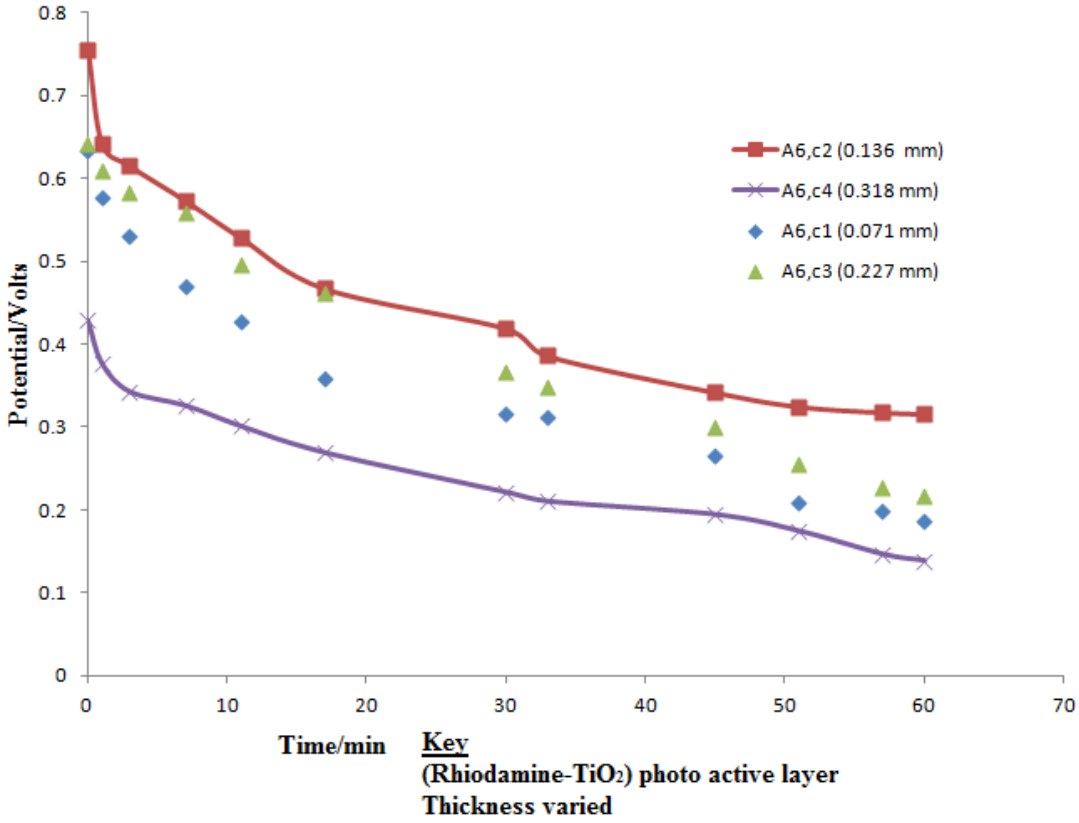

Figure 4.42: Potential (V_{OC})-Time characteristics of (Rhiodamine -TiO_2) varied photo active layer thicknesses solar cells

Figure 4.42 shows declining (0.114 and 0.085) V surge voltage signals for (0.136 and 0.318) mm thick (Rhiodamine/TiO_2) layers observed between {(0 - 1) and (0 - 3) minutes intervals, respectively. Gradually reducing (0.227, 0.18, 0.175 and 0.135) V ramp signal occurred in {(1- 17) and (0 - 30)} minutes for {(0.071 and 0.136,) and (0.227 and 0.318)} mm, respectively. Short term rectangular (0.033) V response occurred between (30-33) minutes for A_6, c2 (0.136) mm thickness. For the rest of the transients period, the decaying responses displayed continuous signal characteristics with gradual nonlinear signal of varied amplitudes terminating at (0.187, 0.316, 0.217 and 0.138) V. The improved potential delay characteristics were attributed to the electrode thickness broad spectrum absorption by rhodamine structure and efficient charge separation at low energy loss. Different thicknesses

supported separately the band gap energy alignment proportionately to charge carriers extraction rates (Jia *et al.*, 2020). Reports by Ye *et al.* (2021) noted that critical parameters were contributed by varying flexibility in recombination rates due diverse optical absorption frequency bands with separate electron transition at varying internal ionic lattice energy levels.

4.10.3 Effect of Organic Flourene doped TiO_2 luminescent photo active layer thickness variation on radiation delay

To evaluate the photovoltaic characteristics of flourene chemical material within the structure of the organic flourene -TiO_2 luminescent electrode, the L_6 luminescent solar cell with highest (0.73 and 0.408) V open circuit and residual potentials respectively was selected. Four cells of (0.071, 0.136, 0.227 and 0.318) mm varied thicknesses were fabricated and their I-V characteristics were recorded in Table 4.51.

Table 4.51: I-V characterization of (Flourene doped TiO2) layer varied thickness employing constant (0.545 mm) receptive layer

Cell (Flourene-TiO_2) thickness	**$V_{(OC)}$ (V)**	**$I_{(SC)}$ (mA) ($\pm$0.001)**	**FF**	**PCE%**
$L_{6,c1}$ (0.071mm)	0.551	4.381	0.174	0.421
$L_{6,c2}$ (0.136mm)	0.613	7.252	0.311	1.383
$L_{6,c3}$ (0.227mm)	0.518	5.763	0.137	0.409
$L_{6,c4}$ (0.318mm)	0.418	4.352	0.123	0.224

Table 4.51 shows varying (0.062, 0.095 and 0.195) V I-V characteristics potentials relative to (0.613) V of L_6, c2 (0.136) mm cell maximum generated potential (V_{OC}). The corresponding (4.381, 5.763 and 4.352) mA current transiting depicted a

nonlinear continuous signal. The samples derived FF and PCEs displayed nonlinear {(0.137 and 0.123) and (0.409 and 0.224) % responses with declining properties from the improved (0.311 and 1.383) % 0.136mm thickness.

This reduced potential in 0.071mm thick layer was attributed to excitation of few holes – electrons pairs. Reports by noted Khan *et al.* (2021) indicated that presence of active dismal devices excitons was a consequence of marginalized radiation absorption. The potential against time characteristics of the cells under minimum solar radiation was presented in Table 4.52.

Table 4.52: Potential (V_{OC}) –Time characterization of (Flourene-TiO_2) photoactive varied thickness employing constant (0.545mm) receptive layer on radiation delay

Time/ Min	Potential(V_{OC}) ($\pm$0.005)V			
	$L_{6,c1}$ (0.071 mm)	$L_{6,c2}$ (0.136 mm)	$L_{6,c3}$ (0.227 mm)	$L_{6,c4}$ (0.318 mm)
0	0.55	0.613	0.518	0.418
1	0.511	0.573	0.501	0.389
3	0.483	0.479	0.456	0.341
7	0.421	0.423	0.419	0.329
11	0.393	0.367	0.345	0.299
17	0.309	0.324	0.317	0.274
30	0.266	0.301	0.246	0.239
33	0.257	0.299	0.233	0.214
45	0.224	0.264	0.213	0.209
51	0.21	0.239	0.201	0.187
57	0.178	0.235	0.189	0.119
60	0.143	0.227	0.181	0.111

From the results recorded in Table 4.52, a graphical presentation of open circuit voltage (V_{OC}) against time was made as shown in Figure 4.43.

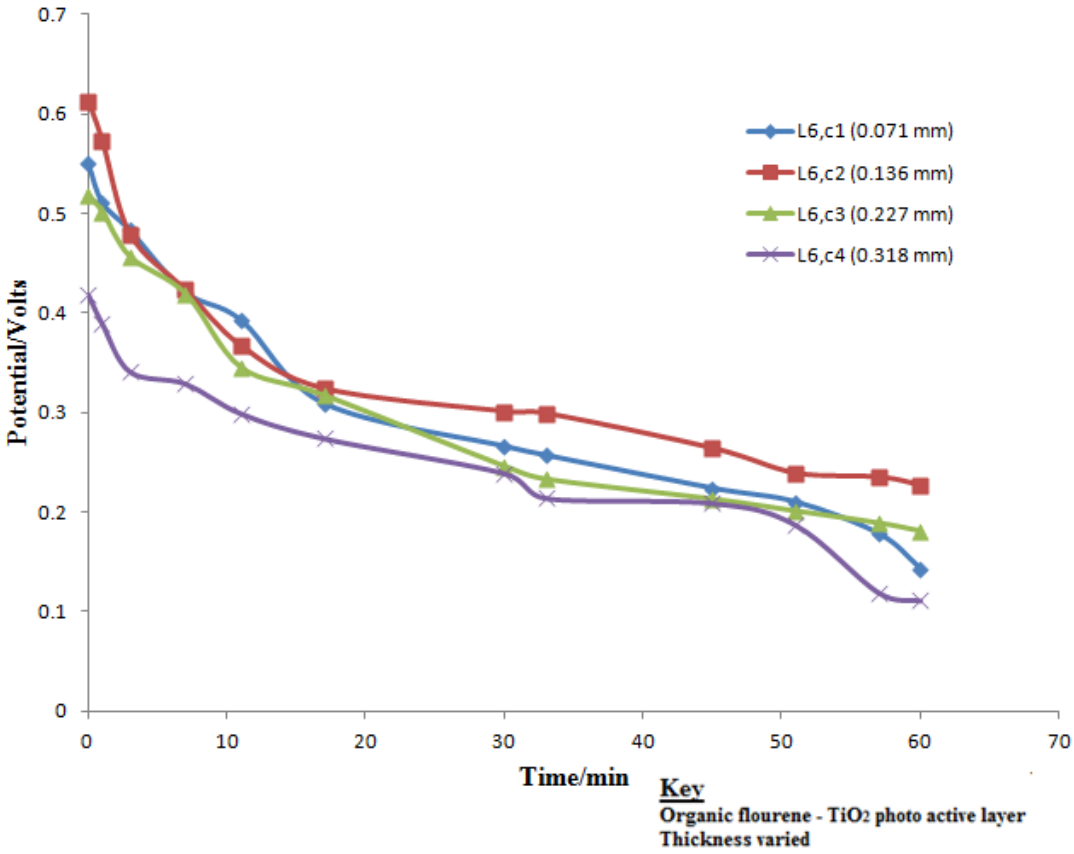

Figure 4.43: Potential-Time characteristics of (Flourene -TiO_2) photo active layer thickness varied employing constant (0.545mm) receptive layer on radiation delay

Short term L_6, C_4 (0.318) mm (0.077) V declining signal appeared between (0 to 3) minutes as displayed in Figure 4.42. The negligible stabilized signal condition was observed between (3 to 7) minutes. Relatively interactive responses were demonstrated by {L_6, C_1 (0.071) mm, L_6, C_2 (0.136) mm and L_6, C_3 (0.227) mm} cells thicknesses between (0 to 17) minutes transient period. These states were attributed to relative common wavelength triggered spectral traps, exciting equivalent charge densities. Cell L_6, C_2 sustained a stable continuous signal condition with minimum variation terminating at (0.227) V in the next 43 minutes of the experiment. Significant (0.166, 0.136 and 0.163) V declining potential shifts were presented by (0.071, 0.227 and0.318) mm thickness terminating at (0.143, 0.181 and 0.111) V. The

higher (0.318 mm) thickness was thought to shorten free exciton's lifetime due to the long path the charge carriers migrated through. A study by Caironi *et al.* (2011) indicated that dimensions of charge modulating spectroscopy (CMS) translated to interference of intramolecular polarization, dipole interaction with energetic disorder. Enhanced surface molecular ordering improved uniform landscape for charge transport (Pearton *et al.*, 2016).

4.10.4 Effect of organic Allicin–TiO_2 photo active layer thickness variation of luminescent solar cells

The samples investigated herein were prepared from Allicin–TiO_2 photo fluorescent material at (C_X/I_2/KI) 0.545mm constant and their I-V characteristics in clear daylight presented in Table 4.53. The Q_6 luminescent solar cell with highest (0.84 and 0.48) V open circuit and residual potentials respectively were taken at 0.136mm photo active layer.

Table 4.53: I-V characterization of (Allicin–TiO_2) layer varied thickness employing constant (0.545 mm) receptive layer

Cell (Flourene-TiO_2)thickness	**$V_{(OC)}$ (V)**	**$I_{(SC)}$ (mA) ($\pm$0.001)**	**FF**	**PCE%**
$L_{6,c1}$ (0.071mm)	0.532	4.246	0.167	0.426
$L_{6,c2}$ (0.136mm)	0.627	7.134	0.323	1.374
$L_{6,c3}$ (0.227mm)	0.511	5.678	0.141	0.403
$L_{6,c4}$ (0.318mm)	0.421	4.443	0.134	0.219

The contribution of varying allicin-TiO_2 photo active layer thickness to I-V characteristics presented in Table 4.53 shows (0.532, 0.627, 0.511 and 0.421) V ramp and nonlinear declining V_{OC} characteristic. The corresponding excited electron-hole pairs presented (0.167, 0.323, 141 and 134) FF with conforming (0.426, 1.374, 0.403 and 0.219) % derived PCEs. The varied (0.071 to 0.227) mm thicknesses were thought to present negligible dynamic deformity counterbalance charge pigment transition impediments. That contribution improved substrate interspacing for fine-tuned stability compensation. Research by Koo *et al*. (2021) noted that conformed thicknesses adjusted the nanocomposites interspaces with subsequent restructured band gap for adequate charge pigments optical dynamics interaction with improved parameters. That resizing of thickness layer improved band gap edges for higher electron–hole pairs density with moderated coefficient of absorption and photon recycling (Koo *et al*., 2021). The Allicin–TiO_2 FSCs P-T responses under minimum solar radiation characteristics were recorded in Table 4.54.

Table 4.54: Potential (VOC) - Time characterization of (organic Allicin - TiO2) photoactive layer varied thickness employing 0.545mm (CX/I2/KI) layer constant

Time/ Min	**Potential(V_{OC}) ($\pm$0.005)V**			
	$Q_{6,c1}$ (0.071 mm)	**$Q_{6,c2}$ (0.136 mm)**	**$Q_{6,c3}$ (0.227 mm)**	**$Q_{6,c4}$ (0.318 mm)**
0	0.48	0.672	0.41	0.37
1	0.416	0.531	0.391	0.35
3	0.388	0.494	0.357	0.296
7	0.341	0.477	0.319	0.248
11	0.298	0.423	0.262	0.237
17	0.269	0.411	0.257	0.215
30	0.247	0.362	0.242	0.21
33	0.217	0.349	0.239	0.199
45	0.206	0.311	0.219	0.167
51	0.198	0.296	0.165	0.142
57	0.169	0.268	0.179	0.124
60	0.142	0.263	0.132	0.117

From the information recorded in Table 4.54, a graphical presentation of potential (V_{OC}) against the time was made as shown in Figure 4.44.

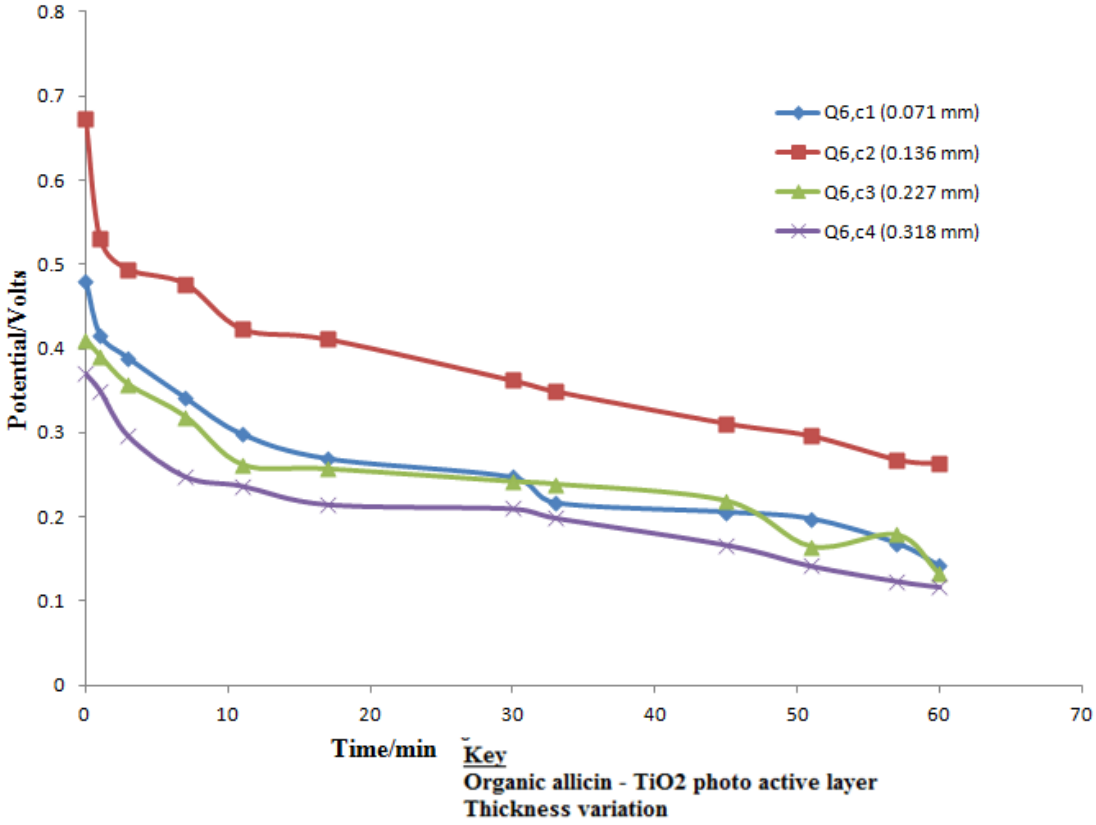

Figure 4.44: Potential-Time characteristics of (organic Allicin-TiO_2) photo active layer varied thickness employing constant (0.545mm) receptive layer on radiation delay

Figure 4.44 shows Q_6, c2 (0.136) mm short-term (0.141) V sharp decline at the (0 - 1) minute interval followed by (0.108) V potential differtence rise lasting for 10 minutes later. Cells Q_6, c1 (0.071) mm, Q_6, c3 (0.227) mm and Q_6, c4 (0.318) mm were characterized with diminishing (0.182, 0.148 and 0.133) V potential in the first (0 - 11) minutes. The voltage due to the 0.071 mm thickness stabilized at (0.247) V for the (11 to 30) minute experiencing a unit step (0.030) V negative amplitude between (30 to 33) minute interval. Marginally stable voltage characteristics due to (0.071, 0.227 and 0.318) mm thicknesses settled at (0.142, 0.132 and 0.117) V consecutively. The (0.071) mm thick layer contributed to shallow wave defects of varied band gaps configurations limits. The (0.136) mm thickness sustained a stable

linearly varying (0.16) V amplitude signal for the (11 to 60) interval. A study by Jin-Wook *et al.* (2019) noted that photo active thickness resizing modified trap levels relative to conduction band for improved absorption coefficient. That modelling dictated optics interaction for complimentary refractive index and absorption coefficient (Jin-Wook *et al.,* 2019).

4.10.5 Photoelectric response of Gingerol-TiO_2 photoactive layer varied thicknesses

By varying mass ratios of gingerol-TiO_2 photo active material, the terminal voltage (V_{OC}) was monitored in diminished soalar radiation and the results were recorded in Table 4.55. Characterization of the gingerol-TiO_2 FSCs in clear daylight were presented in Table 4.54. The R_6 fluorescent solar cell whose highest (0.719 and 0.601) V open circuit and residual potentials respectively was opted at constant 0.136 mm photo active layer thickness.

Table 4.55: I-V characterization of (Gingerol-TiO_2) layer varied thickness employing constant (0.545 mm) receptive layer

Cell (Gingerol-TiO_2) thickness	**$V_{(OC)}$ (V)**	**$I_{(SC)}$ (mA) ($\pm$0.001)**	**FF**	**PCE%**
$R_{6,c1}$ (0.071 mm)	0.419	5.361	0.108	0.243
$R_{6,c2}$ (0.136 mm)	0.653	6.583	0.178	0.765
$R_{6,c3}$ (0.227 mm)	0.378	4.362	0.121	0.199
$R_{6,c4}$ (0.318 mm)	0.336	2.181	0.092	0.067

Wide (0.522, 0.566 and 0.698) % disparity PCEs were derived from (0.071, 0.227 and 0.318) mm thicknesses relative to (0.765)% of 0.136 mm indicated in Table 4.55. The proportionate (0.070, 0.057 and 0.086) FF discrepancies compared to 0.178, indicated that the corresponding

I-V characteristic V_{MAX} and I_{MAX} were low. Relative (0.134, 0.275 and 0.317) V output potential (V_{OC}) compared to 0.653 V were proportional to the charge migration rates (I_{SC}). The variation of gingerol-TiO_2 thickness was thought to promote wavelength blending for radiation enhancement and PCEs improvement through charge rate duplication and potential (V_{OC}) maximization. A study by Micha *et al.* (2018) indicated that compatibility variation contributed to composite configuration which introduced radiation recurrence in the photo sensitive electrode pigments defects for moderated optical attributes. Increase in charged species population improved the photo sensitive electrode charge capacities relative to the base reference and consequential escalation charge transition rate (I_{SC}) due to the enhanced power conversion efficiency (Chandiran *et al*., 2014).

Table 4.56: Potential (V_{OC}) –Time characterization of (Gingerol-TiO_2) photo active layer varied thickness employing 0.545 mm (C_X/I_2/KI) layer constant

Time/min	Potential(V_{OC}) ($\pm$0.005)V			
	$R_{6,c1}$ (0.071 mm)	$R_{6,c2}$ (0.136 mm)	$R_{6,c3}$ (0.227 mm)	$R_{6,c4}$ (0.318 mm)
0	0.419	0.653	0.378	0.336
1	0.406	0.633	0.317	0.301
3	0.383	0.598	0.299	0.277
7	0.375	0.544	0.262	0.258
11	0.349	0.487	0.239	0.212
17	0.324	0.467	0.219	0.197
30	0.283	0.407	0.179	0.205
33	0.269	0.386	0.176	0.185
45	0.224	0.349	0.147	0.161
51	0.218	0.299	0.134	0.149
57	0.197	0.283	0.123	0.127
60	0.182	0.278	0.115	0.108

The results of potential against time in Table 4.56, were presented graphically as shown in Figure 4.45.

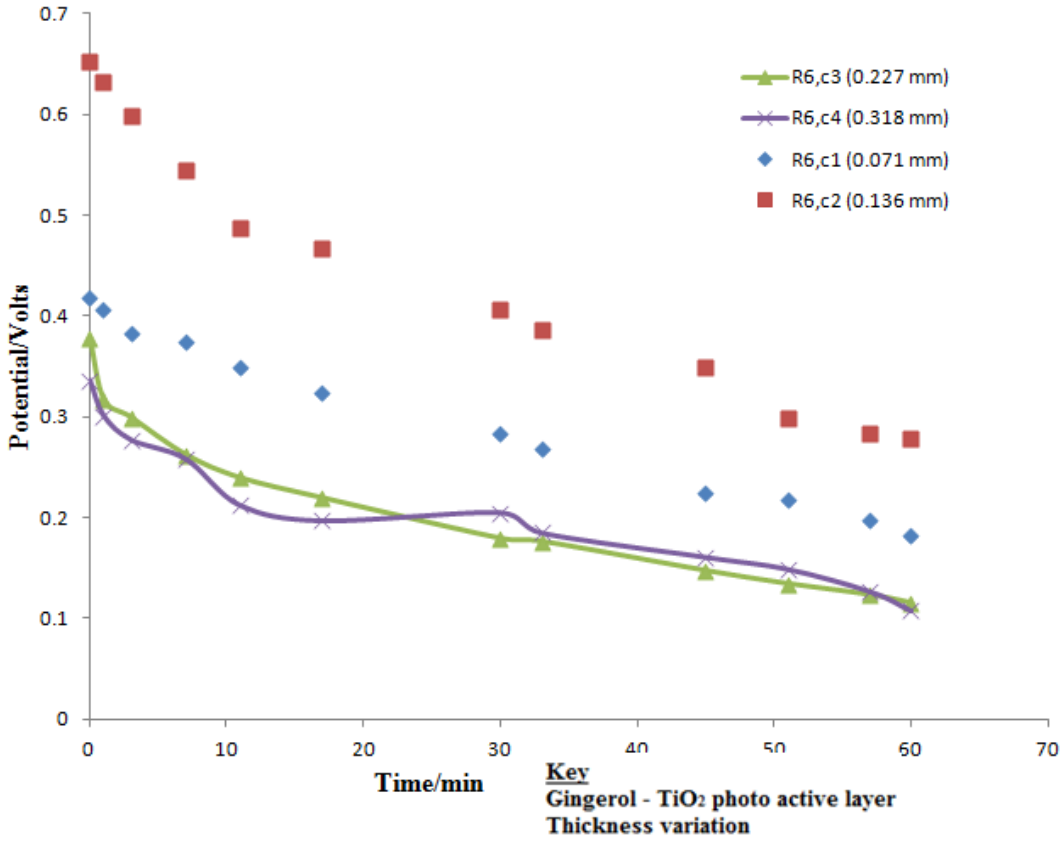

Figure 4.45: Voltage -Time characteristics of (Gingerol-TiO_2) photo active layer thickness varied at 0. 545 mm receptive layer constant for radiation delay

Figure 4.45 shows linearly depolarized (0.136mm) thickness signal, whose electronic charges presented (0.166) V between {(0 - 11) minutes. The signal displayed (0.021) V negative ramp characteristics between (30-33) minutes, before settling with (0.278) V amplitude parabolic response between (51-60) minutes. Similar characteristics were observed from R_6, c_1 (0.071mm) cell with a negative (0.036) g ramp response at (0 - 3) minutes interval and (0.087) V settling magnitude signal between (33-60) minutes interval. Varying {-(0.089 and 0.101)} V stable ramp signal features were displayed by R_6, c_3 (0.227mm) and R_6, c_4(0.318mm) between {(0 to 1) and (0 - 3)} minutes. The (0.227) mm gingerol-TiO_2 layer thickness generated a stable parabolic signal terminating at (0.115) V in the (3 to 60) minutes interval. The non-linearity

features suggest that molecular bonds were excited by varying frequency bands radiated energy. A study by Gao *et al.* (2020) reported that reduction of stress within the radiation dependence devices was a consequence of the components dimensions. According to Tsai & Hamblin (2017), high charge carrier populations were activated by the spectral traps dynamics complemented by the incident energy on the photo active fractional devices.

4.10.6 Radiation delay characteristics of organic Quinoline -TiO_2 photo active layer thickness variation

The photo electric response of (0.136, 0.227 and 0.318)mm varied photo active layers thicknesses fabricated from organic quinoline -TiO_2 mixture of tonic water origin, was observed as its receptive layer was held constant at 0.545mm in a light diminished environment. The T_6(0.05/0.4) g cell was preferred for photo active thickness variation due to its improved residual potential against time characteristics and its results presented in Table 4.57. Their I-V characteristics were presented in Table 4.57.

Table 4.57: I-V characterization of (Quinoline -TiO_2) layer varied thickness employing constant (0.545 mm) receptive layer

Cell (Quinoline -TiO_2) thickness	$V_{(OC)}$ (V)	$I_{(SC)}$ (mA)	FF	PCE%
$T_{6,c1}$ (0.071mm)	0.101	1.983	6.332E-4	1.256E-4
$T_{6,c2}$ (0.136 mm)	0.175	2.901	7.892E-4	4.007E-4
$T_{6,c3}$ (0.227 mm)	0.138	1.971	5.699E-4	1.551E-4
$T_{6,c4}$ (0.318 mm)	0.111	1.824	3.559E-4	7.206E-5

The quinoline –TiO_2 varied photo active thickness had (7.892E-4 to 3.559E-4) fill factors as shown in Table 4.57. The contribution of the different (0.071, 0.136, 0.227 and 0.318) mm layers was {(0.101 -0.175) V and (1.824 – 2.901) mA} potential difference (V_{OC}) and short circuit current (I_{SC}) output generated parameters. These resulted to (7.206E- 5 to 1.256E-4) % derived PCEs values. This confirms on the internal properties supporting production of charge densities. Majority of fluorescent structures in quinoline were joined to the main molecule by σ strong bond, whose consequence was absorption of short wavelength energy with few excited defects states. A study by Wang *et al*. (2014) noted that varied composite dimensions, their suitability relative to energy bands sites reordering and balance in the solvent and density produced fundamental dynamic ratios proportional to radiation absorbance densities. Reports by Chandiran *et al*. (2014) noted that scaling down of charge carriers capacity minimizes the uniformity scope of the dissociated electron-hole in the host material transition region. That interferes with the band gap edges with a consequence of low potential and short circuit current with a proportional value of the fill factor and power conversion efficiency (Chandiran *et al*., 2014).

Table 4.58: Potential (V_{OC}) - Time characterization of Organic (Quinoline - TiO_2) photo active layer varied thickness employing constant (0.545mm) receptive layer on radiation delay

Time/ Min	Potential (V_{OC}) ($\pm$0.005) V			
	$T_{6.c1}$ (0.071 mm)	$T_{6,c2}$ (0.136 mm)	$T_{6,c3}$ (0.227 mm)	$T_{6,c4}$ (0.318 mm)
0	0.101	0.175	0.138	0.111
1	0.091	0.162	0.129	0.106
3	0.073	0.168	0.132	0.097
7	0.038	0.125	0.117	0.072
11		0.121	0.123	0.043
17		0.111	0.11	0.031
30		0.106	0.08	
33		0.101	0.058	
45		0.097	0.045	
51		0.071		
57		0.063		
60		0.059		

From the information recorded in Table 4.58, a graphical presentation of potentials against the Time was made as shown in Figure 4.46.

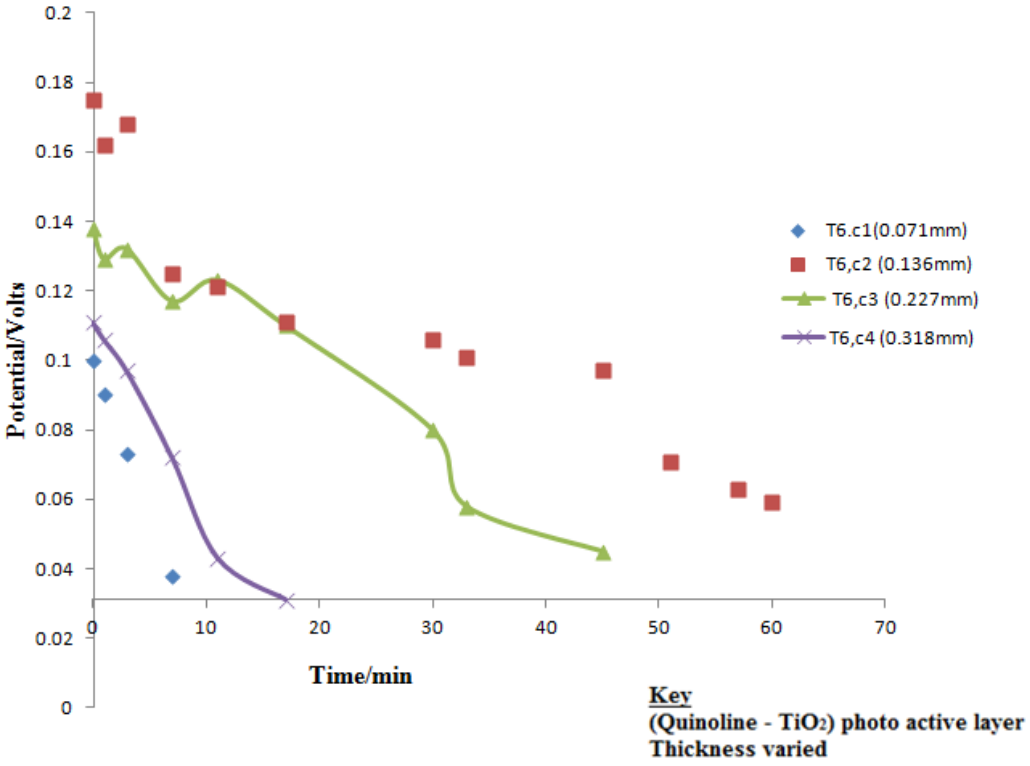

Figure 4.46: Potential-Time characteristics of (Quinoline-TiO_2) photo active layer

Figure 4.46 shows non-linear reducing (0.050 and 0.016) V potentials from the voltage generated by {T_6, c_2 (0.136mm) and T_6, c_2 (0.136mm)} between {(0 to 11) and (0 to 7)} minutes respectively. The (0.227) mm thickness conformed to (0.013) V amplitude sine wave at the (7 to 17) interval, with sudden negative surge settling at (0.058) V after (13) minutes lapse (0.045)V for the next 15minutes. Cell T_6, c_2 (0.136mm) displayed stabilized characteristics of (1) V between (11 to 45) minutes interval terminating at (0.059) V after 15 minutes. The compliance of 0.136mm (quinoline-TiO_2) thickness enhanced fluorescence turn-on by creating frequent intramolecular motions enhanced with flexibile sample segments environment. The signals generated by (0.071 and 0.318) mm distinguished after (0 - 7) and (0 to 17) minutes respectively of the experiment. The unsatisfactory performance of the (0.071,

0.227 and 0.318) mm thicknesses varied quinoline –TiO_2 FSCs was contributed to the occasioned radiationless energy dissipation within the nanoparticles exciton aggregates energy pathways. A study by Maçôas *et al.* (2014) noted that non-radiative pathway dominating relaxation of exciton energy had fluorescence quenching consequences. The high non-radiative molecular states restricted intramolecular motions with low aggregation-induced emission (Feng e*t al.*, 2017). Further investigation was done on the effect of varying organic neohesperidosyl-TiO_2 K_6 (0.05 g) photo active cell thickness due to its improved residual potential with time and the results observed were presented in Table 4.60. The responses of samples in clear daylight were presented in Table 4.59.

Table 4.59: I-V characterization of (Neohesperidosyl -TiO_2) layer varied thickness employing constant (0.545 mm) receptive layer

Cell (Neohesperidosyl - TiO_2) thickness	**$V_{(OC)}$ (V)**	**$I_{(SC)}$ (mA)**	**FF**	**PCE%**
$K_{6.c1}$ (0.071mm)	0.163	1.764	3.476E-5	9.995E-6
$K_{6,c2}$ (0.136 mm)	0.221	2.949	7.628E-4	4.971E-4
$K_{6,c3}$ (0.227 mm)	0.157	2.082	5.932E-4	1.939E-4
$K_{6,c4}$ (0.318 mm)	0.127	1.648	1.709E-4	3.577E-5

Insignificant (1.867) mA charge transition gaps between (0.136 and 0.227) mm thicknesses of neohesperidosyl-TiO_2 layers was observed. Beyond these edges, (1.764 and 1.648) mA limited short circuit current (I_{SC}) were facilitated by (0.071 and 0.318) mm extreme thicknesses. The respective (0.136 and 0.227) mm thicknesses (0.074) V potential disparity, with (0.163 and 0.127) V different margins were generated. Table 4.59 also enumerates the {(3.476E-5 to 1.709E-4) and (9.995E-6 to

1.939E-4) %} the fill factors and conversion efficiencies derived from the output parameters. The low fill factors derived from neohesperidosyl doped TiO_2 layers varied thicknesses was occasioned by scantly tuned radiation for lower density charged species excitation. Reports by Hu *et al*. (2017) indicated that variation in environmental ambient conditions moderated FSCs interacting systems. The internally generated discontinuities strongly influenced the fill factor and short circuit current (Hu *et al*. (2017). A study by Gao *et al.* (2017) noted that favorable compartments band alignment improved photo conversion efficiency. The lower absorbance proportionately effect of fill factor and power conversion efficiency (Mahata *et al*., 2020).

Table 4.60: Potential (V_{OC}) - Time characterization of Organic (Neohesperidosyl -TiO_2) photo active layer varied thickness employing constant (0.545mm) receptive layer on radiation delay

Time/ Min	Potential(V_{OC}) ($\pm$0.005)V			
	$K_{6.c1}$ (0.071mm)	$K_{6,c2}$ (0.136mm)	$K_{6,c3}$ (0.227mm)	$K_{6,c4}$ (0.318mm)
0	0.163	0.221	0.157	0.127
1	0.146	0.218	0.139	0.119
3	0.137	0.202	0.124	0.114
7	0.119	0.165	0.125	0.106
11	0.114	0.143	0.121	0.085
17	0.109	0.133	0.117	0.045
30	0.089	0.114	0.103	0.031
33	0.082	0.11	0.097	
45	0.057	0.098	0.051	
51	0.047	0.073	0.045	
57		0.057		
60		0.054		

From the information recorded in Table 4.60, graphical presentations of potentials (V_{OC}) against time were made as shown in Figures 4.47.

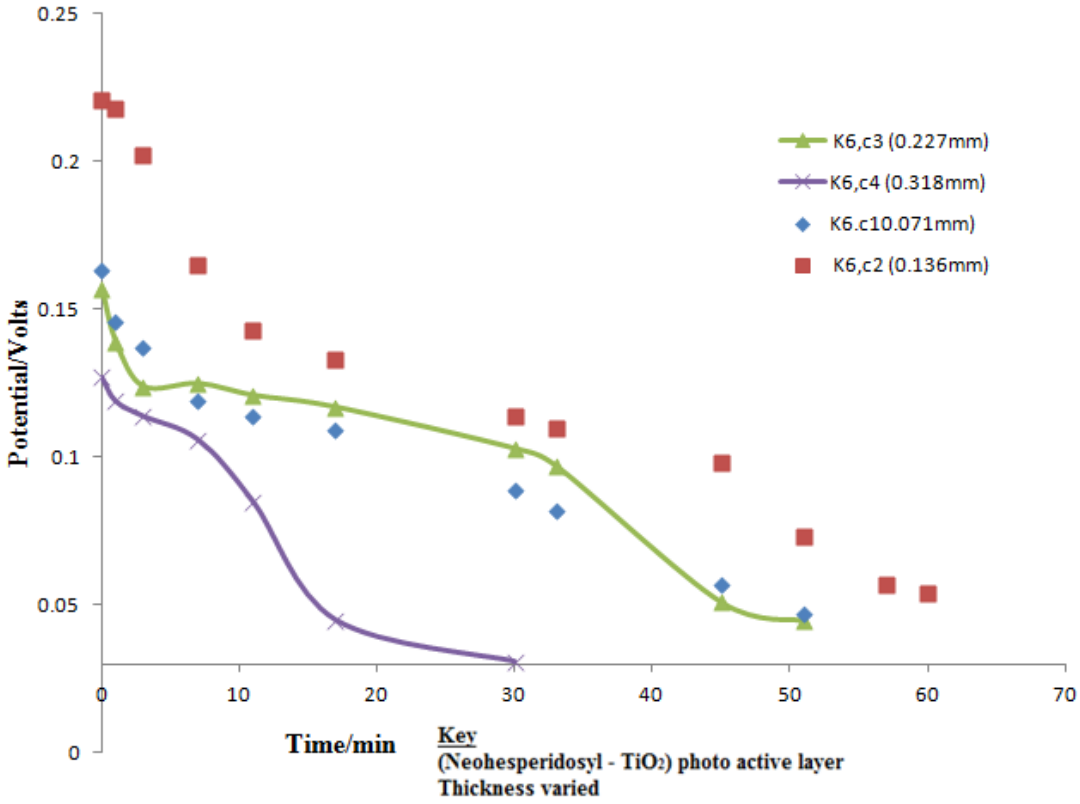

Figure 4.47: Potential-Time characteristics of (Neohesperidosyl -TiO_2) photo active layer thickness varied employing constant 0.545 *m*m receptive layer on radiation delay

Deductions from Figure 4.47 showed that the (0.136) mm thick (neohesperidosyl - TiO_2) layer, generated a hyperbolic characterized (0.003) V voltage in the (0 -1) minute interval. That was followed by a declining (0.075) V ramp trend for the next 10 minutes. The potential was observed to stabilize with (0.033) V amplitude between (11 to 33) minutes settling zone. The sine-usoidal (half-wave) characteristic of (0.037) V magnitude was observed in the interval (33 to 51) minutes before terminating at (0.054) V for the last 9 minute of the experiment. Varying declining (0.044, 0.033 and 0.021) V magnitude negative ramp signals between the {(0 - 7), (0 - 3) and (0 - 7)} minutes intervals were observed from (K_6, C_1 (0.071)mm, (K_6, C_3 (0.227)mm and (K_6, C_4(0.318)mm) thick cells. A steep distinguishing (0.061) V ramp

was characterized between (7 - 17) minutes (0.318) mm before terminating at 0.031 V in the last 13 minutes of the signal. The (0.071 and 0.227) mm thick layers generated varying stable signals between (10 -33) minutes before settling with (0.047 and 0.045) V ramp characteristics in the (33 - 51) minutes interval. This was attributed to excitation of electron hole pairs at different frequency bands d- orbital radiated energy. The 0.136 mm substrate thickness offered flexible broadband light absorption with favourable fluorescence properties and trapping defects. That dimension provided narrow absorption bands which did not overlap the band excitation. The results observed from each luminescent solar cell (0.136 mm) photo active layers resulted to the most improved open circuit and residual potentials. Liang et al. (2021) noted that favourable dimensions of radiation depedent devices facilitated adequate defect convergencies closer to the conduction orbitals of the host material. A study by Chandiran *et al*. (2014) noted that the impact of microscopic radiance compeled charged species activation in the host solvent at varying intervals (Chandiran *et al*. 2014). That thickness was preferred for the constant mass to investigate optimal receptive layer thickness.

4.11 Receptive (C_X/I_2/KI) layer variation of thicknesses

The effect of varying C_x/I_2/KI receptive layers thickness on potential against time was investigated at minimum solar radiation for both inorganic and organic solar cells.

4.11.1 Receptive C_X/I_2/KI layer thickness variation of inorganic (Sb/Ca/Mn/Ag)-(TiO_2) luminescent solar cells

Effect of variation of C_X/I_2/KI receptive layer thickness was investigated at constant 0.136mm (Sb/Ca/Mn/Ag-TiO_2) photoactive layer thick. The I-V characteristics and their response of potential-time (P-T) in minimum solar radiation were presented in Tables 4.61 and 4.62 respectively. The $Z_{6,C2}$ luminescent solar cell with improved (0.712 and 0.306) V open circuit and residual potentials respectively was considered for the inorganic solar cell receptive layer variation.

Table 4.61: I-V characterization of (I_2/KI/C_x) receptive layer thickness varied employing constant 0.136mm (Sb/Ca/Mn/Ag-TiO_2) photoactive layer

Cell (I_2/KI/C_x) layer thickness	$V_{(OC)}$ (V)	$I_{(SC)}$ (mA) ($\pm$0.001)	FF	PCE%
Z_6, d_1 (0.109mm)	0.541	3.842	0.027	0.056
Z_6, d_2 (0.164mm)	0.922	6.381	0.126	0.741
Z_6, d_3 (0.273mm)	0.625	5.143	0.081	0.261
Z_6, d_4 (0.382mm)	0.493	4.361	0.093	0.199

The fill factor of {(Sb/Ca/Mn/Ag)-TiO_2} cell varied receptive layer (0.164 and 0.273) mm varied thickness had 0.045 discrepancy. That gap changed by (0.033 and 0.099) compared to (0.126) of (0.382 and 0.109) mm thickness. The same PCEs variance proportion was observed from the results of Table 4.61 with an outstanding (0.741 %) of (0.164mm) receptive layer thickness. However, the (0.541 V) potential generated by (0.109mm) thick layer improved compared to (0.493 V) of (0.382 mm)

with (0.922 V) outstanding for (0.164 mm) layer thickness. The rate of charge carriers transition was proportional to the potential observed. The parameter variations was attributed to the (C_X/I/KI) receptive electrodes thickness charge carriers transisting paths imperfections. A study by Jena *et al*. (2019) noted that imperfections between constituents particles interfaces interfered with the propagating charged species.

Table 4.62: Potential (V_{OC}) - Time characteristics of (I_2/KI/C_x) receptive layer thickness varied employing constant 0.136mm (Sb/Ca/Mn/Ag-TiO_2) photoactive layer

Time/ Min	**Potential(V_{OC}) ($\pm$0.005) V**			
	Z_6,d_1 (0.109mm)	**Z_6,d_2 (0.164mm)**	**Z_6,d_3 (0.273mm)**	**Z_6,d_4 (0.382mm)**
0	0.541	0.922	0.625	0.412
1	0.435	0.812	0.51	0.493
3	0.415	0.712	0.485	0.45
7	0.405	0.638	0.47	0.372
11	0.395	0.59	0.475	0.358
17	0.448	0.546	0.438	0.314
30	0.372	0.538	0.38	0.281
33	0.295	0.514	0.36	0.259
45	0.275	0.508	0.26	0.198
51	0.235	0.495	0.24	0.167
57	0.216	0.493	0.235	0.146
60	0.212	0.487	0.231	0.143

A graphical presentation of potential against time of the data in Table 4.62 was made as shown in Figure 4.48.

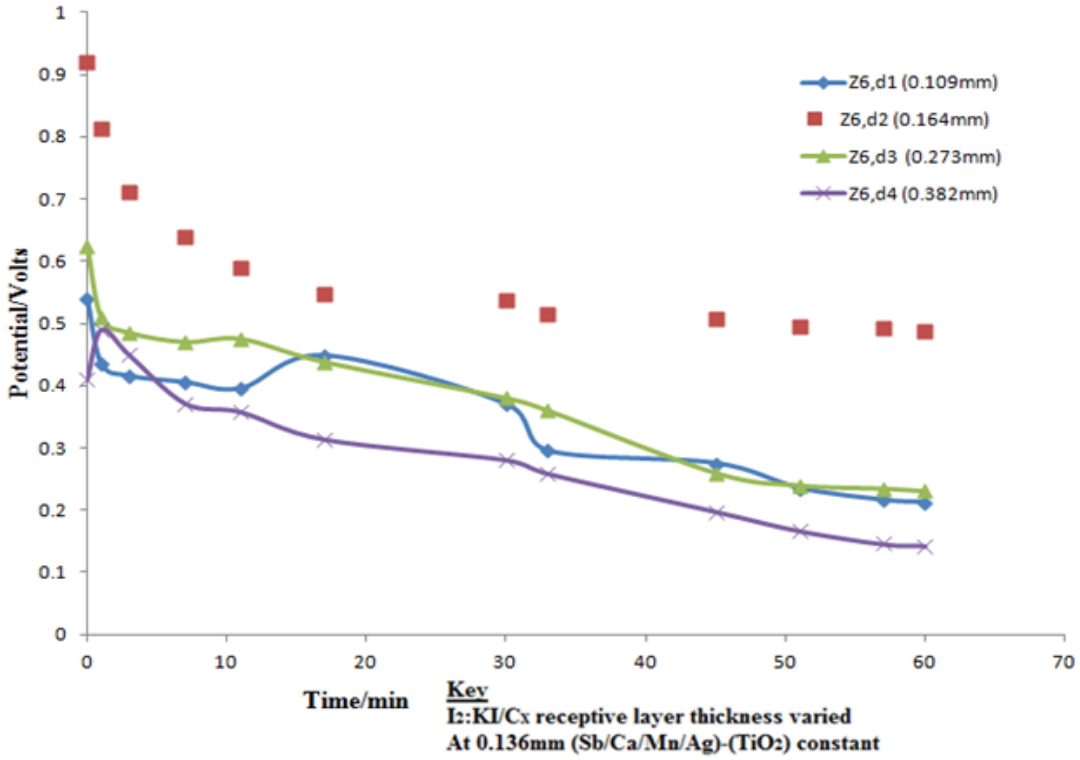

Figure 4.48: Potential-Time characteristics of $C_x/I_2/KI$ receptive layer varied thickness employing constant (Sb/Ca/Mn/Ag)-TiO_2 photo active layer thickness on radiation delay

Figure 4.48 shows an exponential Z_6, d_2 (0.164 mm) dependence signal varied from (0.922 to 0.538) V in 30 minutes, with a negligible (-0.024 V) ramp voltage change between (30 - 33) minutes period. The stable (0.514 – 0.487) V progression was observed with (0.027) V settling zone for the next 27 minutes. Similar {(0.50 – 0.47) V and (0.435 – 0.405) V} were monitored between (0 - 7) minutes from the (0.273mm and 0.109 mm) layers. That was preceded by brief {-(0.115 and 0.03)} V transients between (0 - 1) minute respectively. Lengthy {(0.023) V and (0.372) V) ramp voltage signals above (0.372 and 0.261) V developed from (0.109 and 0.273) mm thick receptive layer during the experiment between {(11 - 30) and (7 - 45)} minutes respectively. That change was succeeded by reducing transient terminating at (0.212 and 0.231) V respectively. Exponential (0.081) V growth and (0.121) V decay was

observed Z_6,d_4 (0.382 mm) from {(0 -1) and (1 – 7)}minutes. The improved Z_6,d_2 (0.164)mm receptive layer potential delay was thought to be contributed by the minimized electron deprived holes migrating paths imperfections. A study by and Chandiran *et al*. (2014) indicated that improved steady charged particles dispersion different medium commensurated varying potential characteristics. A similar study by Jena *et al*. (2019) reported that variation of the basic components contributed to the internal path limitations and their compounded imperfections.

4.11.2 Receptive $C_X/I_2/KI$ layer thickness variation of organic (Rhodamine-TiO_2) luminescent solar cells

To investigate the effect of receptive layer varied thicknes due to Rhiodamine doped TiO_2, the fluorescent solar cells were characterized under minimum natural radiation. The generated (0.978 and 0.586) V open circuit and residual potentials difference respectively by the 0.136 mm photo active layer thickness were preferred. The monitored I-V characteristics and potential with time were presented in Table 4.63 and 4.64 respectively.

Table 4.63: I-V characterization of (I_2/KI/C_x) receptive layer thickness varied employing constant 0.136mm (Rhiodamine -TiO_2) photoactive layer on radiation delay

Cell (I_2/KI/C_x) layer thickness	$V_{(OC)}$ (V)	$I_{(SC)}$ (mA) ($\pm$0.001)	FF	PCE%
A_6, d_1 (0.109mm)	0.765	4.531	0.042	0.146
A_6, d_2 (0.164mm)	1.023	6.852	0.122	0.855
A_6, d_3 (0.273mm)	0.841	5.343	0.064	0.288
A_6, d_4 (0.382mm)	0.626	3.821	0.086	0.206

The comparable {0.382mm (I_2/KI/C_X)/ 0.136mm (Rhiodamine-TiO_2)} cell contributed to 0.086 fill factor in contrast to (0.64, and 0.42) of (0.109 and 0.273) mm thick receptive electrodes. This Indicated that useful power was appreciably facilitated by the electrodes homogeneity. The (0.082 and 0.06) % PCEs narrow margins was attributed to improved charged species density transiting rate. Ease of propagating higher (6.852) mA charge density was facilitated by the (0.164 mm) layer thickness with improved (0.122 and 0.855%) fill factor and power conversion efficiency. That was contributed by imperfections developed during the cell preparation process. Fabrication procedures were accompanied by different cell thickness sizing which adversely affected uniform charge distribution, and collection and recombination. Sai-Anand *et al.* (2016) reported that moderation of charge mobility was fundamental for electrons-hole pairs excitation and sustenance until they reach their recombination sites.

Table 4.64: Potential (V_{OC}) - Time characteristics of (I_2/KI/C_x) receptive layer thickness varied employing constant 0.136mm (Rhiodamine -TiO_2) photoactive layer on radiation delay

Time/ Min	Potential (V_{OC}) ($\pm$0.005)V			
	$A_{6,}$ d_1 (0.109mm)	$A_{6,}$ $_{d2}$ (0.164mm)	$A_{6,d3}$ (0.273mm)	$A_{6,}$ $_{d4}$ (0.382mm)
0	0.765	0.978	0.841	0.626
1	0.671	1.02	0.817	0.593
3	0.556	0.975	0.799	0.481
7	0.438	0.943	0.661	0.369
11	0.425	0.907	0.593	0.354
17	0.393	0.869	0.489	0.345
30	0.331	0.711	0.457	0.333
33	0.299	0.683	0.433	0.324
45	0.251	0.612	0.366	0.312
51	0.235	0.597	0.315	0.233
57	0.233	0.588	0.289	0.225
60	0.231	0.581	0.291	0.211

From the results recorded in Table 4.64, a graphical presentation was made as shown in Figure 4.49.

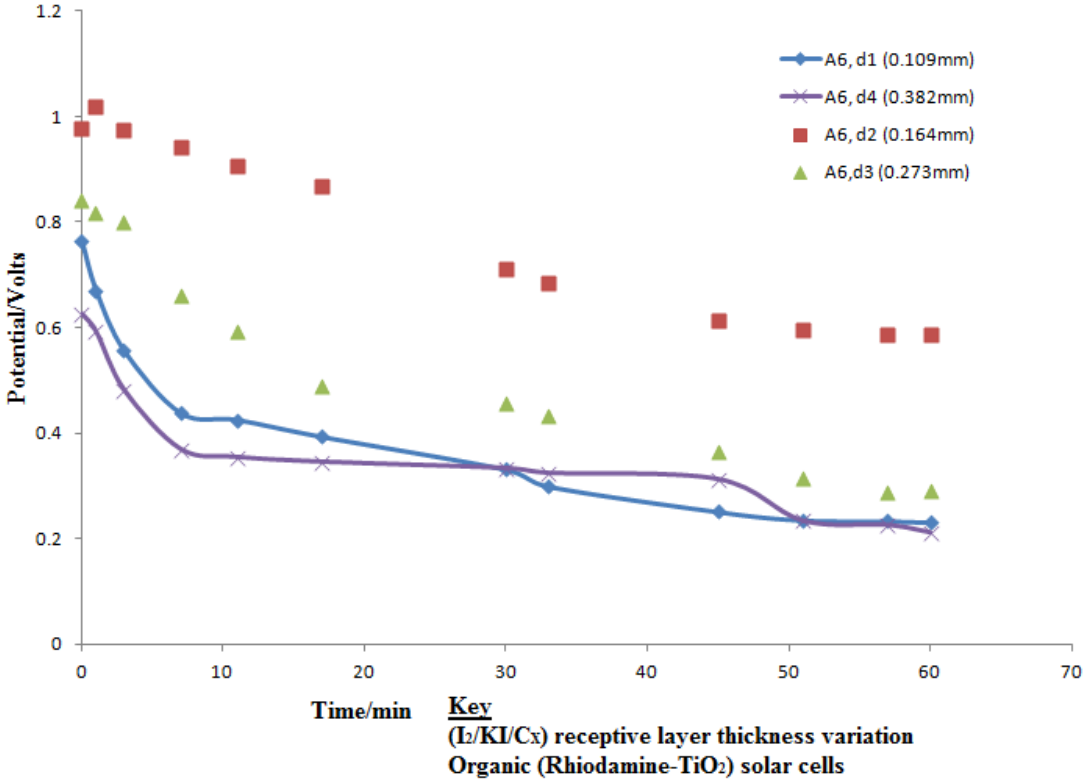

Figure 4.49: Potential-Time characteristics of $C_x/I_2/KI$ receptive layer varied thickness employing constant 0.136mm (Rhodamine-TiO_2) photoactive layer on radiation delay

Figure 4.49 shows an abrupt voltage increase characterized by (0.042) V amplitude sine wave feature and a short (0.032)V stable response observed from A_6,d_2 (0.164mm) thick layer sample between {(0-1) and (3 - 7)}minutes interval. The reducing (0.232) V sine wave voltage tail signal was observed between (7-30) interval. That characteristic was ensued by a hyperbolic (0.125) V declining response in the last (30-60) minutes settling period terminating at 0.586 V residual potential. Stable (0.384, 0.273 and 0.340) V hyperbolic potential difference signals were generated by (0.273, 0.382 and 0.109) mm receptive layers dimensions between {(0-30) and (0-11)} minutes respectively. Negligible negative [(0.021, 0.032 and 0.068) V change occurred between {(30 - 45), (30-33) and (7-11) minutes due to {(0.382, 0.109 and 0.273)} mm thick layers before settling at (0.211, 0.231 and 0.291) V.

The declining potential difference was attributed to non-linear energy barrier heights within the electrode. Irregular steeply declining profiles were attributed to non-uniformity in ohmic paths through which the migrating charge carriers transited. A study by Chowdhury and Balasubramanian (2017) noted that energy barrier heights promoted ohmic contact in the waveguides. The anode layer resulted to inefficient collection and minimized charge recombination at the receptive /active layers interface (Chowdhury & Balasubramanian, 2017). Proximity to optimization initiated energy balancing and complemented for improved excitons dissociation into free charge carriers (Wang & Zhan, 2016). The precise electrodes curtailed opposition to charge migration and escalated surface recombination (Zhang *et al.*, 2020).

4.11.3 Receptive $C_X/I_2/KI$ layer thickness variation of organic (Flourene-TiO_2) luminescent solar cells

To investigate the effect of varied ($C_X/I_2/KI$) receptive layer thickness to organic flourene -TiO_2 solar cell performance, four cells were prepared and their I-V together with potential against time characteristics presented in Table 4.65 and 4.66. The (0.935 and 0.581) V open circuit and delayed potential differences respectively generated by the OFSC were preferred for the constant L_6, C_2 (0.136 mm) photoactive layer dimension.

Table 4.65: I-V characterization of C_X/I_2/KI receptive layer varied thickness employing constant 0.136mm (Flourene - TiO_2) photoactive layer thickness on radiation delay

Cell (I_2/KI/C_x) layer thickness	$V_{(OC)}$ (V)	$I_{(SC)}$ (mA) ($\pm$0.001)	FF	PCE%
L_6, d_1 (0.109mm)	0.631	4.382	0.259	0.716
L_6, d_2 (0.164mm)	0.935	7.253	0.307	2.317
L_6,d_3 (0.273mm)	0.667	5.861	0.179	0.699
L_6,d_4 (0.382mm)	0.612	4.352	0.147	0.392

Table 4.65 shows flourene doped FSCs varying generated (0.304, 0.268 and 0.323) V potential margins as the (0.109, 0.173 and 0.382) mm thickness receptive layers increased referenced to relative to (0.935) V of (0.164) mm thickness. Proportional (2.871, 1.392 and 2.401) mA gaps charge transfer rates were observed referenced to 7.253mA short circuit current (I_{SC}) of (0.164) mm layer. The derived (0.416 and 2.821 %) FF and PCE parameters resulted due to (0.164 mm) thick anode layer. Increased depletion junctions hindered considerably active transition of charged species to the electron replenishing centres. A study by Laquai *et al*. (2015) noted that charged species transition between interfacing bilayers contributed to varieties of electrical properties in the entire device.

Table 4.66: Potential Difference (V_{OC}) –Time characteristics of $C_x/I_2/KI$ receptive layer varied thickness employing constant 0.136mm (Flourene - TiO_2) photoactive layer thickness on radiation delay

Time /min	**Potential(V_{OC}) ($\pm$0.005)V**			
	$L_{6,d1}$ (0.109 mm)	**$L_{6,d2}$ (0.164 mm)**	**$L_{6,d3}$ (0.273 mm)**	**$L_{6,d4}$ (0.382 mm)**
0	0.63	0.935	0.667	0.612
1	0.621	0.933	0.658	0.591
3	0.589	0.897	0.622	0.565
7	0.528	0.868	0.609	0.547
11	0.459	0.743	0.593	0.449
17	0.401	0.653	0.542	0.441
30	0.397	0.622	0.499	0.357
33	0.385	0.619	0.485	0.333
45	0.341	0.597	0.429	0.3
51	0.312	0.591	0.408	0.295
57	0.303	0.583	0.39	0.273
60	0.301	0.579	0.37	0.271

The graph illustrating the varied receptive electrodes thickness response of the Flourene-TiO_2 solar cell photo electric behaviour was made as presented in Figure 4.50.

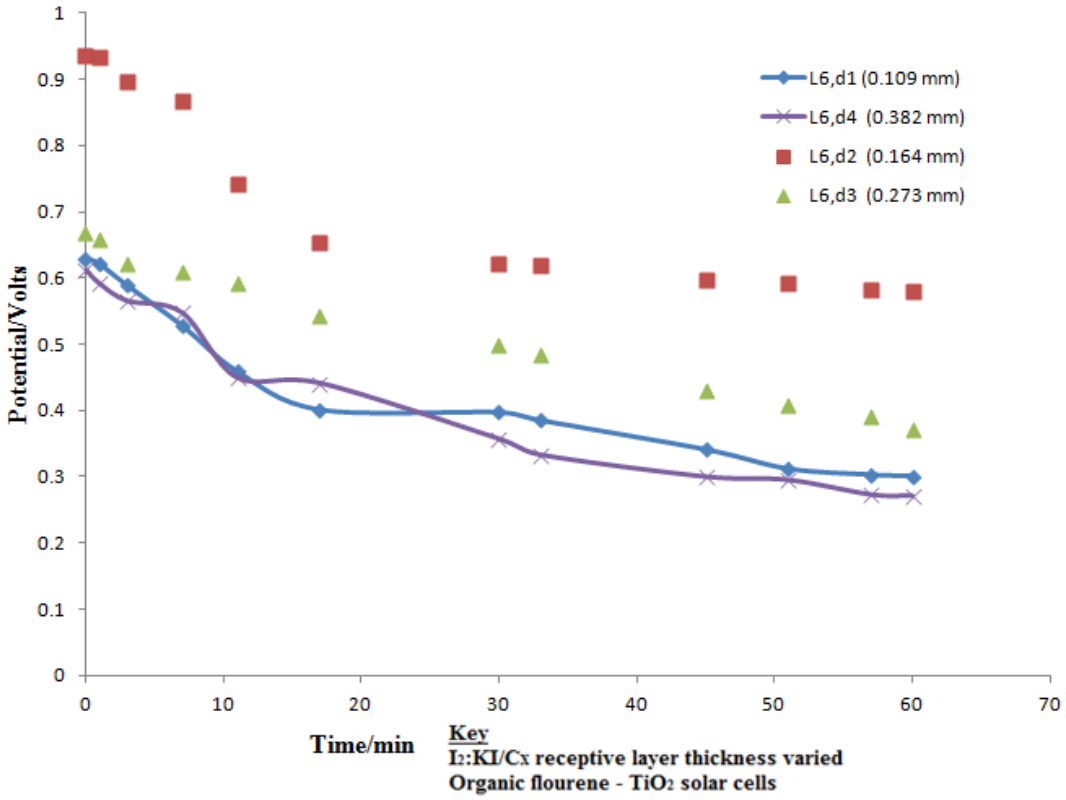

Figure 4.50: Potential-Time characteristics of Cx/I_2/KI receptive layer thickness variation employing constant 0.136mm (Flourene-TiO_2) photoactive layer on radiation delay

Figure 4.50 shows varying (0.246) V magnitude depolarization states signals between (7-60) minutes delay time of Flourene-TiO_2 doped FSCs receptive (C_X/I_2/KI) layer (0.164) mm thickness terminating at (0.581) V delayed potential. Similar varying (0.110 and 0.224) V magnitude signal states conditions were observed on (0.273 and 0.109) mm layer varied thicknesses, between {(7-30) and (1-30)} minutes delay time. Defected excited varied charge carrier densities at different wavelengths resulted to the preceding conditions of (0.067 and 0.009) V votage signal states at {(0-7) and (1-0)} minutes interval. Declining (0.129) V ramp voltage delayed characteristic ensued the (0.273) mm thick layer for the last (30-60) minutes. The (0.109) mm layer, (0.056) V voltage decreasing ramp condition occurred for 15 minutes settling at varied (0.341- 0.301) V for the last 15 minutes of the experiment. The (0.283) mm layer had

varying ramp and depolarizing conditions throughout the experiment terminating at (0.271) V delay potential.

The d- defects radiated optical energy resonated at varying wavelengths which was sustained throughout the experiment. This resulted to varied charge species excited states depicting gradual potential difference diminishing conditions. The overlaying each other profiles was contributed to overlapping bandwidth radiations with varied intensities A study by Hädrich *et al*. (2016) noted that excitation of high intensity short wavelength lasted for a shorter period leaving long wavelength optical energy radiating molecular ions. Reports by Alighanbari *et al.* (2018) indicated that momentum of ionized species exhibited comparable spin conditions of varied spectrum intensities due to localized state populations.

4.11.4 Receptive Cx/I2/KI layer thickness variation of organic (Allicin-TiO2) luminescent solar cells

Operation lifetime of organic Allicin-TiO_2 luminescent solar cell was investigated by varying the (C_X/I_2/KI) receptive layer thickness holding the Q_6, C_2 (0.136) mm photo active layer constant. That OFSC whose highest (0.85 and 0.419) V open circuit and residual potentials respectively were preferred at 0.136 mm photo active layer mass ratio. Table 4.63 and 6.64 shows the I-V and potential against time characteristics observed clear daylight and diminished natural radiation environments.

Table 4.67: I-V characterization of $C_x/I_2/KI$ receptive layer varied thickness employing constant 0.136mm (Allicin- TiO_2) photoactive layer thickness on radiation delay

Cell ($I_2/KI/C_x$) layer thickness	**$V_{(OC)}$ (V)**	**$I_{(SC)}$ (mA) ($\pm$0.001)**	**FF**	**PCE%**
Q_6, d_1 (0.109mm)	0.582	4.431	0.205	0.529
Q_6, d_2 (0.164mm)	0.853	6.374	0.271	1.473
Q_6,d_3 (0.273mm)	0.641	3.872	0.207	0.514
Q_6,d_4 (0.382mm)	0.514	4.363	0.136	0.305

The (0.109 and 0.273) mm thick receptive layers, recorded (0.205 and 0.207) fill factors disperities with wide (4.431 and 3.872) mA short circuit currents (I_{SC}) descrepancies were presented in Table 4.67. Similar (0.582 and0.641) V trend was observed in potential (V_{OC}) gaps. Cell Q_6, d_4 (0.382 mm) presented the lowest output and derived parameters. However, cell Q_6,d_2 (0.164 mm) presented improved (0.853 and 6.374) output potential (V_{OC}) and short circuit current (I_{SC}) and (0.271 and 1.473%) fill factor and power conversion efficiency. Lack of balance between the electron replenishing and the charge supplying layers contributed to the parameters disparity. A research by Hermes *et al*. (2018) noted that electrons were transported smoothly in the device without significant barriers that decreased recombination under short circuit conditions

Table 4.68: Potential (V_{OC}) –Time characteristics of C_x/I_2/KI receptive layer varied thickness employing constant 0.136 mm (Allicin- TiO_2) photoactive layer thickness

Time/ Min	Potential(V_{OC}) ($\pm$0.005)V			
	$Q_{6,d1}$ (0.109mm)	$Q_{6,d2}$ (0.164mm)	$Q_{6,d3}$ (0.273mm)	$Q_{6,d4}$ (0.382mm)
0	0.58	0.85	0.64	0.51
1	0.525	0.799	0.625	0.425
3	0.44	0.738	0.598	0.399
7	0.385	0.598	0.435	0.374
11	0.322	0.554	0.541	0.343
17	0.319	0.526	0.372	0.398
30	0.294	0.487	0.347	0.238
33	0.288	0.452	0.341	0.197
45	0.276	0.451	0.317	0.156
51	0.212	0.439	0.278	0.156
57	0.208	0.42	0.245	0.152
60	0.196	0.419	0.238	0.148

The energy mismatch of the four cells shown in Table 4.68 was analysed and presented as shown in Figure 4.51.

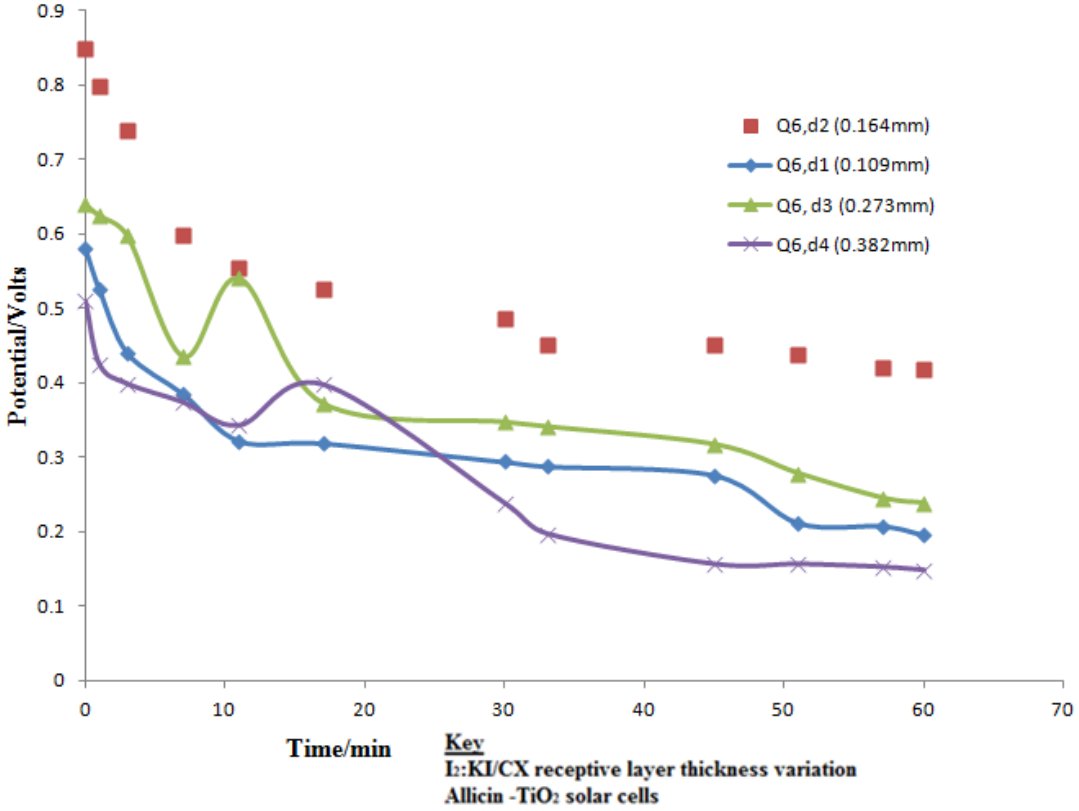

Figure 4.51: Potential-Time characteristics of C_X/I_2/KI receptive layer varied thickness employing constant 0.136mm (Allicin-TiO_2) photo active layer on radiation delay

Figure 4.51 shows hyperbolic varying (0.331, 0.200, 0.091 and 0.242) V at {(0-60), (11-33), (7-30) and (17-45) minutes of (0.164, 0.273, 0.109 and 0.382) mm allicin-TiO_2 (C_X/I_2/KI) receptive layer. The sinusoidal characterized (0.163 and 0.106) V varying magnitude voltage signals were generated due to (0.273) mm layer between [(3-11) and (7-17)] minutes. Similar features with varying (0.055) V voltage signal were exhibited due to the (0.382) mm thick varied receptive layer between (11-21) minutes. Different (0.042 and 0.075) V voltage amplitude ramp responses were generated between {(0-3) and (45-60)} minutes by (0.273) mm layer thickness terminating at 0.238 V delayed potential. Similar conditions with intermittent changes were identified from (0.382 and 0.109) mm layer signals, terminated at (0.148 and

0.109) V respectively. Different thicknesses were thought to accommodate varied (S=O and S-S) disulfide groups with diverse homogeneity and impediments. A study Hermes *et al*. (2018) noted that divergent charge carrier densities conveyance encountered significant barriers resulting recombination variance under short circuit conditions. A study by Bi *et al.* (2020) noted that stable states above 80% complementary intervals were observed when the counter electrode thicknesses was varied to 28% of their initial mass.

4.11.5 Receptive C_X/I_2/KI layer thickness variation of organic (Gingerol-TiO_2) luminescent solar cells

The conductivity of four organic fluorescent Gingerol-TiO_2 luminescent solar cells receptive electrodes were evaluated and the potential - time photo activated characteristics recorded as presented in Table 4.69. The R_6, C_2 fluorescent solar cell whose (0.864) V and (0.489) V open circuit and residual potentials respectively was opted with the constant 0.136mm thickness photoactive layer.

Table 4.69: I-V characterization of C_X/I_2/KI receptive layer varied thickness employing constant 0.136mm (Gingerol-TiO_2) photoactive layer thickness on radiation delay

Cell (I_2/KI/C_x) layer thickness	$V_{(OC)}$ (V)	$I_{(SC)}$ (mA) ($\pm$0.001)	FF	PCE%
R_6, d_1 (0.109mm)	0.555	3.824	0.241	0.511
R_6, d_2 (0.164mm)	0.864	5.842	0.253	1.277
R_6,d_3 (0.273mm)	0.826	5.313	0.134	0.588
R_6,d_4 (0.382mm)	0.429	4.533	0.113	0.219

From the results of Table 4.69, R_6,d_3 (0.273mm) receptive layer contributed to (0.134 and 0.588%) fill factor and PCE respectively compared to (0.241 and 0.511%) derived parameters of (0.109 mm) cell dimensions. The moderating {(0.826V and 5.313mA) and (0.555V and 3.824 mA)} output parameters were observed. The (1.277 and 0.588) % wide gap resulted to {(0.864 and 0.826) V and (5.842 and 5.313) mA} output parameters small margins. This indicated that the relatively wide (0.253 and 0.134) fill factors difference contributed majorly to their PCEs diversity. Charge restrictions across bilayers interfaces was thought to consolidate the different properties of C_X/I_2/KI varied material ratios. Reports by Kavitha and Kumar (2019) indicated that presence of ohmic contacts between interfacing surfaces contributed to varying resistance in the charge transiting paths. That introduced channels of diverse impediments upto the charge replenishing sites. A study by Anja *et al*., (2014) noted that moderated point resistances for asymmetrical layer dimensions contribute contrasting potential energy than definite resistance regions.

Table 4.70: Potential (V_{OC})–Time characteristics of C_x/I_2/KI receptive layer varied thickness employing constant 0.136mm (Gingerol-TiO_2) photoactive layer thickness

Time/ Min	Potential (V_{OC}) ($\pm$0.005)V			
	$R_{6,d1}$ (0.109mm)	$R_{6,d2}$ (0.164mm)	$R_{6,d3}$ (0.273mm)	$R_{6,d4}$ (0.382mm)
0	0.555	0.864	0.826	0.497
1	0.493	0.854	0.812	0.432
3	0.437	0.809	0.792	0.368
7	0.381	0.764	0.787	0.355
11	0.354	0.719	0.627	0.313
17	0.361	0.678	0.609	0.267
30	0.333	0.624	0.567	0.271
33	0.327	0.593	0.473	0.264
45	0.319	0.568	0.417	0.231
51	0.306	0.538	0.397	0.227
57	0.258	0.498	0.381	0.214
60	0.236	0.489	0.374	0.197

The influence of gingerol-TiO_2 solar cell varied thicknesses receptive electrodes on potential output was presented graphically as shown in Figure 4.52.

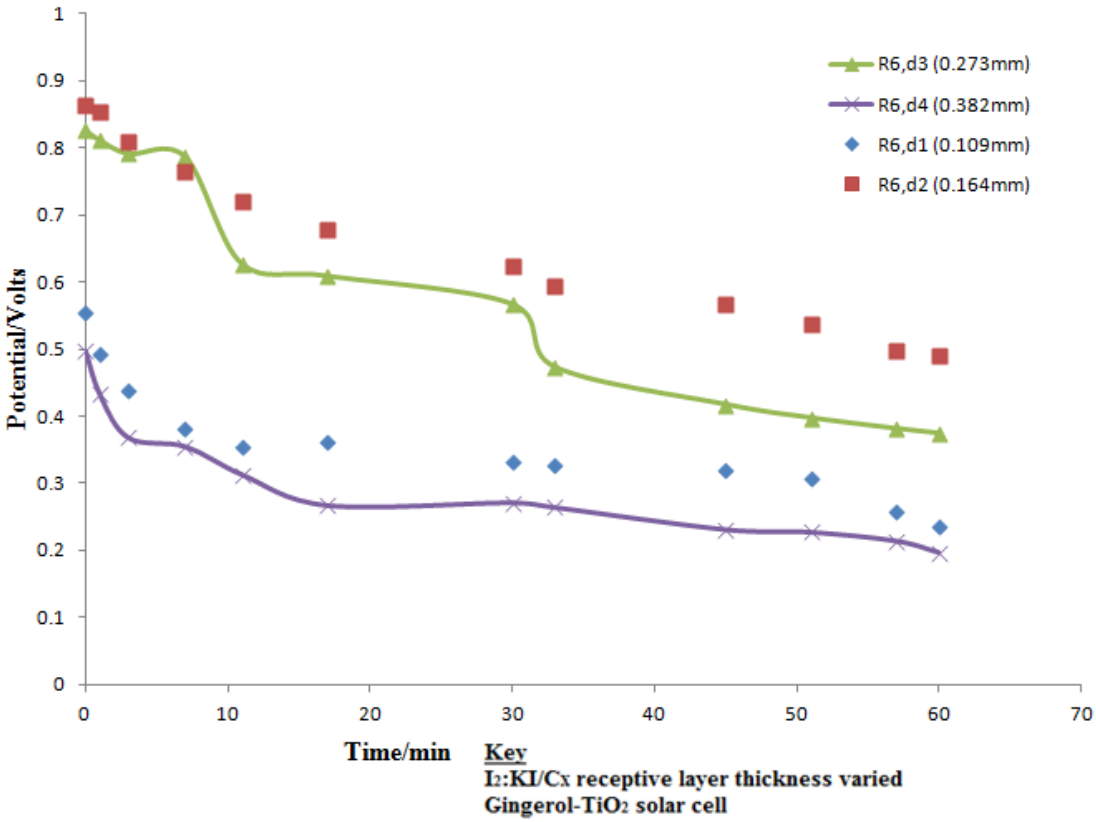

Figure 4.52: Potential-Time profiles of $C_x/I_2/KI$ receptive layer thickness variation employing constant 0.136mm (Gingerol- TiO_2) photoactive layer on radiation delay

Figure 4.52 shows sinusoidal (0.055, 0.013 and 0.049) responses for (Gingerol- TiO_2) OFSCs (0.164, 0.273 and 0.382) mm varied receptive layer thicknesses in (0-3), (3-7) and (4-11) minutes. Ramp (0.034, 0.094) V conditions were observed between [(0-3) and (30-33)] minutes interval due to (0.273) mm thick layer. The (0.220, 0.142 and 0.084) V amplitude voltage hyperbolic signal features were generated between {(0-30), (0-7) and (7-30)} minutes by (0.273 and 0.382) mm receptive thick layers terminating at (0.374 and 0.197) V potential delay by the end of the experiment. Similar varying (0.320 and 0.319) V conditions were observed due to (0.164 and 0.109) mm layers between [(3-60) and (0-60)] minutes terminating at (0.489 and 0.319) V delayed potential. The delayed potential was observed to improve

proportionally to layer thickness up to a point of consensus when a sudden deviation occurred. That was attributed to favorable migrating paths for the electronic particles as the thickness increased. A study by Ishida *et al.* (2016) indicated that bulk resistance formed pinhole-rich interface thereby weakening the interface contact between receptive and photoactive electrodes. That increase in thickness interfered with spinning momentum of molecular ions in organic fluorescent dopants (Ishida *et al*., 2016).

The effect of quinoline-TiO_2 OFSCs receptive (C_X/I_2/KI) layer varied thickness was investigated and the results of I-V and potential against time presented in Table 4.67 and 4.68. The $T_{6,}c_2$ (136mm) layer with (0.148) V and (0.045) V open circuit and residual potentials respectively was considered for receptive layer thickness variation.

Table 4.71: I-V characterization of C_X/I_2/KI receptive layer varied thickness employing constant 0.136mm (Quinoline -TiO_2) photoactive layer

Cell (Quinoline -TiO_2) thickness	**$V_{(OC)}$ (V)**	**$I_{(SC)}$ (mA) ($\pm$0.001)**	**FF**	**PCE%**
$T_{6,d2}$ (0.164mm)	0.148	2.898	3.819E-4	1.638E-5
$T_{6,d3}$ (0.273mm)	0.129	1.792	3.532E-4	8.165E-5
$T_{6,d4}$ (0.382mm)	0.103	1.781	2.204E-4	4.043E-5

Table 4.71 shows depreciating {(0.148, 0.129 and 0.103) V and (2.898, 1.792 and 1.781) mA, relative to (0.164, 0.273 and 0.382) mm appreciating reception layer thickness of (quinolone-TiO_2) OFSCs. However, the contrasting improving (3.819E-4, 3.532E-4 and 2.204E-4) fill factors resulted to degenerated (1.638E-4, 8.165E-5 and 4.043E-5)% PCEs. This was attributed to stable electron replenishing

components within the receptive layer. Reduction in the harvested charged species was thought to de-moderate excitation centers during the fabrication process. A study by Holliday *et al*. (2014) noted that variation of the photosensitive and receptive layers interfacing angles and their irregular interpenetrations affected photo sensitive dependent devices performance.

Table 4.72: Potential (V_{OC}) –Time characteristics of $C_X/I_2/KI$ receptive layer varied thickness employing constant (0.136mm Quinoline -TiO_2) photoactive layer thickness

Time/ Min	**Potential (V_{OC}) ($\pm$0.005)V**		
	$T_{6,d2}$ (0.164mm)	**$T_{6,d3}$ (0.273mm)**	**$T_{6,d4}$ (0.382mm)**
0	0.148	0.129	0.103
1	0.138	0.126	0.098
3	0.131	0.119	0.08
7	0.121	0.113	0.049
11	0.109	0.105	0.025
17	0.106	0.097	
30	0.102	0.076	
33	0.087	0.045	
45	0.073	0.03	
51	0.051		
57	0.045		
60			

The influence of ($I_2/KI/C_X$) receptive electrodes varied thickness on quinoline-TiO_2 solar cell potential output was presented graphically as shown in Figure 4.53.

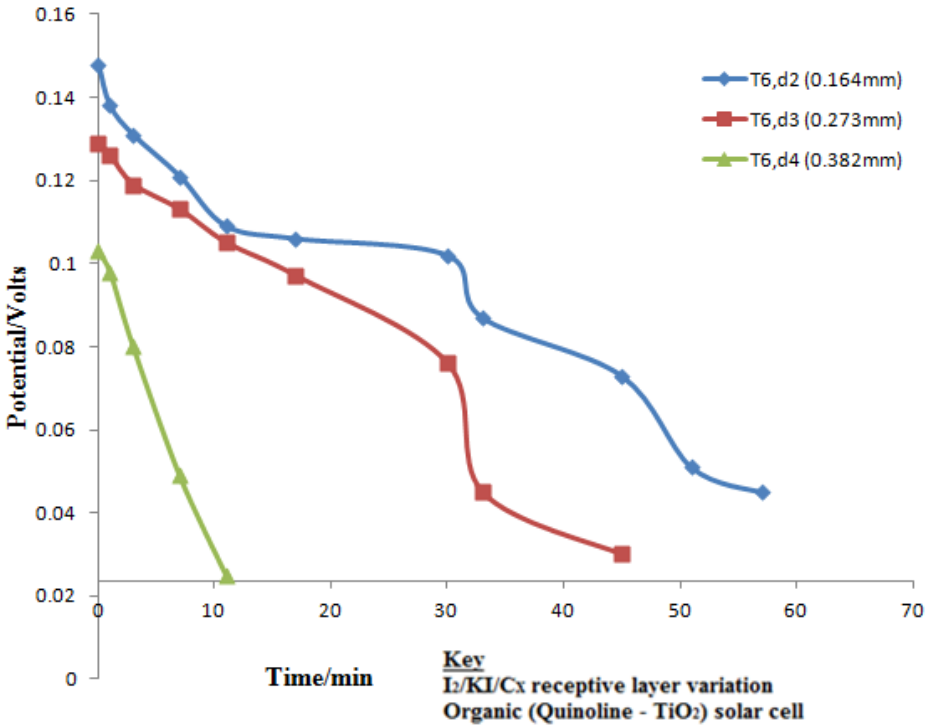

Figure 4.53: Potential-Time profiles of $C_X/I_2/KI$ receptive layer thickness variation employing constant 0.136mm (Quinoline- TiO_2) photoactive layer on radiation delay

Figure 4.53 shows gradually varying (0.015 and 0.036) V voltages signals due to the photon triggered field electrostatics generated by (0.164) mm varied ($C_X/I_2/KI$) receptive thick layer of (Quinoline- TiO_2) OFSCs terminating at 0.045 V delay potential. Similar progressive fluctuating (0.013 and 0.015) V features were observed between {(1-7) and (30-45)} minutes from (0.273) mm thick layer terminating at (0.03) V. The rapidly changing ramp (0.078) V was generated by the varied (0.382) mm thick layer terminating at 0.025 V delayed potential. The uniform bilayers interfacing was attributed to improved charge carriers excitation and the conductivity properties of the entire solar energy device. Injection of charge carriers between the bilayers shifted threshold voltages margins due to change in dipole moment. A research by Sonmezoglu and Akin (2020) reported that contact angle improved

current density and consequently reduced parasitic resistance for enhanced better capacitive dielectric and electrical properties of photovoltaic devices. The change in dipole moment considerably contributed to the charge carrier mobility with a negative shift consequence of threshold voltage over a wide range photovoltaic devices (Fahlman *et al.,* 2019).

The effect of neohesperidosyl -TiO_2 receptive layer thickness variation was investigated and the results presented in Table 4.73. The thickness of $K_{6,}d_2$ (136µm) solar cell was preferred due to its improved delayed potential with time constant of (0.269 and 0.115) V respectively.

Table 4.73: I-V characterization of C_x/I_2/KI receptive layer varied thickness employing constant 0.136mm (Neohesperidosyl -TiO_2) photoactive layer thickness on radiation delay

Cell (I_2/KI/C_x) layer thickness	**$V_{(OC)}$ (V)**	**$I_{(SC)}$ (mA) (±0.001)**	**FF**	**PCE%**
K_6, d_1 (0.109mm)	0.166	2.968	3.707E-4	1.826E-4
K_6, d_2 (0.164mm)	0.269	3.301	6.234E-4	5.536E-4
K_6,d_3 (0.273mm)	0.183	3.222	3.755E-4	2.214E-4
K_6,d_4 (0.382mm)	0.145	2.246	3.556E-4	1.158E-4

Table 4.73 presents relatively moderated {(3.301 – 2.246) mA and comparable (0.269 – 0.145) V} short circuit current (I_{SC}) and voltage (V_{OC}) generated by the varied receptive layer of neohesperidosyl doped TiO_2 FSCs. The improved output parameters of K_6, d_2 (0.164 mm) yielded low (6.234E-4 and 5.536E-4) FF and PCE derived parameters. That was evidence due to the presence of gaps between the charge

electrostatics and balancing of the electrons deprived holes. It was thought to consequently increase losses due to varied channels introduced by capacitive components in $C_X/I_2/KI$ layer. The charge transitions were thus misguided with diverse directions of charged species. A study by Wang *et al*. (2016) indicated that slow response was a consequence of low counter-ion species degraded diffusion coefficient. Irregular lamination creped internal properties and imminent solar dependent devices failure (Wang *et al*., 2016).

Table 4.74: Potential (V_{OC}) –Time characteristics of $C_x/I_2/KI$ receptive layer varied thickness employing constant 0.136mm (Neohesperidosyl - TiO_2) photoactive layer thickness

Time/ Min	Potential (V_{OC}) ($\pm$0.005)V			
	$K_{6.d1}$ (0.109mm)	$K_{6,d2}$ (0.164mm)	$K_{6,d3}$ (0.273mm)	$K_{6,d4}$ (0.382mm)
0	0.166	0.269	0.183	0.145
1	0.153	0.261	0.174	0.139
3	0.131	0.254	0.168	0.141
7	0.127	0.237	0.152	0.133
11	0.119	0.231	0.149	0.126
17	0.111	0.226	0.133	0.118
30	0.09	0.189	0.13	0.105
33	0.084	0.178	0.128	0.093
45	0.054	0.143	0.115	0.086
51		0.125	0.107	0.079
57		0.119	0.101	
60		0.115	0.096	

The effect of neohesperidosyl -TiO_2 solar cell varied thicknesses receptive electrodes on potential (V_{OC}) with time is presented graphically in Figure 4.54.

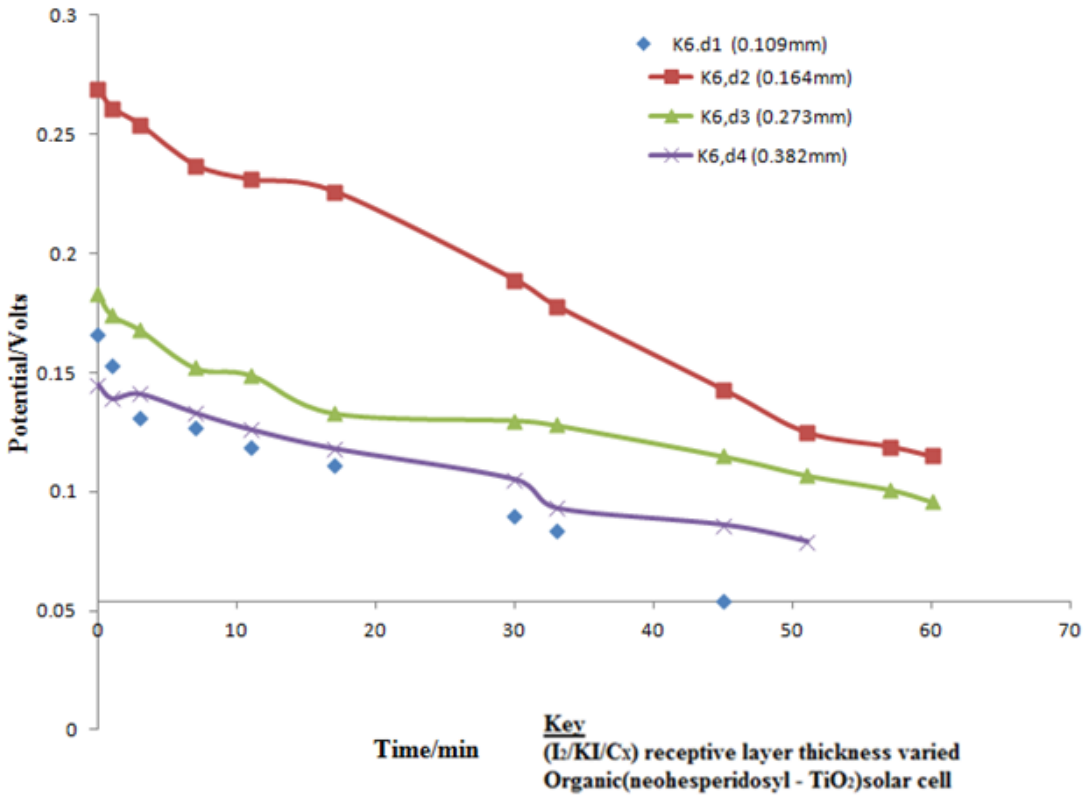

Figure 4.54: Potential-Time profiles of Cx/I2/KI receptive layer thickness variation employing constant 0.136mm (Neohesperidosyl - TiO_2) photoactive layer on radiation delay

Figure 4.54 shows (Neohesperidosyl - TiO_2) OFSCs varying hyperbolic (0.026, 0.024, 0.019, 0.047 and 0.004) V potential signals, for the {(0.0164, 0.273, 0.109 and 0.382)} mm receptive thickness layers, terminating at (0.115, 0.096, 0.054 and 0.079) V potential delay. These responses were observed at {[(3-15) and (45-57)], [(3-11) and (11-30)],(0-11) and (0-3)}minutes intervals. Varying (0.005 and 0.013) V amplitude parabolic featured voltage signals were observed between [(11-17) and (7-14)] minutes time delay. The improved potential delay was attributed to enhanced dissociated electron-hole pairs diffusion, complemented by the reformed thickness ability to moderate charged particles transition. Reports by Li *et al*. (2019) indicated that variation of solar dependent devices dimensions influenced ionic particals

distribution. According to Rahman *et al.* (2018) the thickness of photovoltaic devices were controlled to maintain charge carriers diffusion for enhanced charge transition.

4.12 Photo electric response of optimized luminescent solar cells in terms of thicknesses

The disparity in the open circuit potential (V_{OC}) against Time obtained from the (Z_6, A_6, L_6, Q_6, R_6 T_6 and K_6) luminescent solar cells of varied photo active and the receptive electrodes thicknesses were considered to fabricate the luminescent solar cells whose radiation delay characteristics were monitored and recorded as presented in Table 4.75.

Table 4.75: Potential (V_{OC}) - time characterization of the optimized Luminescent Solar Cells

Time/ Min	Potential(V_{OC}) ($\pm$0.005)V						
	$Z_{6,e}$ (0.136/ 0.164)mm	$A_{6,e}$ (0.136/ 0.164)mm	$L_{6,e}$ (0.136/ 0.164)mm	$Q_{6,e}$ (0.136/ 0.164)mm	$R_{6,e}$ (0.136/ 0.164)mm	$T_{6,c2}$ (0.136/ 0.164)mm	$K_{6,2}$ (0.136/ 0.164)mm
0	0.921	0.998	0.965	0.856	0.864	0.382	0.469
1	0.772	0.942	0.923	0.759	0.847	0.343	0.407
3	0.664	0.895	0.867	0.638	0.781	0.289	0.338
7	0.573	0.815	0.772	0.538	0.714	0.211	0.263
11	0.532	0.744	0.713	0.487	0.659	0.173	0.231
17	0.515	0.679	0.645	0.453	0.613	0.146	0.21
30	0.503	0.621	0.586	0.444	0.564	0.121	0.182
33	0.5	0.615	0.577	0.442	0.557	0.114	0.178
45	0.491	0.596	0.568	0.441	0.548	0.095	0.156
51	0.486	0.587	0.561	0.436	0.538	0.081	0.144
57	0.483	0.584	0.559	0.432	0.528	0.073	0.135
60	0.478	0.586	0.556	0.428	0.525	0.069	0.125

The observed potentials of the moderated (TiO_2 luminescent material) mass with their optimized thicknesses FSCs exhibited in Table 4.75 were presented graphically in Figure 4.55**.**

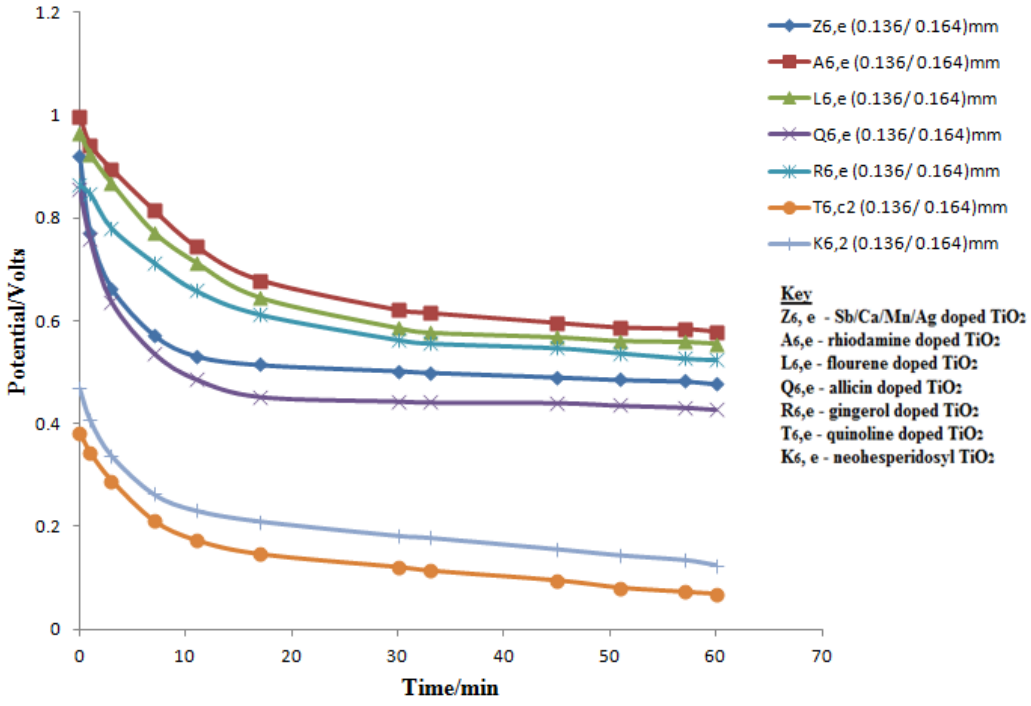

Figure 4.55: Potential decay profiles of the Optimized Luminescent Solar cells

The most improved potential (Voc) - time response of ($Z_{6,e}$, $A_{6,e}$,$L_{6,e}$,$Q_{6,e}$,$R_{6,e}$,$T_{6,e2}$ and $K_{6,e2}$)

luminescent solar cells presented in Figure 4.55 shows that rhiodamine in ($A_{6,e}$) generated the highest 0.998V potential V_{OC}, yielding (FF and efficiency) of (0.307 and 2.317%) respectively, with residual retention of 0.579V open circuit potential(V_{OC}) observed for 60 minutes. The fluorescence associated to (C=O) and (C=N) functional groups in the pink highlighter dye active structure was excited at (1636.63 and 1963.37) cm^{-1} peaks wavenumbers. Voltage signals generated by ($Z_{6,e}$ and $Q_{6,e}$) strongly dropped in the first few minutes due to d-d traps filling, resulting to significant loss of photoluminescence in the LSCs. This was in agreement with studies conducted by Kan *et al.* (2020) which noted that optimized rhiodamine face orientation and improved crystallinity in their blend films, lead to PVs higher and more balanced charge transportation for improved potentials and efficiency.

The (Flourene, Sb/Ca/Mn/Ag, Gingerol, Allicin) LSCs were observed to generate (0.965, 0.921, 0.864, 0.856) V highest open circuit potentials with (7.351, 6.517, 6.637 and 6.795) mA I_{SC} yielding (FF and efficiency) of {(0.246, 1.745%), (0.265, 1.591%), (0.175, 1.003%) and (0.246, 1.745%) respectively.

The flourene functional groups shifted radiation from (1230– 1631,) cm^{-1} to (1825 - 2900) cm^{-1} frequency bands of (blue to red) colour transition which had a reasonably long excited state lifetime with favourable species stability. Li *et al.* (2019) reported that higher charge delocalization of the anion allowed induced stacking low transverse resistivity which resulted to improved performance. The disparities between the activation dopants of the luminescent cells (measured and derived parameters) fabricated in this study were as recorded in Table 4.76.

Table 4.76: Effect of inorganic/organic dopants on the optimized luminescent solar cells Parameters

Luminescent dopant	Key excitation band wavelengths cm^{-1}	**Isc (mA)**	**Initial Potential (Voc)**	**Residual potential (Voc) after 60 minutes**	**FF**	**PCE**
Sb/Ca/Mn/Ag ($Z_{6,e}$)	1385 - 2100	6.517	0.921	0.478	0.265	1.591
Rhiodamine ($A_{6,e}$)	1636.63 – 1963.37	7.562	1.023	0.586	0.416	2.821
Flourene ($L_{6,e}$)	1825-2900	7.351	0.965	0.556	0.307	2.317
Allicin ($Q_{6,e}$)	1631.81 - 2033.01	6.795	0.856	0.428	0.281	1.634
Gingerol ($R_{6,e}$)	1575 - 1631.63	6.637	0.864	0.525	0.175	1.003
Neohesperidosyl ($K_{6,c2}$)	3255.90 - 921.99	3.301	0.469	0.125	0.0006	0.0005
Quinoline ($T_{6,c2}$)	3247.22-1021.11	2.901	0.382	0.069	0.0005	0.0004

From the information recorded in Table 4.76, graphical presentations of dopant against delayed potential (V) was made as presented in Figures 4.56.

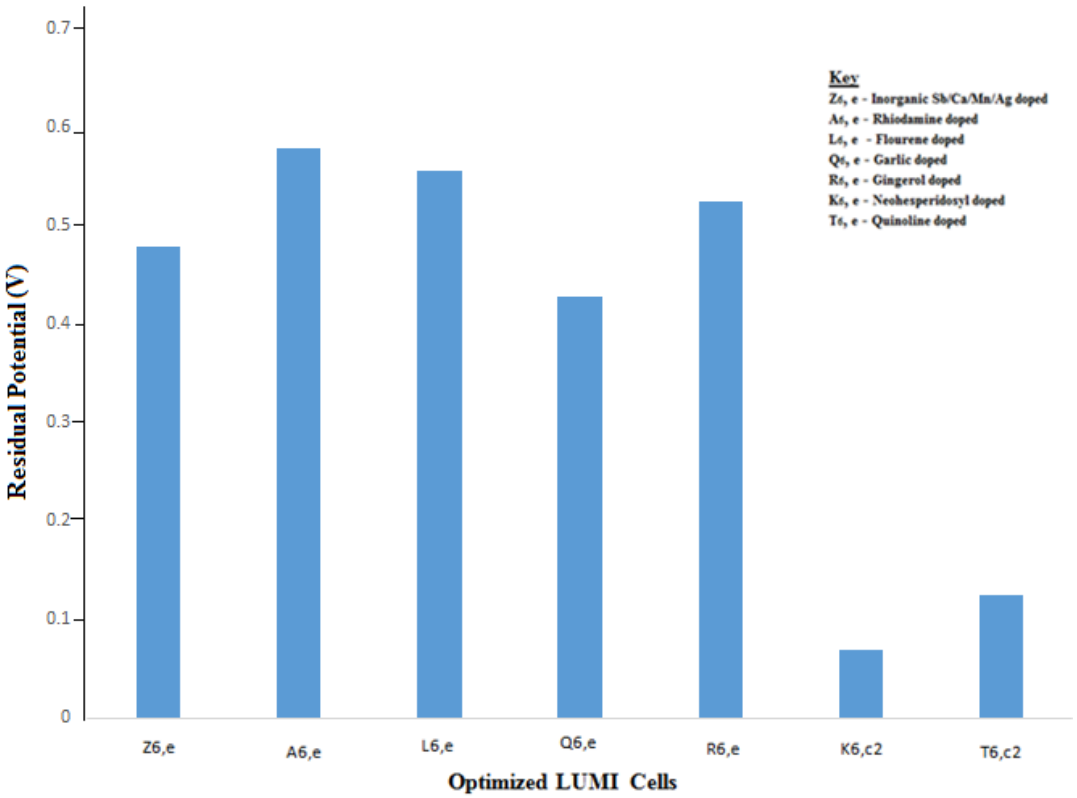

Figure 4.56: Influence of luminescent dopants on residual potential (V) of the LUMI cells

Figure 4.56 shows (0.101, 0.023, 0.151, 0.054, 0.510 and 0.454) V potential delay disparities contributed by the different (Z_6,e, L_6,e, Q_6,e, R_6, e, K_6, e and T_6, e) FSCs compared to 0.579 V of rhiodamine doped cell. The (Sb-PO_4, (Sb–O) complexes bands between 1650-2100 and 800-1000cm^{-1} offered (0.101) V lower than 0.579 V due (C-O, C-N and C-OH) in rhiodamine which delayed radiation by (2364.77, 2159.35 and 2033.97) cm^{-1} frequency bands in 60 minutes. The gap between the amount delayed by (neohesperidosyl and quinolone) compared to that of rhiodamine increased to (0.510 and 0.454) V with negligible (0.023 and 0.054) V difference of (flourene and gingerol). This was attributed to the ionic groups resonance capacity to shift the absorbed radiation to different wavelength for varied time constants. A study by Huang et al., (2014) noted that multiple defect states in solvents contributed to

improved quantum yield. According to Bi *et al.* (2016), noted that the amount of contribution to the luminescent dopants was guided majorly by the extent of band to-band recombination. Similar findings were reported by Borazan *et al.* (2019) of blended solar cells with 20wt % of (PCDTBT) luminescent material. However, the observation indicated that the stoke shift due rhiodamine active structure excited majority of charge carriers which resulted to the highest residual potential after 60 minutes of the experiments.

4.13 Summary of the Findings

In summary the inorganic Sb/Ca/Mn/Ag doped [Z_6,c_2 (0.136mm) and Z_6,d_2 (0.164mm] FSCs photoactive and receptive layers thicknesses, generated the highest[(0.712 and 0.306) and (0.922 and 0.487)] V open circuit (V_{OC}) and delayed potentials respectively. The corresponding short circuit currents (I_{SC}) were (6.38 and 6.381) mA with {(0.294 and 0.126) FF with (1.336 and 0.741) %} PCEs respectively. The organic rhiodamine doped [A_6,c_2(0.136mm and A_6,d_2(0.164mm] FSCs photoactive and receptive layers thicknesses, generated the highest[(0. 756 and 0.316) and (1.023 and 0.586)] V open circuit (V_{OC}) and delayed potentials respectively. The corresponding short circuit currents (I_{SC}) were (6.841 and 6.852) mA with {(0.223 and 0.122) FF with (1.153 and 0.855) %} PCEs respectively. The organic flourene doped [L_6,c_2(0.136mm and L_6,d_2(0.164mm] FSCs photoactive and receptive layers thicknesses, generated the highest[(0. 613 and 0.227) and (0.935 and 0.581)] V open circuit (V_{OC}) and delayed potentials respectively. The corresponding short circuit currents (I_{SC}) were (7.252 and 7.253) mA with {(0.311 and 0.416) FF with (1.383 and 2.821) %} PCEs respectively. The organic allicin doped [Q_6,c_2(0.136mm and Q_6,d_2(0.164mm] FSCs photoactive and receptive layers thicknesses, generated the

highest[(0. 672 and 0.263) and (0.853 and 0.419)] V open circuit (V_{OC}) and delayed potentials respectively. The corresponding short circuit currents (I_{SC}) were (7.252 and 6.374) mA with {(0.311and 0.271) FF with (1.383 and 1.473) %} PCEs respectively. The organic gingerol doped [R_6,c_2(0.136mm and R_6,d_2(0.164mm] FSCs photoactive and receptive layers thicknesses, generated the highest[(0. 653 and 0.278) and (0.864 and 0.489)] V open circuit (V_{OC}) and delayed potentials respectively. The corresponding short circuit currents (I_{SC}) were (6.53 and 6.374) mA with {(0.178 and 0.253) FF with (0.765 and 1.277) %} PCEs respectively. The organic quinoline doped [T_6,c_2(0.136mm and T_6,d_2(0.164mm] FSCs photoactive and receptive layers thicknesses, generated the highest[(0. 175 and 0.059) and (0.148 and 0.045)] V open circuit (V_{OC}) and delayed potentials respectively. The corresponding short circuit currents (I_{SC}) were (2.901 and 2.898) mA with {(7.892E-4 and 3.819E-4) FF with (4.007E-4 and 1.638E-5) %} PCEs respectively. The organic neohesperidosyl doped [K_6,c_2(0.136mm and K_6,d_2(0.164mm] FSCs photoactive and receptive layers thicknesses, generated the highest[(0. 221 and 0.054) and (0.269 and 0.0115)] V open circuit (V_{OC}) and delayed potentials respectively. The corresponding short circuit currents (I_{SC}) were (2.949 and 3.301) mA with {(7.628E-4 and 6.234E-4) FF with (4.971E-4 and 5.536E-4) %} PCEs respectively.

CHAPTER FIVE: CONCLUSION AND RECOMMENDATION

5.1 Conclusion

The inorganic (antimony, calcium hydroxide, manganese oxide and silver nitrates) powders were successfully synthesized and the organic (rhiodamine, allicin, gingerol, quinolone and neohesperidosyl) successfully extracted from their fresh organic complexes. The (Sb/Ca/Mn/Ag) inorganic semiconductor-metal (sc/m) hybrid interface nanostructure powder varied in colour from brown, light blue, blue to red before fading gradually under UV radiation observation. Rhiodamine produced greenish-yellow coloured radiation, as flourene exhibited a characteristic of violet – bluish flourescence radiation. Allicin progressively varied from blue, red and brown, while gingerol exhibited long yellow colouring under UV radiation with low aqueous solubility. Quinoline double-ring structure of benzene and pyridine rings fluorescenced with varied frequencies as neohesperidosyl showed highly blue emissive radiation when subjected to UV radiation sourced from a UV lamp. The chemical characterization revealed that the inorganic and organic dopants absorbed IR radiation at {(360 – 3750), (434.96-3950), (697.28-3750), (290.29-3850), (463.89-3850), (260.39-3750) and (273.90-3700)} cm^{-1} frequency bands respectively. Evidently the fabricated active solid TiO_2 based solar cell doped with different inorganic and organic fluorescent materials had voltage generation delay characteristics which has potential for application for a period of 60 minutes in a diminished natural radiation environment. The observed variation in potential difference delay against time indicated that there is potential in development of fluorescent photocell using TiO_2 solid {(Sb/Ca/Mn/Ag), flourene, allicin, gingerol, quinoline and neohesperidosyl,} together with aqueous rhiodamine solution in the (0.4: 0.05) mass and 50 % volume of rhiodamine for application at the point of use.

These ratios demonstrated outstanding performance of {(0.45, 0.44, 0.48, 0.601, 0.121, 0.168) and 0.195} V potential delay after 60 minutes in minimum natural radiation. The gingerol doped TiO_2 FSC (0.5 and 4) g mass ratio generated the highest 0.719 V (V_{OC}) and 0.601 V potential delay with (0.372 and 0.519%) fill factor and (PCE) respectively. Variation of thickness (0.071, 0.136, 0.227 and 0.318) mm TiO_2 doped with inorganic and organic fluorescent materials photo active electrodes thicknesses at constant (0.540) mm graphite based receptive layer generated fluctuating potential delays. The respective (0.308, 0.227, 0.263, 0.278, 0.059, 0.054 and 0.361) V residual potentials were observed from the TiO_2 doped solar cells. The TiO_2 rhiodamine doped (0.136/0.540) mm thick FSC, indicated the highest 0.756 V (V_{OC}) and 0.361 V potential delay with (0.223 and 1.153%) fill factor and PCE respectively.

The graphite based receptive (0.109, 0.164, 0.273 and 0.382) mm layers thicknesses prepared at constant (0.136) mm TiO_2 doped thickness photo active layer, generated varied delayed potentials. The changing (0.487, 0.579, 0.419, 0.489, 0.045, 0.115 and 0.581) V residual potentials were observed from the combined optimized 20% mass ratios which resulted to 0.164mm receptive and 0.136 mm photo active thick layers respectively. The (0.164/0.136) mm thick rhiodamine TiO_2 doped FSC generated the highest 0.998 V (V_{OC}) and (0.581) V potential delay with (0.122 and 0.855%) fill factor and PCE respectively. The 0.136 mm and 0.164 mm thicknesses of TiO_2 – doped FSCs and graphite respectively yielded the most improved (0.487,0.556, 0.428, 0.525, 0.125 and 0.069) V potential delay with {(0.265, 0.246, 0.281, 0.175, 6.0E-5 and 5.0E-5) and (1.591, 1.282, 1.745, 1.634, 1.003, 5.0E-4 and 4.0E-4)% fill factors and PCEs parameters, respectively. The optimized

rhiodamine TiO_2 – doped FSC thickness displayed the highest 1.023 V (V_{OC}) and 0.586 V potential delay with (0.416 and 2.821%) fill factor and PCE respectively. From the characterized cells, even at uniform radiation, the (V_{OC}) of the undoped TiO_2 solar cell differed in the level of the generated potential difference with varied residual voltage with time in diminished natural radiation. The highest open circuit potential (V_{OC}) and short circuit current density (J_{SC}) of 0.518 V and 0.868 mA/cm^2 were observed. These results confirmed that the dopants contributed to excitation of higher charge density. In conclusion, the inorganic and organic dopants applied in this study had promising properties for improving solar cell potential, current density and effective time of utilization in diminished radiation.

5.2 Recommendations

5.2.1 Radiation response of luminescent dopants

The study recommends that dopant synthesis should be expanded to enhance further d-orbitals splitting for improved charged species d→d transitions and transpose IR spectrum into fluorescence. Dopants blending strategy that establish multiple (triple and quadrature) conjugated bonds should be explored to curtail strainous narrow absorption bands. Characterization equipment that monitor selectively on specific colour variation with down-conversion of absorbed radiation should be investigated as opposed to the ordinally UV lamp that provided general view of colour variation.

5.2.2 Solar Dependent Fluorescent Cells Actualization

The study at hand was prone to optical energy instability relative to the output parameter conformities. Incident energy attenuation (reflection, scattering absorption

of radiation and refractive index) within the samples' matrix affected excited particles' lifetime and inhibited the FSCs improved constant output actualization. Further research is recommended to extend the dopants molecular size with less energy instability should be extended to achieve uniform potential difference with less attenuation. Matrices with more s-p anti-bonding coupling, strong defect tolerance and shallow point defects should be investigated for favourable band gap and reduced surface recombination. The applied fluorescent dopants failed to display fluorescence due to nonradiative activation. Dopant matrices that bond homogeneously should be investigated to reduce straining of active composites and minimise losses that lead to irregular scattering of absorbed radiation and enable excitation for improved charge carriers' density. The study finding observed that FSCs matrices are not independent of external energy interferences with a consequence of pigments lamping and altering composite absorptivity. Strategies to minimize intensity of such occurrences would minimize dominant binding energies and promote clear charge carrier guided paths to the outer surface for improved output parameters.

5.2.3 Variation of Titanium Dioxide: Dopant Quantities for Enhanced I-V and P-T Parameters

Investigation of wider dopants complexes ratios should be done to minimize recombination at the convergence within the solute and enhance quantum yield for higher charge carriers' densities excitation. Further investigate strategies that suppresses atomic non conformity that hinder processes of charge carriers' versatility. Such would promote three dimensional particals moments and supplement fluorescence lifetime in shallow and deep diffused centres.

5.2.4 Fluorescent Solar Cell Cathode: Anode Layers Thickness variation

The modified ratios relative to layer thicknesses should further be investigated to establish a strategy to promote higher donor – acceptor interdependence for higher photosensitivity response. This would improve photosensitivity and contribute to equitable charge alignment and transition. Such conditions would improve the photo active environment flexibility in diversified absorptivity and promote external electron transition from internal ionic lattice energy levels for attainment of critical terminal parameters. Relative dimensions with ambient conditions moderating pigments would balance FSCs interacting systems for uniform output parameters. Such compounded species relative cell dimensions would impede spectroscopy interference and translate to intramolecular polarization, due to the dipole: energy alignment.

However, with the results observed from (Sb/Ca/Mn/Ag, rhiodamine and flourene) inorganic and organic dopants offered favourable considerations for improved potential delay and time constant luminescent solar cells.

REFERENCES

Abderrazak, Y., Bhattacharyya, A., & Reiser, O. (2021). Visible-Light-Induced Homolysis of Earth-Abundant Metal-Substrate Complexes: A Complementary Activation Strategy in Photoredox Catalysis. *Angewandte Chemie International Edition*, 60(39), 21100-21115.

Adegbenro, A. (2016). *Comparison of novel and state of the art solar cells*. University of Kessel: Germany.

Ahmadi, M., Alves, B., Baker, C., Bertsche, W., Butler, E., Capra, A., Carruth, C., Cesar, C., Charlton, M., Cohen, S., Collister, R., Eriksson, S., Evans, A., Evetts, N., Fajans, J., Friesen, T., Fujiwara, M., Gill, D., Gutierre, A., Hangst, J., Hardy, W., Hayden, M., Isaac, C., Ishida, A., Johnson, M., Jones, S., Jonsell, S., Kurchaninov, L., Madsen, N., Mathers, M., Maxwell, D., McKenna, J., Menary, S., Michan, J., Momose, T., Munich, J. , Nolan, P., Olchanski, K., Olin, A., Pusa1, P., Rasmussen, C., Robicheaux, F., Sacramento, R., Sameed, M., Sarid, E., Silveira, M., Stracka, S., Stutter, G., So, C., Tharp, T., Thompson, J., Thompson, R., van der Werf, D. and Wurtele, J. (2017). Observation of the 1S–2S transition in trapped antihydrogen. *Nature*, *541*(7638), 506-510.

Ahmed, H., Doran, J., & McCormack, S. J. (2016). Increased short-circuit current density and external quantum efficiency of silicon and dye sensitised solar cells through plasmonic luminescent down-shifting layers. *Solar Energy*, *126*, 146-155.

Ahn, S., Jeong, S. H., Han, T. H., & Lee, T. W. (2017). Conducting polymers as anode buffer materials in organic and perovskite optoelectronics. *Advanced Optical Materials*, 5(3), 1600512.

Al-Alwani, M. A., Mohamad, A. B., Ludin, N. A., Kadhum, A. A. H., & Sopian, K. (2016). Dye-sensitised solar cells: Development, structure, operation principles, electron kinetics, characterisation, synthesis materials and natural photosensitisers. *Renewable and Sustainable Energy Reviews*, 65, 183-213.

Alexey, K., Casey, J., Rohan, R., Jan, G., Nino, L., David, F., Juri, Z. and Svetlana, A. (2016). Light- induced reversible change of roughness and thickness of photosensitive polymer brushes.University of North Carolina State: USA.

Alighanbari, S., Hansen, M. G., Korobov, V. I., & Schiller, S. (2018). Rotational spectroscopy of cold and trapped molecular ions in the Lamb–Dicke regime. *Nature Physics*, *14*(6), 555-559.

Alkiswani, M. (2015). *Spectrum conversion in solar cells industry: Novel model concept and steps towards commercialization*.

Ameta, R., Solanki, M. S., Benjamin, S., & Ameta, S. C. (2018). Photocatalysis. In *Advanced oxidation processes for waste water treatment* (pp. 135-175). Academic Press.

Anja, H., Christian, L., Chanwoo, P., Francesco, O., Francesco, B., Giancarlo, P., Stephan, M., Rainer, Wand Regina, D (2014).Spectroscopic Proof of the Correlation between Redox-State and Charge-Carrier Transport at the Interface of Resistively Switching Ti/PCMO Devices. *Advanced Materials*, 36 (3), 1521-4095.

Babu, B. H., Lyu, C., Yu, C., Wen, Z., Li, F., & Hao, X. T. (2018). Role of Central Metal Ions in 8-Hydroxyquinoline-Doped ZnO Interfacial Layers for Improving the Performance of Polymer Solar Cells. *Advanced Materials Interfaces*, 5(22), 1801172.

Baloch, A. A., Alharbi, F. H., Grancini, G., Hossain, M. I., Nazeeruddin, M. K., & Tabet, N. (2018). Analysis of photocarrier dynamics at interfaces in perovskite solar cells by time-resolved photoluminescence. *The Journal of Physical Chemistry C*, *122*(47), 26805-26815.

Barbooti, M. (Ed.). (2015). *Environmental applications of instrumental chemical analysis*. Apple Academic Press: New York.

Basnet, P., Anderson, E., & Zhao, Y. (2019). Hybrid Cu x O–TiO2 Nanopowders Prepared by Ball Milling for Solar Energy Conversion and Visible-Light-Induced Wastewater Treatment. *ACS Applied Nano Materials*, 2(4), 2446-2455.

Belisle, R. A., Jain, P., Prasanna, R., Leijtens, T., & McGehee, M. D. (2016). Minimal effect of the hole-transport material ionization potential on the open-circuit voltage of perovskite solar cells. *ACS Energy Letters*, 1(3), 556-560.

Belitz, H. D., & Wieser, H. (2013). Bitter compounds: Occurrence and structure-activity relationships. *Food Reviews International*, 1(2), 271-354.

Beng, S., Barkev, K., Trevor, I., and Gord, H. (2020). Synthesis, molecular and electron transport properties of 2-alkyltrinitrofluoren-9-ones. Canadian Journal of Chemistry, 63(1), 147-152.

Berkley, S. (2009). *The Fabrication and Characterization of Organic Solar Cells.* (Unpublished thesis, Texas University, Austin).

Bi, D., Tress, W., Dar, M. I., Gao, P., Luo, J., Renevier, C., ... & Hagfeldt, A. (2016). Efficient luminescent solar cells based on tailored mixed-cation perovskites. Science advances, 2(1), e1501170.

Bi, W., Wu, Y., Chen, C., Zhou, D., Song, Z., Li, D., Chen, G., Dai, Q., Zhu, Y. & Song, H. (2020). Dye sensitization and local surface plasmon resonance-enhanced upconversion luminescence for efficient perovskite solar cells. *ACS applied materials & interfaces*, 12(22), 24737-24746.

Borazan, I., Altin, Y., Demir, A., & Celik Bedeloglu, A. (2019). Characterization of organic solar cells using semiconducting polymers with different bandgaps. *Journal of Polymer Engineering*, 39(7), 636-641.

Caironi, M., Bird, M., Fazzi, D., Chen, Z., Di Pietro, R., Newman, C., ... & Sirringhaus, H. (2011). Very Low Degree of Energetic Disorder as the Origin of High Mobility in an n-channel Polymer Semiconductor. *Advanced Functional Materials*, 21(17), 3371-3381.

Campos-Fernández, C., Azofeifa, D. E., Hernández-Jiménez, M., Ruiz-Ruiz, A., & Vargas, W. E. (2011). Visible light reflection spectra from cuticle layered materials. *Optical Materials Express*, 1(1), 85-100.

Chain Conformations, Packing, and Electronic Couplings. *Advanced Materials*, 28(37):8197-8205.

Chandiran, A. K., Nazeeruddin, M. K., & Grätzel, M. (2014). *The Role of Insulating Oxides in Blocking the Charge Carrier Recombination in Dye-Sensitized Solar Cells. Advanced Functional Materials, 24(11), 1615–1623.*

Chatterjee, S., Webre, W. A., Patra, S., Rout, B., Glass, G. A., D'Souza, F., & Chatterjee, S. (2020). Achievement of superior efficiency of TiO2 nanorod-nanoparticle composite photoanode in dye sensitized solar cell. *Journal of Alloys and Compounds*, 826, 154188.

Chellamuthu, P., Naughton, K., Pirbadian, S., Silva, K. P. T., Chavez, M. S., El-Naggar, M. Y., & Boedicker, J. (2019). Biogenic control of manganese doping in zinc sulfide nanomaterial using Shewanella oneidensis MR-1. *Frontiers in Microbiology*, 10, 938.

Chen, B. & Wu, T. (2016). A mechanically and electrically self-healing graphite composite dough for stencil-printable stretchable conductors. *Journal of Materials Chemistry C*, 4(19), 4150-4154.

Chen, S., Walsh, A., Gong, X. G., & Wei, S. H. (2013). Classification of lattice defects in the kesterite Cu2ZnSnS4 and Cu2ZnSnSe4 earth-abundant solar cell absorbers. *Advanced materials*, 25(11), 1522-1539.

Chen, X., Xu, W., Song, H., Chen, C., Xia, H., Zhu, Y., ... & Zhang, J. (2016). Highly efficient LiYF4: Yb3+, Er3+ upconversion single crystal under solar cell spectrum excitation and photovoltaic application. *ACS Applied Materials & Interfaces*, 8(14), 9071-9079.

Chen, Y., Qu, Y., Zhou, X., Li, D., Xu, P., & Sun, J. (2020). Phenyl-bridged graphitic carbon nitride with a porous and hollow sphere structure to enhance dissociation of photogenerated charge carriers and visible-light-driven H2 generation. *ACS Applied Materials & Interfaces*, 12(37), 41527-41537.

Chen, Y., Zou, C., Mastalerz, M., Hu, S., Gasaway, C., & Tao, X. (2015). Applications of micro-fourier transform infrared spectroscopy (FTIR) in the geological sciences—a review. *International journal of molecular sciences*, 16(12), 30223-30250.

Cheng, C., Li, J., & Cheng, X. (2017). Photoluminescence lifetime and absorption spectrum of PbS nanocrystal quantum dots. *Journal of Luminescence*, *188*, 252-257.

Chowdhury, S., & Balasubramanian, R. (2017). Three-dimensional graphene-based macrostructures for sustainable energy applications and climate change mitigation. *Progress in Materials Science*, 90, 224-275.

Das, P., Pathak, N., Sanyal, B., Dash, S., & Kadam, R. M. (2019). Exploring Na0. 1Sr9. 8Eu0. 1 (PO4) 6F2 both as a potential phosphor material and host for radioactive waste immobilization. *Journal of Alloys and Compounds*, 810, 151906.

Dayal, G., Chin, X. Y., Soci, C., & Singh, R. (2017). High-Q Plasmonic Fano Resonance for Multiband Surface-Enhanced Infrared Absorption of Molecular Vibrational Sensing. *Advanced Optical Materials*, 5(2), 1600559.

de Carvalho, A. B., de Souza, Í. P., de Andrade, L. M., Binatti, I., Pedroso, E. F., Krambrock, K., ... & Silva-Caldeira, P. P. (2018). Novel copper (II) coordination polymer containing the drugs nalidixic acid and 8-hydroxyquinoline: Evaluation of the structural, magnetic, electronic, and antitumor properties. *Polyhedron*, 156, 312-319.

De, J., Gupta, S. P., Sudheendran Swayamprabha, S., Dubey, D. K., Bala, I., Sarkar, I., ... & Pal, S. K. (2018). Blue luminescent organic light emitting diode devices of a new class of star-shaped columnar mesogens exhibiting π–π driven supergelation. *The Journal of Physical Chemistry C*, 122(41), 23659-23674.

Dhall, A., Islam, S., Park, M., Zhang, Y., Kim, A., & Hwang, G. (2021). Bimodal nanocomposite platform with antibiofilm and self-powering functionalities for biomedical applications. *ACS applied materials & interfaces*, *13*(34), 40379-40391.

Do, K., Saleem, Q., Ravva, M. K., Cruciani, F., Kan, Z., Wolf, J., Hansen, M. R., Beaujuge, P. M. & Brédas, J. (2016). Impact of Fluorine Substituents on π-Conjugated Polymer Main

Dong, G., Lu, Q., Jiang, H., Li, C., Gong, Y., Zhang, H., & Li, W. (2020). Electrocatalytic glucose oxidation at coral-like Pd/C3N4-C nanocomposites in alkaline media. *Catalysts*, 10(4), 440.

Du, X., Yuan, Y., Zhou, L., Lin, H., Zheng, C., Luo, J., Chen, Z., Tao, S. & Liao, L. S. (2020). Delayed fluorescence emitter enables near 17% efficiency ternary organic solar cells with enhanced storage stability and reduced recombination energy loss. *Advanced Functional Materials*, 30(15), 1909837.

Duward, F., Shriver, P., W. and Cooper, H. (2019). *Introduction to Crystal Field Theory*. California State University, USA.

Emami, M., Shahroosvand, H., Bikas, R., Lis, T., Daneluik, C., & Pilkington, M. (2021). Synthesis, study, and application of Pd (II) hydrazone complexes as the emissive components of single-layer light-emitting electrochemical cells. *Inorganic Chemistry*, 60(2), 982-994.4

Enesca, A., Baneto, M., Perniu, D., Isac, L., Bogatu, C., & Duta, A. (2016). Solar-activated tandem thin films based on CuInS2, TiO2 and SnO2 in optimized wastewater treatment processes. *Applied Catalysis B: Environmental*, *186*, 69-76.

Esmaelpourfarkhani, M., Ramezani, M., Alibolandi, M., Abnous, K., & Taghdisi, S. M. (2023). Time-resolved Fluorescence DNA-based Sensors for R9educing Background Fluorescence of Environment. *Journal of Fluorescence*, 1-16.

Fahlman, M., Fabiano, S., Gueskine, V., Simon, D., Berggren, M., & Crispin, X. (2019). Interfaces in organic electronics. *Nature Reviews Materials*, 4(10), 627-650.

Fakharuddin, A., Shabbir, U., Qiu, W., Iqbal, T., Sultan, M., Heremans, P., & Schmidt-Mende, L. (2019). Inorganic and Layered Perovskites for Optoelectronic Devices. *Advanced Materials*, 95,1-32.

Fang, H., Jing, H., Zhang, A., Ge, H., Yao, Z., Brothers, P. J., & Fu, X. (2016). Synthesis, electronic structure, and reactivity studies of a 4-coordinate square planar germanium (IV) cation. *Journal of the American Chemical Society*, 138(24), 7705-7710.

Feng, G., Kwok, R. T., Tang, B. Z., & Liu, B. (2017). Functionality and versatility of aggregation-induced emission luminogens. *Applied Physics Reviews*, *4*(2).

Gao, W., An, Q., Hao, M., Sun, R., Yuan, J., Zhang, F., Ma, W., Min, J. & Yang, C. (2020). Thick-film organic solar cells achieving over 11% efficiency and nearly 70% fill factor at thickness over 400 nm. Advanced Functional Materials, 30(10), 1908336.

Ghanipour, M., & Dorranian, D. (2013). Effect of Ag-nanoparticles doped in polyvinyl alcohol on the structural and optical properties of PVA films. *Journal of Nanomaterials*, 2013, 2-2.

Gong, J., Sumathy, K., Qiao, Q., & Zhou, Z. (2017). Review on dye-sensitized solar cells (DSSCs): Advanced techniques and research trends. *Renewable and Sustainable Energy Reviews*, 68, 234-246.

Gong, X., Voznyy, O., Jain, A., Liu, W., Sabatini, R., Piontkowski, Z., Walters, G., Bappi, G., Nokhrin, S., Bushuyev, O. & Sargent, E. H. (2018). Electron–phonon interaction in efficient perovskite blue emitters. *Nature materials*, 17(6), 550-556.

Guo, M. X., Yang, L., Jiang, Z. W., Peng, Z. W., & Li, Y. F. (2017). Al-based metal-organic gels for selective fluorescence recognition of hydroxyl nitro aromatic compounds. *Spectrochimica Acta Part A: Molecular and Biomolecular Spectroscopy*, 187, 43-48.

Guo, X., Wu, F., Ni, Y., & Kokot, S. (2016). Synthesizing a nano-composite of BSA-capped Au nanoclusters/graphitic carbon nitride nanosheets as a new fluorescent probe for dopamine detection. *Analytica chimica acta*, 942, 112-120.

Hädrich, S., Rothhardt, J., Krebs, M., Demmler, S., Klenke, A., Tünnermann, A., & Limpert, J. (2016). Single-pass high harmonic generation at high repetition rate and photon flux. *Journal of Physics B: Atomic, Molecular and Optical Physics*, 49(17), 172002.

Hamdoush, M., Nikitin, K., Skvortsov, I., Somov, N., Zhabanov, Y., & Stuzhin, P. A. (2019). Influence of heteroatom substitution in benzene rings on structural features and spectral properties of subphthalocyanine dyes. *Dyes and Pigments*, 170, 107584.

Harrison, M. A. (2012). *Heterogeneously alloyed semiconductor nanocrystals with induced chemical composition gradients.* Vanderbilt University.

Harvey, D. (2020). *Photoluminescent Spectroscopy.* LibreTexts: California State University, USA.

Haubitz, T., John, L., Freyse, D., Wessig, P., & Kumke, M. U. (2020). Investigating the Sulfur "Twist" on the Photophysics of DBD Dyes. *The Journal of Physical Chemistry A*, 124(22), 4345-4353.

He, X., Guo, Y., Li, X., & Liu, J. (2020). Light harvesting enhancement by hierarchical Au/TiO2 microspheres consisted with nanorod units for dye sensitized solar cells. *Solar Energy*, 207, 592-598.

Hermes, I. M., Hou, Y., Bergmann, V. W., Brabec, C. J., & Weber, S. A. (2018). The interplay of contact layers: How the electron transport layer influences interfacial recombination and hole extraction in perovskite solar cells. *The journal of physical chemistry letters*, 9(21), 6249-6256.

Hildebrandt, N. (2011). Biofunctional quantum dots: controlled conjugation for multiplexed biosensors. *Acs Nano*, 5(7), 5286-5290.

Holliday, S., Donaghey, J. E., & McCulloch, I. (2014). Advances in charge carrier mobilities of semiconducting polymers used in organic transistors. *Chemistry of Materials*, 26(1), 647-663.

Horoz, S., & Sahin, Ö. (2017). Synthesis, characterization and photovoltaic properties of Mn-doped Sb2S3 thin film. *Materials Science-Poland*, 35(4).

Hu, L., Sun, K., Wang, M., Chen, W., Yang, B., Fu, J., Xiong, Z., Li, X., Tang, X., Zang, Z., Zhang, S., Sun, L., & Li, M. (2017). Inverted Planar Perovskite Solar Cells with a High Fill Factor and Negligible Hysteresis by the Dual Effect of NaCl-Doped PEDOT:PSS. *ACS Applied Materials & Interfaces*, 9(50), 43902-43909.

Huang, J. J., Zhong, Z. F., Rong, M. Z., Zhou, X., Chen, X. D., & Zhang, M. Q. (2014). An easy approach of preparing strongly luminescent carbon dots and their polymer based composites for enhancing solar cell efficiency. *Carbon*, 70, 190-198.

Huang, K., Jiao, X., Liu, C., Wang, Q., Qiu, X., He, S. & Zeng, X. (2017). Synthesis of a novel π-extended hybrid rhodamine dye with far-red fluorescence emission and its application in bioimaging. *Dyes and Pigments*, 145, 561-569.

Hunt, A. M., & Speakman, R. J. (2015). Portable XRF analysis of archaeological sediments and ceramics. Journal of Archaeological Science, 53, 626-638.

Hussein, E. M. (2010). *Radiation mechanics: Principles and practice*. Elsevier.

Ishida, N., Wakamiya, A., & Saeki, A. (2016). Quantifying hole transfer yield from perovskite to polymer layer: statistical correlation of solar cell outputs with kinetic and energetic properties. *ACS Photonics*, 3(9), 1678-1688.

Jahani Bahnamiri, F. (2016). *Synthetic strategies for modifying dielectric properties and the electron mobility of fullerene derivatives.* University of Groningen.

Jain, N. (2011). Design of III-V multijunction solar cells on silicon substrate (Doctoral dissertation, Virginia Tech).

Jaiswal, R., Bharambe, J., Patel, N., Dashora, A., Kothari, D. C., & Miotello, A. (2015). Copper and Nitrogen co-doped TiO2 photocatalyst with enhanced optical absorption and catalytic activity. *Applied Catalysis B: Environmental*, 168, 333-341.

Jao, M. H., Liao, H. C., & Su, W. F. (2016). Achieving a high fill factor for organic solar cells. *Journal of Materials Chemistry A*, 4(16), 5784-5801.

Jena, A. K., Kulkarni, A., & Miyasaka, T. (2019). Halide perovskite photovoltaics: background, status, and future prospects. *Chemical reviews*, *119*(5), 3036-3103.

Jia, T., Zhang, J., Zhong, W., Liang, Y., Zhang, K., Dong, S., Ying, L., Liu, F., Wang, X., Huang, F. & Cao, Y. (2020). 14.4% efficiency all-polymer solar cell with broad absorption and low energy loss enabled by a novel polymer acceptor. *Nano Energy*, 72, 104718.

Jiang, H., He, X., Ma, Y., Fu, B., Xu, X., Subramanian, B., & Hu, C. (2021). Isotropic hedgehog-shaped-TiO2/functional-multiwall-carbon-nanotube micromotors with phototactic motility in fuel-free environments. *ACS Applied Materials & Interfaces,* 13(4), 5406-5417.

Jiang, Y., Qahouq, J. A. A., & Batarseh, I. (2010, May). Improved solar PV cell Matlab simulation model and comparison. In *2010 IEEE international symposium on circuits and systems (ISCAS)* (pp. 2770-2773). IEEE.

Jin-Wook, L., Sang-Hoon, B., Nicholas D., Yao-Tsung, H., Zhenghong, D., & Yang, Y. (2019). The role of grain boundaries in perovskite solar cells. *Materials Today Energy*, 7, 149-160.

Joanna, M., Lauren, E. and Shea-R. (2014). Down Conversion Materials for Solid State Lighting, Dept. Mechanical and Aerospace Engineering and Materials Science and Engineering. *Sandia National Laboratories,* 87185-1425.

Jun, J. V., Petersson, E. J., & Chenoweth, D. M. (2018). Rational design and facile synthesis of a highly tunable quinoline-based fluorescent small-molecule scaffold for live cell imaging. *Journal of the American Chemical Society*, 140(30), 9486-9493.

Kalpani W. K., Sanjeevadharshini, N., Lakshman D. and Senadeera, G.K.R. (2016). The effect of TiO2 photo anode film thickness on photovoltaic properties of dye-sensitized solar cells. *Ceylon Journal of Science,* 45(1):33

Kan, B., Kan, Y., Zuo, L., Shi, X., & Gao, K. (2021). Recent progress on all-small molecule organic solar cells using small-molecule nonfullerene acceptors. *InfoMat*, *3*(2), 175-200.

Kapil, G., Bessho, T., Ng, C. H., Hamada, K., Pandey, M., Kamarudin, M. A. & Hayase, S. (2019). Strain relaxation and light management in tin–lead perovskite solar cells to achieve high efficiencies. *ACS Energy Letters*, 4(8), 1991-1998.

Kashif, H., & Khan, M. N. (2020). Future of free space communication systems (FSCS): An overview. *2020 Intermountain Engineering, Technology and Computing (IETC),* 1-5.

Kavitha, R., & Kumar, S. G. (2019). A review on plasmonic Au-ZnO heterojunction photocatalysts: Preparation, modifications and related charge carrier dynamics. *Materials Science in Semiconductor Processing*, 93, 59-91.

Kaviyarasu, K., Sajan, D., Devarajan, P. A. (2013). A rapid and versatile method for solvothermal synthesis of Sb2O3nanocrystals under mild conditions. *Applied Nanoscience,* 3(6), 529–533.

Ken, O. S., Zhukov, E. A., Akimov, I. A., Korenev, V. L., Kopteva, N. E., Kalitukha, I. V., Sapega, V.F., Wieck, A.D., Ludwig, A., Schott, R. & Bayer, M. (2020). Effect of electric current on the optical orientation of interface electrons in AlGaAs/GaAs heterostructures. *Physical Review B*, 102(4), 045302.

Khan, S. A., Li, C., Jalil, A., Xin, X., Rauf, M., Ahmed, J., Khan, M.M., Dong, B., Zhu, J. & Agathopoulos, S. (2021). Development of structure and tuning ability of the luminescence of lead-free halide perovskite nanocrystals (NCs). *Chemical Engineering Journal*, 420, 127603.

Kim, H., Lim, K. G., & Lee, T. W. (2016). Planar heterojunction organometal halide perovskite solar cells: roles of interfacial layers. *Energy & Environmental Science*, 9(1), 12-30.

Kim, J. H., Ahmad, Z., Kim, Y., Kim, W., Ahn, H., Lee, J. S., & Yoon, M. H. (2020). Decoupling critical parameters in large-range crystallinity-controlled polypyrrole-based high-performance organic electrochemical transistors. Chemistry of Materials, 32(19), 8606-8618.

Komolafe, A. A., Adegboyega, S. A. A., Anifowose, A. Y., Akinluyi, F. O., & Awoniran, D. R. (2014). Air pollution and climate change in Lagos, Nigeria: needs for proactive approaches to risk management and adaptation. *American Journal of Environmental Sciences*, *10*(4), 412-423.

Koo, S. J., Kim, J. H., Kim, Y. K., Shin, M., Choi, J. W., Oh, J. W., ... & Song, M. (2021). Improved Light Harvesting of Fiber-Shaped Dye-Sensitized Solar Cells by Using a Bacteriophage Doping Method. *Nanomaterials*, 11(12), 3421.

Kumaravel, V., Bartlett, J., & Pillai, S. C. (2020). Photoelectrochemical conversion of carbon dioxide (CO2) into fuels and value-added products. *ACS Energy Letters*, 5(2), 486-519.

Kužel, P., & Němec, H. (2020). Terahertz spectroscopy of nanomaterials: a close look at charge-carrier transport. *Advanced Optical Materials*, 8(3), 1900623.

Kwanghee, K., Hyemi, J., Taewoo, L., and Sung, K., (2010). Synthesis and Structure of Benzotriazolyl Flourenes. *Bulletin of the Korean Chemical Society*, 31 (4), 984-988

Kwon, S., Kang, H., Lee, J. H., Lee, J., Hong, S., Kim, H., & Lee, K. (2017). Effect of processing additives on organic photovoltaics: recent progress and future prospects. *Advanced Energy Materials*, 7(10), 1601496.

Lakshmanan, R., & Daniel, S. K. (2018). Engineered nanomaterials for organic light-emitting diodes (OLEDs). In *Handbook of nanomaterials for industrial applications* (pp. 312-323). Elsevier.

Laquai, F., Andrienko, D., Mauer, R., & Blom, P. W. (2015). Charge carrier transport and photogeneration in P3HT: PCBM photovoltaic blends. *Macromolecular rapid communications*, 36(11), 1001-1025.

Lee, C., Lee, S., Kim, G. U., Lee, W., & Kim, B. J. (2019). Recent advances, design guidelines, and prospects of all-polymer solar cells. *Chemical reviews*, 119(13), 8028-8086.

Lee, S. (2013). Synthesis of Optimized InP/ZnS Core/Shell Nanocrystals and TiO2 Nanotubes for Quantum Dot Sensitized Solar Cells. (Graduate Theses and Dissertations, University of Purdue).

Li, S., Luo, J., Liu, J., & Tang, J. (2019). Self-trapped excitons in all-inorganic halide perovskites: fundamentals, status, and potential applications. *The journal of physical chemistry letters*, 10(8), 1999-2007.

Li, Y., Gecevicius, M., & Qiu, J. (2016). Long persistent phosphors—from fundamentals to applications. *Chemical Society Reviews*, 45(8), 2090-2136.

Liang, H., Xiang, H., Zhu, R., Liu, C and Jia, Y (2021). Structural stability and defect-tolerance of ionic spinel semiconductor for high-efficiency solar cells. *Journal of Materials Chemistry A*, 9(25), 14566-14575.

Liang, J., Gao, H., Yi, M., Shi, W., Liu, Y., Zhang, Z., & Mao, Y. (2018). β-NaYF4: Yb3+, Tm3+@ TiO2 core-shell nanoparticles incorporated into the mesoporous layer for high efficiency perovskite solar cells. Electrochimica acta, 261, 14-22.

Liao, H., Jiang, C., Liu, W., Vera, J. M., Seni, O. D., Demera, K., Yu, C. & Tan, M. (2015). Fluorescent nanoparticles from several commercial beverages: Their properties and potential application for bioimaging. *Journal of agricultural and food chemistry*, 63(38), 8527-8533.

Liaw, D. J., Wang, K. L., Huang, Y. C., Lee, K. R., Lai, J. Y., & Ha, C. S. (2012). Advanced polyimide materials: Syntheses, physical properties and applications. *Progress in Polymer Science*, *37*(7), 907-974.

Liu, Q., Cao, J., Ji, Y., Li, X., Li, W., Zhu, Y., ... & Yang, Y. (2020). Construction of a direct Z-scheme ZnS quantum dot (QD)-Fe2O3 QD heterojunction/reduced graphene oxide nanocomposite with enhanced photocatalytic activity. *Applied Surface Science*, 506, 144922.

Liu, X., Du, Y., Xu, X., Zhou, X., Dai, Z., & Bao, J. (2016). Enhancing the anode performance of antimony through nitrogen-doped carbon and carbon nanotubes. *The Journal of Physical Chemistry C*, 120(6), 3214-3220.

Liu, Y., Li, C., Ren, Z., Yan, S., & Bryce, M. R. (2018). All-organic thermally activated delayed fluorescence materials for organic light-emitting diodes. *Nature Reviews Materials*, 3(4), 1-20.

Luo, B., Li, F., Xu, K., Guo, Y., Liu, Y., Xia, Z., & Zhang, J. (2019). B-Site Doped Lead Halide Perovskites: Synthesis, Band Engineering, Photophysics, and Light Emission Applications. *Journal of Materials Chemistry C*, 7(10),3-62.

Luo, X., Ahn, J. Y., & Kim, S. H. (2019). Aerosol synthesis and luminescent properties of CaAl2O4: Eu2+, Nd3+ down-conversion phosphor particles for enhanced light harvesting of dye-sensitized solar cells. *Solar Energy*, 178, 173-180.

Lv, M., Zheng, D., Ye, M., Xiao, J., Guo, W., Lai, Y., ... & Zuo, J. (2020). Optimized porous rutile TiO 2 nanorod arrays for enhancing the efficiency of dye-sensitized solar cells. *Energy & Environmental Science*, 6(5), 1615-1622.

Ma, B., Chen, J., Wang, M., Xu, X., Qian, J., Lu, Y., Zhang, W., Xia, P., Qin, M., Zhu, W. and Zhang, L., & Huang, W. (2020). Passivating charged defects with 1, 6 hexamethylenediamine to realize efficient and stable tin-based perovskite solar cells. *The Journal of Physical Chemistry C*, *124*(30), 16289-16299.

Ma, et al., (2021) .Over 17% Efficiency of Ternary Organic Photovoltaics Employing Two Acceptors with an Acceptor–Donor–Acceptor Configuration. *ACS Applied Materials & Interfaces*, *13*(48), 57684–57692.

Maçôas, E., Santos, C., Mariz, I., Correia, C., & Martinho, J. G. (2014). On the origin of the emission of carbon nanodots: molecule-like fluorophores vs nanographene-like clusters. Program 6JIF, 40.

Mahata, A., Mosconi, E., Meggiolaro, D., & De Angelis, F. (2019). *Modulating Band Alignment in Mixed Dimensionality 3D/2D Perovskites by Surface Termination Ligand Engineering. Chemistry of Materials*, 1,1-22.

Manyasree, D., Kiranmayi, P., & Venkata, R. K. (2018). Characterization and antibacterial activity of ZnO nanoparticles synthesized by co-precipitation method. *Int J App Pharm*, 10(6), 224-8.

Manzoor, S., Husain, S., Somvanshi, A., Fatema, M., & Zarrin, N. (2019). Exploring the role of Zn doping on the structure, morphology, and optical properties of LaFeO 3. *Applied Physics A*, 125, 1-11.

Marjańska, E., & Szpakowska, M. (2017). Qualitative and quantitative analysis of selected tonic waters by potentiometric taste sensor with all-solid-state electrodes. *IEEE Sensors Journal*, 18(3), 1250-1255.

Martínez-Abadía, M., Giménez, R., & Ros, M. B. (2018). Self-assembled α-cyanostilbenes for advanced functional materials. *Advanced Materials*, 30(5), 1704161.

McArthur, E. A., Morris-Cohen, A. J., Knowles, K. E., & Weiss, E. A. (2010). Charge carrier resolved relaxation of the first excitonic state in CdSe quantum dots probed with near-infrared transient absorption spectroscopy. *The Journal of Physical Chemistry B*, 114(45), 14514-14520.

Mehta, A., Mishra, A., Basu, S., Shetti, N. P., Reddy, K. R., Saleh, T. A., & Aminabhavi, T. M. (2019). Band gap tuning and surface modification of carbon dots for sustainable environmental remediation and photocatalytic hydrogen production–A review. *Journal of environmental management*, *250*, 109486.

Meng, L. (2017). *Interface Engineering and Morphology Study of Thin Film Organic-Inorganic Halide Perovskite Optoelectronic Devices* (Doctoral dissertation, UCLA).

Meng, W., Bai, X., Wang, B., Liu, Z., Lu, S., & Yang, B. (2019). Biomass-derived carbon dots and their applications. *Energy & Environmental Materials*, 2(3), 172-192.

Micha, D. N., Höhn, O., Oliva, E., Klinger, V., Bett, A. W., & Dimroth, F. (2019). Development of back side technology for light trapping and photon recycling in GaAs solar cells. *Progress in Photovoltaics: Research and Applications*, 27(2), 163-170.

Mondal, B., Bag, R., Roisnel, T. & Ghosh, S. (2019). Use of Single-Metal Fragments for Cluster Building: Synthesis, Structure, and Bonding of Heterometallaboranes. *Inorganic Chemistry*, 58(4), 1-8.

Morris, W. A., Kolpaczynska, M., & Fraser, C. L. (2016). Effects of α-substitution on mechanochromic luminescence and aggregation-induced emission of difluoroboron β-diketonate dyes. *The Journal of Physical Chemistry C*, 120(39), 22539-22548.

Muench, S., Wild, A., Friebe, C., Haupler, B., Janoschka, T., & Schubert, U. S. (2016). Polymer-based organic batteries. *Chemical reviews*, 116(16), 9438-9484.

Nahyoon, N. A., Liu, L., Rabé, K., Nahyoon, S. A., Abro, A. H., & Yang, F. (2019). Efficient degradation of rhodamine B with sustainable electricity generation in a photocatalytic fuel cell using visible light Ag3PO4/Fe/GTiP photoanode and ZnIn2S4 photocathode. *Journal of the Taiwan Institute of Chemical Engineers*, 96, 137-147.

Nakano, K., & Tajima, K. (2016). Organic Planar Heterojunctions: From Models for Interfaces in Bulk Heterojunctions to High-Performance Solar Cells. *Advanced Materials*, 29 (25), 1603269.

National science Foundation (2016).*Vibration and rotation of Molecules: Infrared and Microwave Spectrscopy.* University of Minnesota Press:USA,

Nikolai, G. K. & Lev, A. D. (2010*). Optical properties and biomedical applications of plasmonic nanoparticles,* 111(1), 1–35

Niu, T., Xue, Q., & Yip, H. L. (2021). Molecularly engineered interfaces in metal halide perovskite solar cells. *The Journal of Physical Chemistry Letters,* 12(20), 4882-4901.

N'Sondé, W. & Lindo, K. (2018). *Concrete Flower*. University of Indiana: USA.

Ochsmann, J. R. (2015). Excited-state dynamics in donor-acceptor systems for energy conversion (Doctoral dissertation, Johannes Gutenberg-Universität Mainz).

Ogutman, N. K. (2018). Hole Selective *Tunneling Oxide Applications with Insight into Sophisticated Characterization Techniques*. (Electronic Thesis and Dissertation, University of Central Florida).

Olajire, A. A., Ifediora, N. F., Bello, M. D., & Benson, N. U. (2018). Green synthesis of copper nanoparticles using Alchornea laxiflora leaf extract and their catalytic application for oxidative desulphurization of model oil. *Iranian Journal of Science and Technology, Transactions A*: *Science*, 42, 1935-1946.

Pandey, S., Verma, P., & Pandey, A. C. (2006). Synthesis of highly luminescent manganese doped ZnS nanophosphor. *Proceedings of the ASID '06, New Delhi, India*, 8-12.

Park, Y. (2018). Developing MOS structures in gallium oxide for high-power electronics and energy savings applications (Master's thesis, University of Oslo).

Parola, S., Julián-López, B., Carlos, L. D., & Sanchez, C. (2016). Optical properties of hybrid organic-inorganic materials and their applications. *Advanced Functional Materials,* 26(36), 6506-6544.

Pearton, S. J., Ren, F., Patrick, E., Law, M. E., & Polyakov, A. Y. (2016). Ionizing radiation damage effects on GaN devices. *ECS Journal of solid state science and technology*, 5(2), Q35.

Peiris, S., de Silva, H. B., Ranasinghe, K. N., Bandara, S. V., & Perera, I. R. (2021). Recent development and future prospects of TiO2 photocatalysis. *Journal of the Chinese Chemical Society*, 68(5), 738-769.

Potscavage, (2011). Physics and Engineering of Organic Solar Cells. *Journal of Physical Chemistry Letters*. 2 (15), 1950-1964.

Poulsen, T. (2010). *Introduction to Chemistry*. CK-12 Foundation Press:USA.

Previtali, A. (2021). New organic and hybrid organic/inorganic materials with intriguing solid state optoelectronic properties. Unpublished thesis, University of Milan, Italy.

Prushan, M. (2018). *Instrumental Analysis Lab Manual*. La Salle University Press: Philadelphia.

Pu, Y. C., Wang, G., Chang, K. D., Ling, Y., Lin, Y. K., Fitzmorris, B. C., ... & Li, Y. (2013). Au nanostructure-decorated TiO2 nanowires exhibiting photoactivity across entire UV-visible region for photoelectrochemical water splitting. *Nano letters*, 13(8), 3817-3823.

Pupkaite, J. (2020). Collagen Hydrogels for Regenerative Medicine (Doctoral dissertation, Université d'Ottawa/University of Ottawa).

Qu, B., Zhang, B., Wang, L., Zhou, R., & Zeng, X. (2015). Mechanistic Study of the Persistent Luminescence of CaAl₂O₄:Eu,Nd. *Chemistry of Materials, 27(6), 2195–2202.*

Quan, L. N., Yuan, M., Comin, R., Voznyy, O., Beauregard, E. M., Hoogland, S., Buin, A., Kirmani, A. R., Zhao, K., Amassian, Aram; Kim, Dong Ha; Sargent, Edward H. (2016). Ligand-Stabilized Reduced-Dimensionality Perovskites. *Journal of the American Chemical Society*, 138 (8), 2649–2655

Quan, L. N., Rand, B. P., Friend, R. H., Mhaisalkar, S. G., Lee, T. W., & Sargent, E. H. (2019). Perovskites for next-generation optical sources. *Chemical reviews*, 119(12), 7444-7477.

Rahman, M. M., Wang, J., Nath, N. C. D., & Lee, J. J. (2018). A non-absorbing organic redox couple for sensitization-based solar cells with metal-free polymer counter electrode. *Electrochimica Acta*, 286, 39-46.

Ray, S. C. (2015). Applications of Graphene and Graphene-Oxide Based Nanomaterials || *Application and Uses of Graphene Oxide and Reduced Graphene Oxide*, 39–55.

Ren, G., Han, W., Deng, Y., Wu, W., Li, Z., Guo, J., Bao, H., Liu, C. & Guo, W. (2021). Strategies of modifying spiro-OMeTAD materials for perovskite solar cells: a review. *Journal of Materials Chemistry A*, 9(8), 4589-4625.

Rezaie, M. N., Mohammadnejad, S., & Ahadzadeh, S. (2021). Hybrid inorganic-organic light-emitting heterostructure devices based on ZnO. *Optics & Laser Technology*, 138, 106896.

Rezazgui, O. (2016). *Towards a bio-inspired photoherbicide: Synthesis and studies of fluorescent tagged or water-soluble* (Doctoral dissertation, Université de Limoges).

Ruiz-Jorge, F., Portela, J. R., Sánchez-Oneto, J., & Martínez de la Ossa, E. J. (2020). Synthesis of micro-and nanoparticles in sub-and supercritical water: from the laboratory to larger scales. *Applied Sciences*, 10(16), 5508.

Ryu, S., Nguyen, D. C., Ha, N. Y., Park, H. J., Ahn, Y. H., Park, J. Y., & Lee, S. (2019). Light intensity-dependent variation in defect contributions to charge transport and recombination in a planar MAPbI3 perovskite solar cell. *Scientific reports*, 9(1), 19846.

Sai-Anand, G., Gopalan, A. I., Lee, K. P., Venkatesan, S., Qiao, Q., Kang, B. H., Lee, S.W., Lee, J.S & Kang, S. W. (2016). Electrostatic nanoassembly of contact interfacial layer for enhanced photovoltaic performance in polymer solar cells. *Solar Energy Materials and Solar Cells*, *153*, 148-163.

Santos-Sánchez, N. F., Salas-Coronado, R., Valadez-Blanco, R., Hernández-Carlos, B., & Guadarrama-Mendoza, P. C. (2017). Natural antioxidant extracts as food preservatives. *Acta Scientiarum Polonorum Technologia Alimentaria*, 16(4), 361-370.

Schwede, J. W., Bargatin, I., Riley, D. C., Hardin, B. E., Rosenthal, S. J., Sun, Y., ... & Melosh, N. A. (2010). Photon-enhanced thermionic emission for solar concentrator systems. *Nature materials*, 9(9), 762-767.

Shah, S. K., Khan, J., Ullah, I., & Khan, Y. (2017). Optimization of active-layer thickness, top electrode and annealing temperature for polymeric solar cells. *AIMS Materials Science,* 4(3), 789-799.

Sharma, A., Sharma, A., Averbukh, M., Jately, V., & Azzopardi, B. (2021). An effective method for parameter estimation of a solar cell. *Electronics*, 10(3), 312.

Shi, L., Yin, Y., Zhang, L. C., Wang, S., Sillanpää, M., & Sun, H. (2019). Design and engineering heterojunctions for the photoelectrochemical monitoring of environmental pollutants: A review. *Applied Catalysis B: Environmental*, 248, 405-422.

Singh, O., Agrawal, A., Selvaraj, T., Ghosh, I. K., Vempatapu, B. P., Viswanathan, B., Bal, R & Sarkar, B. (2020). Renewable aromatics from tree-borne oils over zeolite catalysts promoted by transition metals. *ACS applied materials & interfaces*, 12(22), 24756-24766.

Smith, M. D., Connor, B. A., & Karunadasa, H. I. (2019). Tuning the luminescence of layered halide perovskites. *Chemical Reviews*, 119(5), 3104-3139.

Snaith, H. J. (2013). Perovskites: the emergence of a new era for low-cost, high-efficiency solar cells. *The journal of physical chemistry letters*, 4(21), 3623-3630.

Sohrab, S. H. (2021). Some Implications of a Scale Invariant Model of Statistical Mechanics, Kinetic Theory of Ideal Gas, and Riemann Hypothesis. *Current Approaches in Science and Technology Research*, 11, 104-160.

Soni, A. K., & Singh, B. P. (2019). Luminescent materials in lighting, display, solar cell, sensing, and biomedical applications. In *Luminescence-OLED Technology and Applications* (p. 1). London, UK: IntechOpen.

Sonmezoglu, S., & Akin, S. (2020). Suppression of the interface-dependent nonradiative recombination by using 2-methylbenzimidazole as interlayer for highly efficient and stable perovskite solar cells. *Nano Energy*, 76, 105127.

Souza, N. R. S., Silva, D. C., Sampaio, D. V., Rezende, M. V. S., Kucera, C., Trofimov, A. A., ... & Silva, R. S. (2017). Laser sintering of persistent luminescent CaAl2O4: Eu2+ Dy3+ ceramics. *Optical Materials*, 68, 2-6.

Spence, C. (2019). On the changing colour of food & drink. *International Journal of Gastronomy and Food Science*, *17*, 100161.

Steckl, A. J., Heikenfeld, J. C., Lee, D. S., Garter, M. J., Baker, C. C., Wang, Y., & Jones, R. (2012). Rare-earth-doped GaN: growth, properties, and fabrication of electroluminescent devices. *IEEE Journal of Selected Topics in Quantum Electronics*, *8*(4), 749-766.

Stolterfoht, M., Wolff, C. M., Márquez, J. A., Zhang, S., Hages, C. J., Rothhardt, D., ... & Neher, D. (2018). Visualization and suppression of interfacial recombination for high-efficiency large-area pin perovskite solar cells. *Nature Energy*, 3(10), 847-854.

Strunk, J. (Ed.). (2021). *Heterogeneous Photocatalysis: From Fundamentals to Applications in Energy Conversion and Depollution*. John Wiley & Sons.

Sun, X., Chavali, R. V. K., & Alam, M. A. (2019). Real-time monitoring and diagnosis of photovoltaic system degradation only using maximum power point—the Suns-Vmp method. *Progress in Photovoltaics: Research and Applications*, 27(1), 55-66.

Tavares, L., Slim, S., Barreto, C. & Ben-Hlima, H. (2022).Ginger: a systematic review of clinical trials and recent advances in encapsulation of its bioactive compounds. Food & Function, 13(3):1078-1091.

Tran, V. D., Pammi, S. V. N., Park, B. J., Han, Y., Jeon, C., & Yoon, S. G. (2019). Transfer-free graphene electrodes for super-flexible and semi-transparent perovskite solar cells fabricated under ambient air. *Nano Energy*, 65, 104018.

Tress, W. (2017). Perovskite solar cells on the way to their radiative efficiency limit–insights into a success story of high open-circuit voltage and low recombination. *Advanced Energy Materials*, 7(14), 1602358.

Tricoli, A., Tran-Phu, T., Chen, H., Bo, R., Di Bernardo, I., Fusco, Z., & Simonov, A. (2019). High Temperature One-Step Synthesis of Efficient Nanostructured BiVO4 Photoanodes for Water Oxidation. Energy Technology, 7(8).

Tsai, S. R., & Hamblin, M. R. (2017). Biological effects and medical applications of infrared radiation. *Journal of Photochemistry and Photobiology B: Biology*, 170, 197-207.

Tummeltshammer, C., Taylor, A., Kenyon, A. J., & Papakonstantinou, I. (2016). Losses in luminescent solar concentrators unveiled. *Solar Energy Materials and Solar Cells*, 144, 40-47.

Ulatowski, A. M., Wright, A. D., Wenger, B., Buizza, L. R., Motti, S. G., Eggimann, H. J., ... & Herz, L. M. (2020). Charge-carrier trapping dynamics in bismuth-doped thin films of MAPbBr3 perovskite. *The Journal of Physical Chemistry Letters*, *11*(9), 3681-3688.

Umemoto, A., Yoda, H., & Shibuya, N. (2019). Photovoltaic module having light receptive, glass laminate structure and photovoltaic module having light receptive. *U.S. Patent No. 7,202,410*. Washington, DC: U.S. Patent and Trademark Office.

Vardy, E., Robinson, J. E., Li, C., Olsen, R. H., DiBerto, J. F., Giguere, P. M., Sassano, F.M., Huang, X.P., Zhu, H., Urban, D.J. & Roth, B. L. (2015). A new DREADD facilitates the multiplexed chemogenetic interrogation of behavior. *Neuron*, 86(4), 936-946.

Vecellio Segate, R. (2020). Securitizing Innovation to Protect Trade Secrets Between "the East" and "the West": A Neo-Schumpeterian Public Legal Reading. *UCLA Pacific Basin Law* Journal, 37(1).

Wadsworth, A., Hamid, Z., Kosco, J., Gasparini, N., & McCulloch, I. (2020). The bulk heterojunction in organic photovoltaic, photodetector, and photocatalytic applications. *Advanced Materials*, *32*(38), 2001763.

Wang, C., Xu, X., Zhang, W., Dkhil, S. B., Meng, X., Liu, X., Margeat, O., Yartsev, A., Ma, W., Ackermann, J. and Wang, E. & Fahlman, M. (2017). Ternary organic solar cells with enhanced open circuit voltage. *Nano Energy*, 37, 24-31.

Wang, H., Zhong, Y., Du, B., Zhao, Y., & Wang, M. (2018). Recovery of both magnesium and lithium from high Mg/Li ratio brines using a novel process. *Hydrometallurgy*, 175, 102-108.

Wang, K., Shen, P., Li, M., Chen, S., Lin, M., Chen, P., & Guo, T. (2014). Low-Temperature Sputtered Nickel Oxide Compact Thin Film as Effective Electron Blocking Layer for Mesoscopic NiO/CH_3 NH $3PbI_3$ Perovskite Heterojunction Solar Cells. *ACS Applied Materials & Interfaces*, 6(15), 11851–11858

Wang, Q., Li, N., Bolto, B., Hoang, M., & Xie, Z. (2016). Desalination by pervaporation: A review. *Desalination*, 387, 46-60.

Wang, Y., & Zhan, X. (2016). Layer-by-layer processed organic solar cells. *Advanced Energy Materials*, 6(17), 1600414.

Wang, Y., Lee, J., Hou, X., Labanti, C., Yan, J., Mazzolini, E., Parhar, A., Nelson, J., Kim, J.S. & Li, Z. (2021). Recent progress and challenges toward highly stable nonfullerene acceptor-based organic solar cells. *Advanced Energy Materials*, 11(5), 2003002.

Wang, Y., Qiu, M., Won, M., Jung, E., Fan, T., Xie, N., Chi, S.G., Zhang, H. & Kim, J. S. (2019). Emerging 2D material-based nanocarrier for cancer therapy beyond graphene. *Coordination Chemistry Reviews*, 400, 213041.

Wei, R. B., Kuang, P. Y., Cheng, H., Chen, Y. B., Long, J. Y., Zhang, M. Y., & Liu, Z. Q. (2017). Plasmon-enhanced photoelectrochemical water splitting on gold nanoparticle decorated ZnO/CdS nanotube arrays. *ACS Sustainable Chemistry & Engineering*, 5(5), 4249-4257.

Wei, Z., Lu, Y., Zhao, J., Zhao, S., Wang, R., Fu, N., Li, X., Guan, L. & Teng, F. (2018). Synthesis and luminescent modulation of ZnS crystallite by a hydrothermal method. *ACS omega*, 3(1), 137-143.

Wincukiewicz, A., Mech, W., Grankowska, S., Wolos, A., Drabinska, A., Slupinski, T., Korona, K.P. & Kaminska, M. (2018). Radiative recombination and other processes related to excess charge carriers, decisive for efficient performance of electronic devices. *Lithuanian Journal of Physics*, 58(1).

Wu, C., Zhang, Q., Liu, G., Zhang, Z., Wang, D., Qu, B., Chen, Z. & Xiao, L. (2020). From Pb to Bi: A promising family of Pb-free optoelectronic materials and devices. *Advanced Energy Materials*, 10(13), 1902496.

Xia, Z., & Meijerink, A. (2017). Ce 3+-Doped garnet phosphors: composition modification, luminescence properties and applications. *Chemical Society Reviews*, 46(1), 275-299.

Xie, L.-H., Yang, S.-H., Lin, J.-Y. Yi, M.-D., & Huang, W. (2020). Fluorene-based macromolecular nanostructures and nanomaterials for organic (opto)electronics. *Philosophical Transactions of the Royal Society A: Mathematical, Physical and Engineering Sciences*, 371(2000), 20120337–20120337

Xue, J., Lee, J. W., Dai, Z., Wang, R., Nuryyeva, S., Liao, M. E., Chang, S.Y., Meng, L., Meng, D., Sun, P. & Yang, Y. (2018). Surface ligand management for stable FAPbI3 perovskite quantum dot solar cells. Joule, 2(9), 1866-1878.

Yamamoto, K., Hayashi, M., Murakami, Y., Araki, Y., Otsuka, Y., Kashiwagi, T., Shimamura, T., Ukeda, H. (2015). Development of LC-MS/MS analysis of cyclic dipeptides and its application to tea extract. *Bioscience, Biotechnology, and Biochemistry*, 80 (1), 172-177.

Yang, F., Liu, J., Wang, X., Tanaka, K., Shinokita, K., Miyauchi, Y., Wakamiya, A. & Matsuda, K. (2019). Planar perovskite solar cells with high efficiency and fill factor obtained using two-step growth process. *ACS applied materials & interfaces*, 11(17), 15680-15687.

Yang, J., Cong, P., Chen, L., Wang, X., Li, J., Tang, A. & Zhou, E. (2019). Introducing fluorine and sulfur atoms into quinoxaline-based p-type polymers to gradually improve the performance of fullerene-free organic solar cells. *ACS Macro Letters*, 8(6), 743-748.

Ye, J., Li, Y., Medjahed, A. A., Pouget, S., Aldakov, D., Liu, Y., & Reiss, P. (2021). Doped bilayer tin (IV) oxide electron transport layer for high open-circuit voltage planar perovskite solar cells with reduced hysteresis. *Small*, 17(5), 2005671.

Yella, A., Lee, H. W., Tsao, H. N., Yi, C., Chandiran, A. K., Nazeeruddin, M. K., Diau, E.W.G., Yeh, C.Y., Zakeeruddin, S.M. & Grätzel, M. (2011). Porphyrin-sensitized solar cells with cobalt (II/III)–based redox electrolyte exceed 12 percent efficiency. *Science*, 334(6056), 629-634.

Yin, H., Cheung, S. H., Ngai, J. H., Ho, C. H. Y., Chiu, K. L., Hao, X., Li, H.W., Cheng, Y., Tsang, S.W. & So, S. K. (2017). Thick-Film High-Performance Bulk-Heterojunction Solar Cells Retaining 90% PCEs of the Optimized Thin Film Cells. Advanced Electronic Materials, 3(4), 1700007.

Younis, S. A., Lim, D. K., Kim, K. H., & Deep, A. (2020). Metalloporphyrinic metal-organic frameworks: Controlled synthesis for catalytic applications in environmental and biological media. *Advances in Colloid and Interface Science*, 277, 102108.

Yu, C., An, J., Zhou, R., Xu, H., Zhou, J., Chen, Q., Sun, G. & Huang, W. (2020). Microstructure design of carbonaceous fibers: a promising strategy toward high-performance weaveable/wearable supercapacitors. *Small*, 16(25), 2000653.

Yu, W., Zhang, S., Chen, J., Xia, P., Richter, M. H., Chen, L., Xu, W., Jin, J., Chen, S. & Peng, T. (2018). Biomimetic Z-scheme photocatalyst with a tandem solid-state electron flow catalyzing H 2 evolution. *Journal of Materials Chemistry A*, 6(32), 15668-15674.

Yu, Z., Ong, Z. Y., Li, S., Xu, J. B., Zhang, G., Zhang, Y. W., Shi, Y. & Wang, X. (2017). Analyzing the carrier mobility in transition-metal dichalcogenide MoS2 field-effect transistors. *Advanced Functional Materials*, 27(19), 1604093.

Zawada, D. G., & Mazel, C. H. (2014). Fluorescence-based classification of caribbean coral reef organisms and substrates. *PloS one*, 9(1), e84570.

Zhang, C., Shen, H., Sun, L., Yang, J., Wu, S., & Lu, Z. (2020). Bifacial p-type PERC solar cell with efficiency over 22% using laser doped selective emitter. *Energies*, *13*(6), 1388.

Zhang, F. L., Zhou, B. W., Yan, Z. Z., Zhao, J., Zhao, B. C., Liu, W. F. & Liu, K. X. (2020). 6-Gingerol attenuates macrophages pyroptosis via the inhibition of MAPK signaling pathways and predicts a good prognosis in sepsis. *Cytokine,* 125, 154854.

Zhang, J., Tan, C. H., Zhang, K., Jia, T., Cui, Y., Deng, W., ... & Cao, Y. (2021). π-Extended Conjugated Polymer Acceptor Containing Thienylene–Vinylene–Thienylene Unit for High-Performance Thick-Film All-Polymer Solar Cells with Superior Long-Term Stability. *Advanced Energy Materials*, 11(48), 2102559.

Zhang, J., Yang, Y., Deng, H., Farooq, U., Yang, X., Khan, J., ... & Song, H. (2017). High quantum yield blue emission from lead-free inorganic antimony halide perovskite colloidal quantum dots. *Acs Nano,* 11(9), 9294-9302.

Zhang, K., Wang, Z. L., & Yang, Y. (2016). Enhanced P3HT/ZnO nanowire array solar cells by pyro-phototronic effect. *ACS nano,* 10(11), 10331-10338.

Zhang, N., Li, X., Ye, H., Chen, S., Ju, H., Liu, D., ... & Xiong, Y. (2016). Oxide defect engineering enables to couple solar energy into oxygen activation. *Journal of the American Chemical Society*, 138(28), 8928-8935.

Zhang, X. (2013). *Organic photovoltaics: An investigation of interface layers and space-charge effects* (Doctoral dissertation, University of Houston, Texas, United States).

Zhang, Y. W., Wu, G., Dang, H., Ma, K., & Chen, S. (2017). Multicolored Mixed-Organic-Cation Perovskite Quantum Dots (FA x MA1–x PbX3, X= Br and I) for White Light-Emitting Diodes. *Industrial & Engineering Chemistry Research*, 56(36), 10053-10059.

Zhang, Y., Zhong, Y., Connor, A. L., Miller, D. P., Cao, R., Shen, J., Song, B., Baker, E.S., Tang, Q., Pulavarti, S.V. & Gong, B. (2019). Folding and assembly of short α, β, γ-hybrid peptides: Minor variations in sequence and drastic differences in higher-level structures. *Journal of the American Chemical Society*, 141(36), 14239-14248.

Zhao, Y., Jia, X., Waterhouse, G. I., Wu, L. Z., Tung, C. H., O'Hare, D., & Zhang, T. (2016). Layered double hydroxide nanostructured photocatalysts for renewable energy production. *Advanced Energy Materials,* 6(6), 1501974.

Zhong, Z., Li, K., Zhang, J., Ying, L., Xie, R., Yu, G., Huang, F. & Cao, Y. (2019). High-performance all-polymer photodetectors via a thick photoactive layer strategy. *ACS applied materials & interfaces*, 11(15), 14208-14214.

Zhou, C., Zhan, P., Zhao, J., Tang, X., Liu, W., Jin, M., & Wang, X. (2020). Long-lasting CaAl2O4: Eu2+, Nd3+ phosphor-coupled g-C3N4 QDs composites for the round-the-clock photocatalytic methyl orange degradation. *Ceramics International*, *46*(17), 27884-27891.

Zhou, F., Li, Z., Chen, H., Wang, Q., Ding, L., & Jin, Z. (2020). Application of perovskite nanocrystals (NCs)/quantum dots (QDs) in solar cells. *Nano Energy*, 73, 104757.

Zhou, H., Shi, Y., Dong, Q., Zhang, H., Xing, Y., Wang, K., ... & Ma, T. (2014). Hole-conductor-free, metal-electrode-free TiO2/CH3NH3PbI3 heterojunction solar cells based on a low-temperature carbon electrode. *The journal of physical chemistry letters*, 5(18), 3241-3246.

Zhou, N., Kim, M. G., Loser, S., Smith, J., Yoshida, H., Guo, X., ... & Marks, T. J. (2015). Amorphous oxide alloys as interfacial layers with broadly tunable electronic structures for organic photovoltaic cells. *Proceedings of the National Academy of Sciences*, 112(26), 7897-7902.